

AD-A156 589

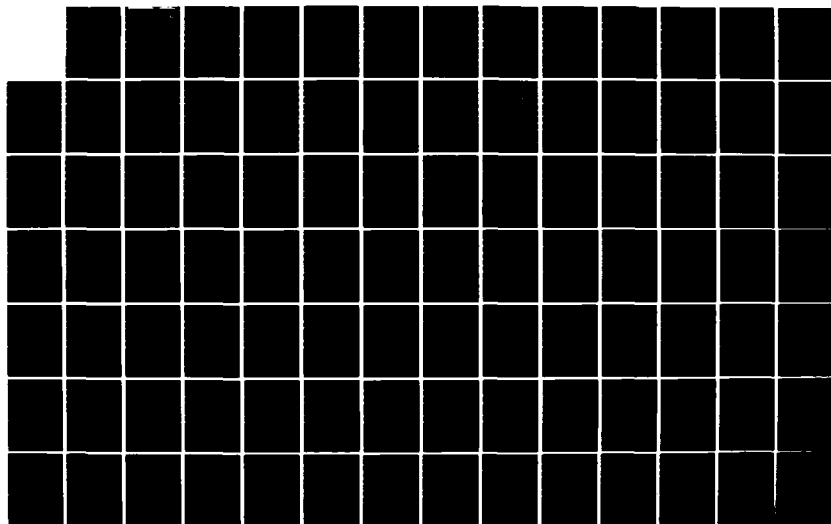
DYNAMIC ANALYSIS OF A SLED TRAVELING ALONG A ROUGH RAIL
(U) ARMAMENT DIV (AFSC) EGLIN AFB FL G L FERGUSON
15 MAY 85 AD-TR-85-39

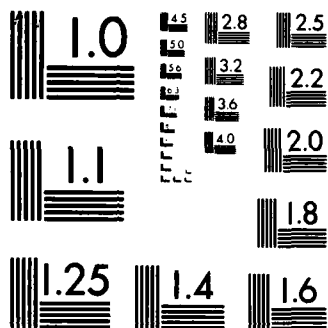
1/4

UNCLASSIFIED

F/G 12/1

NL





MICROCOPY RESOLUTION TEST CHART
NATIONAL BUREAU OF STANDARDS-1963-A

AD-TR-85-39



AD-A156 589

DYNAMIC ANALYSIS OF A SLED
TRAVELING ALONG A ROUGH RAIL

GREGORY L. FERGUSON
TEST TRACK DIVISION

6585TH TEST GROUP
HOLLOMAN AFB, NEW MEXICO 88330

MAY 1985

FINAL REPORT FOR PERIOD NOV 83 - MAY 85

APPROVED FOR PUBLIC RELEASE; DISTRIBUTION IS UNLIMITED.

The Public Affairs Office has reviewed this report, and it is releasable to the National Technical Information Service, where it will be available to the general public, including foreign nationals.

JTIC FILE COPY

RECEIVED
JUL 11 1985

ARMAMENT DIVISION

AIR FORCE SYSTEMS COMMAND • EGLIN AIR FORCE BASE, FLORIDA 32542

85 06 22 026

This report has been reviewed and approved.

A handwritten signature in cursive script, reading "Martin P. Konieczny". The signature is written in dark ink and is positioned above the printed name and title.

MARTIN P. KONIECZNY, Lt Col, USAF
Director, Test Track Division

Unclassified

SECURITY CLASSIFICATION OF THIS PAGE

AD A 156 589

REPORT DOCUMENTATION PAGE

1a. REPORT SECURITY CLASSIFICATION Unclassified			1b. RESTRICTIVE MARKINGS		
2a. SECURITY CLASSIFICATION AUTHORITY			3. DISTRIBUTION/AVAILABILITY OF REPORT Approved for Public Release/Distribution Unlimited		
2b. DECLASSIFICATION/DOWNGRADING SCHEDULE					
4. PERFORMING ORGANIZATION REPORT NUMBER(S) AD-TR-85-39			5. MONITORING ORGANIZATION REPORT NUMBER(S) AD-TR-85-39		
6a. NAME OF PERFORMING ORGANIZATION 6585th Test Group (AFSC) Test Track Division		6b. OFFICE SYMBOL (If applicable) TKEE		7a. NAME OF MONITORING ORGANIZATION	
6c. ADDRESS (City, State and ZIP Code) Holloman AFB NM 88330-5000				7b. ADDRESS (City, State and ZIP Code) JUL 11 1985	
8a. NAME OF FUNDING/SPONSORING ORGANIZATION 6585th Test Group		8b. OFFICE SYMBOL (If applicable) TKEE		9. PROCUREMENT INSTRUMENT IDENTIFICATION NUMBER A	
8c. ADDRESS (City, State and ZIP Code) Holloman AFB NM 88330-5000		10. SOURCE OF FUNDING NOS. PROGRAM ELEMENT NO. JON: TKSI 8000		TASK NO. WORK UNIT NO.	
11. TITLE (Include Security Classification) Dynamic Analysis of A Sled Traveling Along A Rough Rail (UNCLAS)					
12. PERSONAL AUTHOR(S) Ferguson, Gregory Lynn					
13a. TYPE OF REPORT Final		13b. TIME COVERED FROM Nov 83 to May 85		14. DATE OF REPORT (Yr., Mo., Day) 85-5-15	
15. PAGE COUNT 303					
16. SUPPLEMENTARY NOTATION Doctoral Dissertation					
17. COSATI CODES FIELD GROUP SUB. GR. 20 11			18. SUBJECT TERMS (Continue on reverse if necessary and identify by block number) Rocket Sled, Rail Roughness, Test Track, Rail Grinding, Statistical Analysis, Power Spectral Density, Forcing Function, Normal Distribution, Rayleigh Distribution (Cont'd)		
19. ABSTRACT (Continue on reverse if necessary and identify by block number) Rocket sleds are commonly used for simulation of special environments for testing purposes. The motion of a sled on the track induces large quasi-steady-state and dynamic forces on the sled. Design of sleds requires knowledge of these forces and of established techniques for application of measured and theoretical forcing functions to proven mathematical structural simulations. The prediction of the quasi-steady-state sled loads is relatively straightforward and requires few specialized techniques. Dynamic force prediction on the other hand is somewhat of a black art. Several techniques have been theorized but the results have been extremely marginal at best. This research is intended to find a reliable force prediction tool that is not extremely cumbersome to use. (CONTINUED ON REVERSE)					
20. DISTRIBUTION/AVAILABILITY OF ABSTRACT UNCLASSIFIED/UNLIMITED <input checked="" type="checkbox"/> SAME AS RPT <input type="checkbox"/> DTIC USERS <input type="checkbox"/>			21. ABSTRACT SECURITY CLASSIFICATION Unclassified		
22a. NAME OF RESPONSIBLE INDIVIDUAL FERGUSON, GREGORY LYNN		22b. TELEPHONE NUMBER (Include Area Code) (505) 679-2730		22c. OFFICE SYMBOL 6585TESTG/TKEE	

DD FORM 1473, 83 APR

EDITION OF 1 JAN 73 IS OBSOLETE.

UNCLASSIFIED

SECURITY CLASSIFICATION OF THIS PAGE

UNCLASSIFIED

SECURITY CLASSIFICATION OF THIS PAGE

Block 18 (Cont'd)

Gaussian Distribution, NASTRAN, SLEDYNE, DASTARR, QUASI-STEADY-STATE FORCES, Non-linear Dynamics.

Block 19 (Cont'd)

The sled track interaction process through the slipper gap constitutes a non-linear spring problem. When the slipper is in rail contact, linear static theory applies. The approach taken to the problem is based on the assumption that the linear portion of the structural system can be decoupled into two components and their associated responses. The decoupled components are the suspension assembly and the rest of the structure through its modal response. The suspension response is commonly referred to as the rigid body response. A three-dimensional non-linear computer code was developed to solve for the dynamic force contributions. This was accomplished by numerical integration of the equations of motion through the time domain based on the input parameters defining the suspension, structural modal participation, track roughness, quasi-steady-state forces, and the non-linearity of the sled track interface. The result of the program is the time history response of each slipper throughout the simulation.

Simulation results were successfully correlated to existing measured sled slipper data for both dual rail and monorail sleds, in both the vertical and lateral directions. The Test Track now has a viable design tool in DASTARR for predicting sled track interaction forces.

PREFACE

The author would like to thank the United States Air Force and its 6535th Test Group for allowing the necessary time and resources to pursue the research needed to complete this degree. He would like to thank Sgt Phil Birdine, 2Lt Randy Seligman, and Mr. Richard Blood for their invaluable assistance in implementing the non-linear computer code into the machine and for performing the extensive computer simulations required to complete the data base. Additional thanks to Mr. James Chapman for the typing of equations, and to Mr. Ron Swanson for preparing all drawings and figures.

A special thanks to Mr. Daniel Krupovage and Dr. Larry Mixon for their guidance and suggestions during the research. Additional thank yous to the entire Test Track Engineering staff for their encouragement, enlightening discussions and suggestions, and to my wife Audrey for editing this manuscript. Finally thank you to Dr. Wendell Hull for his guidance and counseling during the long pursuit of this degree.



Accession Log	
1	
2	
3	
4	
5	
6	
7	
8	
9	
10	
11	
12	
13	
14	
15	
16	
17	
18	
19	
20	
21	
22	
23	
24	
25	
26	
27	
28	
29	
30	
31	
32	
33	
34	
35	
36	
37	
38	
39	
40	
41	
42	
43	
44	
45	
46	
47	
48	
49	
50	
51	
52	
53	
54	
55	
56	
57	
58	
59	
60	
61	
62	
63	
64	
65	
66	
67	
68	
69	
70	
71	
72	
73	
74	
75	
76	
77	
78	
79	
80	
81	
82	
83	
84	
85	
86	
87	
88	
89	
90	
91	
92	
93	
94	
95	
96	
97	
98	
99	
100	

AI

TABLE OF CONTENTS

	PAGE
LIST OF TABLES.....	vi
LIST OF FIGURES.....	vii
CHAPTER	
1. INTRODUCTION.....	1
1.1 GENERAL.....	1
1.2 DESCRIPTION OF THE HIGH SPEED TRACK...	1
1.3 BACKGROUND ON SLED DESIGN.....	5
1.4 LIMITATIONS IN DYNAMIC ANALYSIS.....	16
1.5 PROPOSED AREAS OF STUDY.....	18
2. DERIVATION OF EQUATIONS OF MOTION.....	20
2.1 GENERAL.....	20
2.2 SIMULATION EQUATIONS--ONE SLED.....	22
2.3 SIMULATION EQUATIONS--COUPLED SLEDS...	57
3. DASTARR COMPUTER PROGRAM.....	60
3.1 GENERAL.....	60
3.2 DASTARR DESCRIPTION.....	60
3.3 DASTARR USER SUPPLIED INPUT.....	61
3.4 DASTARR OUTPUT.....	64
3.5 PRELIMINARY DASTARR VERIFICATION.....	65
3.6 CONCLUSIONS.....	70
4. RAIL ROUGHNESS.....	71
4.1 GENERAL.....	71
4.2 RAIL ROUGHNESS STUDY.....	72
4.3 SLEDYNE/CRUISE MISSILE SIMULATION.....	30

CHAPTER (CONT.)	PAGE
4.4 CONCLUSIONS AND RECOMMENDATIONS.....	34
5. DUAL RAIL SLED SIMULATION--RAMJET.....	33
5.1 GENERAL.....	33
5.2 RIGID BODY SIMULATION.....	96
5.3 MODAL SIMULATION.....	129
5.4 DUAL RAIL CONCLUSIONS.....	157
6. MONORAIL SIMULATION--INSTRUMENTED MONORAIL..	151
6.1 GENERAL.....	161
6.2 RIGID BODY SIMULATION.....	167
6.3 MODAL SIMULATION.....	193
6.4 MONORAIL CONCLUSIONS.....	213
7. CONCLUSIONS AND RECOMMENDATIONS.....	224
7.1 GENERAL.....	224
7.2 CONCLUSIONS.....	225
7.3 RECOMMENDATIONS FOR FUTURE STUDY.....	235
REFERENCES.....	239
APPENDICES	
A. DERIVATION OF DAMPING COEFFICIENTS.....	243
B. DERIVATION OF STEADY STATE SLIPPER FORCES...	252
B.1 COUPLED SLED DEFINITIONS.....	252
B.2 STEADY STATE SLIPPER FORCES.....	256
B.3 COUPLING FORCE DERIVATION.....	257
B.4 COUPLING DISPLACEMENT TERMS.....	264
C. FORCE-TIME SIMULATION PLOTS.....	271

LIST OF TABLES

TABLE	PAGE
2-1 SLIPPER COUNTER DEFINITION.....	41
3-1 ABIT CHECK RUN, DASTARR VERSUS SLEDYNE.....	66
4-1 TEST MATRIX.....	73
5-1 19Y-C1 MISSION, RAMJET QSS LOADS.....	95
5-2 19Y-C1 MISSION, SCALED PEAK FORCES.....	99
5-3 STATISTICAL SUMMARY OF RIGID BODY SIMULATION...	106
5-4 SAMPLE DASTARR OUTPUT.....	115
5-5 STATISTICAL SUMMARY OF MODAL SIMULATION.....	137
5-6 SUMMARY OF RAMJET NATURAL FREQUENCIES.....	160
6-1 INSTRUMENTED MONORAIL QSS LOADS.....	159
6-2 SCALED PEAK FORCES FOR INSTRUMENTED MONORAIL...	171
6-3 STATISTICAL SUMMARY OF RIGID BODY SIMULATION...	178
6-4 STATISTICAL SUMMARY OF MODAL SIMULATION.....	202
6-5 COMPARISON OF RESULTS: DASTARR VS. SLEDYNE.....	204
6-6 SUMMARY OF MONORAIL NATURAL FREQUENCIES.....	223

LIST OF FIGURES

FIGURE	PAGE
1.1 SLED CONFIGURATIONS.....	3
1.2 TRACK DETAILS.....	4
1.3 LAMBDA FACTOR VERSUS VELOCITY.....	7
1.4 FORCE TRANSDUCER DETAILS.....	10
1.5 RIGID BODY MATH MODEL.....	11
1.6 CLASSICAL EXAMPLE OF SPRING WITH GAP.....	12
1.7 PICTORIAL REPRESENTATION OF COUPLED SLEDs.....	19
2.1 RIGID BODY MOTION OF SLED.....	21
2.2 DEFORMATION DUE TO RIGID BODY MOTION.....	25
3.1 DASTARR INPUT SLED DESIGNATIONS.....	63
3.2 DASTARR SIMULATION OF PHASING EFFECTS-SLIPPER 1	69
4.1 RAIL ROUGHNESS-SOUTH 15000 TOP OF RAIL.....	74
4.2 RAIL ROUGHNESS-SOUTH 15000 BOTTOM OF RAIL.....	74
4.3 RAIL ROUGHNESS-NORTH 15000 TOP OF RAIL.....	75
4.4 RAIL ROUGHNESS-NORTH 15000 BOTTOM OF RAIL.....	75
4.5 RAIL ROUGHNESS-TS 34000 TOP OF RAIL.....	76
4.6 RAIL ROUGHNESS-TS 34000 BOTTOM OF RAIL.....	77
4.7 RAIL ROUGHNESS-TS 44000 TOP OF RAIL.....	73
4.8 RAIL ROUGHNESS-TS 44000 BOTTOM OF RAIL.....	79
4.9 LIFT STUDY VELOCITY AT 3000 FPS.....	82
4.10 LIFT STUDY VELOCITY AT 1500 FPS.....	83
4.11 SLIPPER FORCES--LONG PERIOD RAIL.....	85
4.12 SLIPPER FORCES--NO LONG PERIOD RAIL.....	86

FIGURE (CONT.)	PAGE
5.1 RAMJET TEST SLED CONFIGURATION.....	39
5.2 RAMJET MATH MODEL.....	91
5.3 19Y-C1 MISSION, QSS LOADS VS. TIME.....	94
5.4 RAMJET SLED TRAIN.....	97
5.5 SLIPPER 1 PEAK FORCE VS. PREDICTED FORCE.....	100
5.6 SLIPPER 2 PEAK FORCE VS. PREDICTED FORCE.....	101
5.7 SLIPPER 3 PEAK FORCE VS. PREDICTED FORCE.....	102
5.8 SLIPPER 4 PEAK FORCE VS. PREDICTED FORCE.....	103
5.9 SLIPPER BEAM STATISTICAL REPRESENTATION.....	105
5.10 SLIPPER 2 PEAK FORCE VS. TIME PLOTS.....	107
5.11 SLIPPER 4 PEAK FORCE VS. TIME PLOTS.....	103
5.12 SLIPPER 1 PEAK FORCE VS. TIME, MODIFIED RAIL...	112
5.13 HISTOGRAM VS. RAYLEIGH DISTRIBUTION.....	115
5.14 SLIPPER 2 WIDE BAND PSD SPECTRUM.....	120
5.15 SLIPPER 4 WIDE BAND PSD SPECTRUM.....	121
5.16 SLIPPER 2 NARROW BAND PSD SPECTRUM.....	122
5.17 SLIPPER 4 NARROW BAND PSD SPECTRUM.....	123
5.18 SLIPPER 1 PEAK FORCE VS. PREDICTION.....	132
5.19 SLIPPER 2 PEAK FORCE VS. PREDICTION.....	133
5.20 SLIPPER 3 PEAK FORCE VS. PREDICTION.....	134
5.21 SLIPPER 4 PEAK FORCE VS. PREDICTION.....	135
5.22 SLIPPER BEAM STATISTICAL REPRESENTATION.....	136
5.23 SLIPPER 2 PEAK FORCE VS. TIME PLOTS.....	139
5.24 SLIPPER 4 PEAK FORCE VS. TIME PLOTS.....	140
5.25 HISTOGRAM VS. RAYLEIGH DISTRIBUTION.....	143

FIGURE (CONT.)	PAGE
5.26 TYPICAL WIDE BAND PSD SPECTRUM.....	146
5.27 TYPICAL NARROW BAND PSD SPECTRUM.....	147
5.28 VARIABLE VELOCITY DEVIATIONS.....	155
6.1 INSTRUMENTED MONORAIL SLED.....	162
6.2 TRAJECTORY MATCH FOR INSTRUMENTED MONORAIL.....	165
6.3 QSS SLIPPER FORCE MATCH.....	166
6.4 QSS LIFT VS. MACH NUMBER.....	168
6.5 FRONT VERTICAL PEAK FORCE VS. PREDICTED.....	173
6.6 FRONT LATERAL PEAK FORCE VS. PREDICTED.....	174
6.7 AFT VERTICAL PEAK FORCE VS. PREDICTED.....	175
6.8 AFT LATERAL PEAK FORCE VS. PREDICTED.....	176
6.9 FRONT SLIPPER STATISTICAL REPRESENTATION.....	177
6.10 FRONT VERTICAL PEAK FORCES VS. TIME.....	180
6.11 FRONT LATERAL PEAK FORCES VS. TIME.....	181
6.12 HISTOGRAM DISTRIBUTION.....	184
6.13 FRONT SLIPPER VERTICAL-PSD REPRESENTATIONS.....	186
6.14 FRONT SLIPPER LATERAL-PSD REPRESENTATIONS.....	187
6.15 FRONT VERTICAL PEAK FORCE VS. PREDICTED.....	196
6.16 FRONT LATERAL PEAK FORCE VS. PREDICTED.....	197
6.17 AFT VERTICAL PEAK FORCE VS. PREDICTED.....	198
6.18 AFT LATERAL PEAK FORCE VS. PREDICTED.....	199
6.19 FRONT SLIPPER STATISTICAL REPRESENTATION.....	201
6.20 FRONT VERTICAL PEAK FORCES VS. TIME.....	206
6.21 FRONT LATERAL PEAK FORCES VS. TIME.....	207
6.22 HISTOGRAM DISTRIBUTION.....	210

FIGURE (CONT.)	PAGE
6.23 FRONT SLIPPER VERTICAL-PSD REPRESENTATION.....	212
6.24 FRONT SLIPPER LATERAL-PSD REPRESENTATION.....	213
A.1 VERTICAL BOUNCE DAMPING COEFFICIENT.....	243
A.2 PITCH DAMPING COEFFICIENT.....	245
A.3 LATERAL BOUNCE DAMPING COEFFICIENT.....	243
A.4 YAW DAMPING COEFFICIENTS.....	250
B.1 COUPLED SLED SCHEMATIC.....	253
B.2 FREEBODY OF SLED	255
B.3 CROSSTRACK REACTION FORCES.....	253
B.4 TYPICAL COUPLED SLED GEOMETRY.....	263
B.5 TYPICAL COUPLED SLED FORCE GEOMETRY.....	266
C.1 RIGID BODY DUAL RAIL, S15000 TOP.....	272
C.2 RIGID BODY DUAL RAIL, S15000 BOTTOM.....	272
C.3 RIGID BODY DUAL RAIL, N15000 TOP.....	273
C.4 RIGID BODY DUAL RAIL, N15000 BOTTOM.....	273
C.5 RIGID BODY DUAL RAIL, 34000 TOP.....	274
C.6 RIGID BODY DUAL RAIL, 34000 BOTTOM.....	274
C.7 RIGID BODY DUAL RAIL, 44000 TOP.....	275
C.8 RIGID BODY DUAL RAIL, 44000 BOTTOM.....	275
C.9 RIGID BODY DUAL RAIL, S15000 TOP.....	276
C.10 RIGID BODY DUAL RAIL, S15000 BOTTOM.....	276
C.11 RIGID BODY DUAL RAIL, N15000 TOP.....	277
C.12 RIGID BODY DUAL RAIL, N15000 BOTTOM.....	277
C.13 RIGID BODY DUAL RAIL, 34000 TOP.....	278
C.14 RIGID BODY DUAL RAIL, 34000 BOTTOM.....	278

FIGURE (CONT.)	PAGE
C.15 RIGID BODY DUAL RAIL, 44000 TOP.....	279
C.16 RIGID BODY DUAL RAIL, 44000 BOTTOM.....	279
C.17 MODAL DUAL RAIL, S15000 TOP.....	280
C.18 MODAL DUAL RAIL, S15000 BOTTOM.....	280
C.19 MODAL DUAL RAIL, N15000 TOP.....	281
C.20 MODAL DUAL RAIL, N15000 BOTTOM.....	281
C.21 MODAL DUAL RAIL, 34000 TOP.....	282
C.22 MODAL DUAL RAIL, 34000 BOTTOM.....	282
C.23 MODAL DUAL RAIL, 44000 TOP.....	283
C.24 MODAL DUAL RAIL, 44000 BOTTOM.....	283
C.25 MODAL DUAL RAIL, S15000 TOP.....	284
C.26 MODAL DUAL RAIL, S15000 BOTTOM.....	284
C.27 MODAL DUAL RAIL, N15000 TOP.....	285
C.28 MODAL DUAL RAIL, N15000 BOTTOM.....	285
C.29 MODAL DUAL RAIL, 34000 TOP.....	286
C.30 MODAL DUAL RAIL, 34000 BOTTOM.....	286
C.31 MODAL DUAL RAIL, 44000 TOP.....	287
C.32 MODAL DUAL RAIL, 44000 BOTTOM.....	287
C.33 RIGID BODY MONORAIL, S15000 TOP.....	288
C.34 RIGID BODY MONORAIL, S15000 BOTTOM.....	288
C.35 RIGID BODY MONORAIL, N15000 TOP.....	289
C.36 RIGID BODY MONORAIL, N15000 BOTTOM.....	289
C.37 RIGID BODY MONORAIL, 34000 TOP.....	290
C.38 RIGID BODY MONORAIL, 34000 BOTTOM.....	290
C.39 RIGID BODY MONORAIL, 44000 TOP.....	291

FIGURE (CONT.)	PAGE
C.40 RIGID BODY MONORAIL, 44000 BOTTOM.....	291
C.41 RIGID BODY MONORAIL, S15000 TOP.....	292
C.42 RIGID BODY MONORAIL, S15000 BOTTOM.....	292
C.43 RIGID BODY MONORAIL, N15000 TOP.....	293
C.44 RIGID BODY MONORAIL, N15000 BOTTOM.....	293
C.45 RIGID BODY MONORAIL, 34000 TOP.....	294
C.46 RIGID BODY MONORAIL, 34000 BOTTOM.....	294
C.47 RIGID BODY MONORAIL, 44000 TOP.....	295
C.48 RIGID BODY MONORAIL, 44000 BOTTOM.....	295
C.49 MODAL MONORAIL, BASELINE.....	296
C.50 MODAL MONORAIL, S15000 BOTTOM.....	296
C.51 MODAL MONORAIL, N15000 TOP.....	297
C.52 MODAL MONORAIL, N15000 BOTTOM.....	297
C.53 MODAL MONORAIL, 34000 TOP.....	298
C.54 MODAL MONORAIL, 34000 BOTTOM.....	298
C.55 MODAL MONORAIL, 44000 TOP.....	299
C.56 MODAL MONORAIL, 44000 BOTTOM.....	299
C.57 MODAL MONORAIL, BASELINE.....	300
C.58 MODAL MONORAIL, S15000 BOTTOM.....	300
C.59 MODAL MONORAIL, N15000 TOP.....	301
C.60 MODAL MONORAIL, N15000 BOTTOM.....	301
C.61 MODAL MONORAIL, 34000 TOP.....	302
C.62 MODAL MONORAIL, 34000 BOTTOM.....	302
C.63 MODAL MONORAIL, 44000 TOP.....	303
C.64 MODAL MONORAIL, 44000 BOTTOM.....	303

CHAPTER 1

INTRODUCTION

1.1 GENERAL

Located at Holloman Air Force Base, ten miles southwest of Alamogordo, New Mexico, is the United States Air Force's 6585th Test Group, whose prime responsibility is the testing and evaluation of new weapon systems prior to their being introduced into the Air Force inventory. These systems to be tested range from guidance systems and inertial components, to blast interaction tests on various air frames, to aircraft seat ejection tests. This testing is accomplished on a large number of test fixtures, among which a few include a precision high acceleration (g) centrifuge, precision rate tables, vibration tables, three-axis flight simulators, and the high speed test track.

1.2 DESCRIPTION OF THE HIGH SPEED TEST TRACK

The high speed test track is a facility where captive land-based vehicles may be tested to speeds up to 9,000 feet per second. These captive vehicles are called sleds and may be of the configurations of dual rail, monorail, wide gage, narrow gage, or of an outrigger

form. See Figure 1.1 for a pictorial representation of these sled types.

The track facility itself consists of 50,788 feet of continuously welded track. There are two rails spaced 84 inches between centerlines (dual rail spacing) running the entire 50,788 feet. The last 15,200 feet contains a third rail which is 26.32 inches east of the centerline of the east rail of the dual rail section (narrow gage spacing).

The rail is a heavy duty crane rail of 171 pounds per linear yard versus 65 pounds per yard for standard railroad rail, and comes in 39 foot lengths. The rail is tied down in both the lateral and vertical directions every 52 inches. The rail is stretched before being secured by tie downs such that a tensile load will be maintained in the rail at temperatures up to 120 degrees Fahrenheit. The master, or west, rail is aligned to a reference line to within ± 0.005 inches, with the other two rails aligned to within ± 0.010 inches of the true gage spacing from the master rail. The track does not follow earth curvature, but consists of straight segments connected by transition arcs of one million foot radii. See Figure 1.2 for a representation of the track details.^{1,2}

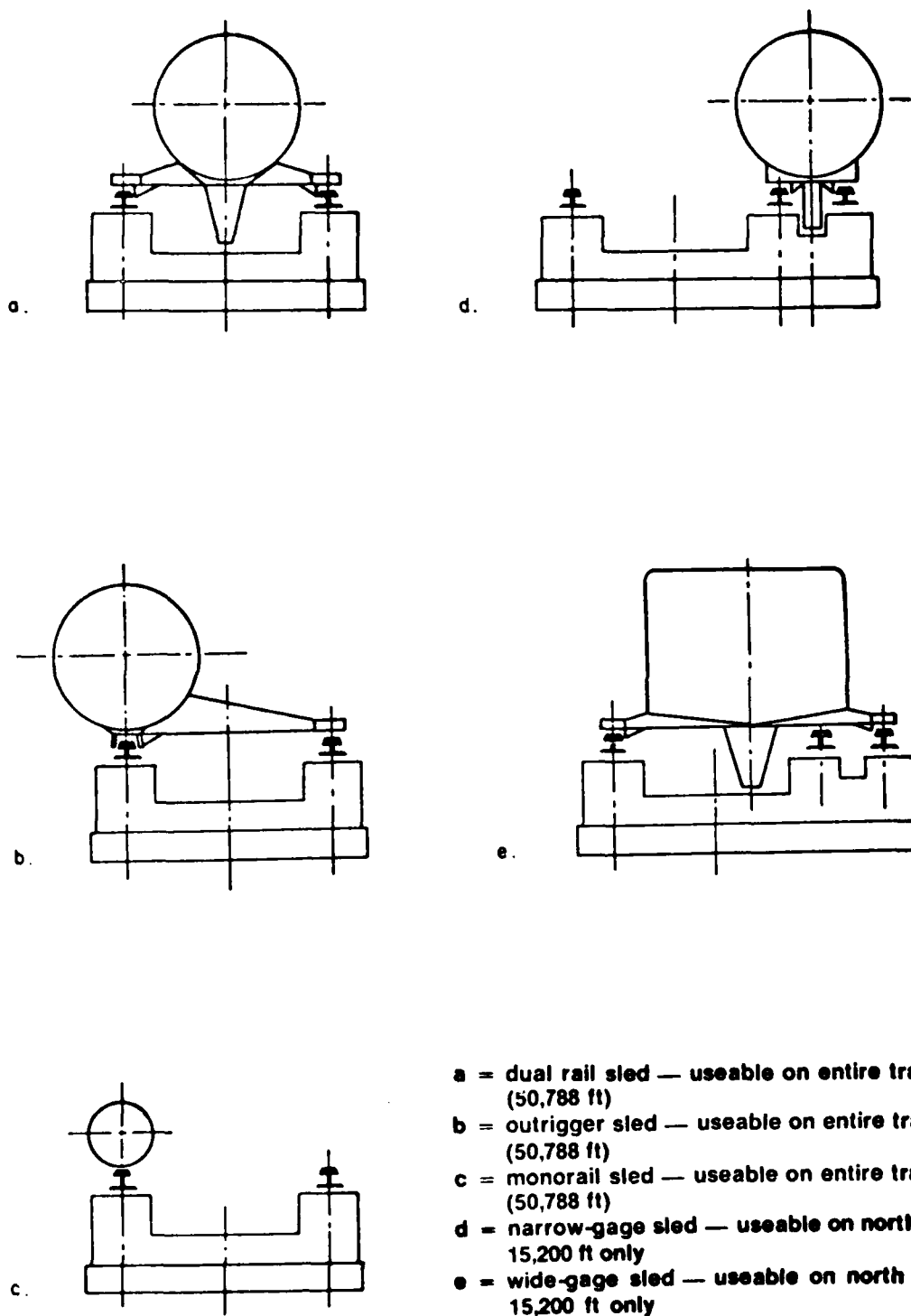


FIGURE 1.1 BASIC SLED CONFIGURATIONS

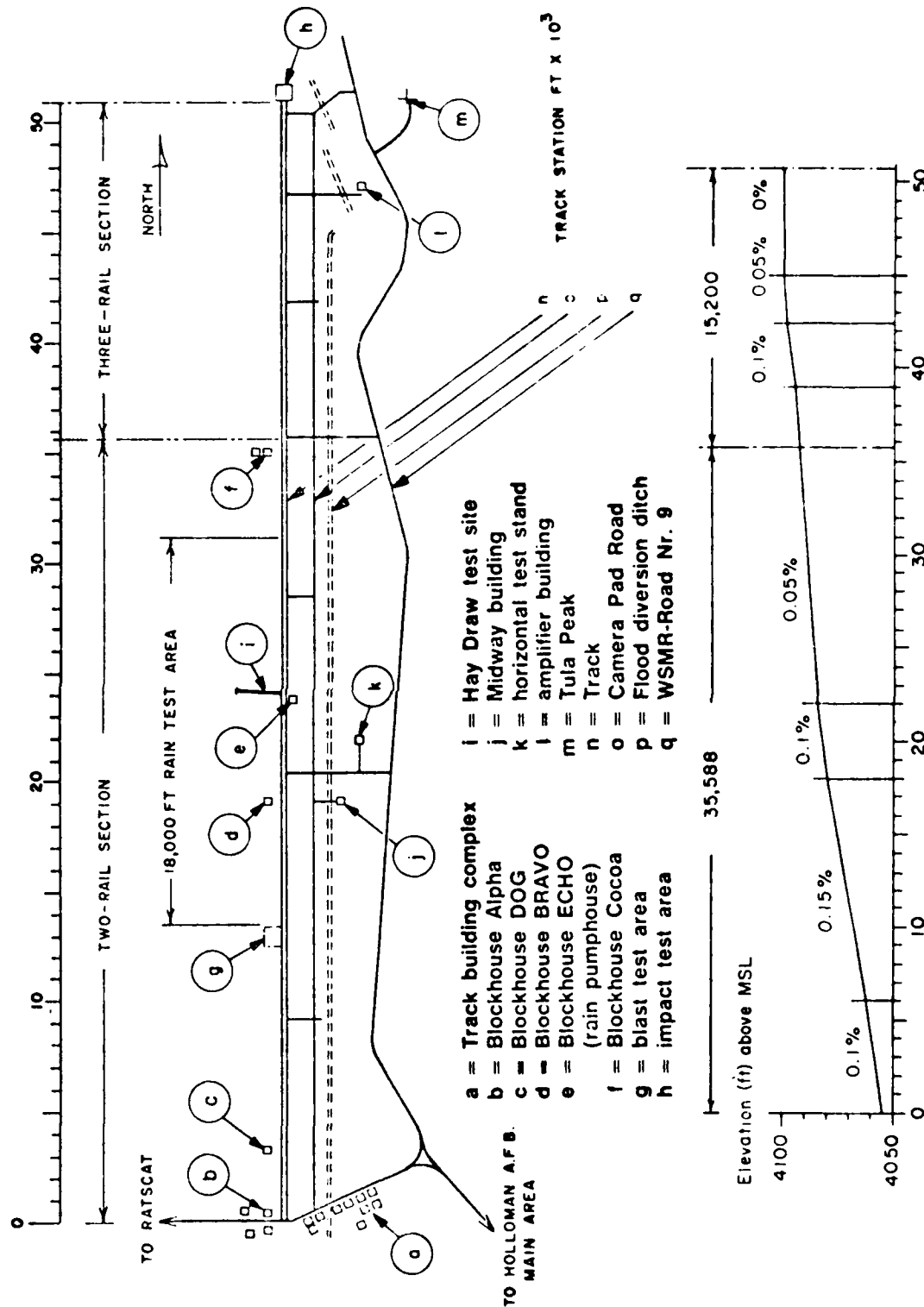


FIGURE 1.2 TRACK DETAILS

1.3 BACKGROUND ON SLED DESIGN

Present day track test programs are requiring sleds which operate in the hypersonic velocity range for monorail sleds and up to Mach 3.0 for dual rail sleds. The design of these sleds demands load prediction techniques that insure sled integrity while minimizing sled weight.

Design loads are based first on the "quasi-steady-state" forces. The quasi-steady-state forces are slowly varying forces and are defined as the forces acting on the sled due to inertia, thrust, friction, braking, and aerodynamics. Inertia, thrust, braking, and the friction forces are adequately estimated based on weight analysis, momentum exchange equations, and past experimental tests. The aerodynamic forces are basically derived from wind tunnel testing. However, the results of the wind tunnel tests are used with some reservation due to the approximations required to implement the wind tunnel tests, i.e., scaling of sleds, boundary layer effects of the ground plane-sled interaction surface, and the fact that the results are only good in the supersonic velocity regime. The equations of motion are solved to estimate the quasi-steady-state forces where tables of sled weight, thrust, and moment arms versus time, as well as aerodynamic forces versus velocity, are interpolated by

means of a computer.

Besides the quasi-steady-state forces, the sled structure is also subjected to significant oscillatory forces caused by surface roughness of the rails, propulsion transients, aerodynamic buffeting, acoustics, and sled-track interactions. These "dynamic" forces have been handled in various ways over the years, none of which have been totally successful in accurately predicting sled dynamic forces. These methods have been successful from the standpoint they yielded a conservative sled design. The history of these sled dynamic estimations will now be briefly discussed.

1.3.1 LAMBDA METHOD³

This method, developed in early track testing, amounts to adding an additional steady-state force on the sled. This additional force was defined in terms of a factor called lambda (λ), which was based on sled velocity. This factor was applied at the sled's center of mass and acted as an inertial loading in the vertical and lateral directions on the sled. Figure 1.3 shows the lambda factors used in previous dual rail and monorail sled designs.

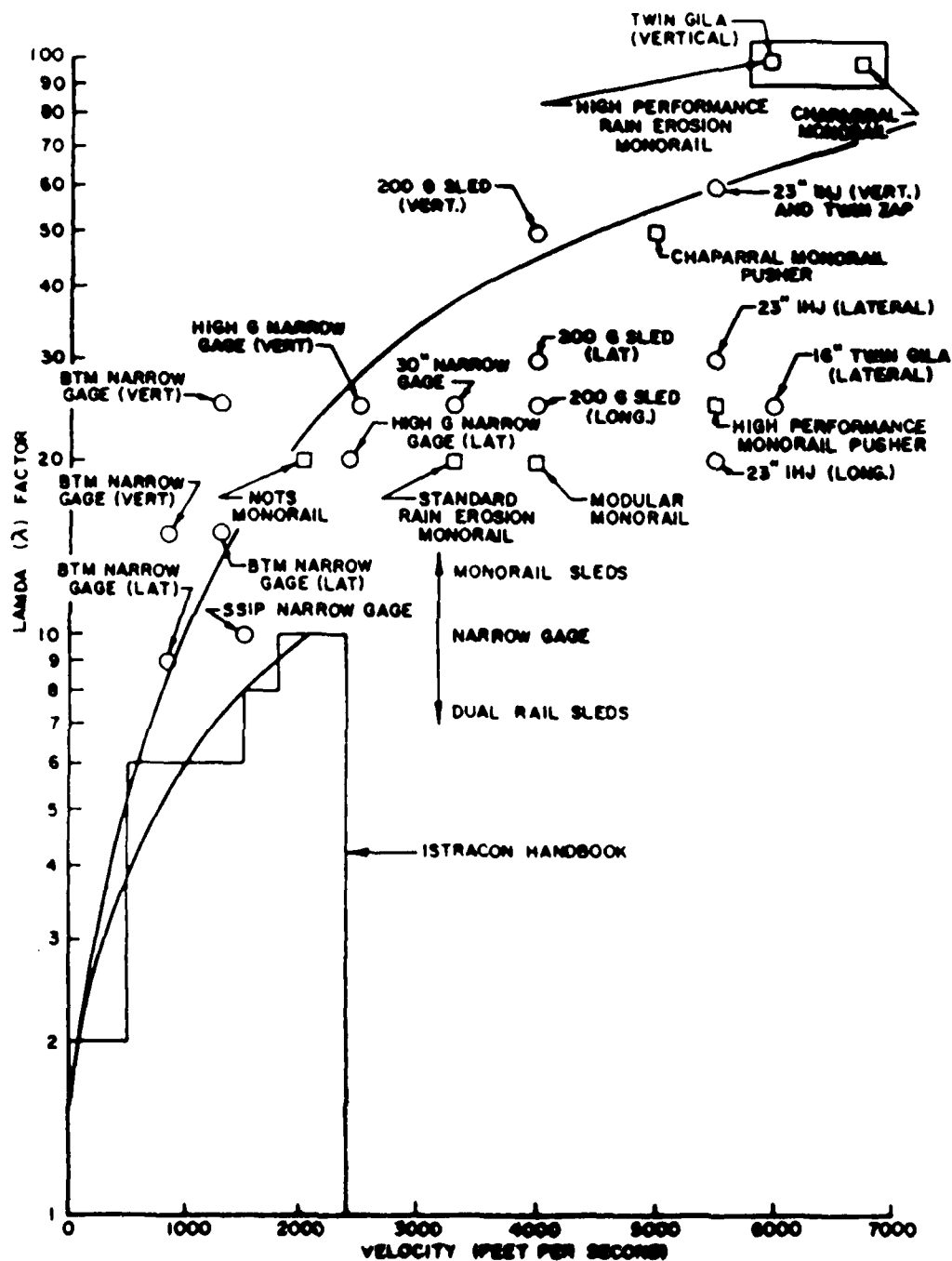


Figure 1.3 LAMBDA FACTOR VERSUS VELOCITY

1.3.2 BETA METHOD⁴

Wind tunnel tests were conducted on dual rail sleds to measure aerodynamic loads (lift and drag) on the slipper beams. These were added to the computer-predicted thrust and acceleration forces to obtain the quasi-steady-state slipper loads. These results were subtracted from actual sled run data and left only the dynamic forces. A beta (β) proportionality factor was derived which related the dynamic forces to the predicted quasi-steady-state forces. The vertical forces were then defined as the product of the beta factor times the predicted quasi-steady-state forces.

1.3.3 MONORAIL SLED DESIGN TECHNIQUES

Neither the lambda nor beta method are acceptably accurate for use on monorail sled designs. This is mainly due to the fact that oscillatory forces in monorail sleds are, in general, an order of magnitude greater than in dual rail sleds. Also, due to the very high stiffnesses, the vibrational amplitudes of the monorail sleds are a function of sled velocity as well as the sled structural response, whereas the dual rail sled vibration strain energies are located at the lowest natural modes of vibration (in the order of 15-20 Hz.).

Many theoretical studies have been performed trying to correlate the predicted vibration results of monorail sleds to the measured results. These have ranged from subjecting a mathematical model of the sled of varying complexity to a nonlinear forcing function of one form or another. ⁵Mixon provides an excellent synopsis of all the theoretical attempts, which in the final analysis yielded only marginal results.

⁶Mixon then went through an extensive design and test program to validate force measuring transducers (Figure 1.4) for use with primarily monorail sleds. All forces were resolved into their respective components within three percent of the applied loading. By the proper addition or subtraction of components, total force in a given direction could be defined. When multiplied by the proper lever arm, the appropriate moments acting on the sled and slipper assemblies are determined.

Mixon then mathematically predicted the resulting dynamic forces due to a sled traversing a "rough" rail. He did this by developing a nonlinear model of a monorail sled. This model consisted of a rigid body approximation of the vehicle with up to six (6) degrees of freedom associated with the center of mass. This resulted in a sled model similar to that shown in Figure 1.5.

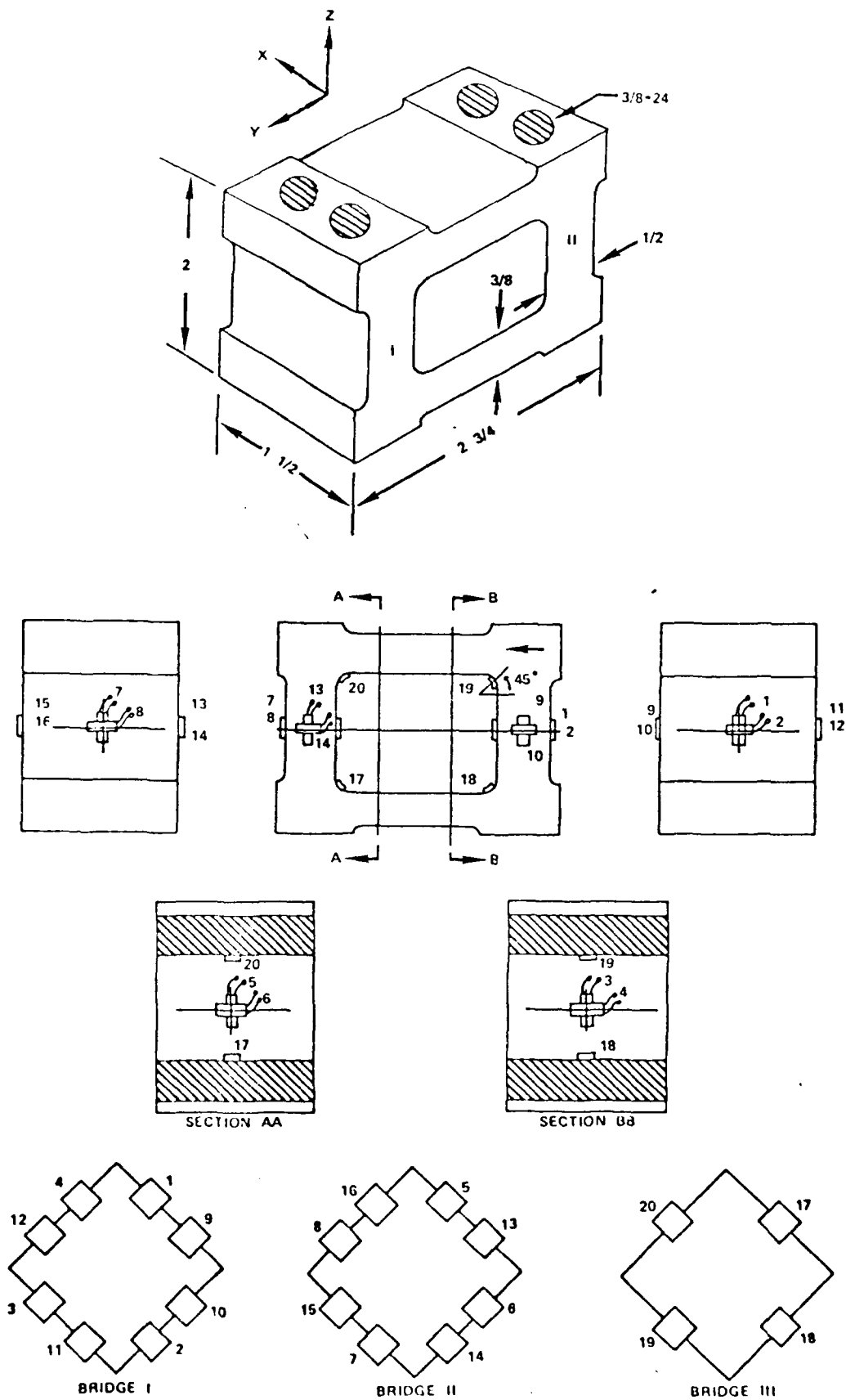


Figure 1.4 Force Transducer Details

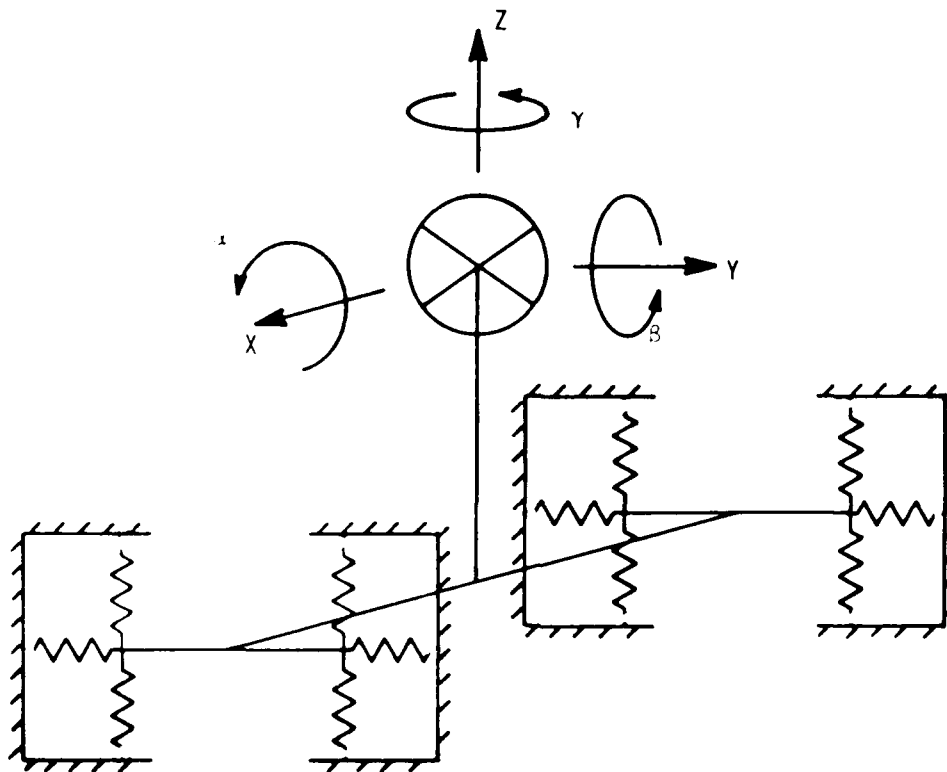


FIGURE 1.5 RIGID BODY MATH MODEL

The supports for the sled, represented as spring/damper assemblies, mathematically allow for the clearance that exists between the slipper and the rail. The slipper gap introduces the nonlinearity to the problem--the classic case of a nonlinear spring system, one with clearances (Figure 1.6).

The problem is attacked by solving the equations of motion about the sled center of mass to find the slipper deflections. If the resultant slipper deflections exceed the specified slipper gap, rail-slipper contact occurs.

This contact induces a dynamic force into the sled through the slipper. By iterating on this concept during a sled run, the maximum dynamic forces acting on the vehicle can be predicted.

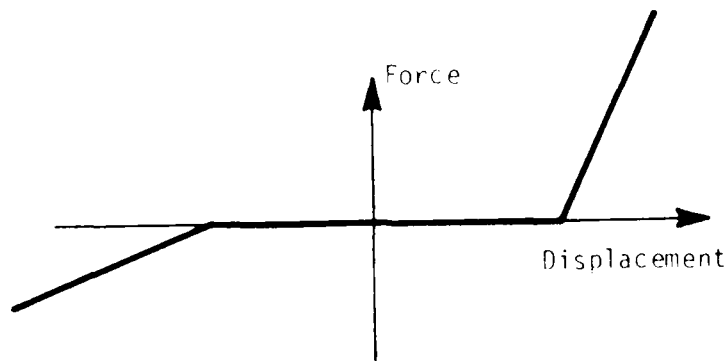


FIGURE 1.6 CLASSICAL EXAMPLE OF SPRING WITH GAP

This approach is totally contingent upon an accurate forcing function (rail roughness) being applied to the model. Original attempts at defining rail roughness were based on a 400 foot section of track that was surveyed on the top surface only at ten inch intervals.

Correlation by Mixon showed that the rigid body approach with a nonlinear forcing function and a five (5) percent structural damping assumption overpredicted the vertical dynamic forces by 20 to 50 percent of measured. However, lateral dynamic forces were consistently underestimated by 50 to 60 percent. The lateral force discrepancies were assumed to be attributable to the

assumptions that (a) the lateral rail forcing function was identical to the vertical rail survey, (b) to neglecting any cross-track wind buffeting effects, or the lateral rail roughness, and (c) to misalignment of the center of gravity in the lateral direction.

1.3.4 SLEDYNE--PHASE I⁷

Based on the results and recommendations of Nixon's monorail work, a contract was let to Mechanics Research Incorporated (MRI) to develop a nonlinear math model for use with dual rail sleds, as well as monorails. What resulted was a design guide and the development of the SLEDYNE computer program for predicting dynamic force resultants on the slippers of a traveling sled.

The development of SLEDYNE was based on the earlier rigid body monorail work of Nixon. Instead of restricting their solution of the equations of motion to rigid body response, the equations allowed for some of the impact energy to be absorbed by the sled's vibrational characteristics. The limiting factor in the derivation was that only pitch plane motions (vertical translations and pitch rotations) were allowed. This did not allow for any lateral (cross-track) inputs. These cross-track dynamic forces were considered to be no greater than the vertical forces to be estimated, and

could be accounted for by the superposition of a properly scaled vertical force.

The one overriding assumption inherent in this derivation was that it be possible to isolate two sled properties and their respective responses. These were the slipper stiffnesses, which transmit only vertical dynamic forces into the remainder of the sled structure, and the sled body, which can be defined by a set of normal vibrational modes. By the proper use of this assumption all of the sled's behavior is preserved.

The approach then taken was to iterate the equations of motion for the given sled trajectory over the prescribed forcing function. Again the forcing function was the original 400-foot section of surveyed rail.

The results of SLEDYNE compared reasonably well with Nixon's monorail measurements. The actual forces were dependent on the number of modes and damping percentages used. Five percent damping and use of six modes predicted vertical slipper forces within ± 10 percent for maximum velocity. No comparison could be made for lateral dynamics. The results also correlated within ± 10 percent of the previously measured vertical dynamic forces for dual rail sleds. The limitations with these results were that they were only considered accurate when predicting forces during the coast phase of the profile. The simulation was never attempted when a thrusting vector

was applied to the model due to engine transients.

One important development for dual rail sleds came from this study. A parameter called the SIMP (Simulated Impact Parameter) factor was fortuitously found. The forward and aft slipper beams, for conventional dual rail sleds, are considerably more flexible than the sled body so the structure could be represented by two spring-mass systems. A simple equation was developed which gave the SIMP factor. This factor could be used to enter a chart and determine a resultant slipper beam force based on actual measurements of the dynamic slipper beam force. A distributed inertial loading could be applied to the sleds from a proper combination of these SIMP factor beam loadings. This yielded an intermediate design stage that allowed for model refinement before proceeding to the SLEDYNE design phase.

1.3.5 SLEDYNE--PHASE II⁸

Several years after the MRI development, the Air Force Flight Dynamics Lab (FIBRA) at Wright-Patterson Air Force Base was contracted to make improvements in the use of the SLEDYNE program. This resulted in adapting the present structural response program, NASTRAN, for use with SLEDYNE. SLEDYNE was originally developed to be compatible with MRI's STARDYNE.

In addition to program adaptation, FIBRA did an extensive study of the forcing function being used. In past analyses, the rail roughness sample set was looped end to end to generate sufficient rail length for the forcing function. FIBRA studied generating a rail from the given data set but randomly defining the sequence of the data points. FIBRA considered using a Monte Carlo method of generation, with each slipper being independent of the others, i.e., for dual rail sleds four rail profiles were generated. Track analysts did not accept this approach as giving reasonable results, so currently the rail forcing function is generated by means of a random generating process to define the start point and then looping the data end to end.

1.4 LIMITATIONS IN DYNAMIC ANALYSIS

Present limitations in the use of SLEDYNE are due to the derivation of the equations only allowing for pitch plane reactions to determine vertical dynamics. However, the roll moment of the sled also inputs forces in the vertical direction. Of prime importance in the final design is the present assumption that the lateral rail dynamics are a proportion of the vertical dynamic forces, which has been verified only for monorail sleds.

Another limitation of the program is the definition

of the rail forcing function that is to be subjected to the sled. This particular problem has been addressed. Mixon, Evans, and Gilliam⁹ had additional rail roughness measurements taken and then performed the statistical analysis. This survey was accomplished by taking fifty-one (51) measurements, one foot apart, in a 2,000 foot section of track. This was repeated each 2,000 feet for the entire 50,000 feet of track. The survey included roughness measurements on the rail's top, side, and bottom of the west rail.

Results of the analysis indicated the rail could be grouped into four (4) distinct statistical roughness categories. Further analysis showed some surprising results: each 39 foot section of rail showed itself in a power spectral analysis, as also did the 52 inch tie down spacing. The final conclusion was that not enough data points were available to accurately define a frequency dependent rail forcing function for dual rail sleds. These additional measurements have been made and analyzed for the final definition of the rail forcing function. These are discussed in Chapter Four.

Other limitations of the program are the inability of the user to define a varying rail-slipper gap, a varying velocity profile, and the requirement for model adaptation for use with SLEDYNE versus NASTRAN.

1.5 AREAS OF STUDY

It is the intent of this study to define new equations of motion that will predict dynamic forces in both the lateral and vertical directions. In addition, the equations are to be defined such that dynamic transmitted thrust between two coupled sleds can be predicted. See Figure 1.7 for a pictorial representation of this concept. The derivations of the sled equations of motion are to be carried out in matrix form so that if only one sled is to be analyzed, the second sled and its coupling effect on the first can be ignored. Finally, it was intended to reduce the equation matrices to analyze monorail, narrow gage, and dual rail sleds, either coupled or singularly.

Another improvement intended to be made is the ability to define a velocity profile for input into the forcing function analysis. Additionally, variable slipper clearance definition for special sleds and a new slipper stiffness definition to eliminate the need for model adaptation between NASTRAN and the existing SLEDYNE are planned.

The final direction of study will be to correlate the equation developments versus real time force measurements. This correlation will be accomplished by comparing predicted forces against existing monorail data

used by Mixon, and for dual rail sleds used by MRI in the SLEDYNE verification. Any additional correlational data necessary will be accomplished on follow-up sled runs yet to be defined.

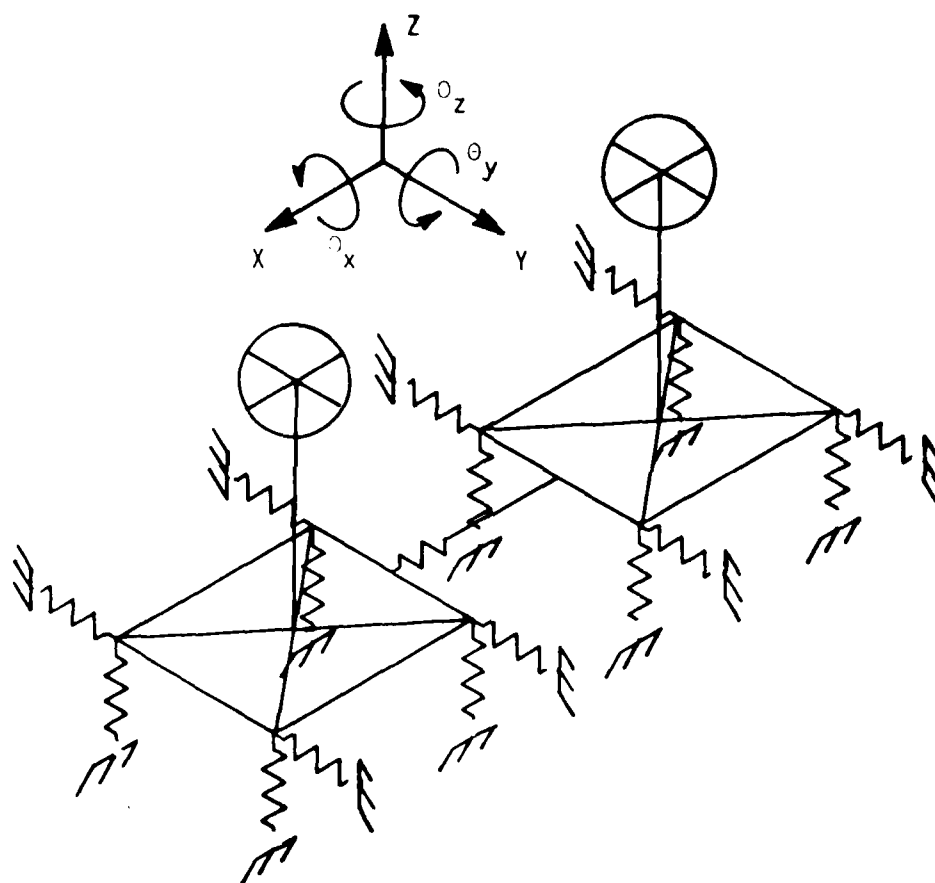


FIGURE 1.7 PICTORIAL REPRESENTATION OF COUPLED SLEDS

CHAPTER 2

DERIVATION OF BASIC EQUATIONS OF MOTION

2.1 GENERAL

The basic sled, whether dual rail, monorail, narrow gage, or outrigger, has five (5) modes of constrained rigid body motion in addition to the downtrack movement of the sled. Based on Figure 2.1 and the given coordinate system, the sled has the following rigid body capabilities:

- 1) vertical bounce--z
- 2) lateral bounce---y
- 3) pitch----- θ_y
- 4) yaw----- θ_z
- 5) roll----- θ_x

Under present design standards it has been assumed that vertical bounce (z) and pitch (θ_y) are the only critical design factors to account for, and the other three modes of excitation, combined, at most result in loads equal to this form of motion. As discussed in Chapter One, several attempts at defining rail roughness forcing functions have been tried using only this assumption. However, satisfactory verification has been

achieved only in limited circumstances.

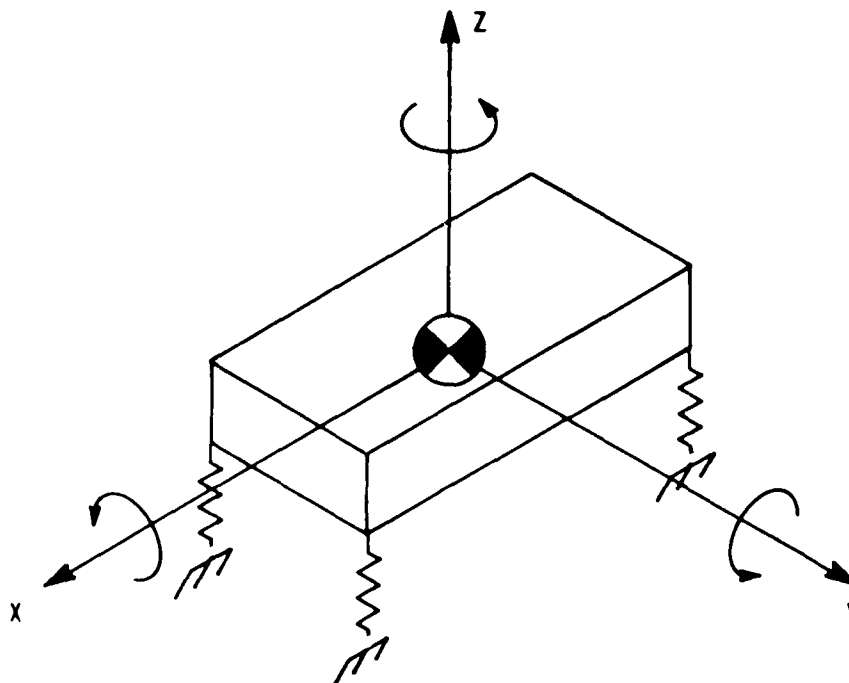


FIGURE 2.1 RIGID BODY MOTION OF SLEDS

Due to the nature of the sled trajectory and the closing of the slipper gaps due to the quasi-steady-state forces, contact between the rail and slipper occurs. Movement of the sled vehicle along the rail during contact induces high inertial forces which produce severe dynamic stresses and displacements. A transient response analysis is required in order to determine the dynamic structural response of the sled. The cost and solution time required for a transient response program (a full modal analysis at each time step) can be reduced by

performing a modal reduction to simulate the dynamic motion of the sled.

The excitation of the sled is due to the five possible rigid body modes plus the elastic modes of free vibration participating in the direction of these rigid body modes. The modal reduction is based on using only the primary modes of free vibration (i.e., the first two or three modes in each rigid body direction) for each time step instead of solving the modal equations each time.

2.2 DEVELOPMENT OF SIMULATION EQUATIONS--ONE SLED

2.2.1 DEFINITION OF SLED DISPLACEMENTS

2.2.1.1 BASIC VIBRATION THEORY

A finite element model of a sled consists of a number of nodes connected by elements. Each node is assumed to have six (6) degrees of freedom (three translational and three rotational). The dynamic equations of motion for free vibrations of a sled constrained at the slippers can be expressed in matrix form as

$$[m] \{\ddot{u}\} + [k] \{u\} = 0 \quad (1)$$

where $\{u\}$ represents the vector of displacements of the degrees of freedom (dof) associated with the sled. The mass is represented by $[m]$ and is a diagonal matrix of the lumped parameter model such that m_{ii} is the lumped mass at the i^{th} node. Finally, $[k]$ is the sled's stiffness matrix.

From basic vibration theory¹⁰, the solution of the harmonic equation represented by equation 1 is given by

$$\{u\} = \{\phi\} \cos(\omega t + \psi) \quad (2)$$

where $\{\phi\}$ is the matrix of eigenvalues, ω is the natural frequency, and ψ represents a phase angle. If equation 2 is differentiated twice and substituted into equation 1, the standard eigenvalue problem results and is given by

$$\omega^2 [m] \{\phi\} = [k] \{\phi\} \quad (3)$$

Solution of this equation gives the appropriate eigenvalues and eigenvectors.

2.2.1.2 DERIVATION OF RIGID BODY DISPLACEMENTS

The mass and stiffness matrices shown in equation 3

were derived under the assumption that the sled was supported against vertical and lateral motion by the slippers. For a true representation of a sled trajectory, this motion must be modified to include the effects of rigid body movements. This enhancement of the sled motion can be expressed as the sum of a set of displacement functions. These functions being defined are the displacements due to the natural sled body frequencies and those associated with the rigid body motions.

In order to define rigid body movements, consider Figure 2.2. For any particle P that is offset from the sled's center-of-gravity (denoted as CG in the figure) by direction vectors $\bar{x}, \bar{y}, \bar{z}$, there will be displacements due to rigid body motions of the CG. This can be expressed by the summation of the translational component and the translational effect of the rotary term. In other words, the sled displacement in the X direction (designated as u) is given by

$$u = x' - \bar{y} \odot_z + \bar{z} \odot_y \quad (4)$$

where x' denotes the translational rigid body motion in the X direction and $l_1 \odot_1$ represents the rotary effect based on small angle theory. It must be noted that since the sled is traveling downtrack (X direction), the rigid

body translational component of u does not contribute to the formulation of system displacements. Also since the sled is moving, each of the rigid body components are dependent on time, so equation 4 should be written as

$$u(t) = -\bar{y} \dot{\theta}_z(t) + \bar{z} \dot{\theta}_y(t) \quad (5)$$

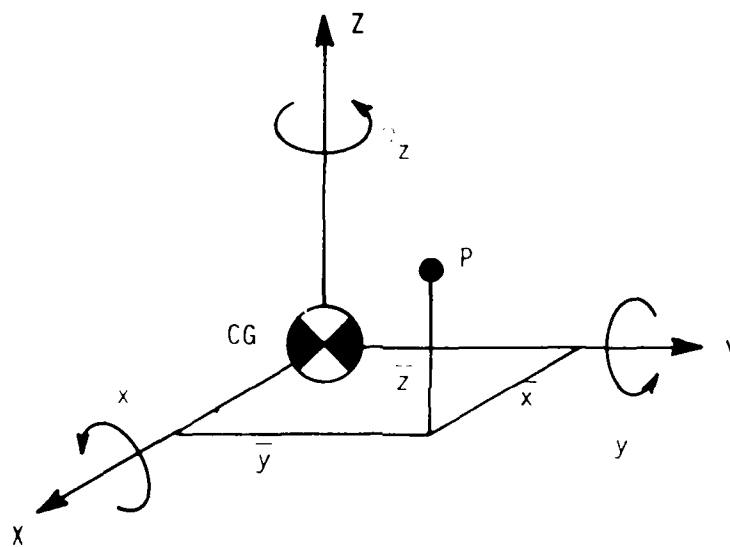


FIGURE 2.2 DEFORMATION DUE TO RIGID BODY MOTION

Similarly, displacements in the $v(Y)$ and $w(Z)$ directions are given by

$$v(t) = y'(t) + \bar{x} \dot{\theta}_z(t) - \bar{z} \dot{\theta}_x(t)$$

and

(6)

$$w(t) = z'(t) - \bar{x} \dot{\theta}_y(t) + \bar{y} \dot{\theta}_x(t)$$

Consequently the rigid body displacements can be symbolized in matrix form as shown in equation 7.

2.2.1.3 DERIVATION OF DISPLACEMENT EQUATIONS

Superimposed on the rigid body motion displacements will be the associated deformations caused by the elastic motion of the sled under natural vibration. Hence the total deflection of a point with respect to time can be written as shown in equation 8, where $q_i(t)$, $r_i(t)$, and $s_i(t)$ are the amplitude components of $\phi_i(x,y,z)$ in the X,Y, or Z directions, respectively.

Since the sled has been divided into a finite number of elements, the final displacement matrix can be written such that $[D]$ is a $N \times 3$ matrix where N represents the number of nodes in the original finite element model as shown in equation 9, where k is the number of elastic modal vibrations being used and must be less than the number of nodes, N .

2.2.2 EQUATIONS OF MOTION

As is the case for all damped linear systems, the equations of motion can be written as

$$[D'(t)] = \begin{Bmatrix} u(t) \\ v(t) \\ w(t) \end{Bmatrix} = \begin{Bmatrix} 0 \\ Y'(t) \\ Z'(t) \end{Bmatrix} + \begin{Bmatrix} 0 \\ -\bar{z} \\ -\bar{y} \end{Bmatrix} \Theta_x(t) + \begin{Bmatrix} \bar{z} \\ 0 \\ -\bar{x} \end{Bmatrix} \Theta_y(t) + \begin{Bmatrix} -\bar{y} \\ -\bar{x} \\ 0 \end{Bmatrix} \Theta_z(t) \quad (7)$$

$$[D(t)] = \begin{Bmatrix} 0 \\ Y'(t) \\ Z'(t) \end{Bmatrix} + \begin{Bmatrix} 0 \\ -\bar{z} \\ -\bar{y} \end{Bmatrix} \Theta_x(t) + \begin{Bmatrix} \bar{z} \\ 0 \\ -\bar{x} \end{Bmatrix} \Theta_y(t) + \begin{Bmatrix} -\bar{y} \\ -\bar{x} \\ 0 \end{Bmatrix} \Theta_z(t) + \sum_1 \left[\phi_1(x, y, z) \right] \begin{Bmatrix} q_1(t) \\ r_1(t) \\ s_1(t) \end{Bmatrix} \quad (8)$$

$$[D(t)] = \begin{bmatrix} u_1(t) & v_1(t) & w_1(t) \\ u_2(t) & v_2(t) & w_2(t) \\ \vdots & \vdots & \vdots \\ u_n(t) & v_n(t) & w_n(t) \end{bmatrix} = \begin{bmatrix} X_1'(t) & Y_1'(t) & Z_1'(t) \\ X_2'(t) & Y_2'(t) & Z_2'(t) \\ \vdots & \vdots & \vdots \\ X_n'(t) & Y_n'(t) & Z_n'(t) \end{bmatrix} + \begin{Bmatrix} 0. & 0. & 0. \\ 0. & 1. & 0. \\ 0. & 0. & 1. \end{Bmatrix} + \begin{bmatrix} \bar{x}_1 & \bar{y}_1 & \bar{z}_1 \\ \bar{x}_2 & \bar{y}_2 & \bar{z}_2 \\ \vdots & \vdots & \vdots \\ \bar{x}_n & \bar{y}_n & \bar{z}_n \end{bmatrix} \begin{Bmatrix} 0. & \Theta_z(t) & -\Theta_y(t) \\ -\Theta_z(t) & 0. & \Theta_x(t) \\ \Theta_y(t) & -\Theta_x(t) & 0. \end{Bmatrix} \quad (9)$$

$$+ \begin{bmatrix} \phi_{11} & \phi_{12} & \phi_{13} & \dots & \phi_{1n} \\ \phi_{21} & \phi_{22} & \phi_{23} & \dots & \phi_{2n} \\ \vdots & \vdots & \vdots & \vdots & \vdots \\ \phi_{n1} & \phi_{n2} & \phi_{n3} & \dots & \phi_{nn} \end{bmatrix} \begin{Bmatrix} q_1(t) & r_1(t) & s_1(t) \\ q_2(t) & r_2(t) & s_2(t) \\ \vdots & \vdots & \vdots \\ q_n(t) & r_n(t) & s_n(t) \end{Bmatrix}$$

$$m\ddot{x} + c\dot{x} + kx = F \quad (10)$$

where m is the system mass, c is the damping constant, k is the stiffness inherent in the system, and F is any external forcing function applied to the system, and x represents the displacement of the system.

In order to perform a dynamic stress analysis on a sled, the external forcing function, F , must be known. Part of the forcing function is known, such as the aerodynamic loads, drag forces, thrust vectors, and accelerations (the quasi-steady-state loads). However, the impact forces into the slippers of the sled are unknown and must be determined.

To solve for these unknown slipper impact forces, the equations of motion will be derived using Lagrange's equation.¹¹ This equation may be written as

$$\frac{d}{dt} \frac{\partial T}{\partial \dot{X}_i} - \frac{\partial W}{\partial X_i} + \frac{\partial R}{\partial \dot{X}_i} + \frac{\partial U}{\partial X_i} = Q_i \quad (11)$$

where T is the kinetic energy of the system, W is the work done by the system, U is the potential energy, R is the Rayleigh dissipation function, and Q_i are the nonconservative forces acting on the system. The X_i represent the independent variables of motion y' , z' , θ_x , θ_y , θ_z , and q_i , r_i , s_i for $i=1$ to k .

2.2.2.1 KINETIC ENERGY DERIVATION

The kinetic energy of a system under displacement i , given by

$$T = \frac{1}{2} m v^2 \quad (12)$$

where v is the velocity of the displacement. In terms of matrix notation this can be written as

$$T = \frac{1}{2} [\dot{D}]^T [m] [\dot{D}] \quad (13)$$

where $[\dot{D}]$ is the velocity of the system and is the derivative of $[D]$ with respect to time. So $[\dot{D}(t)]$ can be written as shown by equation 14.

Hence the kinetic energy term, when expanded in matrix form, can be expressed as

$$T = \frac{1}{2} [A]^T [m] [A] \quad (15)$$

where $[A]^T$ is a $3 \times N$ matrix and defined in equation 16.

The differential terms of $[A]^T$ can be factored out to give $[A]^T$ as the product of a differential matrix and a constant matrix as shown in equation 17, where $[\dot{n}]^T$ is a $1 \times (3N+6)$ matrix and $[C]^T$ is a $(3N+6) \times 3N$ matrix.

So now equation 15 can be rewritten as

$$\begin{aligned}
 \left[\begin{array}{c} \dot{D}(t) \end{array} \right] = & \left[\begin{array}{c} \dot{X}'_1 \quad \dot{Y}'_1 \quad \dot{Z}'_1 \\ \dot{X}'_2 \quad \dot{Y}'_2 \quad \dot{Z}'_2 \\ \cdot \quad \cdot \quad \cdot \\ \cdot \quad \cdot \quad \cdot \\ \dot{X}'_n \quad \dot{Y}'_n \quad \dot{Z}'_n \end{array} \right] \left\{ \begin{array}{ccc} 0. & 0. & 0. \\ 0. & 1. & 0. \\ 0. & 0. & 1. \end{array} \right\} + \left[\begin{array}{ccc} \bar{x}_1 & \bar{y}_1 & \bar{z}_1 \\ \bar{x}_2 & \bar{y}_2 & \bar{z}_2 \\ \cdot & \cdot & \cdot \\ \cdot & \cdot & \cdot \\ \bar{x}_n & \bar{y}_n & \bar{z}_n \end{array} \right] \left\{ \begin{array}{ccc} 0. & \dot{O}_z(t) & -\dot{O}_y(t) \\ -\dot{O}_z(t) & 0. & \dot{O}_x(t) \\ \dot{O}_y(t) & -\dot{O}_x(t) & 0. \end{array} \right\} + \phi_{j1} \left\{ \begin{array}{ccc} \dot{q}_1(t) & \dot{r}_1(t) & \dot{s}_1(t) \\ \dot{q}_2(t) & \dot{r}_2(t) & \dot{s}_2(t) \\ \cdot & \cdot & \cdot \\ \cdot & \cdot & \cdot \\ \dot{q}_n(t) & \dot{r}_n(t) & \dot{s}_n(t) \end{array} \right\} \quad (14)
 \end{aligned}$$

$$\begin{aligned}
 \left[A \right]^T = & \left[\begin{array}{l} \dot{X}'(t)*0. + \dot{Y}'(t)*0. + \dot{Z}'(t)*0. + \bar{x}_1*0. - \bar{y}_1*\dot{O}_z(t) + \bar{z}_1*\dot{O}_y(t) + \phi_{11}*\dot{q}_1(t) \dots\dots\dots + \dot{i}_n*q_n(t) \\ \dot{X}'(t)*0. + \dot{Y}'(t)*1. + \dot{Z}'(t)*0. + \bar{x}_1*\dot{O}_z(t) + \bar{y}_1*0. - \bar{z}_1*\dot{O}_x(t) + \phi_{11}*\dot{r}_1(t) \dots\dots\dots + \dot{i}_n*r_n(t) \\ \dot{X}'(t)*0. + \dot{Y}'(t)*0. + \dot{Z}'(t)*1. - \bar{x}_1*\dot{O}_y(t) + \bar{y}_1*\dot{O}_x(t) + \bar{z}_1*0. + \phi_{11}*\dot{s}_1(t) \dots\dots\dots + \dot{i}_n*s_n(t) \end{array} \right] \quad (16)
 \end{aligned}$$

$$= \begin{bmatrix} \mathbf{A} \\ \mathbf{I} \end{bmatrix} \begin{Bmatrix} \dot{x}^1(t), \dot{x}^2(t), \dot{z}^1(t), \dot{z}^2(t), \dot{y}^1(t), \dot{y}^2(t), \dot{f}^1(t), \dot{f}^2(t), \dot{g}^1(t), \dot{g}^2(t), \dot{h}^1(t), \dot{h}^2(t), \dot{u}^1(t), \dot{u}^2(t), \dot{v}^1(t), \dot{v}^2(t), \dot{w}^1(t), \dot{w}^2(t) \end{Bmatrix}$$

$ \begin{matrix} 0 & \dots & \dots & \dots & 0 \\ 0 & \dots & \dots & \dots & 0 \\ 0 & \dots & \dots & \dots & 0 \\ 0 & \dots & \dots & \dots & 0 \\ \bar{z}_1 & \dots & \dots & \dots & \bar{z}_n \\ -\bar{y}_1 & \dots & \dots & \dots & -\bar{y}_n \end{matrix} $	$ \begin{matrix} 0 & \dots & \dots & \dots & 0 \\ 1 & \dots & \dots & \dots & 1 \\ 0 & \dots & \dots & \dots & 0 \\ -\bar{z}_1 & \dots & \dots & \dots & -\bar{z}_n \\ 0 & \dots & \dots & \dots & 0 \\ \bar{x}_1 & \dots & \dots & \dots & \bar{x}_n \end{matrix} $	$ \begin{matrix} 0 & \dots & \dots & \dots & 0 \\ 0 & \dots & \dots & \dots & 0 \\ 1 & \dots & \dots & \dots & 1 \\ \bar{y}_1 & \dots & \dots & \dots & \bar{y}_n \\ -\bar{x}_1 & \dots & \dots & \dots & -\bar{x}_n \\ 0 & \dots & \dots & \dots & 0 \end{matrix} $
$ \begin{matrix} \phi_{11} & \dots & \dots & \dots & \phi_{1n} \\ \vdots & & \phi_{22} & \dots & \vdots \\ \vdots & & \vdots & \ddots & \vdots \\ \vdots & & \vdots & & \vdots \\ \phi_{n1} & \dots & \dots & \dots & \phi_{nn} \end{matrix} $	$ \begin{matrix} 0 & \dots & \dots & \dots & 0 \\ \phi_{11} & \dots & \dots & \dots & \phi_{1n} \\ \vdots & & \phi_{22} & \dots & \vdots \\ \vdots & & \vdots & \ddots & \vdots \\ \vdots & & \vdots & & \vdots \\ \phi_{n1} & \dots & \dots & \dots & \phi_{nn} \end{matrix} $	$ \begin{matrix} 0 & \dots & \dots & \dots & 0 \\ \phi_{11} & \dots & \dots & \dots & \phi_{1n} \\ \vdots & & \phi_{22} & \dots & \vdots \\ \vdots & & \vdots & \ddots & \vdots \\ \vdots & & \vdots & & \vdots \\ \phi_{n1} & \dots & \dots & \dots & \phi_{nn} \end{matrix} $

$\left[\begin{array}{c} \vdots \\ \vdots \\ \vdots \end{array} \right]$
 $\left[\begin{array}{c} \vdots \\ \vdots \\ \vdots \end{array} \right]$
 $\left[\begin{array}{c} \vdots \\ \vdots \\ \vdots \end{array} \right]$

$$T = \frac{1}{2} [\dot{\eta}]^T [C]^T [m] [C] [\dot{\eta}] \quad (18)$$

If a mass property matrix [M] is defined to be

$$[M] = [C]^T [m] [C] \quad (19)$$

then the kinetic energy of the system can be expressed as

$$T = \frac{1}{2} [\dot{\eta}]^T [M] [\dot{\eta}] \quad (20)$$

with [M] being a matrix of order $(3N+6) \times (3N+6)$. For conformability [m] must be a $3N \times 3N$ matrix and of the form shown in equation 21.

Now the elements of [M] can be defined as

$$M_{11} = \sum_{i=1}^{3N} m_{ii} (1)^2 = m = \text{sled mass in X direction}$$

$$M_{22} = \sum_{i=1}^{3N} m_{ii} (1)^2 = m = \text{sled mass in Y direction}$$

$$M_{33} = \sum_{i=1}^{3N} m_{ii} (1)^2 = m = \text{sled mass in Z direction}$$

$$M_{44} = \sum_{i=1}^{3N} m_{ii} (z^2 + y^2) = \text{mass moment of inertia about X axis} \\ \text{or roll inertia} = I_r$$

$$M_{55} = \sum_{i=1}^{3N} m_{ii} (x^2 + z^2) = \text{mass moment of inertia about Y axis} \\ \text{or pitch inertia} = I_p$$

$$M_{66} = \sum_{i=1}^{3N} m_{ii} (x^2 + y^2) = \text{mass moment of inertia about Z axis} \\ \text{or yaw inertia} = I_y$$

$$[m] =$$

$\begin{matrix} m_{11} & \dots & m_{1n} \\ \vdots & & \vdots \\ m_{n1} & \dots & m_{nn} \end{matrix}$	0	0
0	$\begin{matrix} m_{11} & \dots & m_{1n} \\ \vdots & & \vdots \\ m_{n1} & \dots & m_{nn} \end{matrix}$	0
0	0	$\begin{matrix} m_{11} & \dots & m_{1n} \\ \vdots & & \vdots \\ m_{n1} & \dots & m_{nn} \end{matrix}$

(21)

Or, in a more general form,

$$M_{pl} = \sum_{i=1}^{3N} [C_{i(p-6)}]^T [m_{ii}] [C_{i(p-6)}] \quad \text{for } p, l > 6 \quad (22)$$

Now for the special case where $p=1$ this reduces to

$$M_{pp} = \sum_{i=1}^{3N} [C_{i(p-6)}]^T [m_{ii}] [C_{i(p-6)}] \quad (23)$$

which is the generalized mass of the $(p-6)^{th}$ mode for $p > 6$.

For the case p and $l > 6$ and $p \neq l$ equation 22 reduces to zero since the modes are orthogonal to each other, or

$$M_{pl} = 0 \quad \text{for } p \neq l, p > 6, l > 6 \quad (24)$$

For the case where $p \neq l$ and either p or $l < 6$ results in the equation shown by equation 25.

Finally for the case $p \neq l$, and p and l are less than 6, results in $M_{pl} = 0$ due to the orthogonality of rigid body motion.

Thus $[M]$ can finally be written as indicated by equation 26.

2.2.2.2 POTENTIAL ENERGY DERIVATION

The potential, or strain, energy (U) of a system is

$$M_{pl} = \sum_{i=1}^{3n} \left\{ \begin{array}{cccc} 0. & \bar{z}_1 & -\bar{y}_1 & \phi_{11} \\ 0. & \bar{z}_2 & -\bar{y}_2 & \phi_{1n} \\ \vdots & \vdots & \vdots & \vdots \\ 0. & \bar{z}_n & -\bar{y}_n & \phi_{nn} \end{array} \right\} \left[\begin{array}{c} m_{11} \\ \vdots \\ c_{i(p-6)} \end{array} \right] \quad (25)$$

$$[M] = \begin{array}{c} \begin{array}{c} M \\ M \\ M \\ I_r \\ I_p \\ I_y \end{array} \begin{array}{c} M_{17} \\ M_{67} \\ M_{77} \end{array} \begin{array}{c} M_{17} \\ M_{67} \\ M_{77} \end{array} \begin{array}{c} M_{17} \\ M_{67} \\ M_{77} \end{array} \end{array} \quad (26)$$

given by

$$U = \frac{1}{2} kx^2 \quad (27)$$

where k is the stiffness and x is the generalized displacement experienced by the system. Using previously defined displacements and matrix notation, this becomes

$$U = \frac{1}{2} [D]^T [k] [D] \quad (28)$$

It was shown earlier that the velocity matrix was a product of a differentiated general displacement times a constant matrix. By integrating the velocity matrix the displacement matrix is obtained, and it similarly may be expressed as the product of a general displacement matrix times the constant matrix, or

$$[D] = [\eta] [C] \quad (29)$$

Therefore the potential energy may be expressed as

$$U = \frac{1}{2} [\eta]^T [K] [\eta] \quad (30)$$

where

$$[K] = [C]^T [k] [C] \quad (31)$$

and $[K]$ is a $(3N+6) \times (3N+6)$ matrix.

This matrix has elements based on the following cases:

1. For p and $l < 7$, rigid body motion is occurring and no strain energy is associated with this case, $K_{pl} = 0$.
2. For the case p and $l > 6$ and $p \neq l$, orthogonality controls and again $K_{pl} = 0$.
3. Finally, for p and $l > 6$ and $p = l$

$$K_{pp} = [C_{i(p-6)}]^T [k_{ii}] [C_{i(p-6)}]$$

or

$$K_{pp} = M_{pp} \omega_i^2 \quad i=1, N \quad (32)$$

2.2.2.3 DAMPING FORCE DERIVATION

The Rayleigh dissipation function governs the form of the damping forces. If it is assumed that damping forces are proportional to the velocity, i.e., $R = cV$, the Rayleigh function is given by

$$R = \frac{1}{2} [\dot{n}]^T [CD] [\dot{n}] \quad (33)$$

where $[CD]$ is the system's damping constants. For simplification, this damping matrix is assumed to be a diagonal matrix of order $(3N+6) \times (3N+6)$ and has the form shown in equation 34.

$$[CD]$$

=

$$\begin{bmatrix}
 \begin{array}{ccc}
 0 & \dots & 0 \\
 \vdots & \ddots & \vdots \\
 0 & \dots & 0
 \end{array} & 0 \\
 0 & \begin{array}{c} C_{77} \\ C_{88} \\ \vdots \\ C_{(3N+6)(3N+6)} \end{array}
 \end{bmatrix}$$

(34)

2.2.2.4 DERIVATION OF WORK

The work of a system is defined as the product of the force times displacement. For this problem, work will be the product of the slipper forces times the displacement the slipper undergoes. By the problem definition the structure has been pinned against modal displacements at the slippers. Therefore, only the rigid displacements can cause the slipper "spring" to do work.

Earlier the rigid body displacements for any point of the sled were derived, equations 5 and 6. Now the points on the sled are specified to be the slippers, so the values of x_i , y_i , and z_i are now defined. Let l_f and l_a represent the forward and aft distances from the sled CG to the slippers. Similarly, l_r and l_l will represent the cross track distances for dual rail type sleds. Finally z is the vertical distance that the CG is above the slippers.

From these definitions the vertical slipper deflections are given by

$$\begin{aligned}
 \delta_{FL}^V &= z' - l_f y - l_l x - \Delta_{gap_{FL}}^V \\
 \delta_{FR}^V &= z' - l_f y + l_l x - \Delta_{gap_{FR}}^V \\
 \delta_{AL}^V &= z' + l_a y - l_r x - \Delta_{gap_{AL}}^V \\
 \delta_{AR}^V &= z' + l_a y + l_r x - \Delta_{gap_{AR}}^V
 \end{aligned} \tag{35}$$

where the $\Delta_{ii}^V \text{gap}$ represents the change in slipper gap due to varying rail properties. The subscripts on δ and $\Delta^V \text{gap}$ represent forward (F), aft (A), left (L), or right (R) slippers and the superscript stands for vertical (V) deflections. Also from equation 6 the lateral deflections can be defined as

$$\begin{aligned}\delta_{FL}^L &= y' + l_f \theta_z + \bar{z} \theta_x + \Delta_{FL}^L \text{gap} \\ \delta_{FR}^L &= y' + l_f \theta_z + \bar{z} \theta_x + \Delta_{FR}^L \text{gap} \\ \delta_{AL}^L &= y' - l_a \theta_z + \bar{z} \theta_x + \Delta_{AL}^L \text{gap} \\ \delta_{AR}^L &= y' - l_a \theta_z + \bar{z} \theta_x + \Delta_{AR}^L \text{gap}\end{aligned}\tag{36}$$

From simple spring theory, the force reacting a spring is given by

$$F = K\Delta\tag{37}$$

where K is the spring stiffness and Δ is the distance the spring displaces. For the sled, the slipper spring forces occur only when the slipper and rail have contacted. This happens whenever any slipper displacement exceeds the allowable slipper gap, . Then the slipper forces can be specified as

$$F(i) = K(i) \bar{\delta}(i) \quad (38)$$

where i is a counter of one to eight defined in Table 2-1 and $\bar{\delta}(i)$ is the difference in slipper displacements and slipper gap, or

$$\bar{\delta}(i) = \delta(i) - \epsilon(i) \quad (39)$$

TABLE 2-1 SLIPPER COUNTER DEFINITION	
i	Definition
1	Forward left slipper, vertical force
2	Forward right slipper, vertical force
3	Aft left slipper, vertical force
4	Aft right slipper, vertical force
5	Forward left slipper, lateral force
6	Forward right slipper, lateral force
7	Aft left slipper, lateral force
8	Aft right slipper, lateral force

When rail slipper contact does occur, damping forces

are associated with that contact so the slipper force, equation 38, must be modified to

$$F(i) = K(i)\bar{\delta}(i) - D(i) \quad (40)$$

where $D(i)$ represents the appropriate damping force.

In order to solve for the slipper reaction forces two things must be known: the slipper gap and its change, and the damping forces. The slipper gap is simply the nominal clearance built into the slipper assembly. Normally this clearance, ϵ , is one-eighth (0.125) inch. To perform the analysis an initialized condition must be defined; therefore all slipper gaps will be assumed to be $\epsilon/2$.

The change in slipper gap is dependent on two items. The first is the position downtrack and the rail alignment at that position, hereafter referred to as rail roughness. The second item is the physical change in the rail cross-sectional properties. So the change in slipper gap is written

$$\Delta gap(i) = Y(i)[x] + \gamma(i)[x] \quad (41)$$

So the slipper force dependent on the slipper gap will be zero unless the following relationship holds

$$|\bar{\delta}(i)| = |\delta(i) - \epsilon/2| > 0 \quad (42)$$

By maintaining the proper sign for $\bar{\delta}(i)$, it will establish whether rail contact was made on the upper, lower, inner, or outer slipper surfaces.

From basic structural dynamics, damping forces are generally assumed to be proportional to the velocity, or $F = CV$. For the travel of the sled there is the possibility of four damping forces per slipper, which can act on one of the four above-mentioned surfaces.

The velocity needed for the damping forces will be the velocity at which the slipper impacts the rail. This velocity is dependent on the direction of travel of the slipper, and has been previously defined in terms of displacements, $\bar{\delta}(i)$. To find the velocity at impact it is a matter of differentiating $\bar{\delta}(i)$ with respect to time, or

$$V(i) = \frac{d}{dt}(\bar{\delta}(i)) \quad (43)$$

So for the velocity in direction one (1) this is

$$\begin{aligned} V(1) &= \frac{d}{dt}(z' - l_f \theta_y - l_l \theta_x + Y_{(1)}(x) + Y_{(1)}(x) - \epsilon/2) \\ &= \dot{z}' - l_f \dot{\theta}_y - l_l \dot{\theta}_x + \dot{Y}_{(1)}(x) + \dot{Y}_{(1)}(x) \end{aligned} \quad (44)$$

Since l_f and l_1 are constants no contribution to the velocity term is made.

The problem with equation 44 stems from defining \dot{Y} and δ . This is due to both Y and δ being functions of downtrack position and not time. However, these functions can be made time-dependent since $X = Vt$, where V represents the downtrack instantaneous velocity. So $Y(x) = Y(Vt)$ and

$$\dot{Y}(x) = \frac{d}{dt}(Y(x)) = \frac{d}{dt}(Y(Vt)) = \frac{VdY(t)}{dt} + \frac{tdY(V)}{dt} \quad (45)$$

Since constant velocity is assumed for a given time period, the differential of the velocity is zero. Now $\frac{dY(t)}{dt}$ is the change in track height for a given time increment, or it can be called the local slope. Hence

$$\dot{Y}(x) = V\bar{Y}(\bar{x}) \quad (46)$$

where \bar{x} represents the two track stations encompassed by the time interval, t .

Similarly $\dot{\gamma}(x)$ can be shown to be

$$\dot{\gamma}(x) = V\bar{\gamma}(\bar{x}) \quad (47)$$

Finally, the slipper damping force for direction one (1)

is

$$DF(1) = C(1)[z' - l_f \dot{\theta}_y - l_1 \dot{\theta}_x + V(\bar{y}(\bar{x}) + \bar{y}(\bar{x}))] \quad (48)$$

It only remains to define the damping coefficient terms and these are shown in Appendix A. The results are as follows:

For Vertical Damping

$$C(i) = \frac{4 K(i)}{\sum_{i=1}^4 K(i)} (C_b + C_p + C_r) \quad (49)$$

For Lateral Damping

$$C(i) = \frac{4 K(i)}{\sum_{i=5}^8 K(i)} (C_1 + C_y) \quad (50)$$

where

$$C_b = \frac{\xi_z}{2} \sqrt{m (K_1 + K_2 + K_3 + K_4)}$$

$$C_p = \frac{\xi_p}{(l_f^2 + l_a^2)} \sqrt{I_p (l_f^2 (K_1 + K_2) + l_a^2 (K_3 + K_4))}$$

$$C_r = \frac{\xi_r}{(l_1^2 + l_r^2)} \sqrt{I_r (l_1^2 (K_1 + K_3) + l_r^2 (K_2 + K_4))} \quad (51)$$

$$C_1 = \frac{\xi_1}{2} \sqrt{m (K_1 + K_2 + K_3 + K_4)}$$

$$C_y = \frac{\xi_y}{(l_f^2 + l_a^2)} \sqrt{I_y (l_f^2 (K_1 + K_2) + l_a^2 (K_3 + K_4))}$$

The work done by the spring, W , may be given as the integral over the displacement, or

$$W = \int_0^{\bar{\delta}(i)} \sum_{i=1}^8 [F(i) + D(i)] d\bar{\delta}(i) = \int_0^{\bar{\delta}(i)} \sum_{i=1}^8 K(i) \bar{\delta}(i) d\bar{\delta}(i)$$

$$W = \frac{1}{2} \sum_{i=1}^8 K(i) \bar{\delta}(i)^2 \quad (52)$$

2.2.2.5 EVALUATION OF DERIVATIVES

Now that all of the terms associated with Lagrange's equation of motion (equation 11) have been defined, it is possible to evaluate the partial derivatives and substitute them back into the original equation.

2.2.2.5.1 KINETIC ENERGY

From equations 18 and 19 the kinetic energy was shown to be

$$T = \frac{1}{2} [\dot{n}]^T [M] [\dot{n}] \quad (53)$$

or in non-matrix form

$$T = \frac{1}{2} M \dot{n}^2 \quad (54)$$

So

$$\frac{\delta T}{\delta \dot{\eta}} = \dot{\eta} \quad (55)$$

and

$$\frac{d}{dt} \left(\frac{\delta T}{\delta \dot{\eta}} \right) = M \ddot{\eta} = [M] \{\ddot{\eta}\} \quad (56)$$

2.2.2.5.2 POTENTIAL ENERGY

From equation 30 in a non-matrix form, the potential energy was shown to be

$$U = 1/2 K \eta^2 \quad (57)$$

So

$$\frac{\delta U}{\delta \eta} = K \eta = [K] \{\eta\} \quad (58)$$

2.2.2.5.3 DAMPING FORCE

From equation 34 the damping force was derived as

$$F = 1/2 C D \dot{\eta}^2 \quad (59)$$

Then

$$\frac{\delta F}{\delta \dot{\eta}} = CD\dot{\eta} = [CD][\dot{\eta}] \quad (60)$$

2.2.2.5.4 WORK

From equation 52 work was shown to be

$$W = \frac{1}{2} \sum_{i=1}^8 K(i) \bar{\delta}(i)^2 \quad (61)$$

So

$$\begin{aligned} \frac{\partial W}{\partial \eta} &= \frac{1}{2} \frac{\partial}{\partial \eta} \left(\sum_{i=1}^8 K(i) \bar{\delta}(i)^2 \right) \\ &= \frac{1}{2} \sum_{i=1}^8 \left(\bar{\delta}(i)^2 \frac{\partial K(i)}{\partial \eta} + K(i) \frac{\partial \bar{\delta}(i)^2}{\partial \eta} \right) \quad (62) \end{aligned}$$

but $K(i)$ is constant so the differentiation with respect to $K(i)$ is zero. Therefore

$$\begin{aligned} \frac{\partial W}{\partial \eta} &= \frac{1}{2} \sum_{i=1}^8 K(i) \frac{\partial \bar{\delta}(i)^2}{\partial \eta} \\ &= \frac{1}{2} \sum_{i=1}^8 K(i) \bar{\delta}(i) \frac{\partial \bar{\delta}(i)}{\partial \eta} \quad (63) \end{aligned}$$

but $K(i)$ is the force in spring i , so

$$\frac{\partial W}{\partial \eta} = \sum_{i=1}^8 F_s(i) \frac{\partial \bar{\delta}(i)}{\partial \eta} \quad (64)$$

By the proper substitution of $\bar{\delta}(i)$ the following values for $\partial W / \partial \eta$ are obtained and are shown in equation 65.

2.2.2.5.5 NON-CONSERVATIVE FORCES

The non-conservative forces are those defined by the damping forces. These forces will be derived by finding the virtual work done by the damping. In a mathematical expression this becomes

$$\delta W_{NC} = \sum_{i=1}^N D(i) \bar{\delta}_{\eta i}(i) = Q(i) \quad (66)$$

So by the proper substitution of $\bar{\delta}(i)$ the matrix shown in equation 67 is obtained for $Q(i)$.

2.2.2.5.6 FORCING FUNCTION

If equation 11 is rewritten, a forcing function $F(t)$ can be defined to be

$$\{F(t)\} = \frac{\partial W}{\partial x_i} + Q(i) \quad (68)$$

$$\left\{ \frac{\partial W}{\partial n} \right\} =$$

$$\begin{bmatrix} \partial W / \partial x \\ \partial W / \partial y \\ \partial W / \partial z \\ \partial W / \partial \theta_x \\ \partial W / \partial \theta_y \\ \partial W / \partial \theta_z \\ \partial W / \partial q_j \\ \partial W / \partial r_j \\ \partial W / \partial s_j \end{bmatrix} = \begin{bmatrix} 0 \\ \sum_{i=5}^8 F_S(i) \\ \sum_{i=1}^4 F_S(i) \\ [\lambda_l (F_{S2} + F_{S4}) - \lambda_r (F_{S1} + F_{S3}) + \sum_{i=5}^8 \bar{Z}_i F_S(i)] \\ [\lambda_f (F_{S3} + F_{S4}) - \lambda_a (F_{S1} + F_{S2})] \\ [\lambda_f (F_{S5} + F_{S6}) - \lambda_a (F_{S7} + F_{S8})] \\ 0 \\ \vdots \\ 0 \end{bmatrix}$$

(65)

$$\{q(i)\} =$$

$$\begin{bmatrix} 0 \\ \vdots \\ \sum_{i=5}^{\infty} D(i) \\ \vdots \\ \sum_{i=1}^{\infty} D(i) \\ [x_r (D_3 + D_4) - x_r (D_1 + D_2)] + \sum_{i=5}^{\infty} D(i) \\ [x_a (D_3 + D_4) - x_f (D_1 + D_2)] \\ [x_f (D_5 + D_6) - x_a (D_7 + D_8)] \\ 0 \\ \vdots \\ 0 \end{bmatrix}$$

(67)

This forcing matrix then would look like that shown in equation 69.

2.2.3 SUMMARY

If equations 56, 58, 60, and 68 are combined and substituted into equation 11, the following results

$$[M]\{\ddot{n}\} + [C]\{\dot{n}\} + [K]\{n\} = \{F\} \quad (70)$$

where matrices $[M]$, $[C]$, $[K]$, and $\{F\}$ are defined in equations 25, 34, 32, and 69, respectively.

The system of equations has been developed to include rigid body motion. It is now necessary to define the elements of the damping matrix, $[C]$, of equation 70 corresponding to the elastic modes of vibration. Since the rigid body modes are uncoupled from the elastic modes, equation 70 can be written as the sum of the rigid motions plus the elastic. So the equation can be written for the elastic modes as shown in equation 71, where equation 71 represents $3N$ uncoupled differential equations. For any i this equation can be rewritten as

$$M_{ii}\ddot{x}_{(i-6)} + C_{ii}\dot{x}_{(i-6)} + M_{ii}\omega_{(i-6)}^2 x_{(i-6)} = 0 \quad i=7,8,\dots,N \quad (72)$$

and $x_{(i-6)}$ represents either q_i , r_i , or s_i .

$$\left\{ F \right\}$$

$$= \begin{bmatrix} 0 \\ \sum_{i=5}^8 F(i) \\ 4 \sum_{i=1}^4 F(i) \\ [\ell_r (F_2 + F_4) - \ell_\ell (F_1 + F_3) + \bar{Z} \sum_{i=5}^8 F(i)] \\ [\ell_a (F_3 + F_4) - \ell_f (F_1 + F_2)] \\ [\ell_f (F_5 + F_6) - \ell_a (F_7 + F_8)] \\ 0 \\ \vdots \\ \vdots \\ \vdots \\ \vdots \\ 0 \end{bmatrix} = \begin{bmatrix} 0 \\ F_y \\ F_z \\ M_x \\ M_y \\ M_z \\ 0 \\ \vdots \\ \vdots \\ \vdots \\ \vdots \\ 0 \end{bmatrix} \quad (69)$$

.....

[illegible]

100

1. *Journal of the American Medical Association*, 1997; 277: 1001-1005.

$$p_1 \dots p_n \quad l_1 \dots l_n \quad s_1 \dots s_n$$

From damping theory, it is assumed

$$[C] = 2\gamma[M] \quad (73)$$

so equation 72 becomes

$$M_{ii}\ddot{x}_{(i-6)} + 2\gamma M_{ii}\dot{x}_{(i-6)} + M_{ii}\omega_{(i-6)}^2 x_{(i-6)} = 0 \quad i=7,8,\dots,N \quad (74)$$

This differential equation has the characteristic solution of

$$x_{(i-6)} = Ae^{st} \quad (75)$$

So equation 74 can be written as

$$[s^2 + 2\gamma s + \omega_{(i-6)}^2]M_{ii}Ae^{st} = 0 \quad (76)$$

This equation, for the non-trivial case, has roots at

$$s = \frac{-2\gamma \pm \sqrt{(2\gamma)^2 - 4\omega_{(i-6)}^2}}{2}$$

or

$$s = -\gamma \pm \sqrt{\gamma^2 - \omega_{(i-6)}^2} \quad (77)$$

For the critically damped case,

$$\gamma^2 - \omega_{(i-6)}^2 = 0 \quad (78)$$

where $\gamma = \gamma_0$ or $\omega_{(i-6)} = \gamma_0$ and γ_0 is the value of damping for the critically damped system. For the structural response of the sled the underdamped case is the only one of interest, or $\gamma/\gamma_0 < 1$. If it is assumed that the system damping ratio is the same as the viscous damping ratio, i.e., $\xi_{(i-6)} = \gamma / \gamma_0$, then the damping coefficient becomes

$$C_{ii} = 2\gamma M_{ii} = 2\gamma / \gamma_0 \omega_{(i-6)} M_{ii} \quad (79)$$

or

$$C_{ii} = 2\xi_{(i-6)} \omega_{(i-6)} M_{ii} \quad (80)$$

Now all elements of the generalized coordinate differential equation have been defined. The only additional modification necessary is to include the effects of any quasi-steady-state forces acting on the structure at the time of interest. These forces are defined in Appendix B, and are added to the force definition as indicated in equation 81.

$$\left\{ \begin{matrix} F \end{matrix} \right\} = \begin{bmatrix} 0 \\ F_y + FQ_{sy} \\ F_z + FQ_{sy} \\ M_x + MQ_{sx} \\ M_y + MQ_{sy} \\ M_z + MQ_{sz} \\ 0 \\ \vdots \\ \vdots \\ \vdots \\ 0 \end{bmatrix} \quad (81)$$

2.3 DERIVATION OF SIMULATION EQUATIONS--COUPLED SLEDS

Due to the nature of the types of sled couplings used at the Test Track, the equations of motion for the second sled are identical to those of the first sled, provided the conditions of compatibility are maintained at the coupling joint. Appendix B contains the derivation for the quasi-steady-state forces acting on either sled that are necessary for defining the differential equations of motion in terms of the generalized coordinates. To define the quasi-steady-state force terms, the coupling compatibility conditions

are necessary. These have also been derived in Appendix B.

Using the results of coupling compatibility, the dynamic simulation of sled two is identical to that just discussed in Chapter 2.2, provided that the proper modal displacements and masses are used. When push pad or monoball couplings are used between sleds, the type of coupling allows for decoupling of the sleds during the modal analysis. This means that individual modal analyses for sleds one and two are allowed.

Preliminary thought indicated that using a Coleman coupling between sleds would not allow the decoupling of the sleds into their respective modal analyses. This inability to decouple the sleds led to the investigation of transmitted thrust transients between sleds joined in this manner. ¹²Mixon proceeded to investigate this phenomenon. He concluded that the were due to motor burnout spikes exciting the downtrack mode of the pusher sled and this being transmitted into the forebody sled. In other words, the only coupling effects between sleds is in a downtrack mode. Therefore, individual modal analyses of each sled may also be accomplished for this type of coupling.

The net result is that the downtrack equations of motion for the forebody sled are dependent on the downtrack motions of the pusher sled. This dependency

between sleds means the equations of motion of the front sled will have to be modified. Also, the equations of motion for the back sled will have to be solved prior to solving them for the front sled.

CHAPTER 3

DASTARR

3.1 GENERAL

In Chapter Two, the equations of motion for a system of coupled sleds were derived. This derivation used the normal modes of free vibration for the sled, the natural frequencies, the generalized masses, and the diagonal matrix of the lumped masses. These quantities were assumed to be known, and, in fact, they are. These quantities are obtained by conducting a free vibration analysis of a finite element model of the sled that has been restrained against translation at the slipper support points. At present the eigenvalue extraction is accomplished using the NASTRAN computer program. These parameters are then reformatted into data acceptable to a program called DASTARR¹³ (Dynamic Analysis of a Sled Traveling Along a Rough Rail).

3.2 DASTARR DESCRIPTION

DASTARR is the computer program written as part of this study to assemble and accurately apply the equations of motion. DASTARR computes the time history response of a sled that is traversing a track that has a defined

characteristic rail roughness derived from sample survey measurements.

DASTARR uses a fourth-order Adams-Moulton predictor corrector method based on the classical fourth-order Runge-Kutta method used for time integration.^{14,15} The rationale for using this integration approach is to use the identical method as in the existing SLEDYNE. The overall intent of DASTARR is to have the ability to collapse from a six degree of freedom system into the pitch plane system of SLEDYNE and yield the same results.

The results of DASTARR are a set of force vectors and accelerations associated with each slipper. These forces and accelerations are then converted into equivalent inertial forces acting at all the individual mass points of the sled. These inertial forces are then recombined with the original finite element model and a static analysis can be performed.

3.3 DASTARR USER-SUPPLIED INPUT

DASTARR was written to be a general purpose program in what it would allow for simulation variables. For instance, it will allow for either a variable velocity or a constant velocity simulation. It will examine the "rigid body" system response for gross order of magnitude forces and then accept modal participation for refinement

of the results. It allows for constant quasi-steady-state force input (simulating constant velocity); or time or velocity dependent force input for the variable analysis. The variable force input can be done one of two ways. It can be input as a tabular function or an actual trajectory parameter file containing the information may be used. Also, the slipper force output may be specified as either quasi-steady-state forces, dynamic forces, or as peak slipper forces.

The quasi-steady-state force inputs are actually the nontransient force components acting on the sled. These are the aerodynamic drag and lift forces as well as the thrust, transmitted thrust, and braking forces acting on the sled at that given velocity. In order to handle the simulation, the program must know the magnitude and location of each of these forces. Figure 3.1 shows the graphical representation of these forces and associated locations for program input.

All required inputs into the program amount to an extensive data file. An interactive prompt program was written to facilitate the data input. This program prompts by asking questions about necessary data and properly formats the data for use with DASTARR. This program is called SLEDINP and is documented in its user's manual.¹⁶

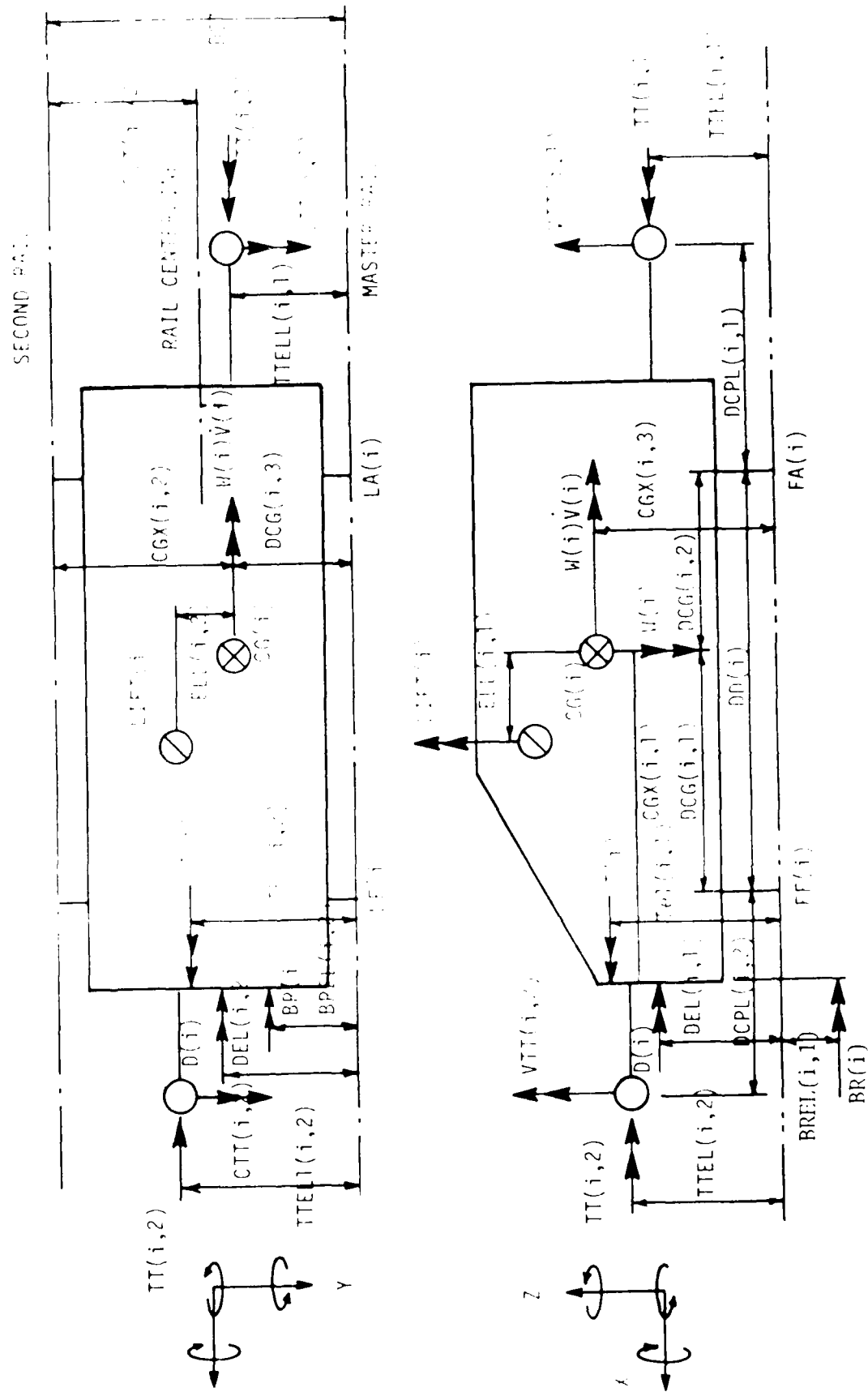


Figure 3.1 DASTARR Input Sled Designations

3.4 DASTARR OUTPUT

DASTARR, in the modal participation mode, allows the user to specify up to five displacement degrees of freedom per sled to be monitored. The program will provide the maximum displacements and accelerations associated with these degrees of freedom that were calculated during the simulation. This output is very important for sled design as some sled components, such as Velocity Measuring System (VMS) heads, are limited in allowable motion and this feature allows for monitoring the effects of dynamics on such an item.

As previously mentioned, DASTARR allows the user to specify slipper force output type versus time. Slipper forces may be defined as dynamic predicted forces, peak forces, or quasi-steady-state forces. Based on the specified type of slipper force, DASTARR will create a histogram of all calculated forces during the simulation. The histogram contains 15 bins for positive forces and 15 bins for negative forces per slipper. The bin size is based on the calculated maximum slipper force seen in the simulation. The histogram feature was added for two reasons. The first reason was to identify the number of maximum peak occurrences, and the second reason to allow for testing of data distribution in the bins. Mixon proved⁶ that dynamic forces were normally distributed and

hypothesized that peak forces were Rayleigh distributed. The histogram feature will allow for testing of these hypotheses. This is discussed further in Chapters Five and Six for dual rail and monorail sleds, respectively.

Finally, DASTARR creates a slipper force versus time output file for the simulation that may be used for external data manipulation. Particular examples of this usage is for force versus time plotting and for creating Power Spectral Density (PSD) plots of the analysis.

3.5 PRELIMINARY DASTARR VERIFICATION

In order to verify the DASTARR program output, a preliminary study was done to compare the pitch plane version of DASTARR to existing SLEDYNE results. The data base for this comparison was the Cruise Missile Sled model used on the ABIT (Aircraft Blast Interaction Test) series. This particular sled had been subjected to extensive simulation on SLEDYNE. This effort was to repeat existing test parameters for comparison purposes.

Results from one particular situation using a rough, periodic rail (Track Station 34000 top) for the forcing function input are summarized in Table 3-1. Rail forcing function inputs are discussed in Chapter Four. In the table, there are four cases investigated for the DASTARR simulation. These may be described as follows. Case

TABLE 3-1 AIRC CREEP RUN
DASTARD VS. SLEEPY

	SLIPPER 1		SLIPPER 2		SLIPPER 3		SLIPPER 4	
	TIME	FORCE	TIME	FORCE	TIME	FORCE	TIME	FORCE
1. ACTUAL SLEEPY EQUATIONS	0.443	18,531	0.145	15,658	0.376	26,770	0.263	22,400
2. DERIVED EQUATIONS (INCLUDES K)	0.003	14,333	0.145	17,009	0.376	26,553	0.671	21,037
3. DERIVED EQUATIONS OF NOTION-RIGID BODY ONLY (+K)	0.206	14,831	0.148	18,223	0.231	21,440	0.051	15,246
4. DASTARD EQUIVALENT TO SLEEPY, NO K, PEOPLE ^p STOP	0.003	14,153	0.213	18,912	0.376	21,050	0.100	18,762
5. SLEEPY	0.172	13,000	0.195	12,270	0.067	18,990	0.221	11,510

Time is actual time in seconds in simulated run where absolute force occurred.

+ sign convention for acceleration vector is wrong sense for pitch plane for DASTARD
(..)
p

Force is in pounds

number one is the derived equations of motion being exactly as in the existing SLEDYNE; however, the sign convention for pitch plane accelerations are in the opposite sense for DASTARR. Case two is the DASTARR-derived equations of motion including the instantaneous downtrack (x-axis) acceleration vector. Case three is the same as case two, only no modal participation is involved. Finally, case four is the DASTARR-derived equations of motion with matching sign convention to SLEDYNE and no downtrack instantaneous acceleration.

Notice from the table that slippers one and three are nearly identical between SLEDYNE and the DASTARR case number 4. The slight differences are attributable to round-off error in the integration of the equations of motion between computers used. The SLEDYNE version is run on a 64-bit machine, whereas the DASTARR version is run on a 16-bit machine. However, for rails two and four the results are significantly different. Upon investigation of this discrepancy, it was found that the phasing of the two rail forcing function start points is critical. Under the existing SLEDYNE simulation, this phasing was unknown and incapable of being repeated due to the random start point generator program used to start the functions. At this point a mini-study was undertaken to determine exactly what the effect was of the rail functions' respective start points.

It was decided to start with zero phase separation between rails and proceed by phasing the second rail to start in 20 foot increments behind the first rail until 200 foot of separation had been achieved. The results of the study are shown in Figure 3.2 for the sled's front two slippers. Marked on the figure are the forces predicted by SLEDYNE. Note that these marks are placed in both the positive and negative directions since SLEDYNE only looks at the absolute maximum and does not maintain signs. As can be seen in the figure, it is possible to have any number of phasing start points that will meet SLEDYNE predictions for these two slippers. Upon examining all four slippers, it was found that slippers one, two, and three could be adequately simulated by a phasing separation of approximately 150 feet. However, slipper four could not be simulated in any manner.

Further study of the model's modal analysis indicated that slipper four was very sensitive to any kind of structural input. For this velocity, the rail is imparting a fundamental frequency of 14.4 hertz due to the long period undulation. Actual vibration data taken on this sled showed slipper four having a fundamental resonance at 14.7 hertz. From this it was concluded that the uncertainty due to round-off error coupled with slipper four's modal sensitivity at this frequency

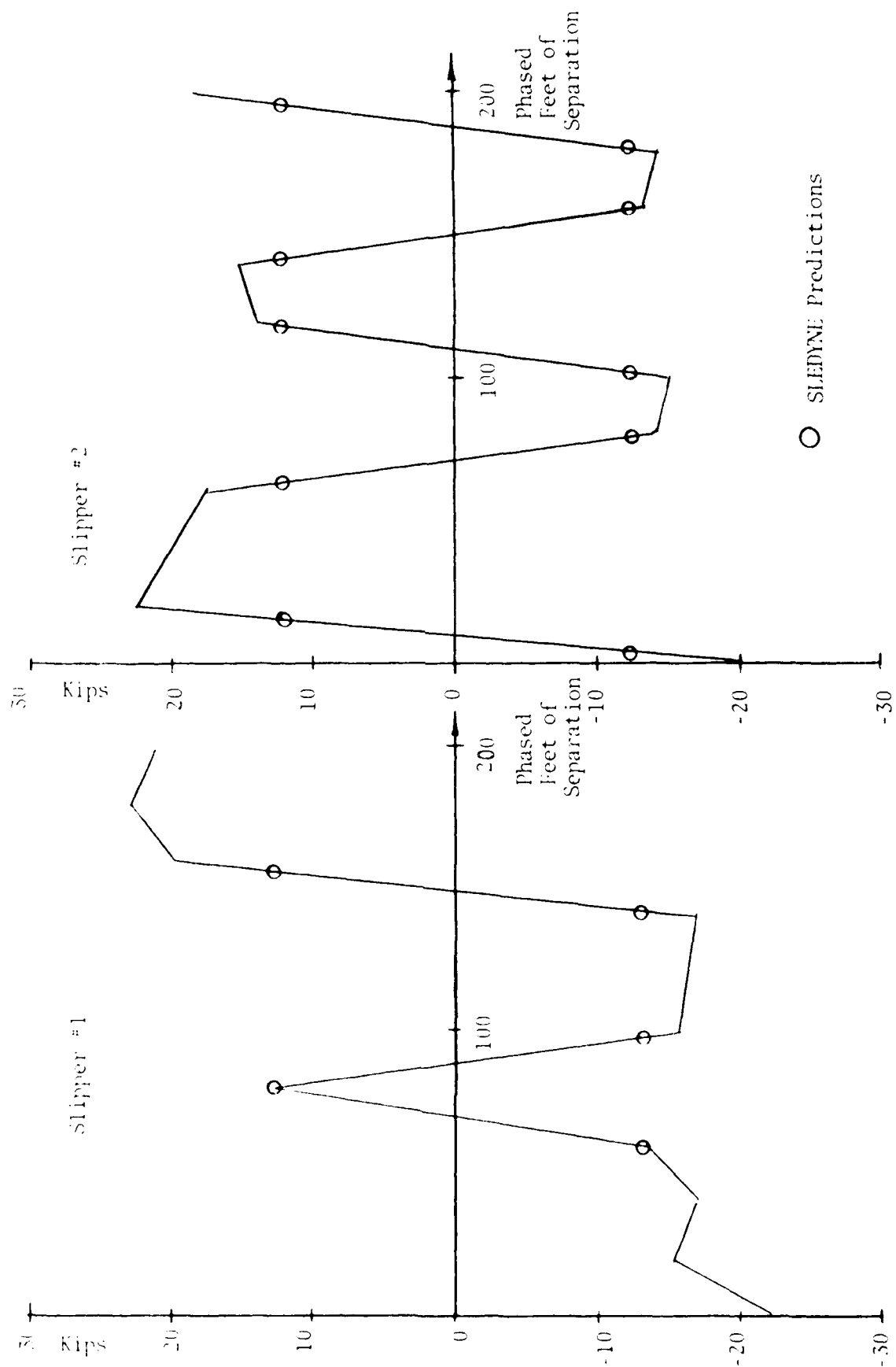


Figure 3.2 DASTARR Simulation of Phasing Effects

contributed to being unable to completely duplicate results between the two simulation programs.

3.6 CONCLUSIONS

Based on the apparent adequacy of simulation between DASTARR and SLEDYNE for pitch plane analysis, it was concluded that DASTARR provided sufficiently accurate results to continue with further studies. At this same time period another dual rail sled's finite element model had been verified through modal test studies.¹⁷ This sled is highly instrumented to measure slipper forces and a sled run had just been accomplished with verifiable slipper data. It was decided to replace the overly sensitive Cruise Missile Sled with the more reliable Ramjet sled model for the balance of the simulation studies for dual rail sleds.

CHAPTER 4

RAIL ROUGHNESS

4.1 GENERAL

Earlier in Chapter One the limitations of the rail forcing function, otherwise known as rail roughness, were discussed. Results of this rail profile study indicated that not enough rail roughness measurements had been taken (51 samples spaced one foot apart every 2000 feet of track). The study indicated that if a low frequency rail undulation (a track period in the neighborhood of 200 feet in length) existed for dual rail sleds traveling at 3000 feet per second, the first sled structural frequency (i.e., 20 hz.) might be excited. Based on this knowledge, further profile measurements were directed. The results of this survey indicated there was one section of track that did have a fundamental period of 208 feet, and another of 270 feet.

From this rail data it was necessary to determine if this profile could excite the fundamental resonances of the sled. This resulted in a directive to perform additional computer simulations with the new rail profiles to define the potential for damaging sleds based on this profile. The objectives of this special study

were four-fold, being

a. To establish a final and fixed rail roughness simulation, if possible, for SLEDYNE or its newer version.

b. To establish a fixed rail length to optimize the existing SLEDYNE prediction forces for a constant velocity run.

c. To establish if long period undulations (track periods of approximately 200 feet in length) introduce significant increases in impact forces.

d. To establish if rail grinding is effective in reducing the sled impact forces.

4.2 RAIL ROUGHNESS STUDY

These requirements resulted in developing a test matrix for performing this study (Table 4-1). This matrix was originally set up to use the existing SLEDYNE program. The tests were to be conducted on both dual rail and monorail sleds traveling at a constant velocity for that particular simulation, but varying the velocity between simulations. The rail profiles to be used are presented in Figures 4.1 through 4.8. These are the results after removing the local mean from the data. The data passed a quality control process, and the resultant

Table 1-1-1. Test Results Summary

Phase	Variable	\bar{y}_x (in)	Sample Size	Tororail		Equal Rail	
				4000lb	8000lb	4000lb	8000lb
RAIL GRINDING EFFECTIVENESS	BASE LINE	0.014	408	Peak Force in Last Cell			
	RAIL LENGTH	0.043	281				
		0.023	281				
		0.023	281				
LONG PERIOD IMPULSIONS	Top of Rail, T.S. 34,000	0.023	281				
	Top of Rail, T.S. 44,000	0.012	281				
	Bottom of Rail, T.S. 34000	0.028	281				
	Bottom of Rail, T.S. 44000	0.013	281				
RAIL GRINDING EFFECTIVENESS	Top of Rail, South 15,000	0.012	408				
	Top of Rail, North 15,000	0.016	408				
	Bottom of Rail, South 15000	0.015	408				
	Bottom of Rail, North 15000	0.020	408				

Comments:

- (1) Use Modified Sleezyne for last 44 tests.
- (2) Use optimum track length for last 32 tests.
- (3) 48 tests total and 2 local extractions.

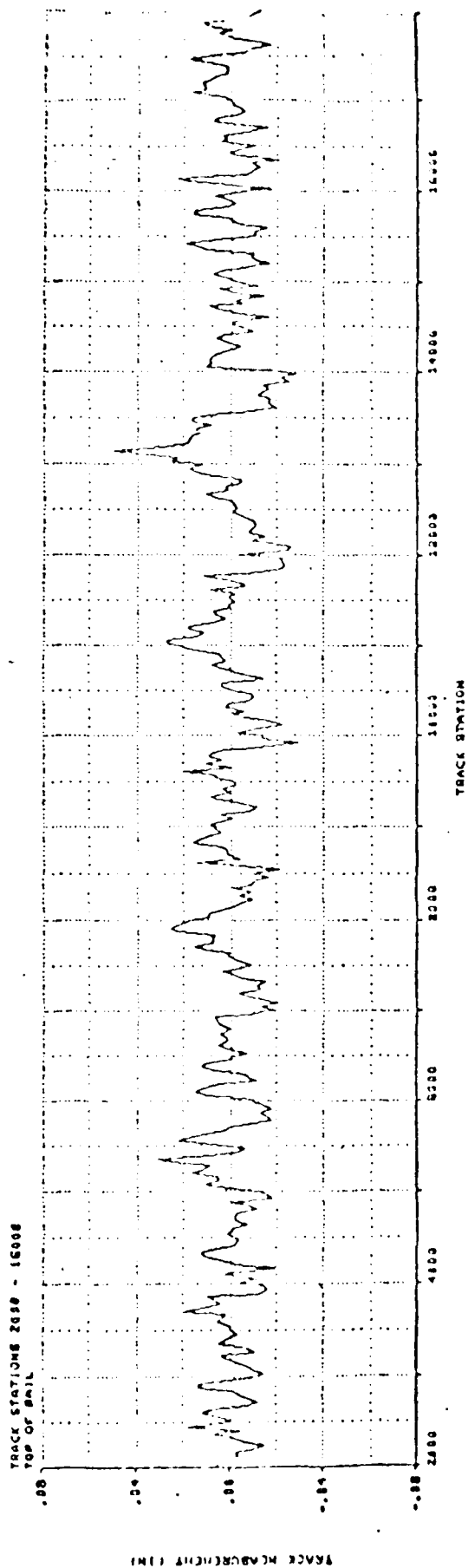


Figure 4.1 South 15000 Rail Top

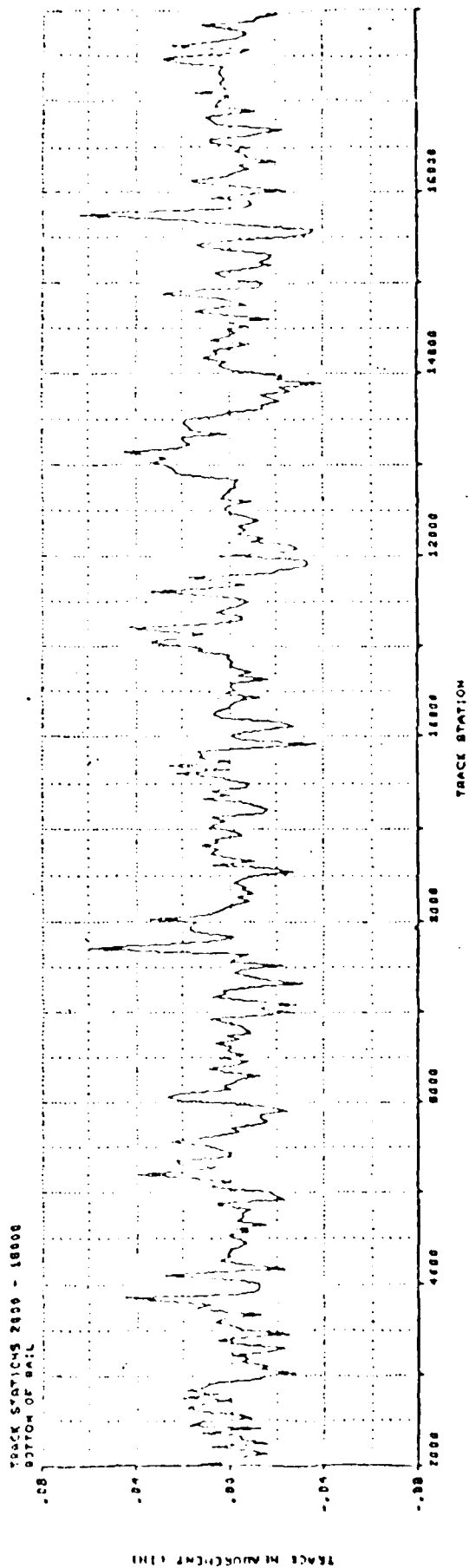


Figure 4.2 South 15000 Rail Bottom

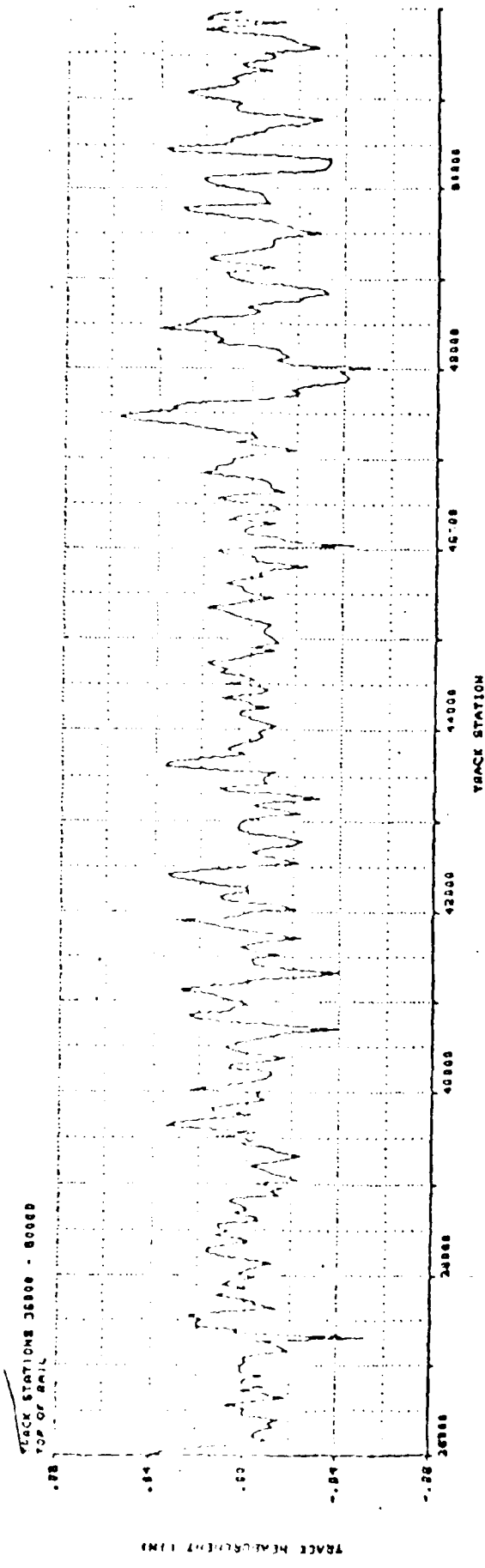


Figure 4.3 North 15000 Rail Top

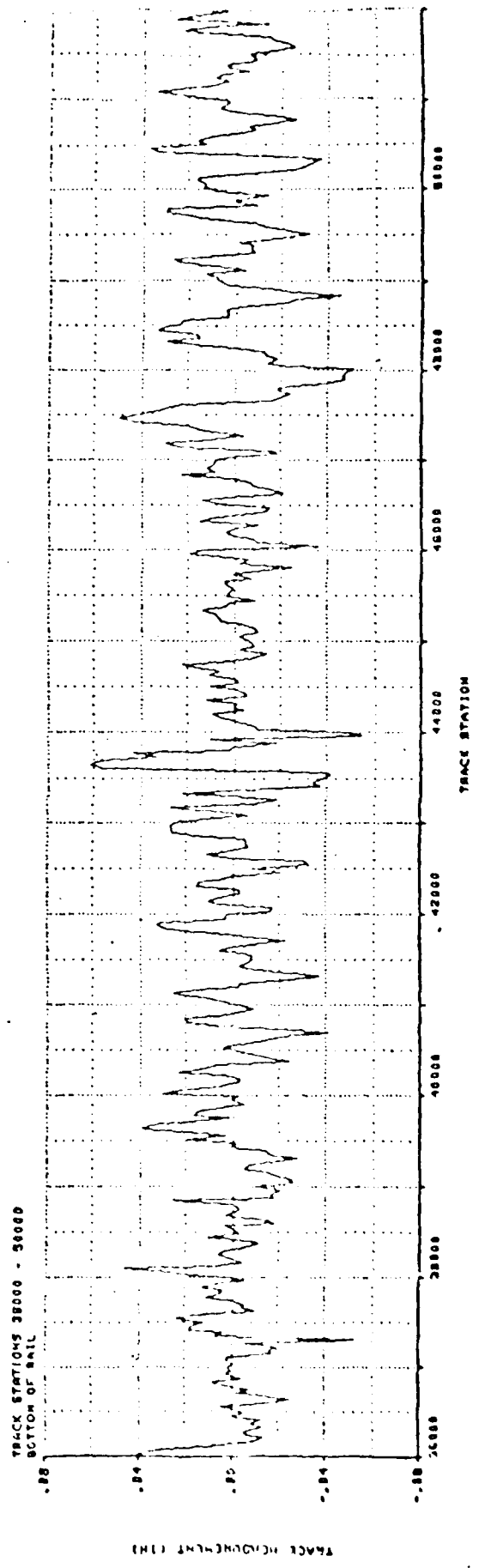


Figure 4.4 North 15000 Rail Bottom

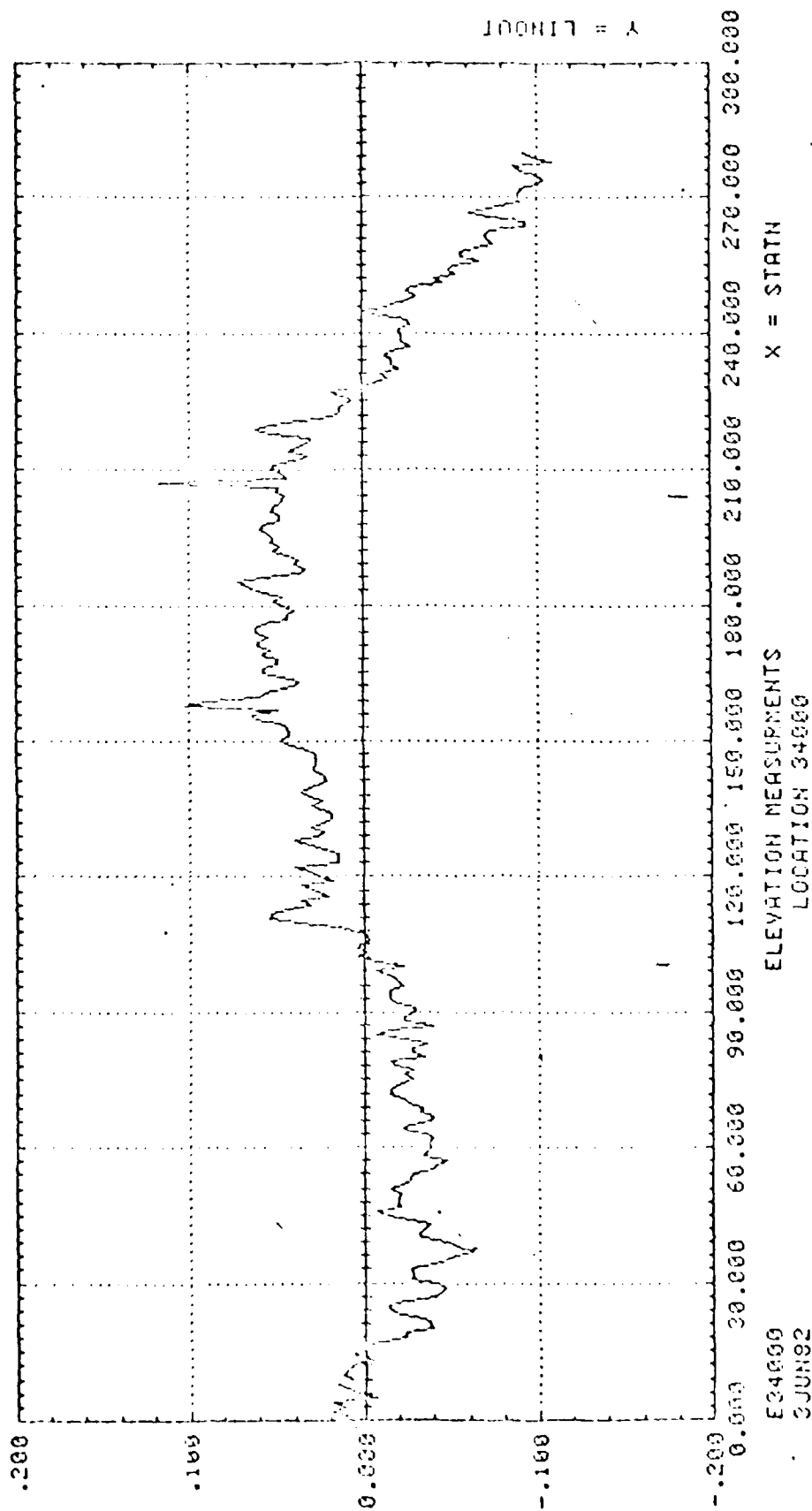


Figure 4.5 TS 34000 Rail Top

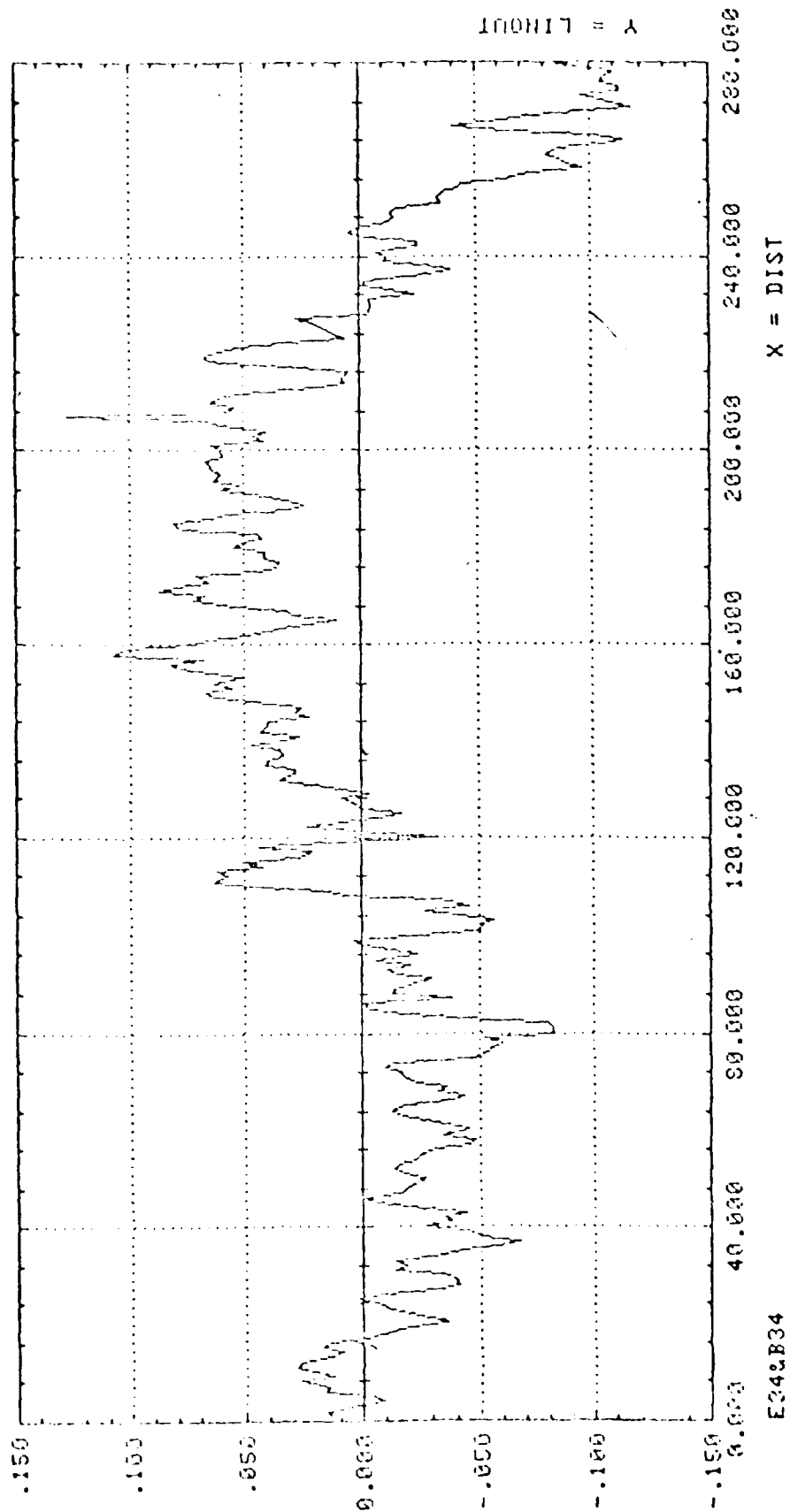
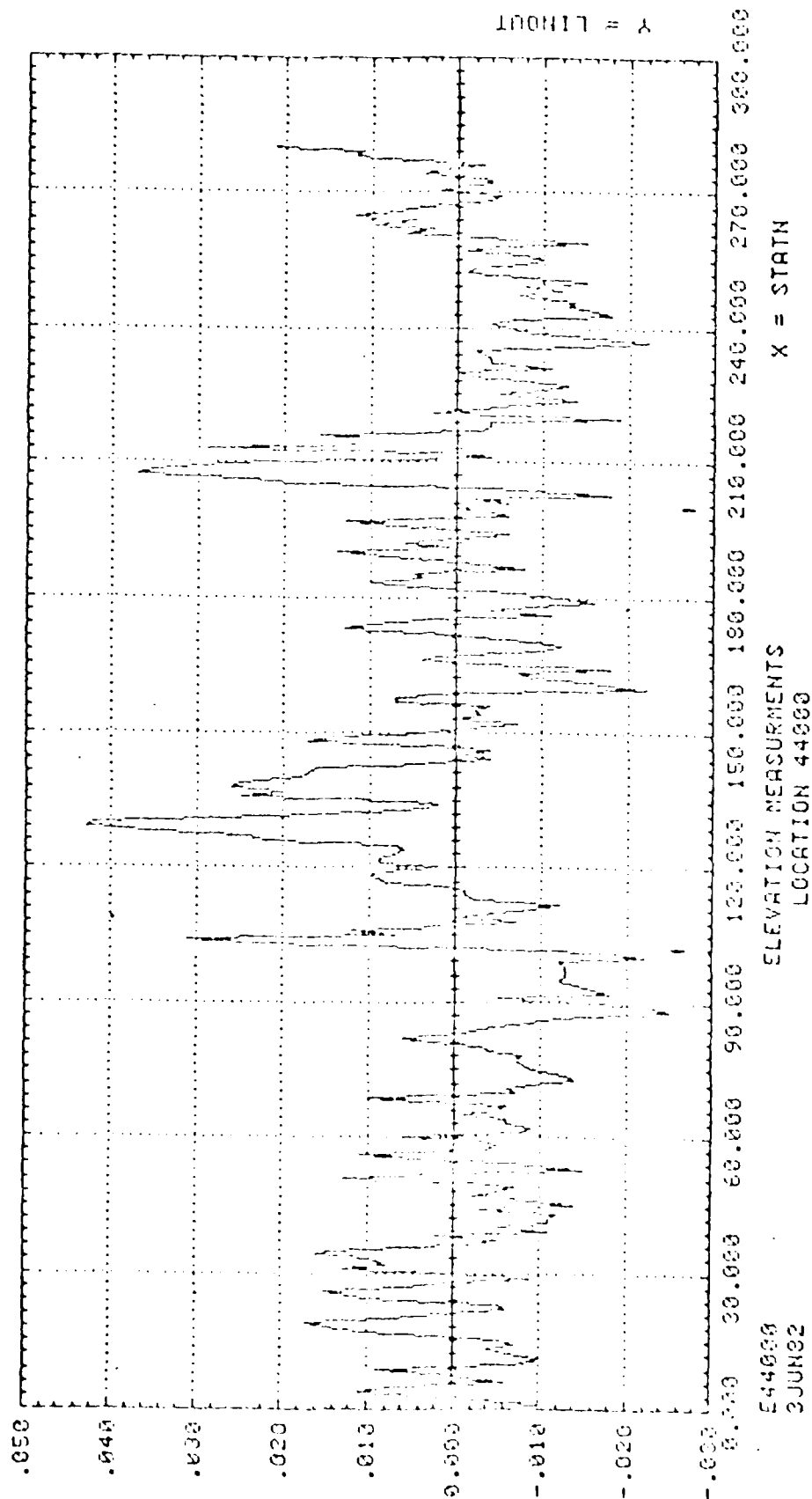


Figure 4.6 TS 34000 Rail Bottom



544000
3JUN82

544000 4.7 TS 44000 Data Top

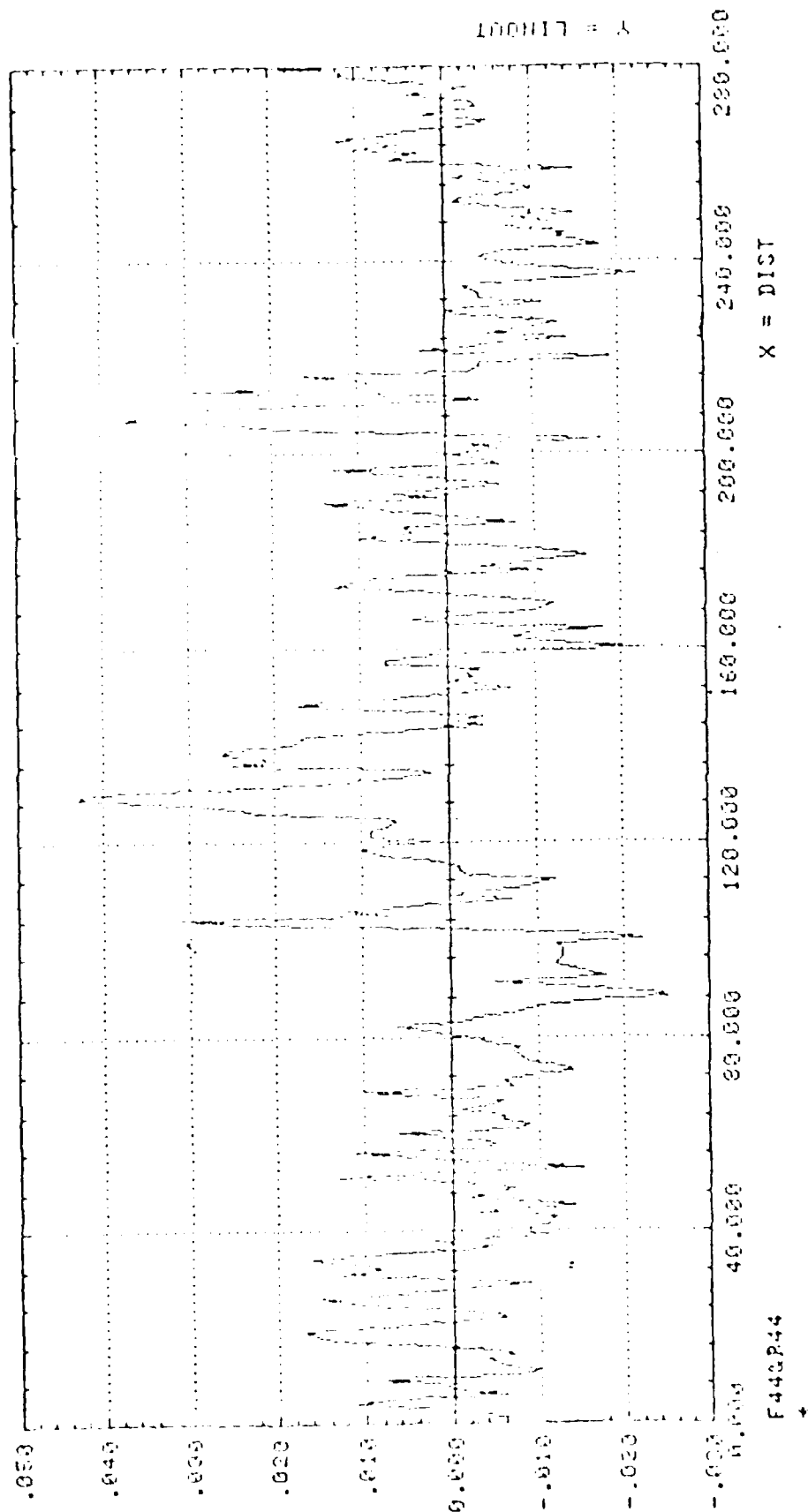


Figure 4.8 TS 44000 Rail Bottom

standard error of the estimates ($S_{y,x}$) for each sample set of rail data are shown in Table 4-1.

These rail profiles were chosen to best represent the actual rail conditions and still answer the basic questions posed by the study. Track Stations (TS) 34000 and 44000, both top and bottom of the rail, contain long period undulations on the order of 200 feet. TS 44000 is smooth compared to the rough TS 34000 rail (an $S_{y,x}$ of 0.012 inches versus 0.043 inches). In addition, the south 15000 feet of rail top had the same standard error as TS 44000 rail top, which has a periodic content. By comparing these two rail functions, the effect of periodicity can be examined. By comparing the periodic rail functions, the cumulative effect of roughness combined with periodicity can be investigated.

By comparing the north and south 15000 feet of track, rail grinding effectiveness can be determined. The north 15000 feet has been extensively ground over the last decade, whereas the south 15000 feet has been continually aligned and straightened over the past 30 years.

4.3 SLEDYNE/CRUISE MISSILE SLED SIMULATIONS

The previously mentioned Cruise Missile Sled/SLEDYNE study of Chapter Three was a direct result of this rail

roughness study directive. Shortly into the simulation sequence it was found that the existing SLEDYNE rail forcing function (referred to hereafter as the baseline rail function) was the controlling factor for rail length. Slipper dynamic forces peaked at about 4000 feet of track simulation for the baseline function, and at lengths slightly less for the other rail functions.

At this point in the study it became apparent that the user-supplied quasi-steady lift forces would drastically affect the slipper results. The results of a mini-lift study showed that using the rough periodic rail, TS 34000 top of rail, slipper forces peaked in phase at a lift of 3000 pounds for the 3000 feet per second velocity. For a velocity of 1500 feet per second, lift forces of 3000 pounds minimized slipper forces and again all were in phase with each other. For a nonperiodic rail function (the baseline function), the lift did not appear to affect slipper forces as drastically. The slipper forces stayed in an operating envelope of about ± 1000 pounds regardless of lift or velocity. No discernible phasing of slipper forces were evident. Figures 4.9 and 4.10 show the graphical results of the lift study on the Cruise Missile Sled.

The balance of the study concentrated on the effect of long period rail undulations and used TS 34000 and TS 44000 rail functions. Graphical results of these studies

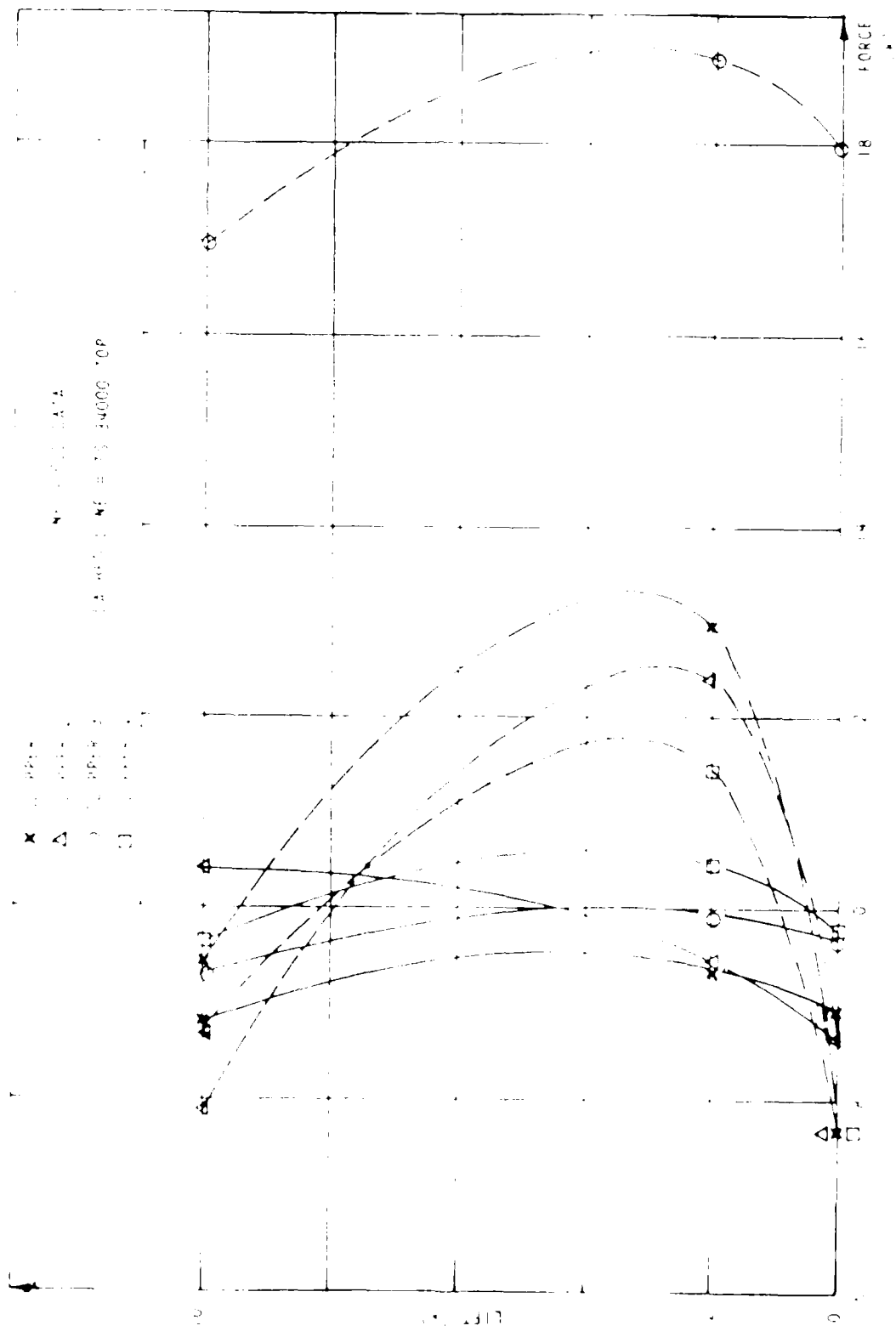


FIGURE 4.4. 1.5 MPa, $\mu = 0.34000$, OP

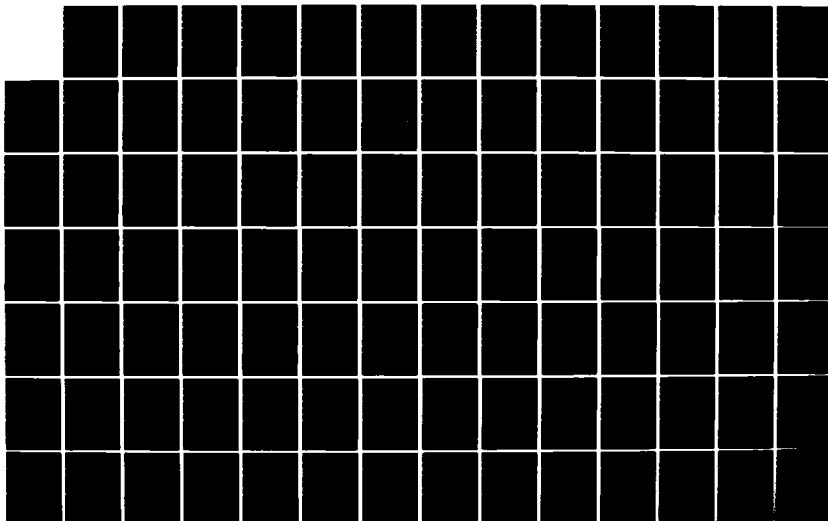
AD-A156 589

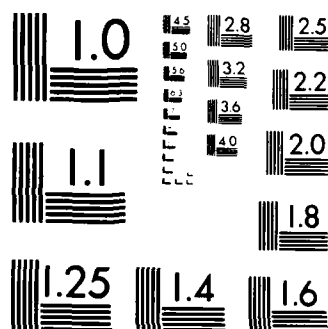
DYNAMIC ANALYSIS OF A SLED TRAVELING ALONG A ROUGH RAIL 2/4
(U) ARMAMENT DIV (AFSC) EGLIN AFB FL G L FERGUSON
15 MAY 85 AD-TR-85-39

UNCLASSIFIED

F/G 12/1

NL





MICROCOPY RESOLUTION TEST CHART
NATIONAL BUREAU OF STANDARDS-1963-A

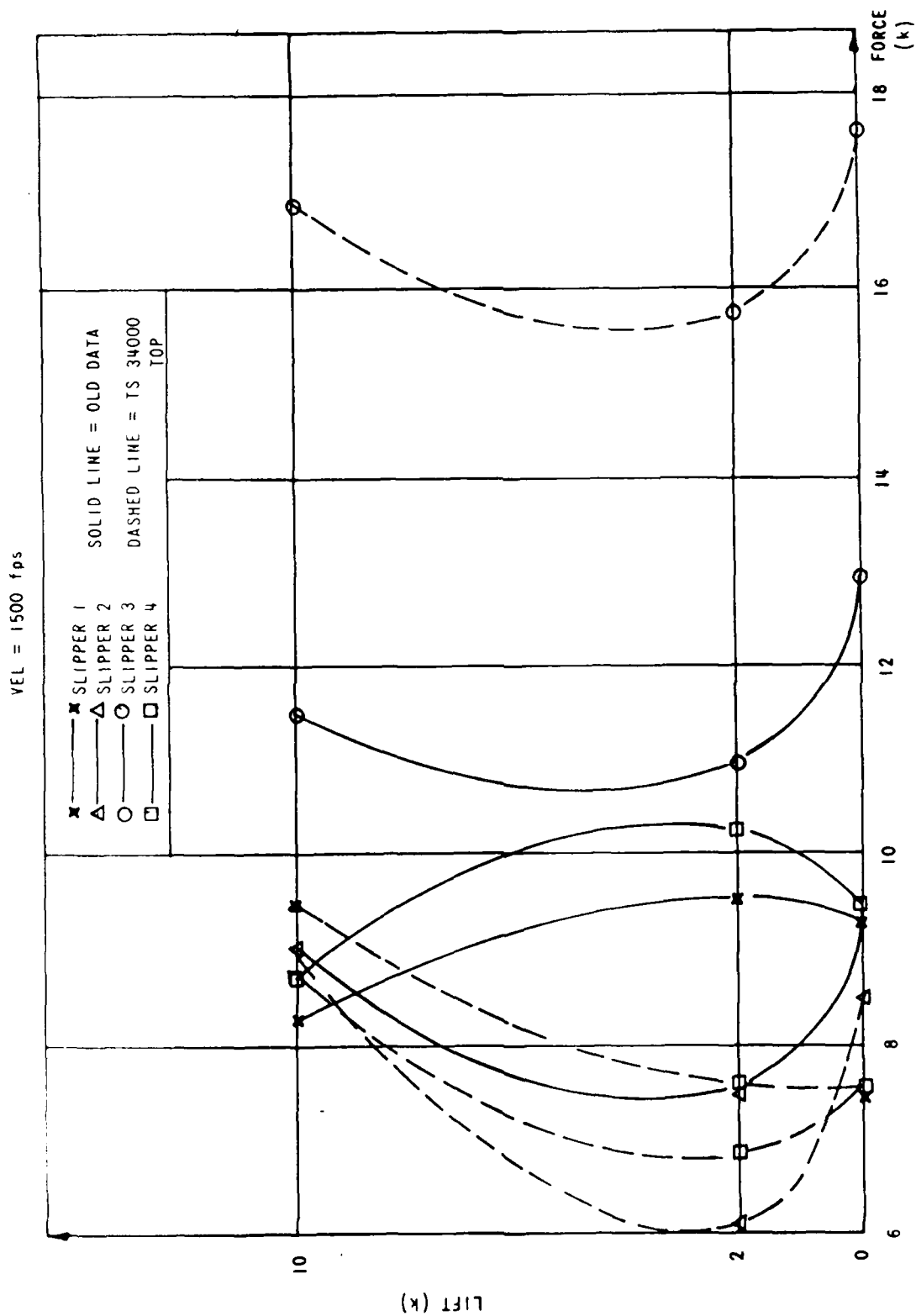


FIGURE 4.10 LIFT STUDY VELOCITY AT 1500 FPS

are shown in Figures 4.11 and 4.12. Upon examination of the figures, several inferences may be made. These are summarized below.

- a. The rougher the rail, the larger the slipper forces.
- b. The higher the velocity, the larger the slipper forces.
- c. Low amplitude, or "smooth", long period undulation (i.e., 200 feet) does not appear to excite the sled.
- d. Large amplitude, or "rough", long period undulation does appear to excite the sled considerably.

4.4 CONCLUSIONS AND RECOMMENDATIONS

No conclusions were possible at this time concerning rail grinding effectiveness nor the extent of periodic content on slipper forces. Computer simulation costs curtailed the rail roughness study at this point without answering the posed questions outside of optimal rail length. Here it was decided to suspend the study until DASTARR was operational and then repeat the study to answer questions left unanswered.

The approach to be used for further study will be to

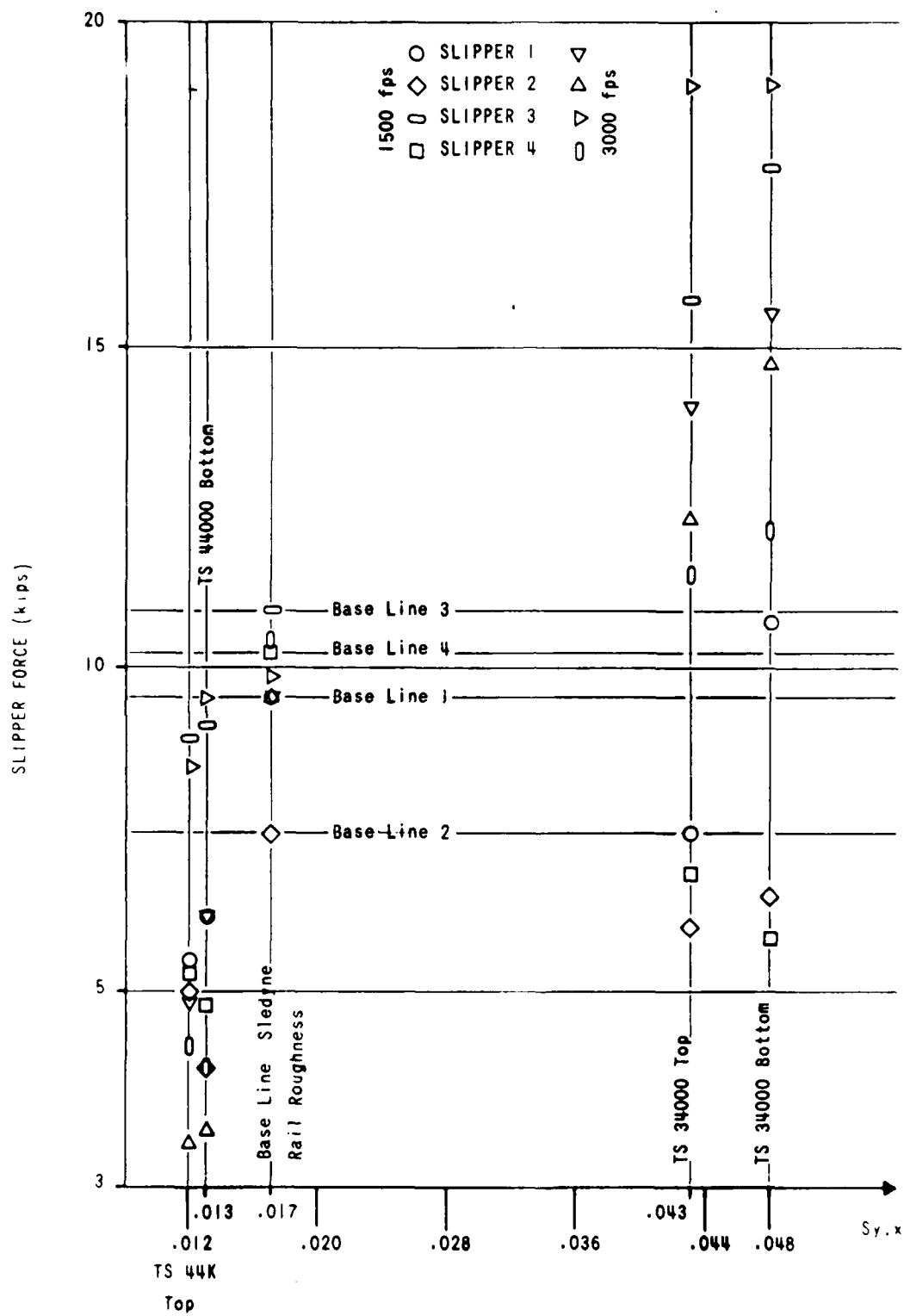


FIGURE 4.11 SLIPPER FORCES - LONG PERIOD RAIL

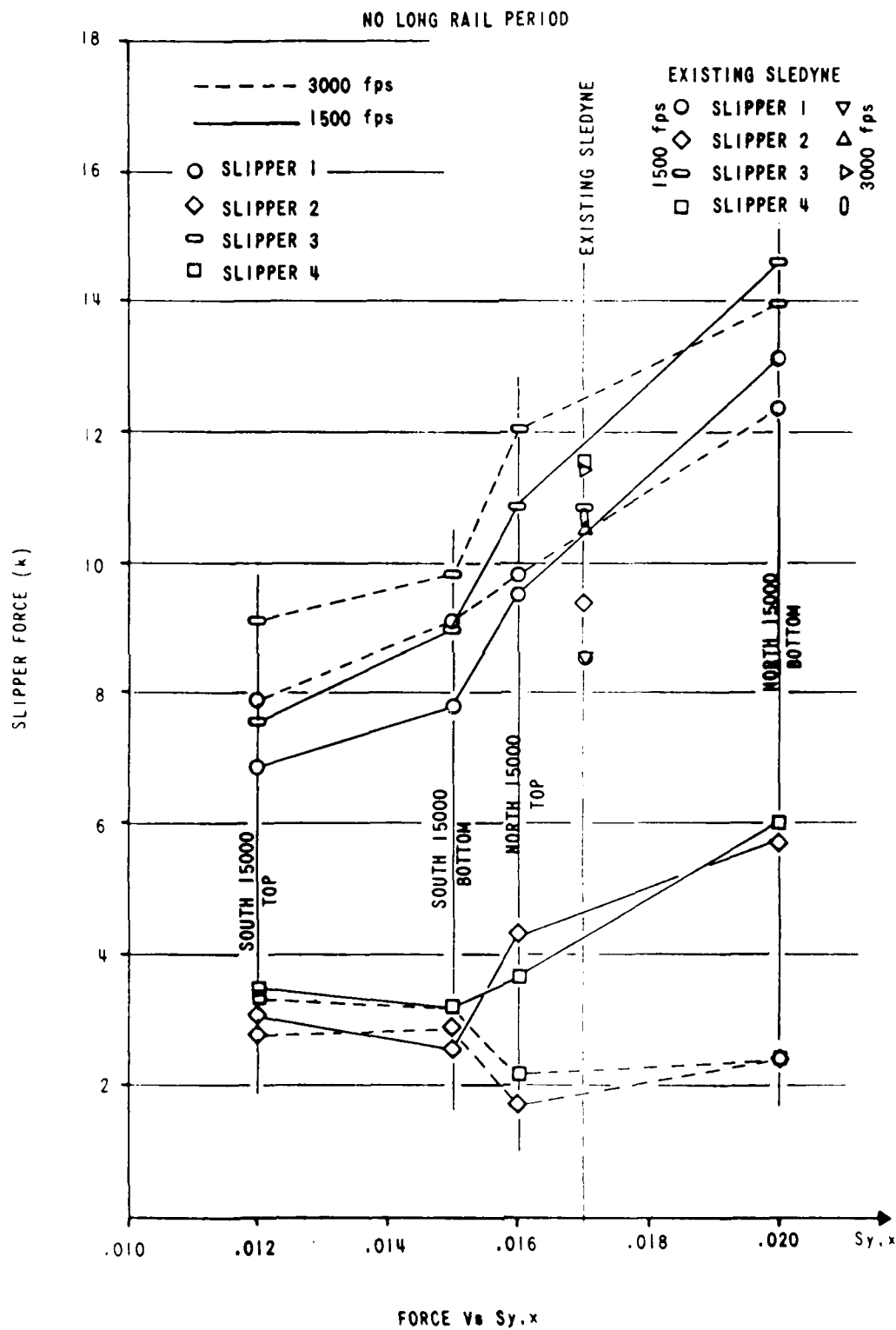


FIGURE 4.12 SLIPPER FORCES - NO LONG PERIOD RAIL

use the same rail function for all rail surfaces during the simulation. To insure repeatability the start point will be controlled and not randomly generated. The start point will be controlled for the lateral surface of rail number one. Each successive rail surface (number one vertical, number two lateral, and number two vertical) will start in increments of 20 feet beyond the start point of its predecessor. To generate a rail of 4000 feet in length, the rail functions will be looped end to end until this distance of simulated track has occurred.

The results of the study as well as program verification will be presented in Chapter Five for dual rail sleds (the Ramjet model) and in Chapter Six for monorail sleds.

CHAPTER 5

DUAL RAIL SLED SIMULATION--RAMJET

5.1 GENERAL

5.1.1 RAMJET SLED DESCRIPTION

The Ramjet Mission Sled is a special purpose sled designed to carry either a ramjet or scramjet engine in a simulated environment at speeds up to Mach 3.5. The engine is isolated from the sled structure through a series of coiled wire isolators that are designed to operate at a 10 hertz frequency. This frequency was chosen to simulate the aircraft environment and also to safely fall into an open envelope of sled operating frequencies.

Due to the unique geometry of the sled (see Figure 5.1), the use of conventional slipper beams was not possible. The sled was mounted on belleville springs to keep the structural response of the sled within historical dual rail sled response (i.e., 20 hz). These springs are designed such that the slipper hangars are connected to the slipper through the springs via a special instrumented slipper pin. The springs were sized to impart a 20 hertz heave frequency and be able to carry loads up to 65 kips each on the front slippers and up to

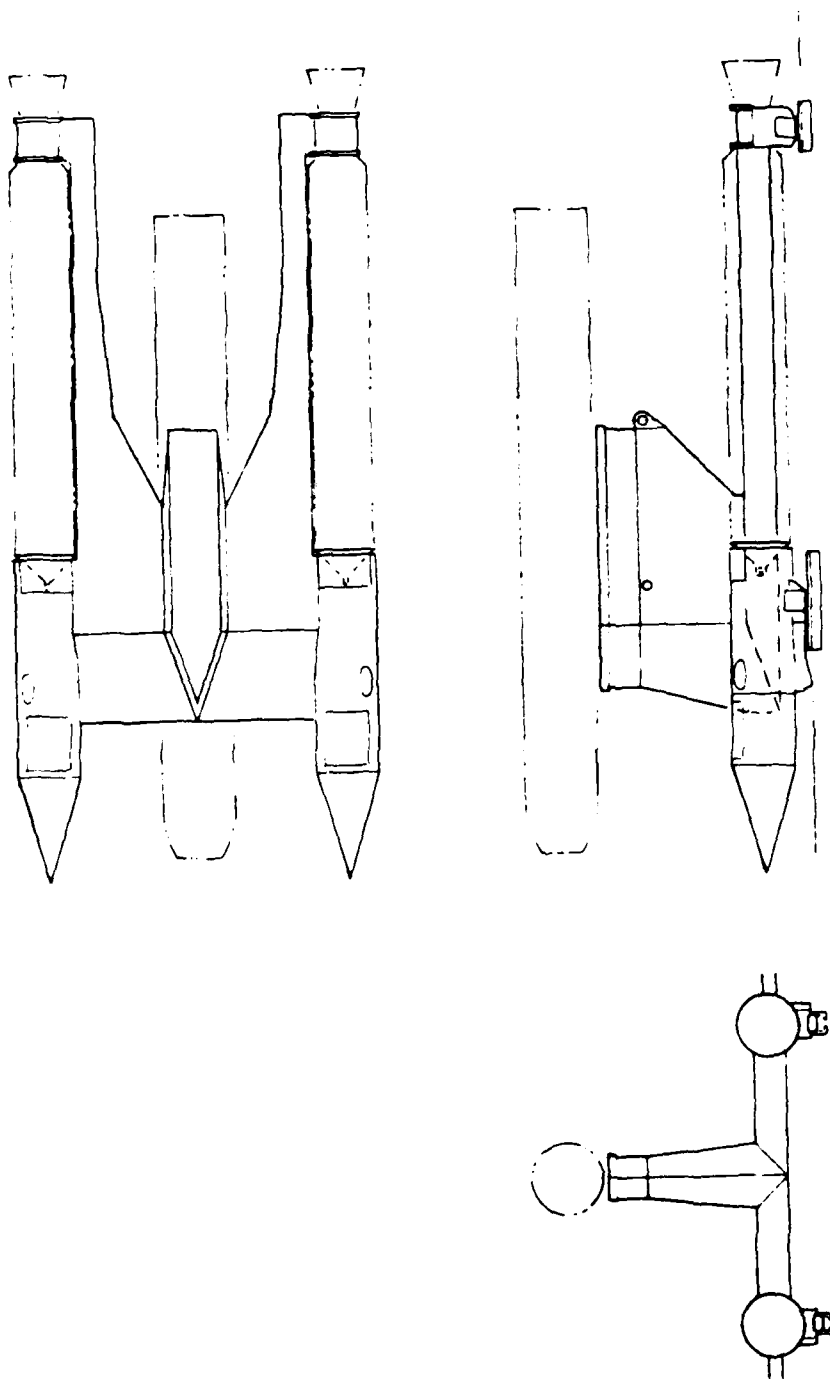


Figure 5-1. Ramjet Test Sled Configuration

35 kips each on the rear.

Using the known sled geometry a math model was created to define eigenvectors, eigenvalues, and mass properties for use in the simulation program DASTARR. The math model was defined to run on MSC NASTRAN version 63. The resultant model is depicted in Figure 5.2. The validity of the math model has been tested through vibration testing to verify the predicted eigenvectors and eigenvalues. The results are summarized in an in-house test report.¹⁷

Special instrumented slipper pins were used to mount the sled to the sprung slippers to measure actual slipper forces. Data from these pins were verified by first calibrating the pins in a tensile test machine using the actual sled-borne instrumentation. The pins were calibrated to within one (1) percent of known load applications in a lab setting. The pins were recalibrated on the track prior to running the sled to further insure the slipper pin response. The calibration was accomplished at the receiving end of the telemetry signal. A post-run calibration was done on the system to insure no signal degradation occurred during the run. The system passed all calibration tests and documentation results of the Ramjet Sled qualification are contained in the in-house report¹⁸ presently being written.

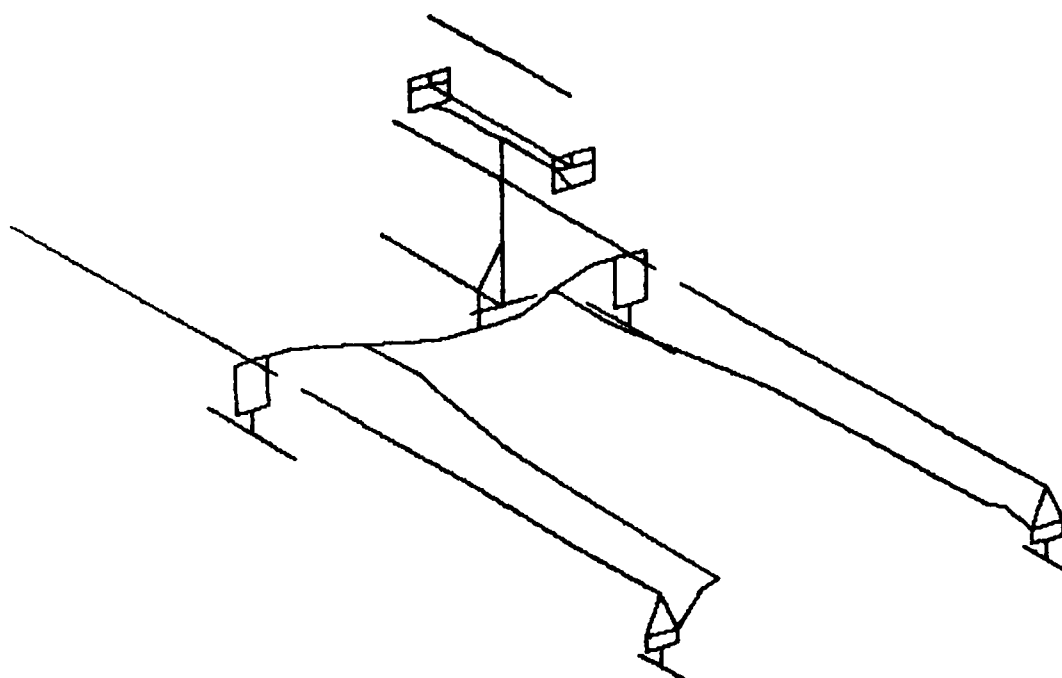


Figure 5.2 RAMJET Math Model

5.1.2 SLED FORCES

Using the results of the mini-lift study mentioned earlier, it was known that the lift and center-of-lift vectors would have to be well defined as a quasi-steady-state force in order to accurately simulate the Ramjet test results. The quasi-steady loads are those that are slowly time varying and are composed of thrust, drag, braking, transmitted thrust, lift, and the downtrack inertia required for equilibrium. Dynamic forces are characterized by oscillatory forces with a frequency content in excess of six to ten hertz. The dynamic forces are generally composed of the rail roughness forcing function, unsteady aerodynamics, and thrust transients like those seen at motor burnout.

5.1.2.1 LIFT FORCE CALCULATION

In February of 1984, the Ramjet sled was run on the track (the 19Y-C1 Mission) to a peak velocity of about 2000 feet per second ($M=1.81$). An extensive amount of data was taken and analyzed, among which were the four slipper forces. The data from the slippers were passed through a two-hertz filter to remove the "dynamic" portion of the forces. The remaining data were digitized

and plotted and consisted of the cumulative slipper forces caused by the "quasi-steady-state" loads. The results of this operation for this run are shown in Figure 5.3.

Based on a given velocity, the instantaneous slipper quasi-steady force is known from the run data. Using the trajectory analysis for the same velocity, the instantaneous drag, thrust, and inertias are known. The lift and its center can be calculated by solving the equilibrium equations around the sled freebody. This procedure was followed for nine (9) thrusting conditions and for eight (8) coasting conditions observed during the 19Y-C1 run. The results of the quasi-steady instantaneous loads are shown in Table 5-1.

Notice from the table there are six centers-of-lift (L) that are flagged. These centers are physically unlikely, and they happen to occur at an instant where extreme transients are present. These transient conditions are explained in the table. Therefore, these points were not used in any further analysis. As a point of interest, notice the difference in the center-of-lift locations between thrust and coast conditions for the same Mach number. The center of lift under thrust is forward on the sled from that under coast. This is explained by the bogie pusher beam used for this sled. See Figure 5.4 for a schematic of the sled train

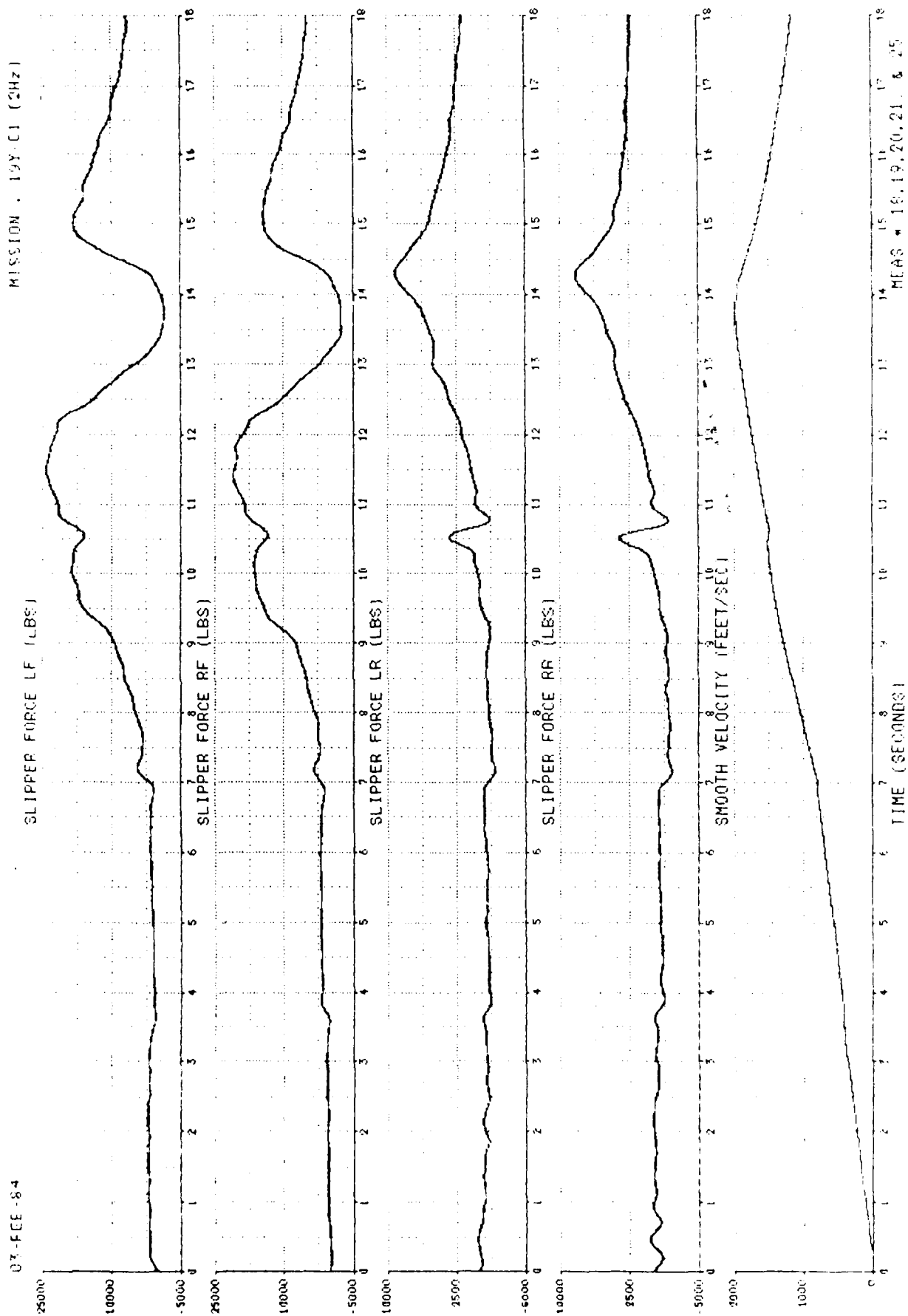


Figure 5.3 19Y-C1 Mission, QSS Loads Vs. Time

TABLE 5-1 TRACK COAST-COAST BEAM

FOR 107-CL BEAM

Beam No.	Velocity (ft/sec)	Weight (lb)	\bar{x} (in.)	\bar{y} (in.)	Accel. (g's)	Drag (lb)	Thrust (lb)	Lift (lb)	\bar{r} (in.)	Time (sec.)
THRUST										
0.850	955.0	7,800	40.610	22.610	7.938	9,807	72,416	3,565	-50.410	4.20
0.900	1,011.0	7,800	40.610	22.610	7.803	11,975	74,602	3,874	-30.270	4.00
1.013	1,138.0	7,800	40.610	22.610	7.260	20,513	79,525	6,571	-6.356	3.52
1.250	1,405.0	7,800	40.610	22.610	5.430	28,770	73,365	31,265	19.300	2.85
1.350	1,517.0	7,623	39.680	22.840	7.060	32,056	86,740	24,988	24.040	2.65
1.467	1,648.0	7,365	38.324	23.192	7.056	37,158	89,856	25,789	12.800	2.45
1.650	1,855.0	6,931	36.044	23.777	7.030	45,408	96,867	21,391	-59.570	2.20
1.770	1,987.0	6,642	34.525	24.166	7.190	49,272	97,760	7,355	-341.17#	2.02
1.810	2,020.0	6,568	34.267	24.232	6.630	49,881	94,160	0,120	-311.46#	2.00
COAST										
1.770	1,987.0	6,290	32.675	24.640	-7.940	49,272	0	9,029	-176.75#	2.02
1.650	1,855.0	6,290	32.675	24.640	-7.330	45,408	0	20,894	-78.70#	2.20
1.467	1,648.0	6,290	32.675	24.640	-6.020	37,158	0	40,293	0.60	2.45
1.350	1,517.0	6,290	32.675	24.640	-5.210	32,056	0	34,027	3.19	2.65
1.250	1,405.0	6,290	32.675	24.640	-4.552	27,942	0	29,989	-6.26	2.85
1.013	1,138.0	6,290	32.675	24.640	-3.374	20,513	0	13,517	-1.52	3.52
0.900	1,011.0	6,290	32.675	24.640	-2.389	14,320	0	1,841	-135.51++	4.00
0.850	955.0	6,290	32.675	24.640	-1.721	10,130	0	-629	332.03++	4.20

Notes:

- \bar{x} is the distance from front slipper beam CG to downtrack sled CG
 - \bar{y} is the distance from rail top to vertical CG of sled
 - \bar{r} is the distance from center of lift to downtrack CG, + is to front beam
 - Time is simulation time to travel approximately 4,000 feet of track
 - Occurs during motor burnout, thrust transients appear to aggravate 1, location
- These locations are physically improbable
- # Sled traveling over braking water set up for pusher
- ++ Transonic effects on lift under coast

configuration. Films of the run showed the bogie push beam creating a standing shock wave at the rear slippers of the Ramjet sled which forced the lift center slightly forward.

Now that all valid lift conditions were known, the simulation for the Ramjet could continue. This analysis was done by looking at the rigid body response at constant velocity, and then by examining the modal participation again at constant velocity.

5.2 RIGID BODY SIMULATION

The concept of rigid body simulation is actually a misnomer: it is in reality confining the modal participation to the first vertical translational sled modes. Typically for dual rail sleds, the rigid body modes are defined by the slipper beams' first vertical bending modes. However, with the Ramjet, the rigid body modes are defined by the belleville spring system used for isolation.

The simulation consisted of running all eleven valid lift conditions for a track distance of 4000 feet for each defined rail function, resulting in 99 simulation runs for the rigid body study. The subsequent analysis compared the predicted peak slipper forces to the actual peak slipper forces scaled from oscillograph records.

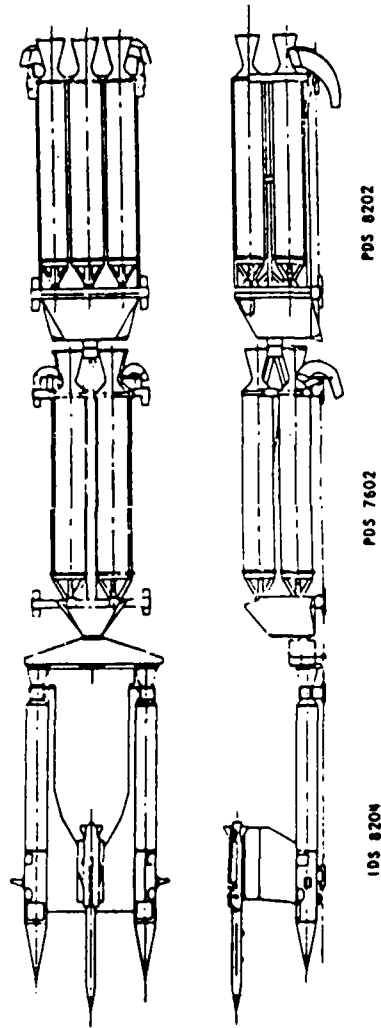


Figure 5.4 RAMJET Sled Train

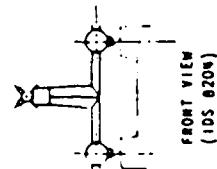


Table 5-2 contains the scaled slipper peaks from the oscillograph records.

Notice that for slippers three and four, the aft beam, the values peak at about half of what they are for the front beam. As a result, the aft beam forces are subject to a larger error in comparison results due to scaling factors.

Each rail roughness simulation, consisting of the eleven conditions, was statistically averaged for each slipper and beam combination. The results of this sampling are presented as a percentage deviation between actual and predicted forces, and also the standard deviation (1-sigma value) about the average deviation.

5.2.1 DATA ANALYSIS--AMPLITUDE DOMAIN

5.2.1.1 PEAK FORCES

The simulation consisted of 99 computer runs of the eleven conditions for each of the nine rail profiles. Results of the peak force simulations are shown plotted in Figures 5.5 through 5.8 for slippers one through four, respectively. The solid line is the actual measured peak force for that condition. The interesting thing to note is that slipper forces tend to exceed the measured value for rank roughness in excess of 0.020 inches.

TABLE 5-2 SCALED PEAK OSCILLOGRAPH FORCES

FROM 19Y-C1 MISSION

Condition	Time	Left Front		Right Front		Left Rear		Right Rear	
		Max	Min	Max	Min	Max	Min	Max	Min
Vel= 955C	7.67	12.00	-5.00	12.50	-3.75	3.75	-8.75	5.00	-9.13
1011T	7.90	12.00	1.88	6.25	-7.50	2.50	-6.25	5.00	-8.75
1138T	8.42	15.94	0.00	13.75	-2.50	5.00	-7.50	7.50	-8.13
1405T	9.64	31.88	5.00	24.38	3.13	6.25	-7.50	8.75	-10.63
1517T	10.80	33.13	10.00	32.50	5.00	11.25	-15.00	10.00	-14.38
1648T	11.50	36.25	8.75	33.75	10.00	6.25	-7.50	5.00	-6.25
1855T	12.78	18.13	-2.50	18.13	-5.50	13.13	-1.00	13.75	1.00
1978T	13.83	3.75	-7.50	4.38	-16.25	15.63	4.25	15.00	5.00
2020T	13.87	5.00	-8.13	5.00	-8.75	15.00	3.75	15.00	3.00
1987C	13.94	5.50	-7.50	3.75	-3.75	15.00	5.00	12.50	3.00
1855C	14.37	7.50	0.00	5.00	-3.75	18.75	7.50	19.38	5.00
1648C	15.03	30.00	18.13	22.50	7.50	15.63	5.00	15.63	3.75
1517C	15.65	26.88	10.00	23.13	12.50	10.00	2.50	9.38	0.00
1405C	16.22	23.13	10.00	16.25	5.00	11.25	-2.00	11.25	0.00
1138C	17.98	12.50	2.00	10.00	1.00	5.50	-3.75	8.75	0.00
1011C	19.27	6.88	-1.00	2.50	-5.00	5.00	0.00	6.25	-1.00
955C	20.11	3.75	-1.00	3.75	-3.75	6.88	-1.25	6.25	1.25

Notes:

1. Time is seconds into actual run
2. Force is units of kips

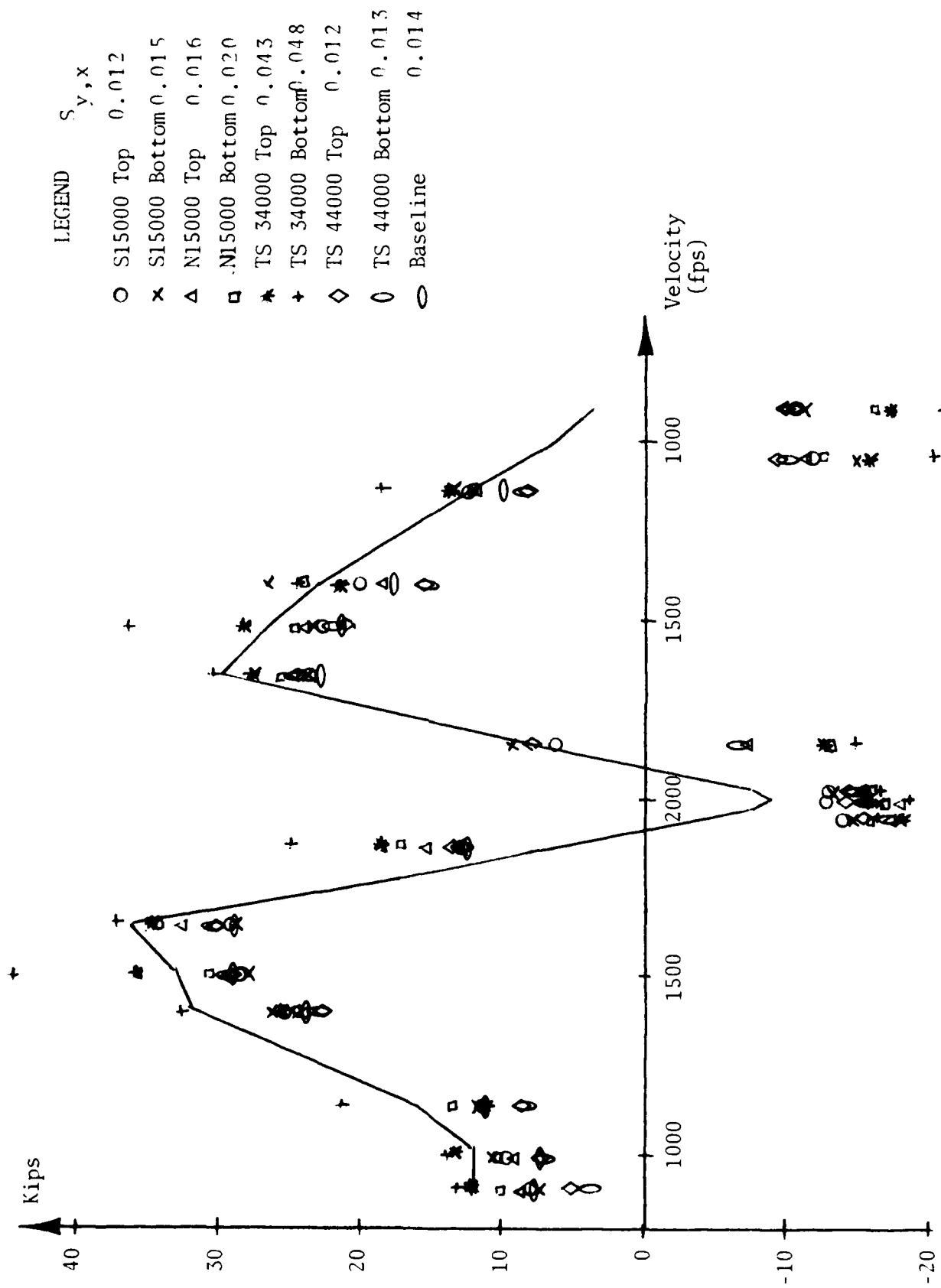


Figure 5.5 Slipper 1 Peak Force Vs. Predicted Force

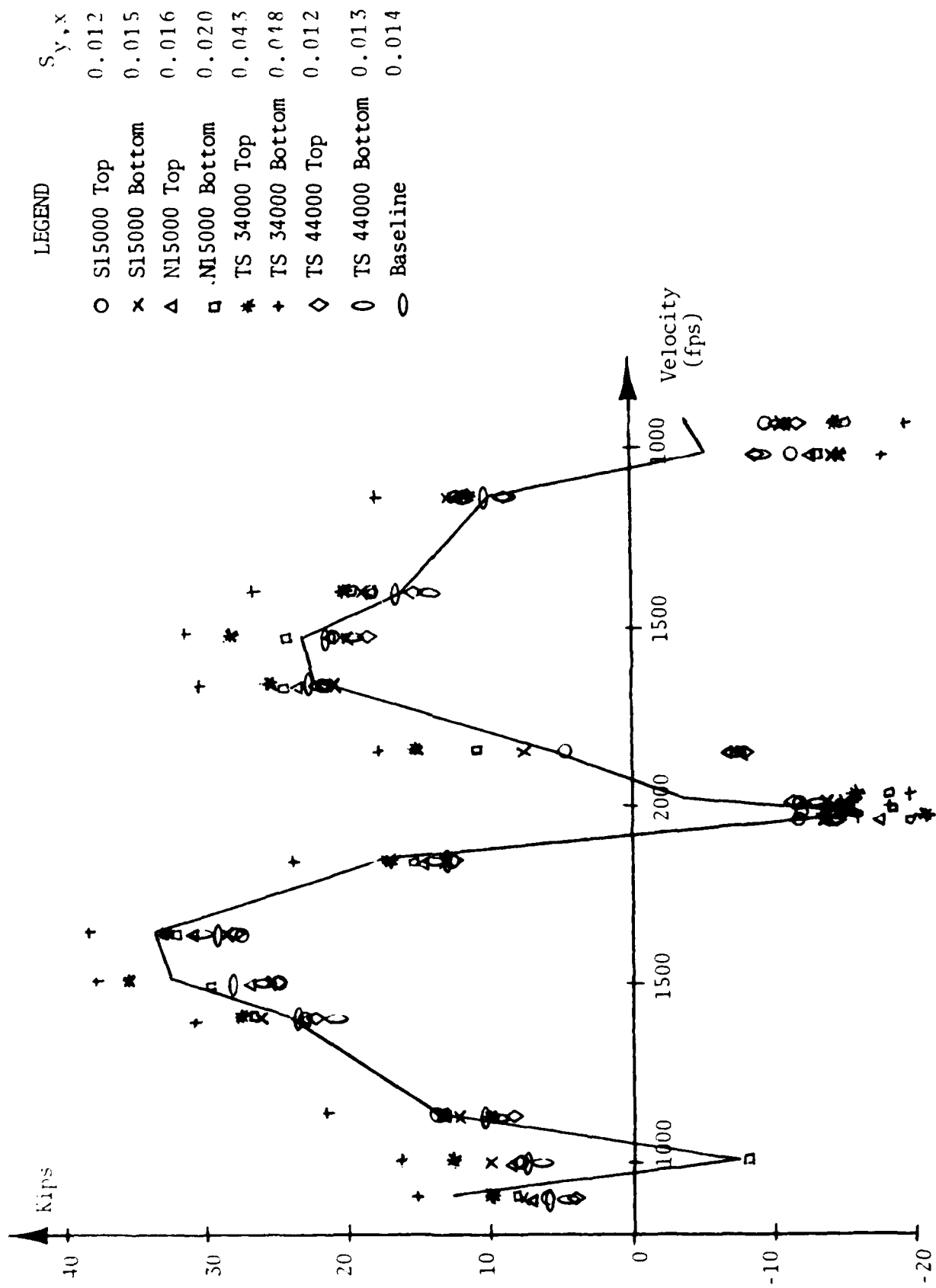


Figure 5.6 Slipper 2 Peak Force Vs. Predicted Force

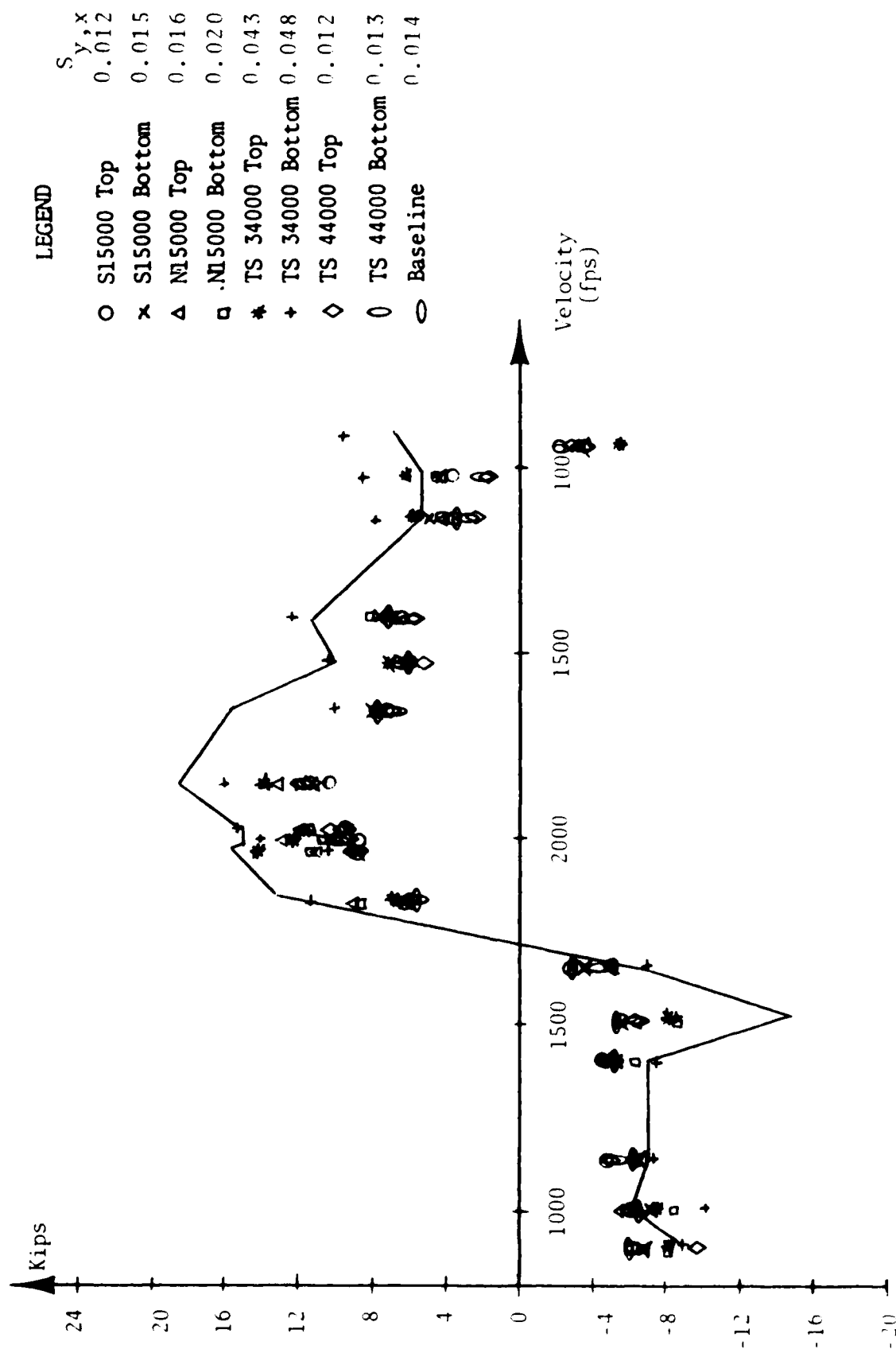


Figure 5.7 Slipper 3 Peak Force Vs. Predicted Force

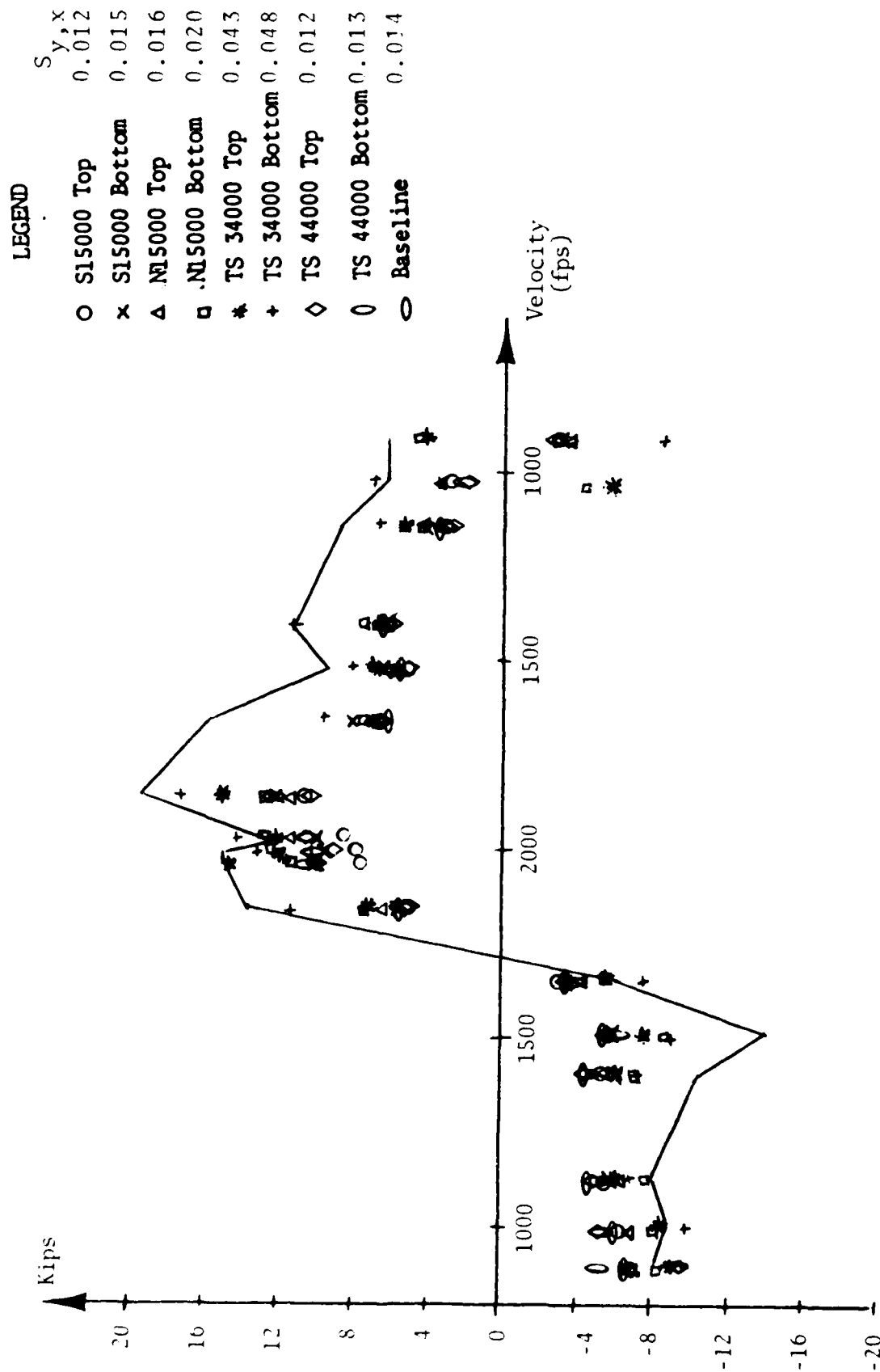


Figure 5.8 Slipper 4 Peak, Force Vs. Predicted Force

The statistical deviation analysis is shown plotted in Figure 5.9 and summarized in Table 5-3 for the front slipper beam. The "x" denotes where the average deviation for the eleven simulations occurs. The heavy arrowed vertical line indicates the +1-sigma value about the average.

Again the break point on rank roughness occurs at about 0.020 inches of roughness. This break point is where the average starts overpredicting the forces instead of underpredicting.

5.2.1.2 PEAK FORCES VERSUS TIME

One output feature of DASTARR is slipper force-time history. This output file can be directly plotted to examine what is actually occurring during the computer simulation. Two of the data plots generated during the 19Y-C1 mission were slipper force versus time plots for slippers two and four during a thrusting condition at an average velocity of 1650 feet per second. This condition happened to coincide with an actual computer simulation condition, so a direct comparison was possible. Figures 5.10a and 5.11a show the actual force-time history for slippers two and four, respectively. Shown in Figures 5.10b and 5.11b are the simulated force-time plots for

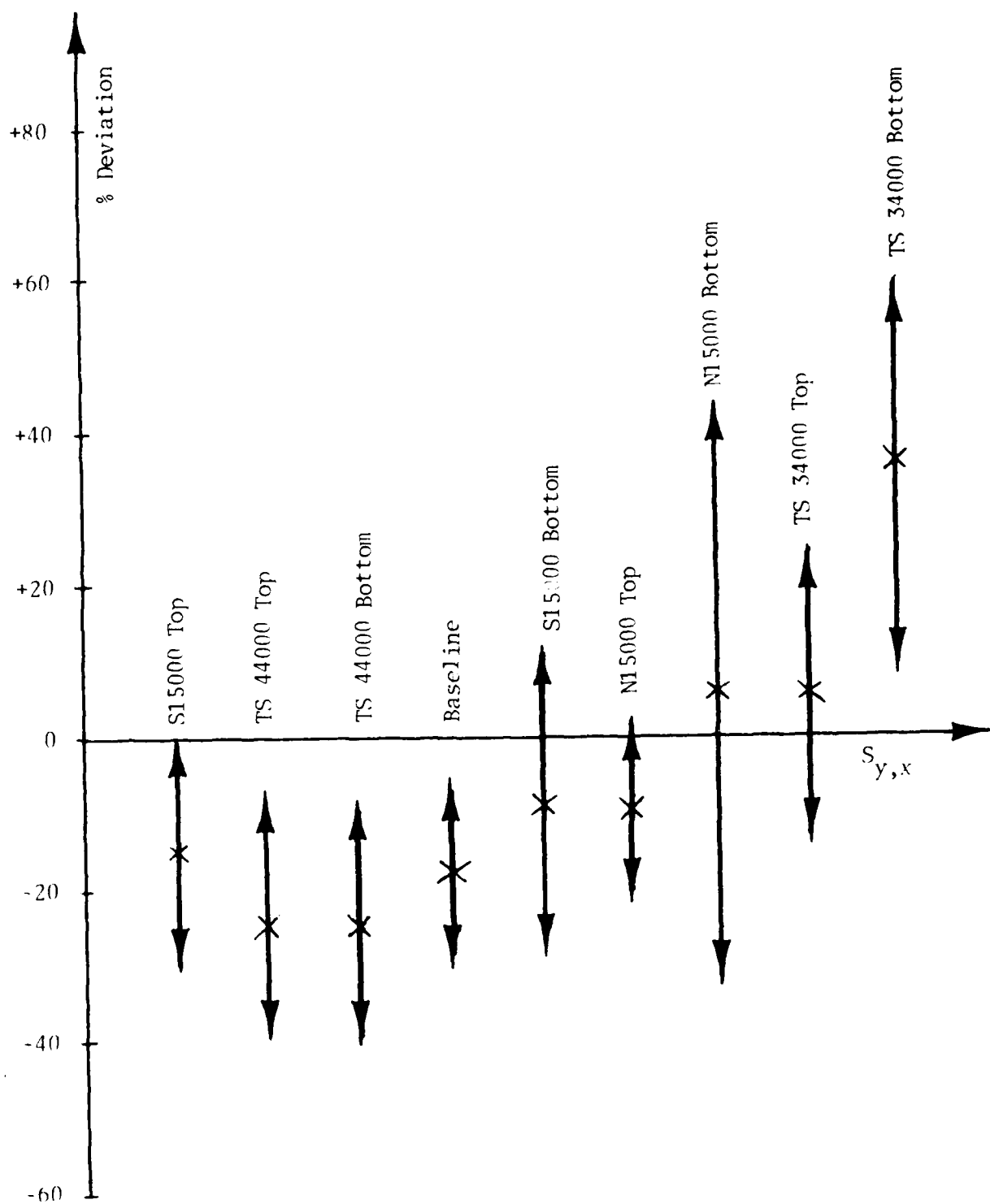


Figure 5.9 Front Beam Statistical Results

TABLE 5-3 STATISTICAL SUMMARY
OF RIGID BODY PREDICTIONS
VERSUS RAIL ROUGHNESS

Rail	$S_{y,x}$ (in.)	Front Beam		Aft Beam	
		Average	1 Sigma	Average	1 Sigma
34,000 Bottom++	0.042	+35.51	24.7	-5.21	22.0
34,000 Top++	0.043	+5.61	19.2	-26.71	16.9
315,000 Bottom	0.020	+5.71	38.3	-23.41	20.0
315,000 Top	0.016	-10.01	12.2	-34.01	16.1
315,000 Bottom	0.015	-8.91	19.2	-35.41	17.7
Baseline	0.014	-17.81	11.2	-42.31	15.6
44,000 Bottom++	0.013	-24.71	15.4	-43.71	13.5
44,000 Top++	0.012	-23.91	15.9	-46.61	12.4
315,000 Top	0.012	-14.91	14.1	-43.91	16.4

Notes:

++ Denotes periodic rail content

1. All values listed are percentages
2. Positive sign denotes overprediction
3. Negative sign denotes underprediction

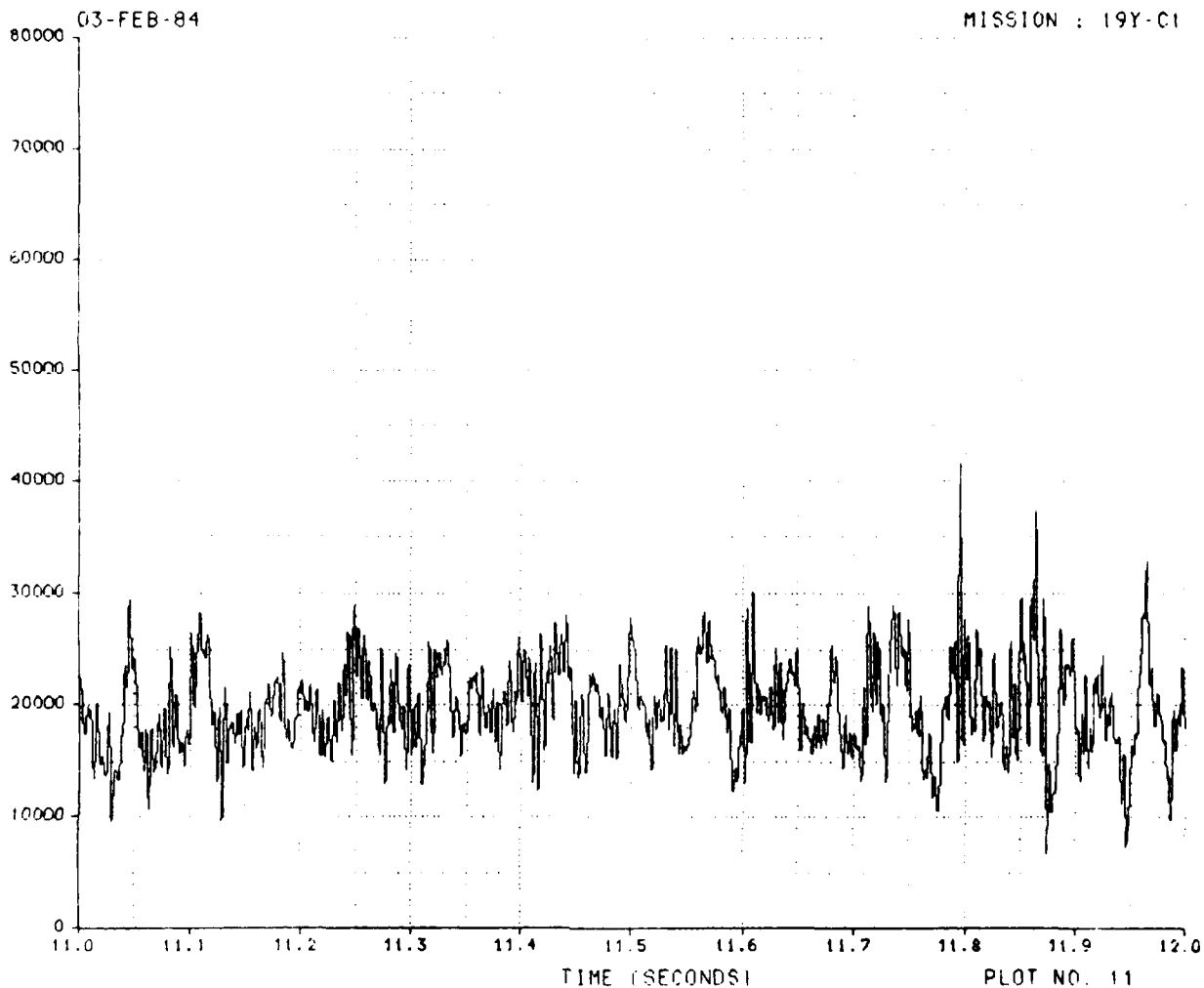


Figure 5.10a SLIPPER FORCE RIGHT FRONT VS TIME

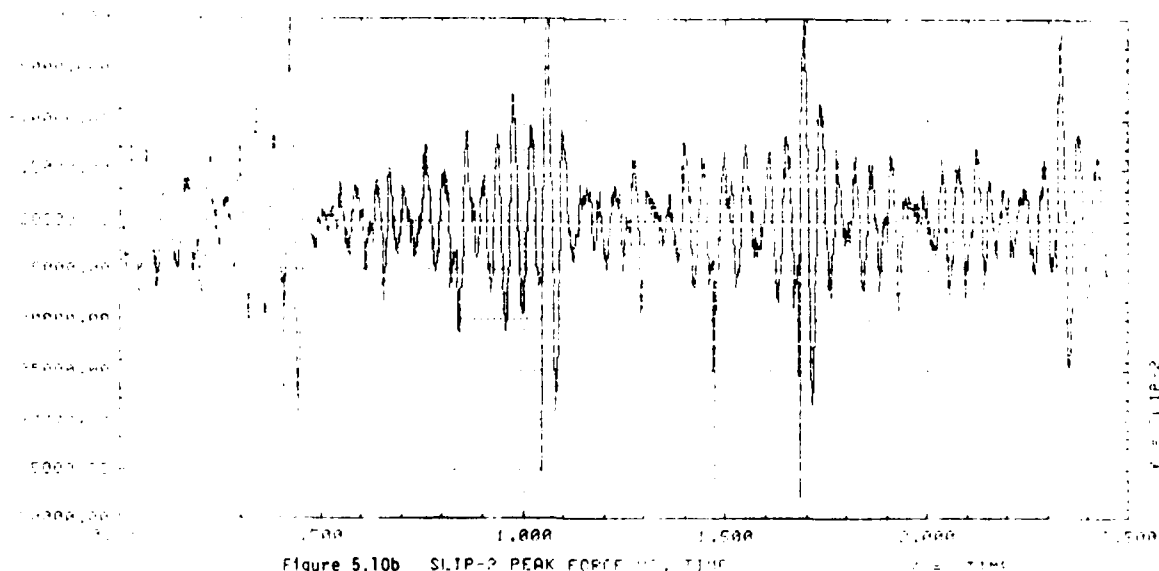


Figure 5.10b SLIP-2 PEAK FORCE VS TIME
RIGID RAMJET, V=14-27, NOT RATED

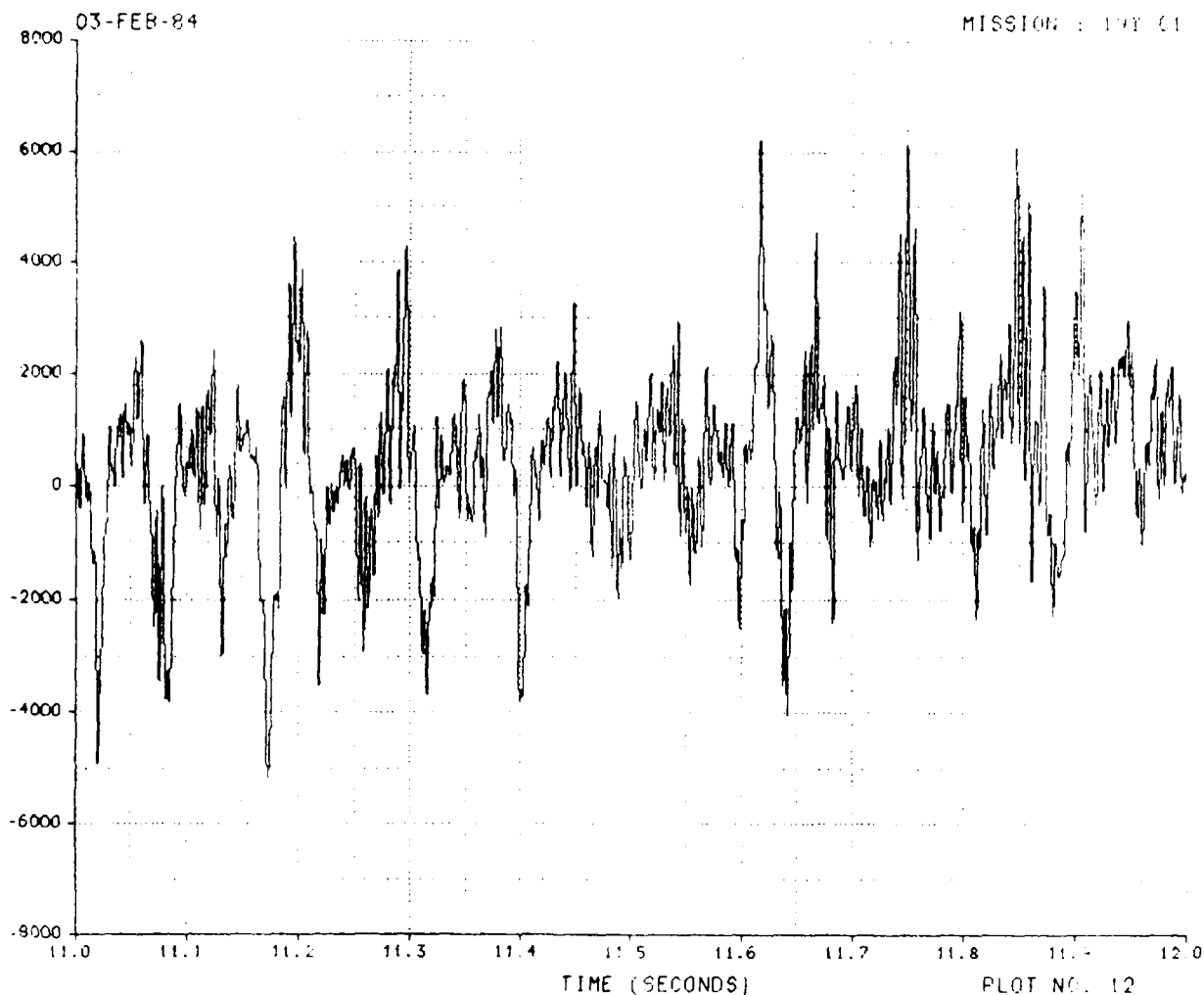


Figure 5.11a SLIPPER FORCE RIGHT REAR VS TIME

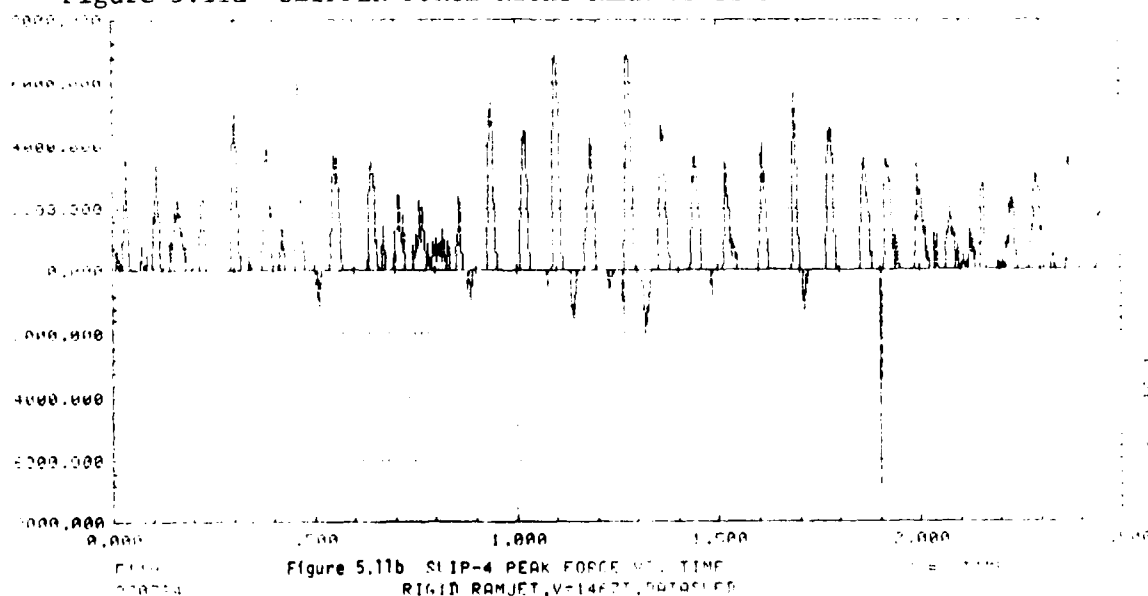


Figure 5.11b SLIP-4 PEAK FORCE VS TIME
RIGID RAMJET, V=14677, 00000000

the baseline rail function. The other eight rail function histories are contained in Appendix C, Figures C.1 through C.16. It should be noted here that the sign convention for the actual run data is in an opposite sense to that of DASTARR.

Notice for slipper two the peak slipper forces stayed in an envelope between 6 and 41 kips and were centered about 20 kips. This indicated that during this time slice there was no flight time associated with this slipper, or the slipper was in contact with the rail at all times. Looking at the plots for the various rail surfaces for this slipper indicated a similar centering about 20 kips with various envelope sizes. The envelope size appeared to be directly related to rail roughness. The rougher the rail, the larger the envelope. The baseline data did give a few occurrences of flight time; however, it was minimal compared to total rail contact time.

Examining actual force data for slipper four indicates the forces fluctuating by about ± 6 kips. The baseline data has the same fluctuating characteristics; however, the envelope is about ± 7 kips. All other profiles are one-sided in the operating envelope (i.e., the centering about 0 kips does not occur) with a large portion of flight time. Forces approached or exceeded the measured peak for roughnesses in excess of 0.020

inches.

The rough rails (those in excess of 0.020 inches) had significant numbers of occurrences in the vicinity of the peak spike for both slippers. However, the number of spikes in the vicinity of the peak from the actual run are few compared to the rough rails.

An interesting side note came from inspecting the plots for the south 15000 rail top data for slippers one and two. There is a distinct cycle, or spike, occurring approximately every quarter second, with the first spike occurring about 50 milliseconds into the simulation. This phenomenon repeated itself for all conditions using this rail function. The quarter second interval at this velocity corresponds to a track length of about 400 feet. This particular rail profile is 402 feet in length. At first it was thought that this was a facsimile created by looping the data end to end with a built-in discontinuity. Reviewing the rail roughness data showed there was no discontinuity created by looping of the data.

The next plausible explanation was a localized rough spot in the rail that was looping on itself at the 400 foot cycle. Taking into account the forced starting point for the rail function and the distance to the first spike, it was calculated the rough spot should be about 275 feet into the data file. Examining the data file

showed three points (277-279 feet into file) that had a roughness twice that of the surrounding points on either side of it and a roughness three to four times that of the overall sample. This theory was further validated by the presence of a secondary spike occurring about 50 feet from the first. Not knowing direction of rail generation, it was determined there should be another rough spot at either data point 225 or 325. Further review of the data indicated another rough spot at data points 224 and 225 that were about 250 percent larger than the total rail roughness.

Returning to original survey data, it was found that the roughness generated at the 277-279 data points were coincidental with track stations 12027-12029. The time that the exceptionally large force spike occurs in Figure 5.10a for the front slipper corresponds to an area of track in the region of TS 12020-12035, which contains the measured rough spot.

The fascinating aspect of this phenomenon is the capability of identifying a definite track location for being ground. Prior to grinding, the overall effect on slipper forces can be examined based on a predetermined rail smoothness. By looking at Figure C.1 and removing the peak force spikes, it appears possible to lower the peak forces by approximately 10 percent by smoothing the two discussed localized rough spots. A follow-on

simulation was made where the identified rough spots were arbitrarily smoothed to 0.020 inches to verify this hypothesized peak force reduction. This plot is shown in Figure 5.12 for this modified rail function.

This modified, or smoothed, rail only reduced peak forces by 4 percent instead of the estimated 10 percent. The smoothed rail did reduce the dynamic range of the forces by 17 percent. This in itself is significant in reducing the fatigue amplitude effects on the sled. Looking at the forcing function data again, several additional rough spots on the order of 0.030 inches were found that corresponded to the predicted peaks shown in the figure.

5.2.1.3 FORCE HISTOGRAM

Discussed in Chapter Three was the histogram feature of DASTARR. The histogram will take the force-time history for a slipper and put each data point into one of the 30 distinct bins. The bins were set up to allow for 15 bins to hold the positive force occurrences and 15 for negative forces. The bin size was set to be an integer multiple of the predicted maximum force from all eight slippers.

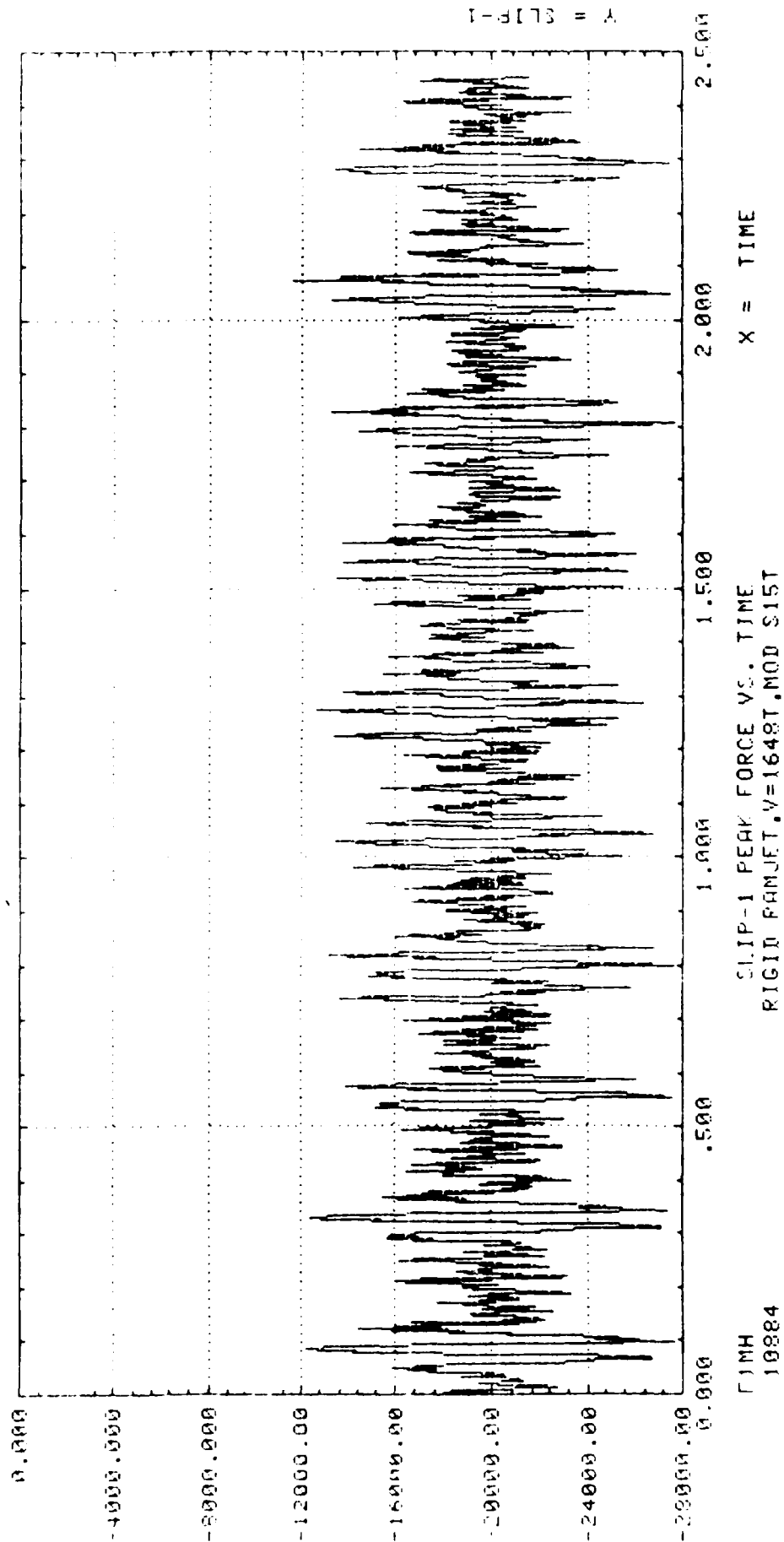


Figure 5.12 Slipper 1 Peak Force Vs. Time, Modified Rail

Mixon proved that dynamic forces were normally distributed and hypothesized that peak forces were Rayleigh distributed. Using the histogram feature, tests were set up to prove or disprove this hypothesis.

Examination of literature¹⁹ indicated that a Rayleigh distribution is a special subset of a normal distribution, hence could be tested as such. The standard test for a normal distribution is with the chi-squared (²) goodness of fit test. The chi-squared test will test the actual discrete distribution of the data for a small range, such as what is contained in an individual bin.

Further literature search revealed a second, less widely used but more accurate test. This is the Kolmogorov-Smirnov test.²⁰ This test concentrates on the deviation between a predicted "cumulative" distribution function and the observed one.

Both tests were programmed to give results in the histogram section of DASTARR. Tables 5-4a and 5-4b show typical DASTARR output. This example was generated using a constant velocity of 1138 feet per second under coasting conditions for the south 15000 feet of track on the top rail. Figure 5.13 shows the plotted values for slipper one for the histogram (the step function) and the predicted true Rayleigh distribution.

TABLE 9.4. MAXIMUM SLIPPER FORCES AND ASSOCIATED ACCELERATIONS

$$A \cap B = \emptyset, \quad A \cup B = \mathbb{R}, \quad A \cap C = \{0\}, \quad A \cup C = \mathbb{R}, \quad A \cap D = \mathbb{Q}, \quad A \cup D = \mathbb{R}, \quad A \cap E = \mathbb{Q}, \quad A \cup E = \mathbb{R}, \quad A \cap F = \mathbb{Q}, \quad A \cup F = \mathbb{R}, \quad A \cap G = \mathbb{Q}, \quad A \cup G = \mathbb{R}, \quad A \cap H = \mathbb{Q}, \quad A \cup H = \mathbb{R}, \quad A \cap I = \mathbb{Q}, \quad A \cup I = \mathbb{R}, \quad A \cap J = \mathbb{Q}, \quad A \cup J = \mathbb{R}, \quad A \cap K = \mathbb{Q}, \quad A \cup K = \mathbb{R}, \quad A \cap L = \mathbb{Q}, \quad A \cup L = \mathbb{R}, \quad A \cap M = \mathbb{Q}, \quad A \cup M = \mathbb{R}, \quad A \cap N = \mathbb{Q}, \quad A \cup N = \mathbb{R}, \quad A \cap O = \mathbb{Q}, \quad A \cup O = \mathbb{R}, \quad A \cap P = \mathbb{Q}, \quad A \cup P = \mathbb{R}, \quad A \cap Q = \mathbb{Q}, \quad A \cup Q = \mathbb{R}, \quad A \cap R = \mathbb{Q}, \quad A \cup R = \mathbb{R}, \quad A \cap S = \mathbb{Q}, \quad A \cup S = \mathbb{R}, \quad A \cap T = \mathbb{Q}, \quad A \cup T = \mathbb{R}, \quad A \cap U = \mathbb{Q}, \quad A \cup U = \mathbb{R}, \quad A \cap V = \mathbb{Q}, \quad A \cup V = \mathbb{R}, \quad A \cap W = \mathbb{Q}, \quad A \cup W = \mathbb{R}, \quad A \cap X = \mathbb{Q}, \quad A \cup X = \mathbb{R}, \quad A \cap Y = \mathbb{Q}, \quad A \cup Y = \mathbb{R}, \quad A \cap Z = \mathbb{Q}, \quad A \cup Z = \mathbb{R}, \quad A \cap \mathbb{Q} = \mathbb{Q}, \quad A \cup \mathbb{Q} = \mathbb{R}, \quad A \cap \mathbb{R} = \mathbb{R}, \quad A \cup \mathbb{R} = \mathbb{R}, \quad A \cap \emptyset = \emptyset, \quad A \cup \emptyset = A.$$

Factor	$\mathbb{Q}(\sqrt{-1})$	$\mathbb{Q}(\sqrt{-3})$	$\mathbb{Q}(\sqrt{-4})$	$\mathbb{Q}(\sqrt{-5})$	$\mathbb{Q}(\sqrt{-6})$	$\mathbb{Q}(\sqrt{-7})$	$\mathbb{Q}(\sqrt{-10})$	$\mathbb{Q}(\sqrt{-11})$	$\mathbb{Q}(\sqrt{-13})$
$\mathbb{Q}(\sqrt{-1})$	$\mathbb{Q}(\sqrt{-1})$	$\mathbb{Q}(\sqrt{-1})$	$\mathbb{Q}(\sqrt{-1})$	$\mathbb{Q}(\sqrt{-1})$	$\mathbb{Q}(\sqrt{-1})$	$\mathbb{Q}(\sqrt{-1})$	$\mathbb{Q}(\sqrt{-1})$	$\mathbb{Q}(\sqrt{-1})$	$\mathbb{Q}(\sqrt{-1})$
$\mathbb{Q}(\sqrt{-3})$	0	0	0	0	0	0	0	0	0
$\mathbb{Q}(\sqrt{-4})$	$\mathbb{Q}(\sqrt{-4})$	0	0	0	$\mathbb{Q}(\sqrt{-4})$	0	0	$\mathbb{Q}(\sqrt{-4})$	0
$\mathbb{Q}(\sqrt{-5})$	0	$\mathbb{Q}(\sqrt{-5})$	0	$\mathbb{Q}(\sqrt{-5})$	0	0	0	0	0
$\mathbb{Q}(\sqrt{-6})$	0	0	$\mathbb{Q}(\sqrt{-6})$	0	$\mathbb{Q}(\sqrt{-6})$	0	$\mathbb{Q}(\sqrt{-6})$	0	0
$\mathbb{Q}(\sqrt{-7})$	0	0	0	0	0	$\mathbb{Q}(\sqrt{-7})$	0	$\mathbb{Q}(\sqrt{-7})$	0
$\mathbb{Q}(\sqrt{-10})$	0	0	0	0	0	0	$\mathbb{Q}(\sqrt{-10})$	0	0
$\mathbb{Q}(\sqrt{-11})$	0	0	0	0	0	0	0	$\mathbb{Q}(\sqrt{-11})$	0
$\mathbb{Q}(\sqrt{-13})$	0	0	0	0	0	0	0	0	$\mathbb{Q}(\sqrt{-13})$

TABLE 1-40D HISTOGRAM

[illegible][illegible][illegible][illegible]

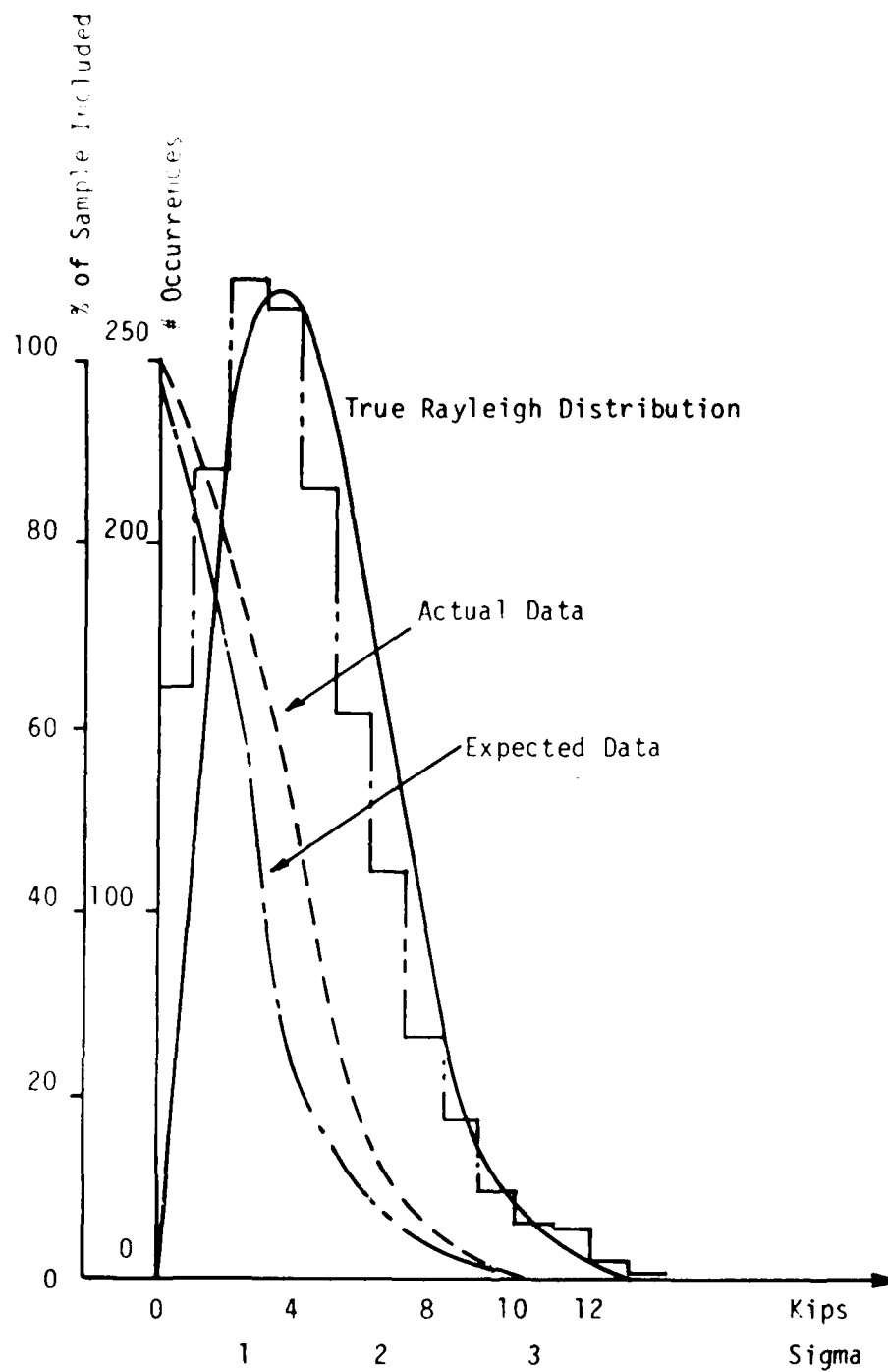


Figure 5.13 Histogram Vs. Rayleigh Distribution

It is inherent in the graph that the trend is toward a Rayleigh distribution except for the first two bins. This discrepancy in the first two bins made the analysis fail both tests for goodness of fit of the data. Reference to statistical acceptance criteria for a data sample this large (approximately 1500 points) indicated the histogram should have 35 bins to handle the distribution instead of 15 as is done due to computer memory limitations.

Noting the inherent Rayleigh-like trend of the data, one last test was performed. A data sample is normally distributed when 99 percent of the data is contained within ± 3 -sigma. A routine was added to the program to determine how many standard deviations were required to encompass 99 percent of the data at the upper bin limit. As can be seen from Table 5-4b, the order of three and one-half (3.5) sigma encompassed the necessary data.

Making note of the Rayleigh-like trend, the bin size limitations that caused test failure, and 99 percent of the data being encompassed by 3.5 sigma, it was concluded that the distribution for peak forces was truly a Rayleigh distribution. Examination of the other loading conditions indicated the same results. However, the extent of failing the acceptance testing was strongly dependent on the magnitude of the quasi-steady loads. The bin sizes became very large and all the data were

contained in just a few bins for large quasi-steady-state forces. The program would have to be rewritten to accommodate 35 bins to alleviate the bin distribution problem. The bins would not be able to be defined as positive or negative as presently, instead the bins would have to be able to encompass the actual force data range only. Each slipper would require a separate bin distribution, and due to computer memory limitations this distribution is impossible to do.

5.2.2 DATA ANALYSIS--FREQUENCY DOMAIN

In the previous section, the data output had been compared to actual run data in the amplitude domain. It remained to be analyzed in the frequency domain to determine whether the frequency and energy content of the simulation was accurate.

The force-time history output from DASTARR was passed through a power spectral density (PSD) program to examine the sled response in the frequency domain. The y, or power, axis for standard PSD's have units of G^2/Hz . However, for this analysis the units are lb_f^2/Hz . Over a given frequency band, the square root of the area of that band is a measure of the root mean square of the slipper force. The cumulative area of the PSD is a measure of the total power, or energy, of the system.

Due to the number of data points being sampled and the time differential between samples, approximately 275 hertz is the maximum frequency that can be generated. For most dual rail sled systems, frequencies above 200 hertz generally have such small deflections associated with those frequencies that little or no mechanical damage results.

Examination of PSD plots for the given run condition under thrust, shown in Figures 5.14a and 5.15a for slippers two and four, shows a sharp rolloff after 30 hertz and mostly noise above 70 hertz. This phenomenon is typical of most sled structural responses. Total power in the front slipper is 20374 pounds force rms for the frequency range 0 through 300 hertz. The aft slipper total power is 1745 pounds force rms for the same frequency spectrum.

Figures 5.14b and 5.15b show typical wide spectrum response for the rigid body sled system for the same thrusting condition from the simulation. Again sharp rolloff is shown above 30 hertz with noise starting about 70 hertz. The local PSD routine used did not contain the feature to accumulate power, so a total system rms power comparison is not possible.

Figures 5.16a and 5.17a are blowups of 5.14a and 5.15a, respectively, in the 0 to 80 hertz range. Similarly Figures 5.16b and 5.17b are blowups of 5.14b

PROCESSED: 07:21 PM THU., 22 MAR 84
DATE: 03 FEB 84

INTEGRAL: 0.000000E+00
MISSING: 19.000

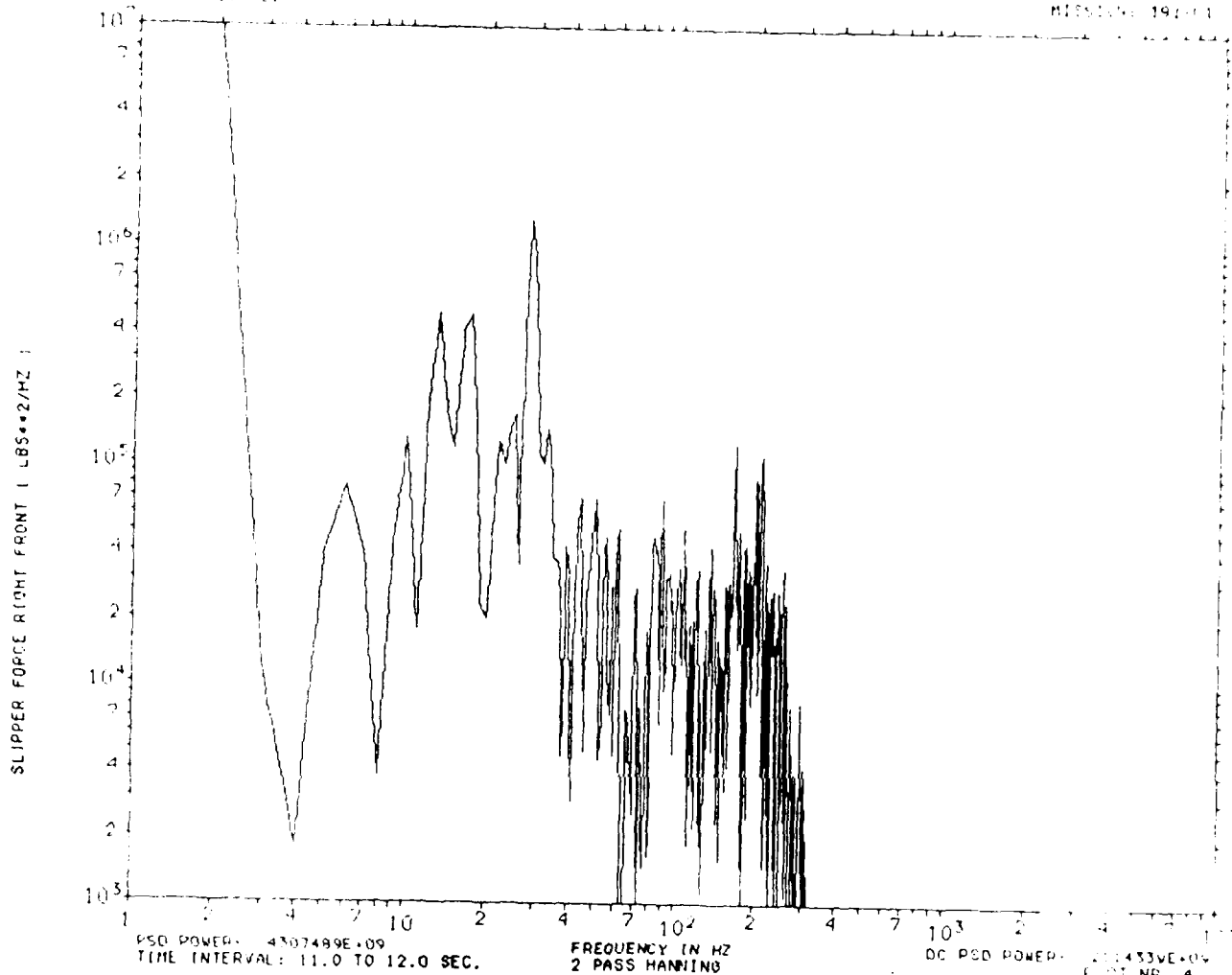
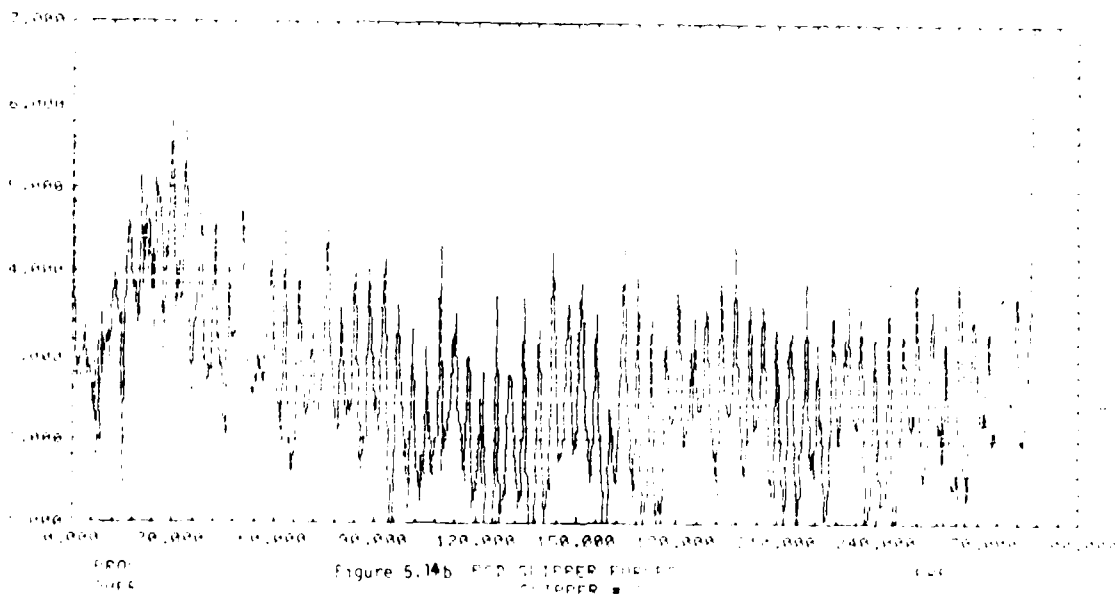


Figure 5.14a POWER SPECTRAL DENSITY



PROCESSED: 03:21 PM THU., 22 MAR 84
DATE: 06 FEB 84

INTEGRAL G-2/T: 1.304521E+07
MISSION: 191-C1

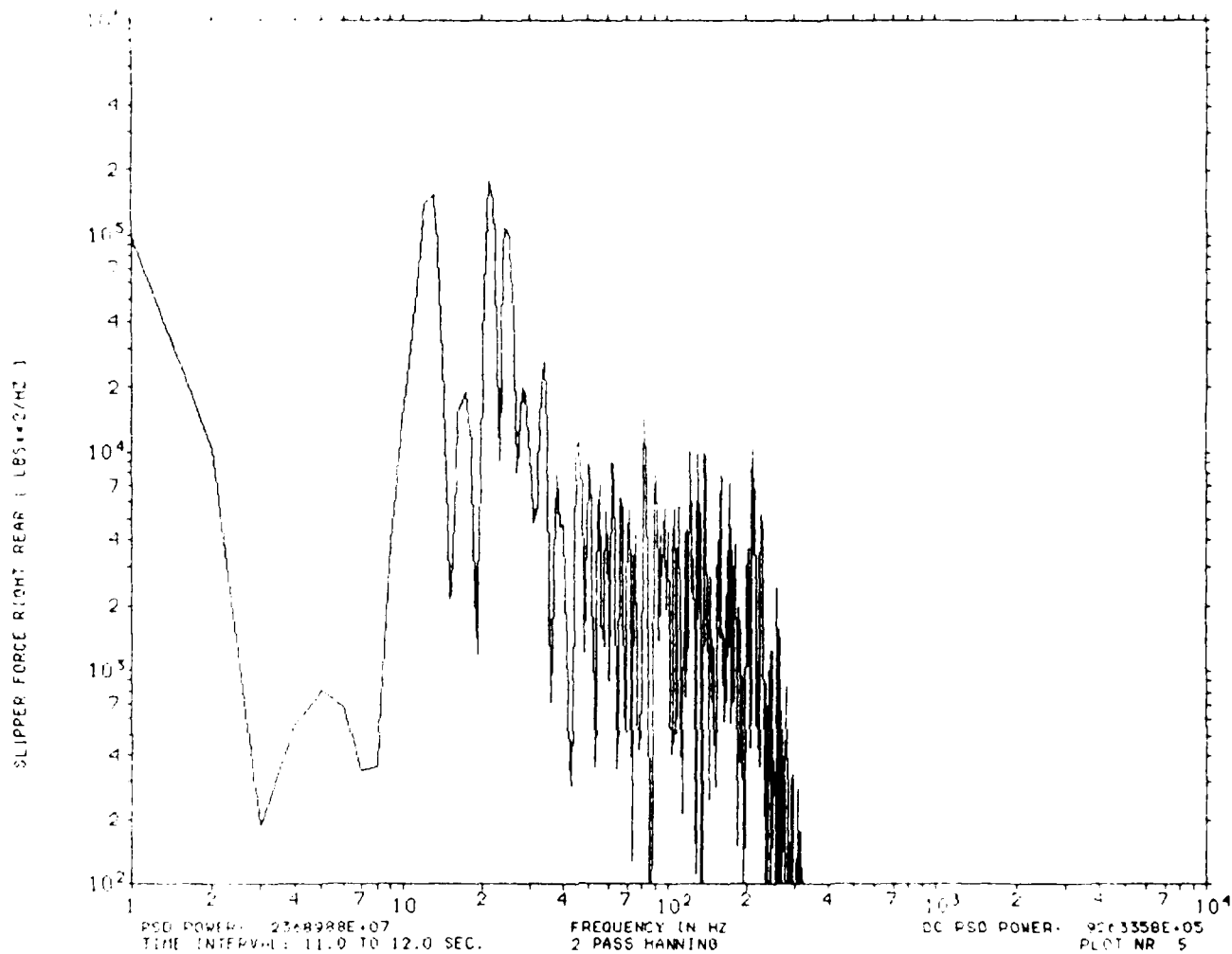


Figure 5.15a POWER SPECTRAL DENSITY

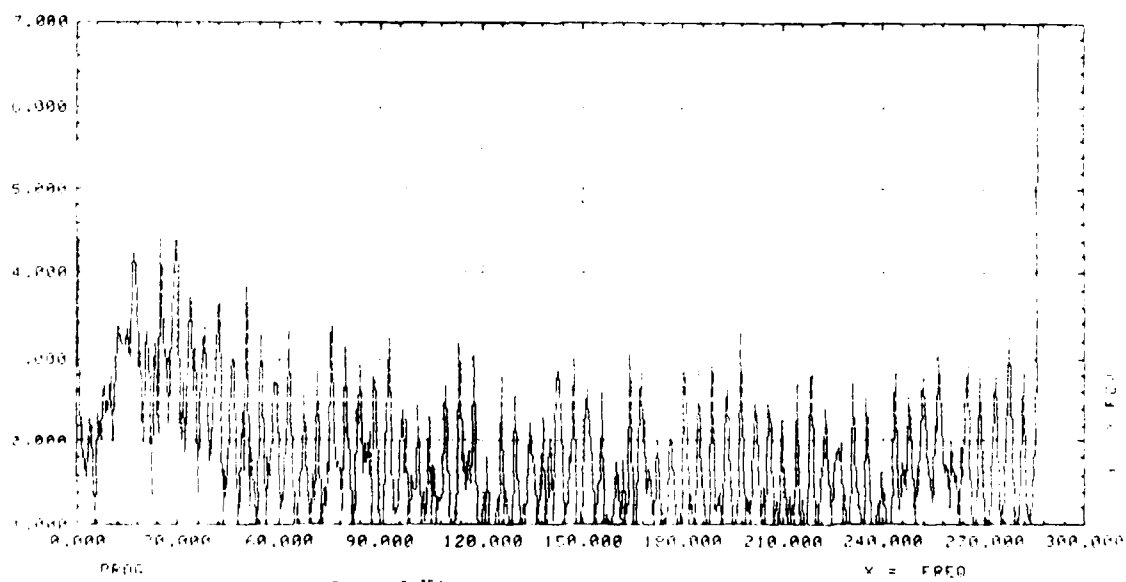


Figure 5.15b SLIPPER # 4

PROCESSED: 07:21 PM THU., 22 MAR 84
 DATE: 03-FEB-84

SLIPPER FORCE RIGHT FRONT 1 LBS/4.2/HZ 1

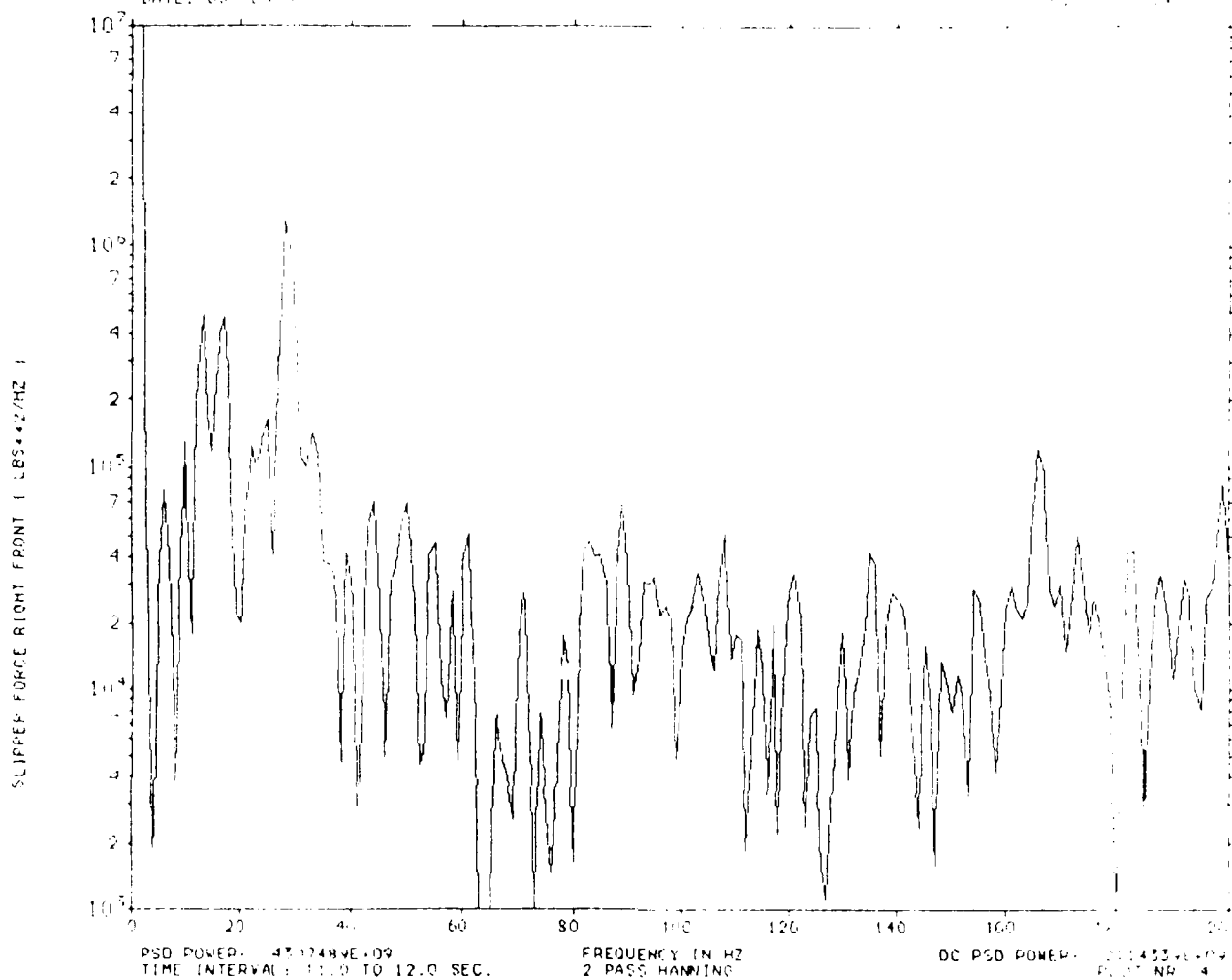
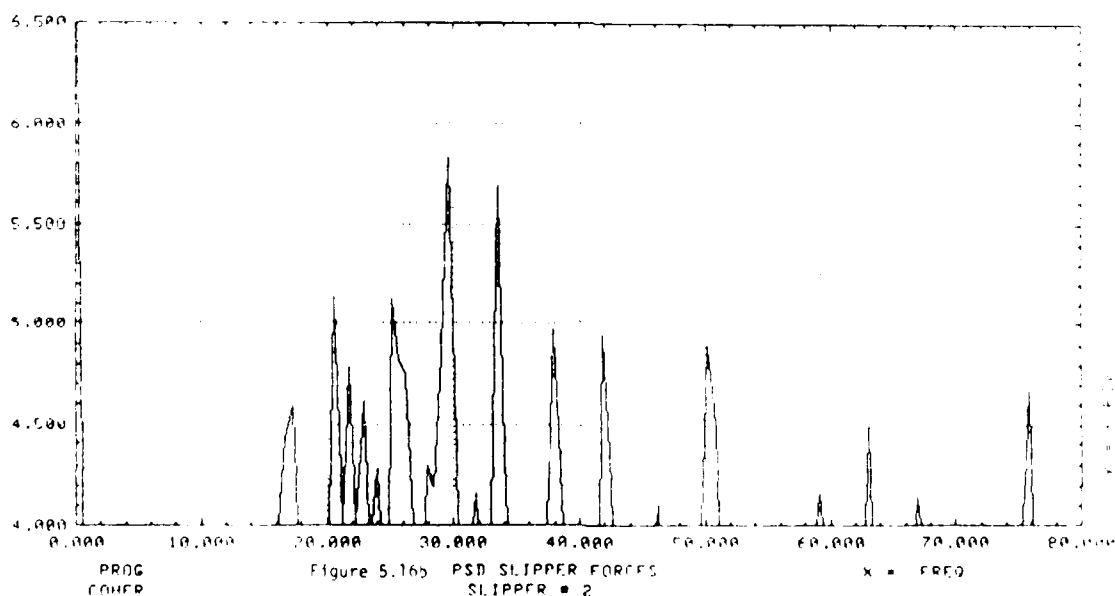


Figure 5.16a POWER SPECTRAL DENSITY



PROCESSED: 03:23 PM THU., 22 MAR 84
DATE: 03-FEB-84

INTEGRAL G**2/T: .3044521E+07
MISSION: 19Y-01

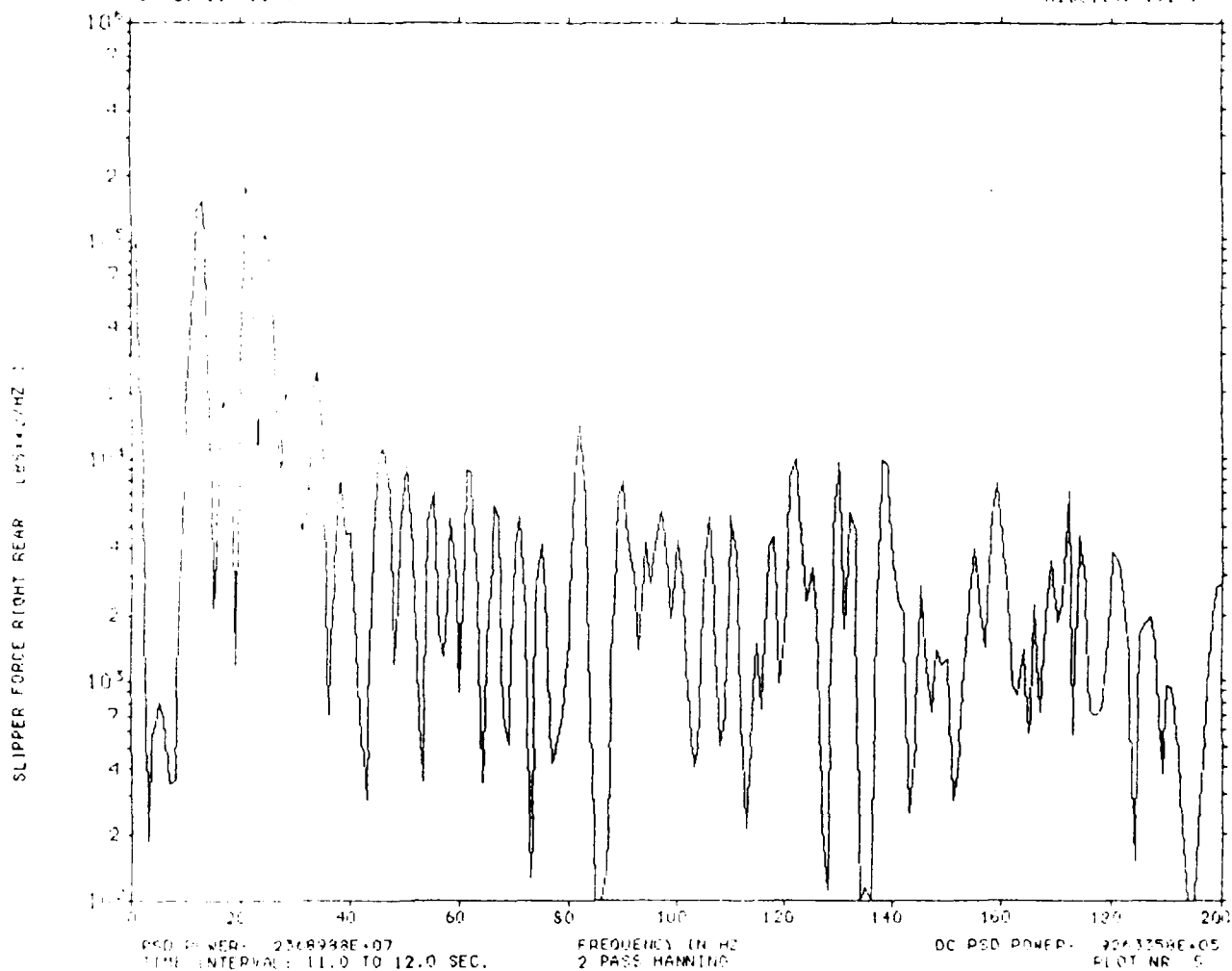


Figure 5.17a POWER SPECTRAL DENSITY

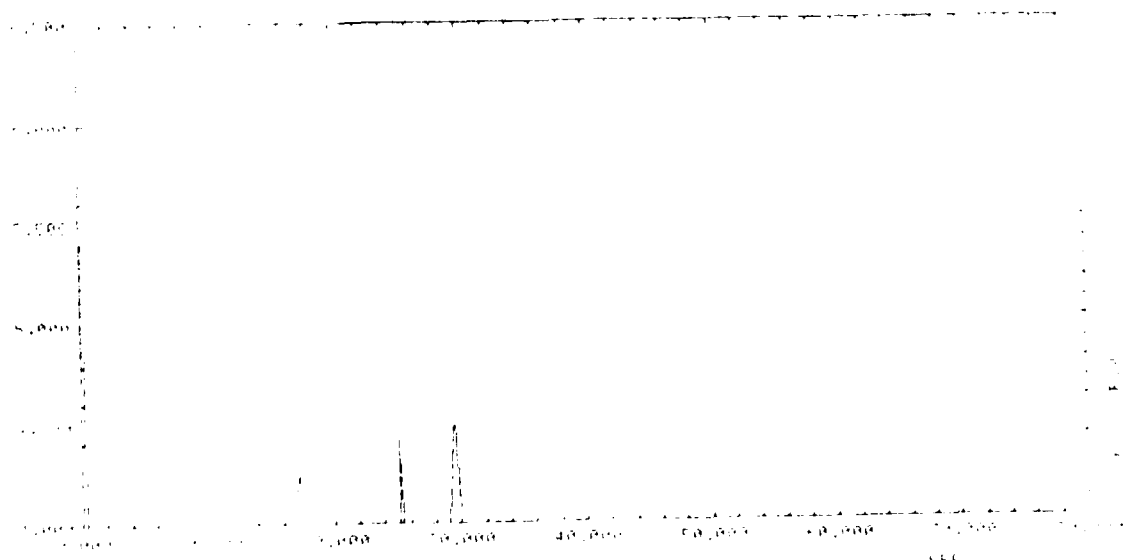


Figure 5.17b

and 5.15b for the same frequency spectrum, only clipping the power axis at 10^4 and $10^{6.5}$. With these figures it is possible to isolate individual frequencies that were excited, and look at the level of energy contained in that frequency.

Close examination of the actual versus the predicted plots show frequency content that are almost identical. The actual plots have frequency content not seen in the predicted, but these have to do with modal participation, which is not considered in this portion of the study. Frequency content is summarized in Table 5-6, in the concluding section for the dual rail sleds.

Power levels for the frequencies fall into the same order of magnitude range for all rail functions. Examining PSD's for the individual rail functions again shows the rail roughness break at 0.020 inches. Roughnesses greater than this have frequency power levels in excess of the measured, and roughnesses less than 0.020 inches have power levels less than measured.

Examination of the frequencies indicated some unexpected occurrences. These were exhibited by all rails unless noted.

The frequency centered around 32 hertz on the data sample sets had to do with a phenomenon associated with the survey. For this velocity of simulation, 32 hertz corresponds to a track distance of 50 feet. The survey

distance for the north and south 15000 feet was 50 feet. The long period surveys were accomplished in 100-foot intervals, only repeating the last 50-foot segment of one section at the beginning of the next 100-foot section. This resulted in a looping phenomenon of 50 feet.

The frequency spike at 42 hertz corresponds to a distance of 39 feet, or the rail length. Mixon noted that for track lengths in excess of 30 feet (and less than 50 feet), the north 15000 was smoother (had less power) than the south end. This is confirmed in the simulations. Energy content in this range for this velocity (i.e., 32 to 46 hertz) is less for the north end of track than for the south. However, for all other frequencies, the north end has larger energy content than the south.

The spike at eight hertz for TS 34000, both top and bottom surfaces, corresponds to the looping of the data period (208 feet) for this velocity. For the sled to be traveling at 3800 feet per second ($M=3.5$), the first fundamental sled suspension mode could be excited by this fundamental looping distance.

5.2.3 RIGID BODY CONCLUSIONS AND SUMMARY

This section concludes the rigid body simulation and analysis phase of the dual rail sled section. It will

address all questions posed in the rail roughness study directive, from a rigid body point of view, that had been left unanswered.

5.2.3.1 CONCLUSIONS

5.2.3.1.1 PERIODICITY VERSUS NON-PERIODICITY

By examining TS 44000 top and the south 15000 top rail function, the statistical effect of periodicity can be examined. Each of these profiles had the same rank rail roughness, $S_{y,x}=0.012$, but only one had a periodic content. Notice from the slipper beam results, the same roughness generated approximately the same standard deviation. However, the periodic rail underpredicted the mean by 70 percent more than the nonperiodic rail (underpredictions of 15% versus 24%) for the front beam. This might be explained by the periodic rail being in phase with the fundamental sled frequency and the slipper just "skimming" the top of the smooth period rail and not being excited. The sled randomly hits the rail and generates a sufficient quantity of larger spikes to move the mean for the nonperiodic rail.

Looking at TS 34000 top and bottom, it is noticeable that rough periodicity strongly affects the mean and standard deviations. These profiles overpredict these

quantities by large amounts. From the frequency and energy plots it is seen that the fundamental sled frequencies contain more energy for rough period rails than for the nonperiodic rail forcing function.

5.2.3.1.2 RAIL GRINDING

Rail grinding effectiveness can be quantitatively considered by examining the north and south 15000 feet of track. The south 15000 is smoother than the north due to a longer period of time to work at smoothing the rail. The simulated results indicate the same thing. The south 15000, both top and bottom, tends to underestimate the average deviation more than the north 15000. However, the south 15000 has a larger standard deviation than the north end.

One hypothesis is that long period frequency content (rail lengths of 30 to 50 feet) controls the standard deviation at this velocity, but the overall roughness controls the mean. This rail length corresponds to sled frequencies in the 30 to 45 hertz range. This range does not contain the fundamental frequency, but is typically in the range that adds the largest secondary effects, that is to the standard deviation. For the north 15000 this range of track is smoother than the south end, and hence the lower standard deviation. The

overall roughness for the north is greater than the south and this explains the higher average forces.

It is apparent that rail grinding is effective in lowering the long period rail effects that contribute to the dynamics of sled forces. This dynamic force reduction in turn reduces the fatigue aspects of the sled design process.

5.2.3.1.3 FINAL RAIL PROFILE DESIGNATION

Based on earlier work for SLEDYNE and Nixon^{7,6} using monorails, it was shown that modal participation absorbed about thirty (30) percent of the predicted forces. Using this fact, an ideal rail would be one that overpredicted forces on the average of less than 30 percent, with a small standard deviation. This criterion is met by all but one of the rail functions. This conclusion is based on monorail modal participation in regard to "stiff" slippers. The validity of this assumption is suspect for the much softer slippers and/or suspension systems of dual rail sleds.

5.2.3.2 RIGID BODY SUMMARY

Using all data examined thus far, it is inherent that a rail roughness greater than 0.020 inches tends to

overpredict rigid body forces. This roughness corresponds to the break point defined by Mixon⁹ between the roughest rail class (class A) and those that are smoother (classes B to D). It is extremely clear from Table 5-3 this value is the break point for both the average and standard deviation, for both the front and aft beams.

Based on this rigid body work, by keeping overall rail roughness below 0.020 inches, the peak forces induced into the slippers can be reduced significantly--that is, by 39 percent from the roughest rail (0.048 inches) to one with a roughness of 0.016. Across the spectrum examined, a one percent reduction in peak force appears possible for a 0.001 inch reduction in total roughness.

Rail smoothing is also effective from a localized roughness standpoint. Peak forces are not reduced drastically (about 4 percent) but the amplitude swing of the dynamic forces can be reduced by as much as 17 percent. This is the range where rail grinding appears to be particularly effective.

5.3 MODAL SIMULATION

In order to accurately simulate the real life performance of the sled, the modal participation will

have to be superimposed on top of the rigid body response. The modal participation has been limited to the structural modes of the sled not directly related to the slipper suspension system. These are hereafter referred to as the secondary structural modes. For the Ramjet sled there are five modes identified, and these are given in Table 5-6 in the concluding section of this chapter.

Once the secondary modal parameters had been defined, the simulation consisted of repeating everything done under the rigid body analysis. In other words, the eleven valid lift conditions were repeated for a track distance of 4000 feet for a constant velocity associated with that lift condition. This was done for each rail roughness function for a total of 99 simulations.

Each rail roughness simulation, consisting of the eleven valid trajectory conditions, was statistically averaged to determine the effect of the modal participation. The results of this analysis are presented as an average percentage deviation between the actual forces (see Table 5-2 for the actual forces) and the predicted values. Also, the standard deviation about the mean deviation is determined.

The effect of modal participation was alluded to in the conclusion of the rigid body work. There it was stated that for one given condition for monorails, using

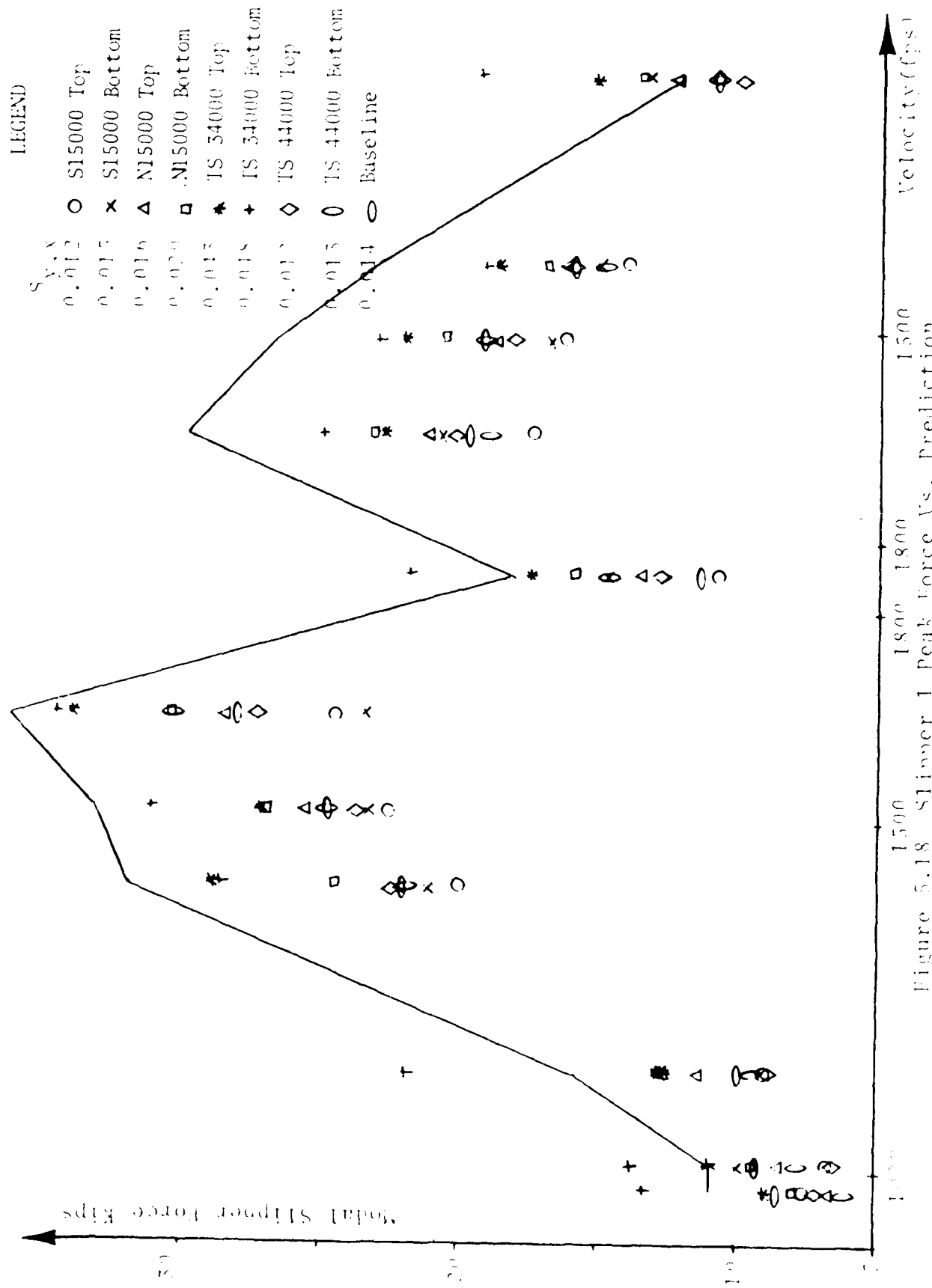
six modes at five percent damping, a reduction in the deviation of about 30 percent can be expected. This amounted to reducing the overprediction from 20 to 40 percent to an error of ± 10 percent. However, it is unknown whether this is applicable to dual rail sleds.

5.3.1 DATA ANALYSIS--AMPLITUDE DOMAIN

5.3.1.1 PEAK FORCES

The simulation consisted of 99 computer runs of the valid lift conditions for each rail roughness function. The analysis contained the participation of five structural modes superimposed on the rigid body work done previously. Results of the peak force predictions are shown plotted in Figures 5.18 through 5.21 for slippers one through four, respectively. The solid line represents the actual peak forces for that condition from the 19Y-C1 mission. The interesting thing here is that only one rail function appears to consistently exceed the measured values. This is TS 34000 bottom and is the same function hypothesized in the final rail profile designation section for rigid body work that would fail.

The statistical analysis is shown plotted in Figure 5.22 and summarized in Table 5-5 for the slipper beams. The "x" denotes where the average percentage deviation



LEGEND

$\gamma_{v,x}$	
0.012	○ S15000 Top
0.015	× S15000 Bottom
0.016	△ N15000 Top
0.020	□ M15000 Bottom
0.013	* TS 34000 Top
0.018	+ TS 34000 Bottom
0.012	◇ TS 44000 Top
0.013	○ TS 44000 Bottom
0.014	○ Baseline

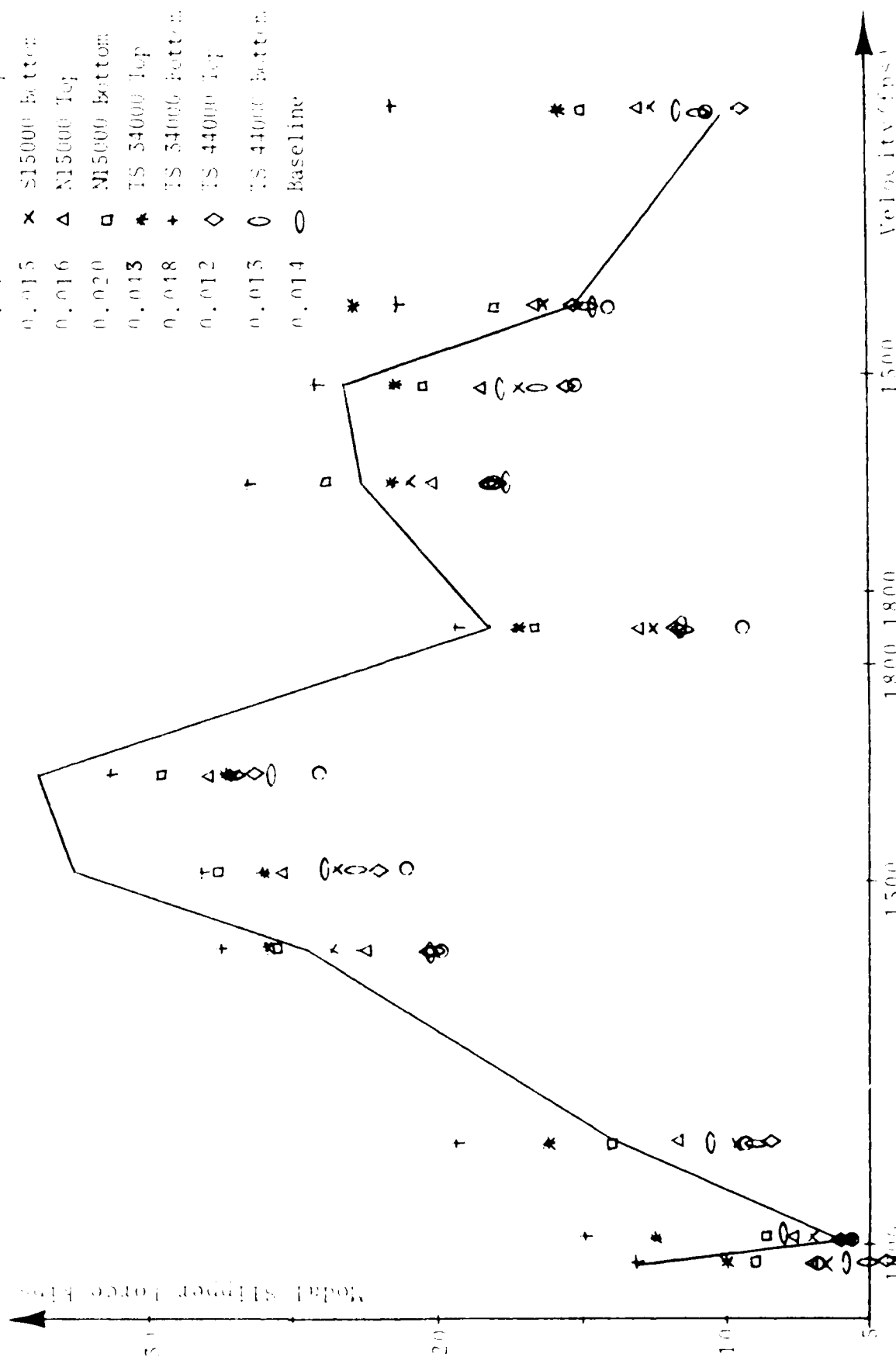


Figure 5.19 Slipper 2 Peak Force Vs. Prediction

LEGEND

$S_{V,X}$	
0.012	○ S15000 Top
0.015	× S15000 Bottom
0.016	△ N15000 Top
0.020	□ N15000 Bottom
0.043	★ TS 34000 Top
0.048	† TS 34000 Bottom
0.012	◇ TS 44000 Top
0.013	○ TS 44000 Bottom
0.014	○ Baseline

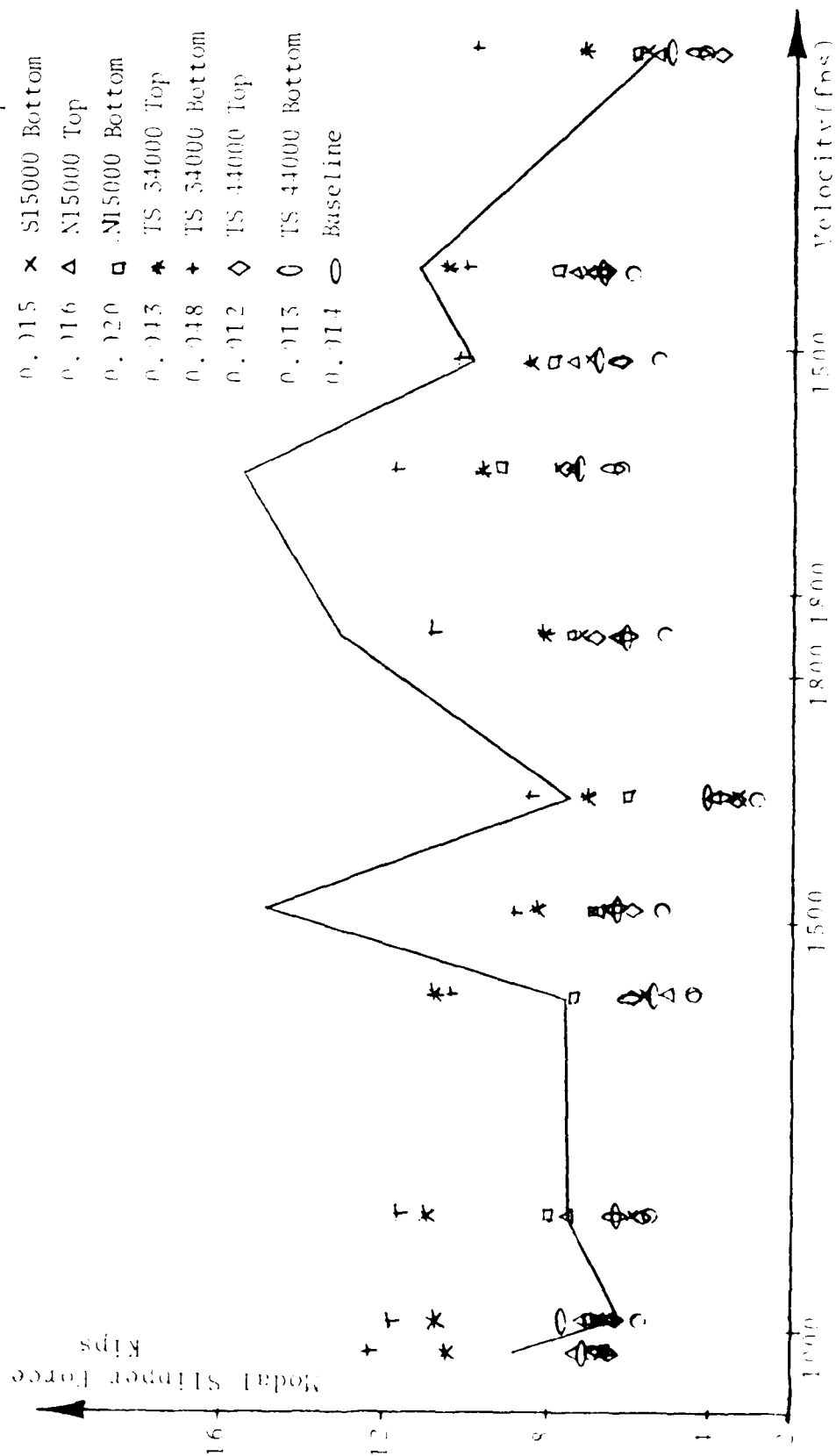


Figure 5.20 Slipper 5 Peak Force Vs. Prediction

135

0.015
 0.015
 0.016
 0.020
 0.013
 0.018
 0.012
 0.013
 0.014

S1500
 S1500 Bottom
 N1500
 N1500 Bottom
 TS 3400
 TS 3400 Bottom
 TS 4400
 TS 4400 Bottom
 Baseline

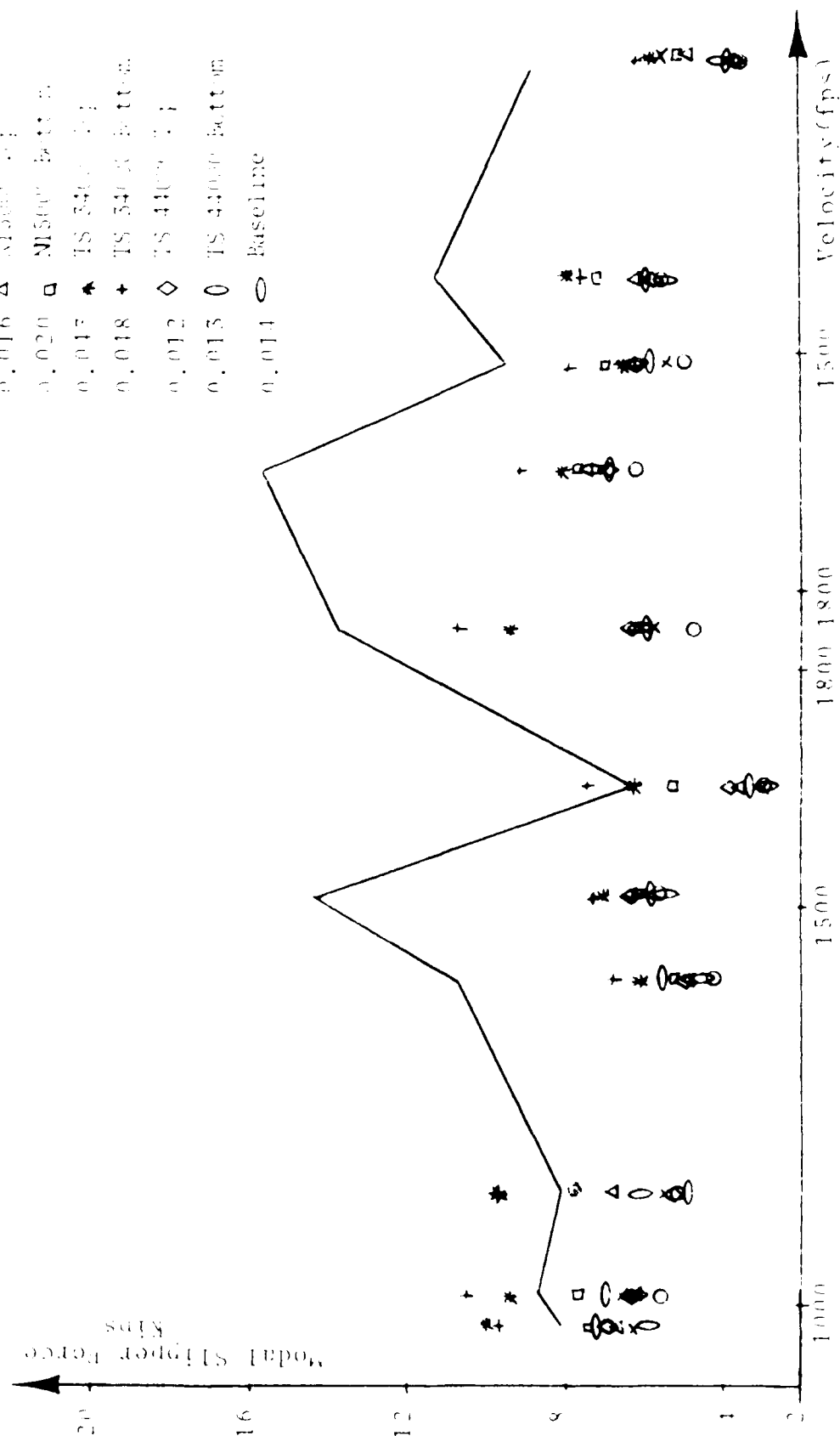


Figure 5.21 Slipper 4 Peak Force Vs. Prediction

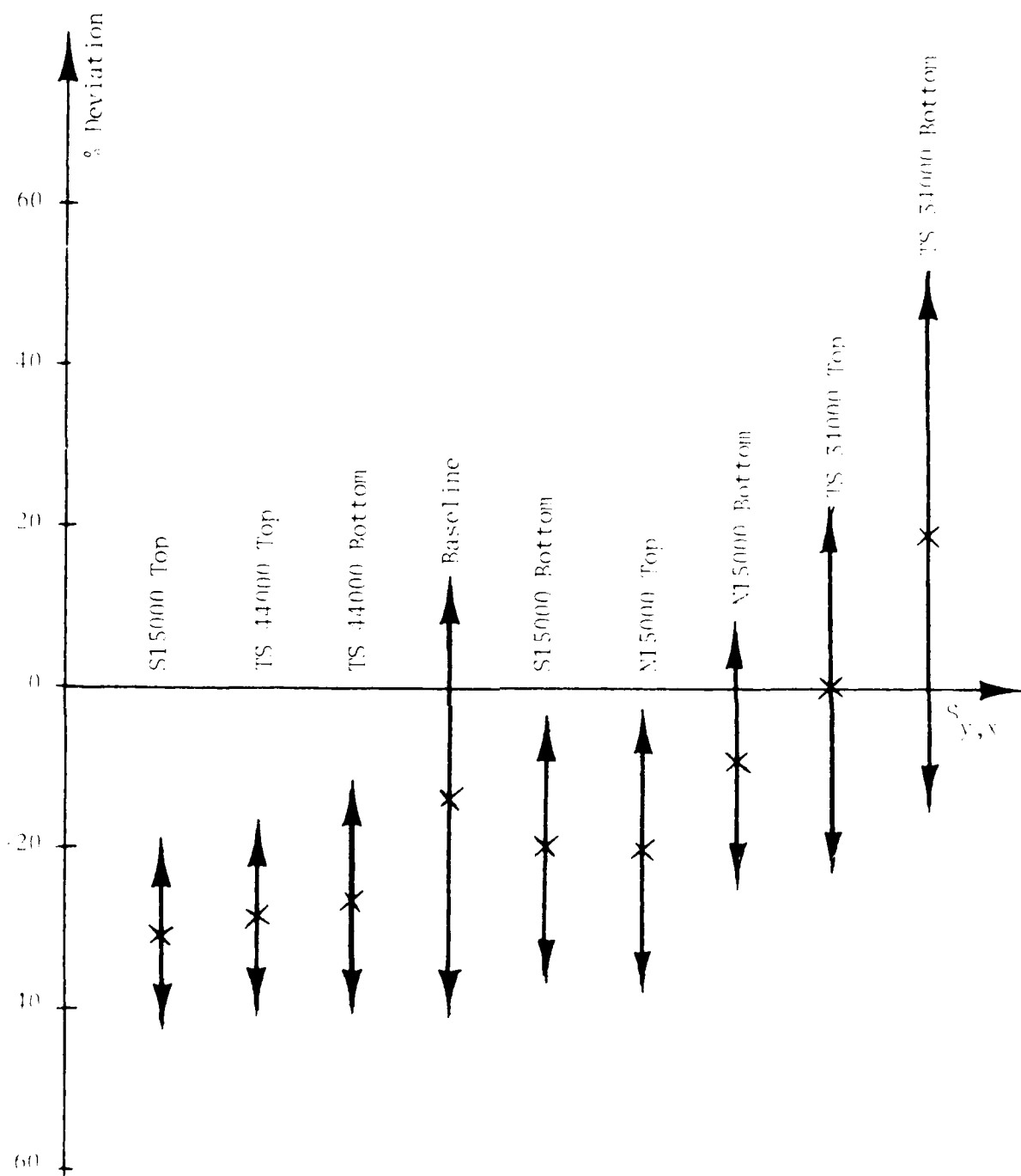


Figure 5.22 Front Beam Statistical Results

TABLE 1-5 STATISTICAL SUMMARY
OF LOCAL PARTICIPATION PREDICTIONS
VERSUS RAIL PERCENTAGE

Cell	$P_{y,x}$ (%)	Front Deck		Aft Deck	
		Average	1 Sigma	Average	1 Sigma
30,000 Bottom++	0.048	+19.41	33.5	-17.41	72.1
30,000 Top++	0.043	+6.71	23.0	-7.21	29.9
15,000 Bottom	0.020	-8.21	15.7	-25.51	18.3
15,000 Top	0.016	-20.01	16.4	-34.91	17.7
815,000 Bottom	0.015	-19.61	15.9	-37.21	16.2
Baseline	0.014	-13.21	27.0	-37.11	19.9
45,000 Bottom++	0.013	-26.01	13.2	-39.01	14.2
45,000 Top++	0.012	-27.71	11.3	-37.81	15.5
155,000 Top	0.012	-30.91	10.8	-45.61	15.6

Notes:

1. denotes periodic rail content

2. All values listed are percentages

3. positive sign denotes overprediction

4. negative sign denotes underprediction

between predicted and actual forces occurs. The heavy arrow represents the ± 1 standard deviation about the mean.

Looking at the table, it is seen that TS34000 bottom severely overpredicts as expected. TS34000 top also overpredicts but only slightly. Further examination of the table reveals a break point in the rank roughness predictions again occurring at 0.020 inches. This break point holds for the aft beam as well as the front.

Comparison of Tables 5-3 and 5-5 will show the effect of modal participation. It is readily seen that the modal participation does absorb energy but not as much as originally estimated based on the monorail work. It was hypothesized the modes would absorb up to 30 percent of the forces; however, the range of force reduction is from 5 to 20 percent for all conditions examined. The standard deviation actually increases for the modal simulations for all cases except the smoothest rails, and then it remains

5.3.1.2 PEAK FORCES VERSUS TIME

As with the rigid body work, the force-time history for slippers two and four was plotted for comparison to the real measured values. Figures 5.23a and 5.24a show the actual force-time history for these two slippers.

03-FEB-84

MISSION : 141 01

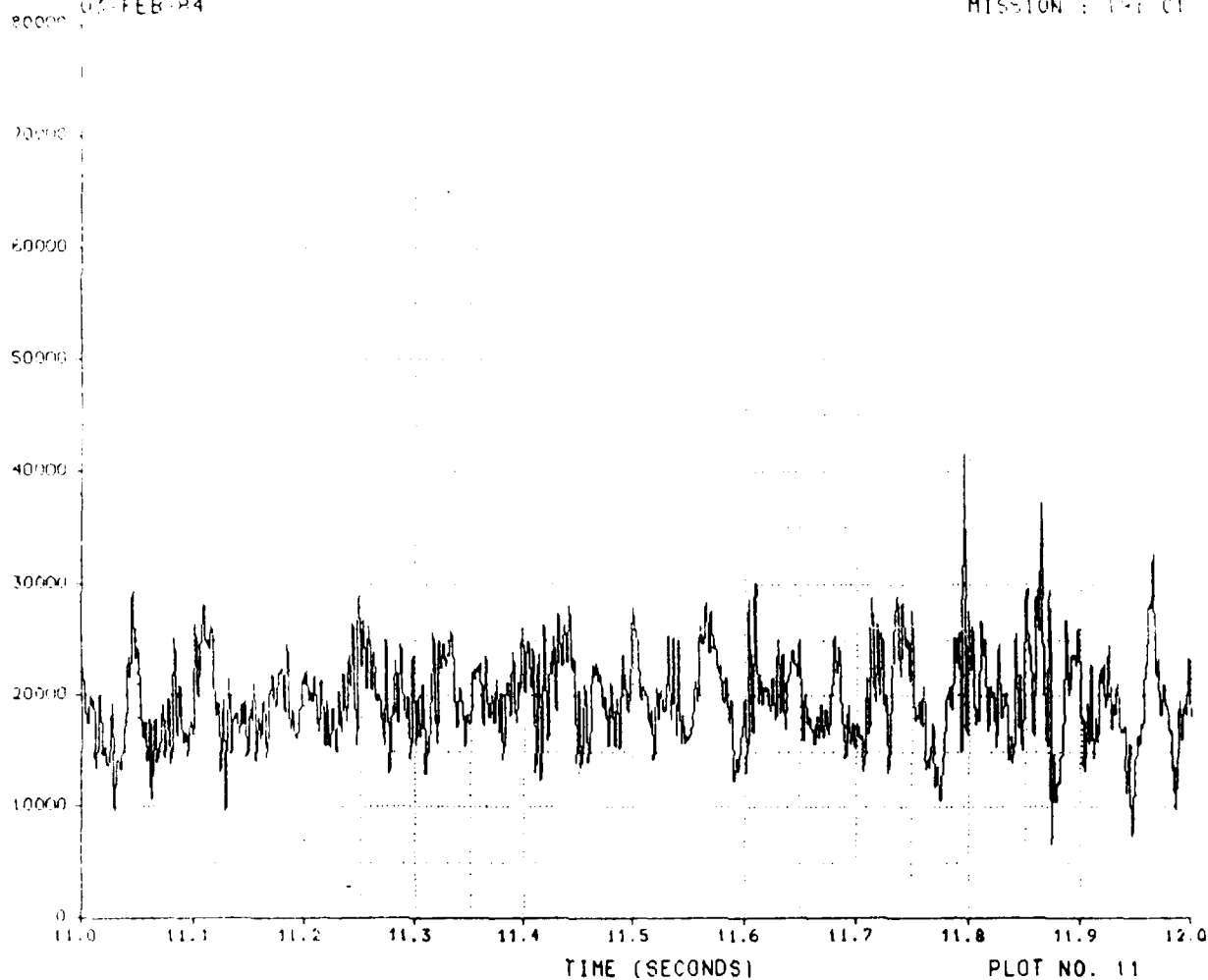
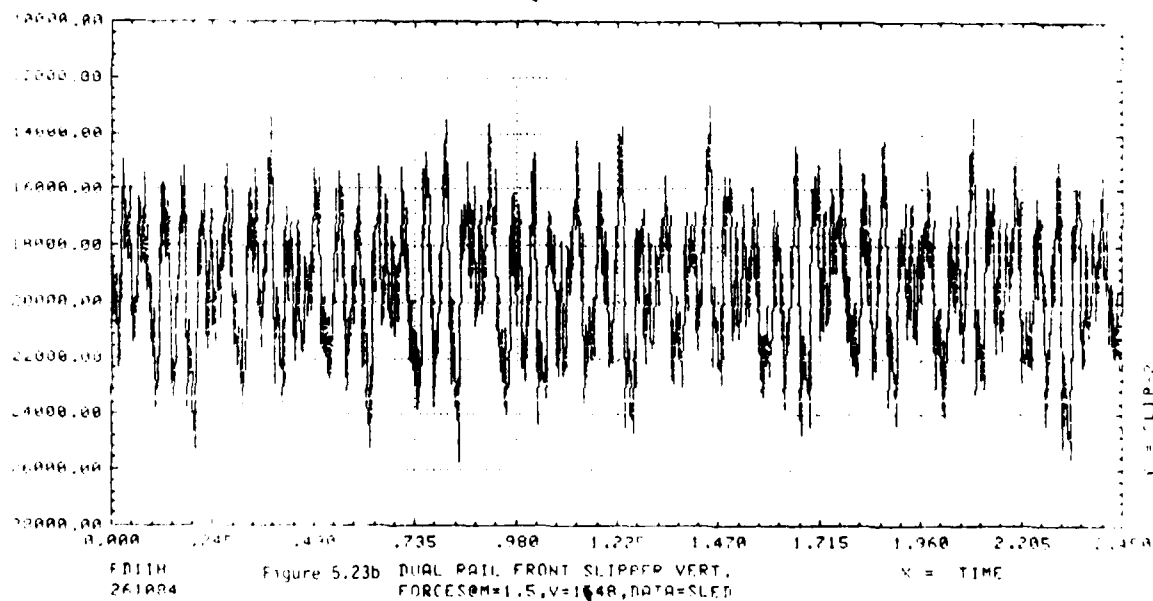


Figure 5.23a SLIPPER FORCE RIGHT FRONT VS TIME



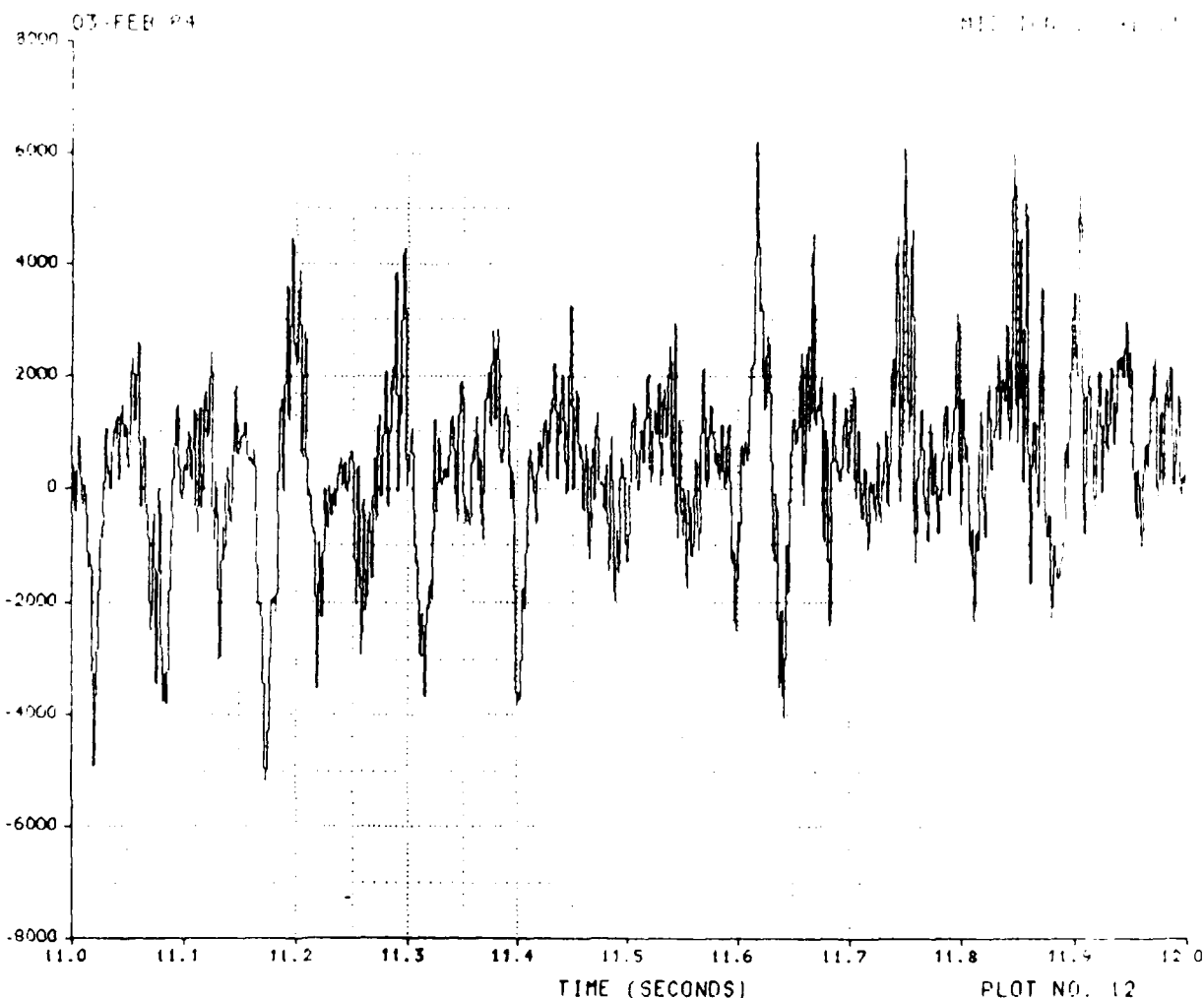
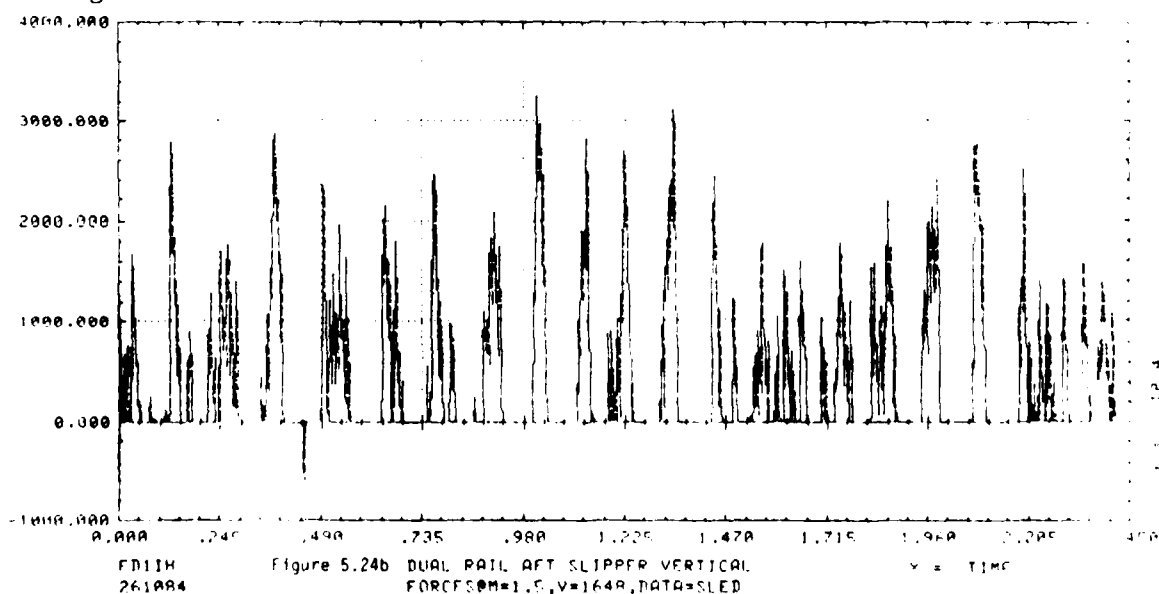


Figure 5.24a SLIPPER FORCE RIGHT REAR VS TIME



Figures 5.23b and 5.24b contain the actual simulation histories for the baseline rail function. The remaining eight rail function histories are contained in Appendix C, Figures C.17 through C.32.

From the actual data, slipper two forces stayed in an envelope between 6 and 41 kips and were centered about 20 kips. The plot also indicates a low frequency content that the data appears to be modulating about. Looking at the modal plots for all nine functions for this slipper indicated the same centering around 20 kips but with envelopes of differing sizes. Generalizing, the rougher the rail the larger the envelope span. Also, all functions exhibited a low frequency content, yet the smooth rails with periodic content (i.e., TS44000 top and bottom) were the most pronounced.

Examining the aft slipper force data for the actual run indicated forces fluctuating by ± 6 kips. All forcing functions exhibited a fluctuating component of up to ± 6 kips; however, they are centered about a positive one kip instead of zero as for the actual run data. The rail functions that did not contain periodic forcing content were extremely one-sided, that is, they ranged from zero kips to a maximum value of about 3.5 kips. The periodic content rails and the rough rail were two-sided functions that resulted in a low frequency content that modulated about one kip.

Peak spike forces all were under the actual measured force for both slippers under this simulation case. The front slipper operating envelope stayed within ± 6 kips of the quasi-steady-state force for the smooth rail functions. The rough rail functions (those in excess of 0.020 inches) all exceeded this dynamic envelope by 50 percent or more.

From the rigid body dual rail work, it was noted that the south 15000 feet of track exhibited a pronounced rough spot in the data that caused distinct force spikes to occur. The modal simulation also exhibited this spike and its cycling just as the rigid body did, only it was not as pronounced. The modal participation absorbed approximately a third of the magnitude of this spike. That is, for the rigid body simulation these rough spots created a nine-kip dynamic spike. whereas with modal participation, this was only a six-kip spike, or a third less than the rigid body case.

5.3.1.3 FORCE HISTOGRAM

The rigid body dual rail simulation concluded that peak forces were Rayleigh distributed, and the extent of deviation from the Rayleigh trend is strongly dependent on the quasi-steady-state forces. The results for the modal participation (see Figure 5.25) exhibits the same

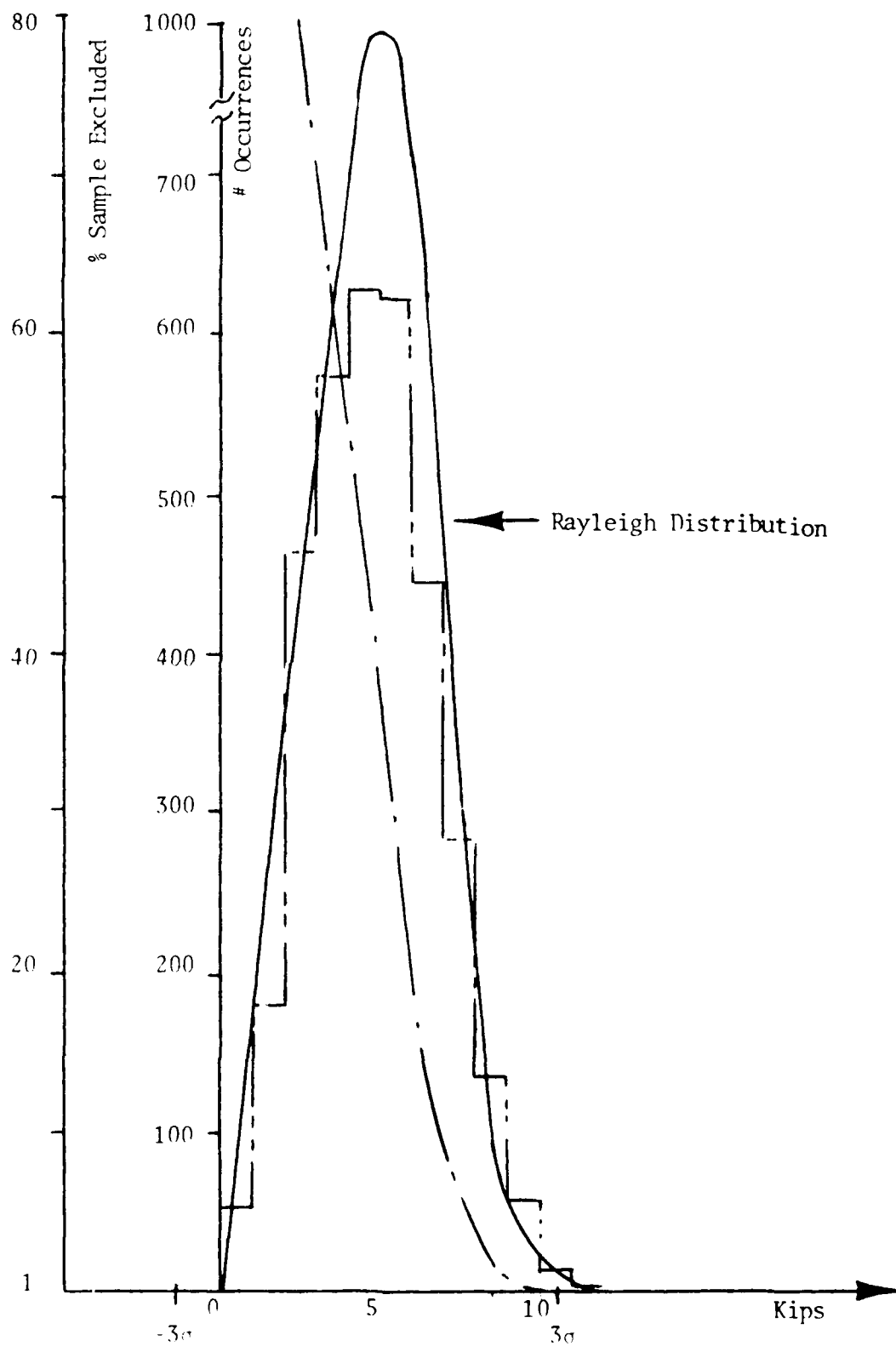


Figure 5.25 Rayleigh Vs. Histogram Distribution

tendency toward a Rayleigh distribution. However, at the expected maximum Rayleigh occurrences the simulation occurrences are only about 67 percent of what they should be. This is a result of a small standard deviation forcing a large expected quantity into the peak occurrence range. The reason for the small standard deviation is the reduction in the dynamic forces due to modal energy absorption. All simulations indicated the same phenomena. The extent of the error in the maximum number of occurrences is related to the range of the standard deviation. The smaller it is, the more extreme the difference in the number of occurrences.

It is concluded that the peak force simulation, including the effects of modal participation, does in fact follow a Rayleigh distribution. The amount of deviation is a direct result of the quasi-steady-state forces and the dynamic force envelope.

5.3.2 DATA ANALYSIS--FREQUENCY DOMAIN

The highest frequency content obtainable was 275 hertz from the rigid body simulation. This limit had to do with the timer integration step sizes which are related to the highest frequency content of the simulation. The largest frequency, for modal participation, deals with the highest mode used, which is

considerably above the rigid body eigenvalues. Therefore, a larger frequency band is obtainable and the upper limit for this series of simulation is 455 hertz.

Recalling PSD plots for slippers two and four discussed earlier (Figures 5.14a and 5.15a) are again summarized at this point. Sharp rolloff is noted above 30 hertz and noise predominates above 70 hertz. Total power in the front slipper is 20374 pounds force rms, and the aft slipper is 1745 pounds rms.

Figures 5.26a and 5.26b show a typical wide spectrum response for these two slippers when modal participation is involved. These figures show a sharp rolloff beginning about 50 hertz and leveling off into noise about 100 hertz. Comparison of rms force content is not available since the local PSD program does not accumulate the power under the PSD.

Figures 5.16a and 5.17a are the narrow spectrum response of the actual run data and were discussed in detail in the rigid body section. Figures 5.27a and 5.27b are the simulation PSDs for the same frequency band. Close examination of the figures shows frequency content identical to that of the actual run; however, the energy in the rigid body frequencies has been reduced by about 37 percent. Frequency content is summarized in Table 5-6 in the concluding section.

Power levels for the modal frequencies fall into the

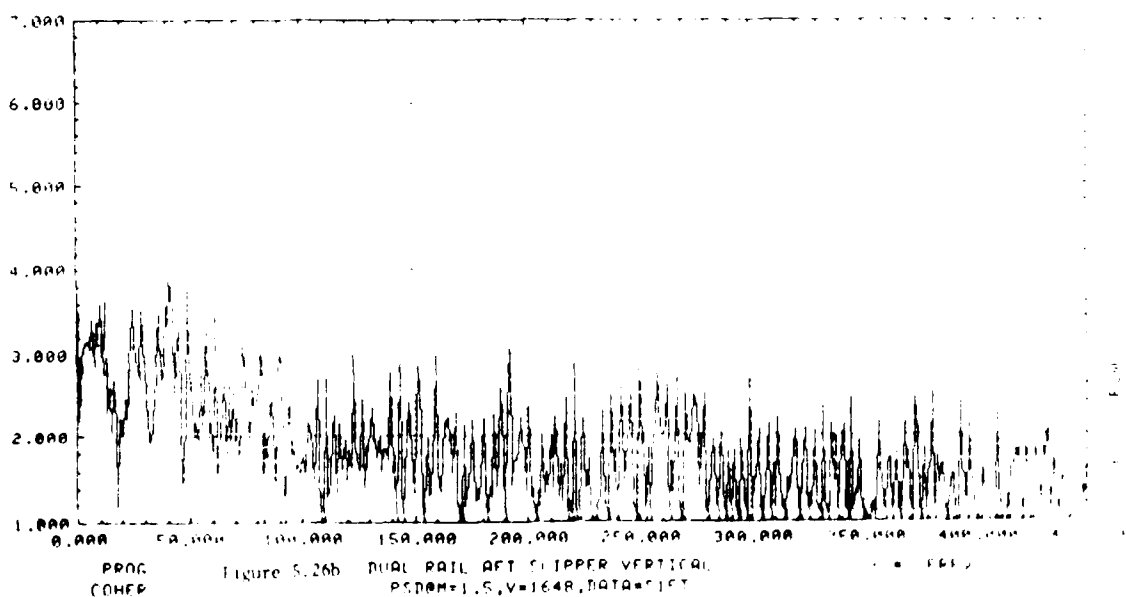
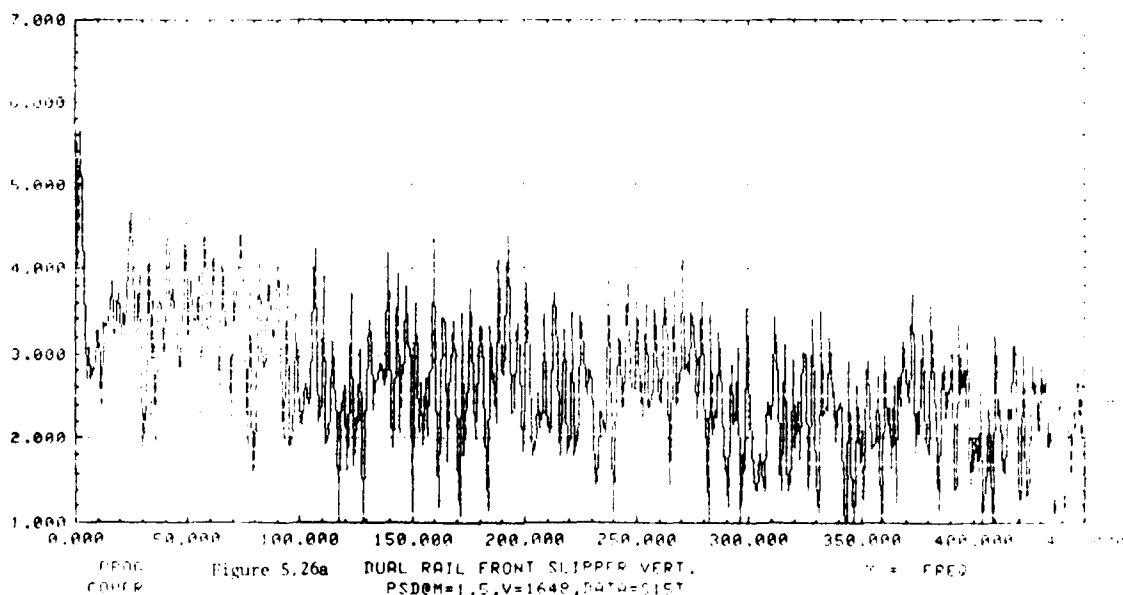


Figure 5.26 Typical Wide Band PSD Spectrum

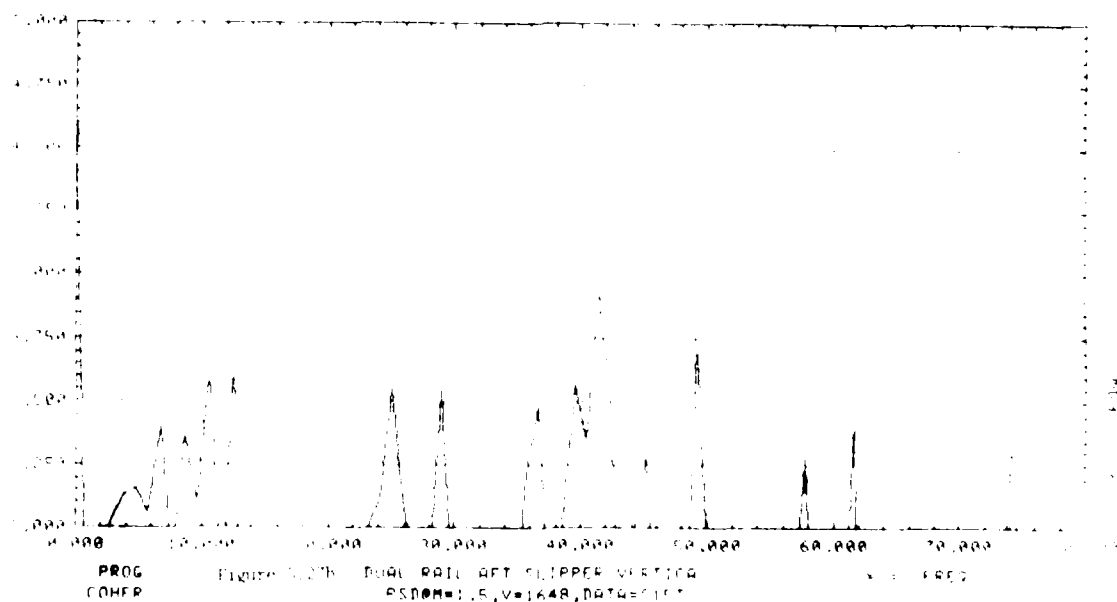
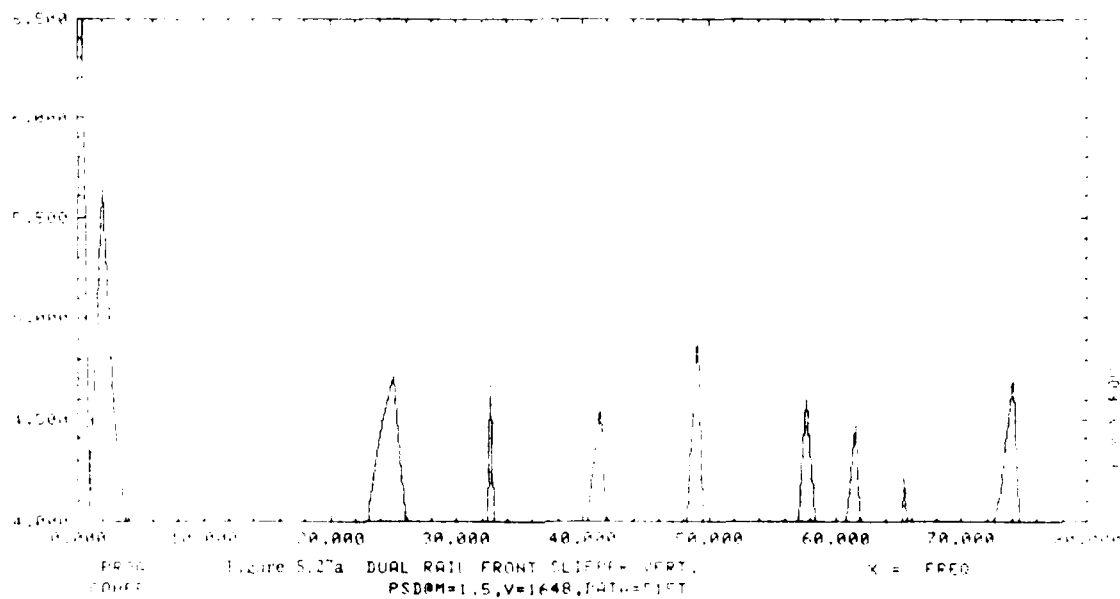


Figure 5.27 Typical Narrow Band PSD Spectrum

same order of magnitude as the measured data for all rail functions. All rail functions except the two roughest (TS34000 top and bottom) fall below the measured levels, and these two rough rails exceed it. At the rank roughness of 0.020 inches, again a distinct separation of power levels occurs. Roughnesses less than this value have power levels distinctly below those of the roughnesses in excess of 0.020 inches.

The same unique frequency phenomena are present here as in the rigid body simulations. However, the facsimiles of the data survey are amplified in this case. The frequency at 32 hertz is the 50-foot survey data sampling. It also coincides with a sled mode at 34 hertz. This coupling induces a large energy spike at this frequency, in fact, it is about 300 percent of that without the mode shape being superimposed. The frequency at 42 hertz couples the physical rail lengths of 39 feet to a sled frequency. In this case the sled's frequency mode shape does not contribute much to the power level as the power is approximately equal to that without the mode shape.

The spike at 4 hertz on the S15000 top data is the data set looping end to end. This frequency has energy content so low in the rigid body simulation that it is apparently nonexistent. However, this spike is the predominant one in the vertical direction, and no

plausible explanation is available outside of possible modal coupling.

The spike at 8 hertz on the 34000 top rough periodic rail is the looping of the rail period. This data facsimile was noted on the rigid body work and is again the controlling energy spike. It is the same magnitude as is the rigid body spike.

5.3.3 MODAL CONCLUSIONS AND SUMMARY

This section concludes the modal simulation analysis for a dual rail sled. It will address all questions posed in the rail roughness study directive from a modal participation point of view.

5.3.3.1 PERIODICITY VERSUS NON-PERIODICITY

As for the rigid body simulation, the smooth periodic rail (TS44000 top) generated the same standard deviation as the smooth nonperiodic rail (TS S15000 top); and this value is 25 percent less than the rigid body value. Unlike the rigid body work, the periodic rail underpredicted by 10 percent less than the nonperiodic rail (underpredictions of 28 percent to 31 percent) for the front beam. This implies that the modal content is moderately excited by the periodic rail content. This

implication is further substantiated when examining the effect of modal energy absorption between the rigid body and modal cases. The modal content reduced the average deviation underprediction by 16 percent for the periodic rail. Comparably the nonperiodic rail modal content reduced its average underprediction by 107 percent.

The comparison between rough periodicity and smooth periodicity is similar to the rigid body case. Rough periodicity strongly affects the mean and standard deviations. However, the reduction in the average force predictions is significantly more for the rough periodic rail than for the smooth periodic rail, i.e., 87 percent compared to 16 percent. Conversely, the rough periodic rail in conjunction with the modal content increases the standard deviation by 20 percent.

5.3.3.2 RAIL GRINDING

The effectiveness of rail grinding can be quantitatively examined by looking at the north versus south 15000 feet of track. The south end of the track underpredicts the mean when compared to the north, as is expected. What was not expected was the standard deviation to be smaller for the south end. The interesting phenomenon here is that the content for the fundamental heave frequency for the north end increased

by 67 percent from the rigid body situation. This increase is apparently due to the first roll structural mode being almost superimposed on the fundamental vertical heave. This coupling of modal roll and rigid body heave is causing a large dynamic force excursion to occur. The other secondary structural frequencies have energy content considerably less than the south end, and these frequencies lie in the smoother north end energy content.

Rail grinding must still be considered effective for reducing the dynamic force range as long as the forcing function frequencies lie in the secondary structural frequency range. This statement must be caveated to account for structural modes acting in the direction and frequency of a rigid body mode, i.e., roll structural mode and a rigid body heave coupling.

5.3.3.3 FINAL RAIL PROFILE DESIGNATION

As hypothesized in the rigid body section, the modal content does reduce the peak forces occurring during the simulation but not up to 30 percent as thought. Based on the original assumption, it was thought all rail functions except TS34000 bottom might provide adequate simulation results. This assumption was subsequently verified as being accurate, with TS34000 top only

marginally overpredicting. To obtain the best average prediction with the smallest standard deviation, the forcing functions to use should be the north 15000 bottom or the baseline function. Preference should be given to the north end bottom function.

5.3.3.4 MODAL SUMMARY

From all data reviewed thus far, it is inherent that rail roughnesses in excess of 0.020 inches tend to overpredict forces even with the modal energy absorption. This break point holds for both the front as well as the aft slipper for both the average deviation as well as the standard deviation.

The modal content affects peak forces in varying degrees but in all cases it reduces the average deviation from the rigid body case. This reduction is in the range of 5 to 20 percent, not 30 percent as originally hypothesized.

Based on the modal simulations, the peak slipper forces can be reduced significantly by reducing the rail roughness. The amount of reduction is similar to that seen for the rigid body case. A one (1) percent reduction in peak forces is obtainable for each 0.001 inch reduction in rail roughness.

From a localized rail roughness point, rail

smoothing is effective in reducing slipper forces in the dynamic envelope by one-third when the modal participation is utilized. This is true unless a mode shape happens to coincide with a rigid body frequency, then this dynamic force reduction does not occur.

5.4 DUAL RAIL SUMMARY AND CONCLUSIONS

In an effort to verify the DASTARR program for dual rail sleds, an extensive number of computer runs were performed. These simulations were all performed using the constant velocity option for a single sled. The variable speed simulation has been performed and is discussed now.

5.4.1 DUAL RAIL VARIABLE VELOCITY SIMULATION

In order to perform variable velocity simulations, a trajectory analysis has to exist. This file is one created by the in-house track trajectory program called TOLED. This file must be hand edited to remove all header information. The resultant file contains information regarding the sled's downtrack velocity, track station, and acceleration. It also generates the aerodynamic drag, the thrust, and sled weight vectors acting on the sled at a given instant of time during the

trajectory. This trajectory analysis was performed to duplicate the velocity profile shown in Figure 5.3. Using these variable inputs from TSLED, the program will linearly interpolate the lift and its center from user-supplied tables. The simulation will then progress as for the constant velocity, using only the variable parameters instead of the constant ones.

The actual simulation for the variable velocity was terminated when a speed of 1517 feet per second under thrust was achieved. This velocity is the time when the on board propulsion ignited and the sled mass started changing. The results of this simulation are shown plotted in Figures 5.28a for the rigid body case and in 5.28b for the modal case. The individual slippers are plotted as the percentage deviation in peak force at the given terminal velocity of the simulation.

Notice from the rigid body simulation that each slipper except for number two tends to underpredict by 10 to 20 percent in all cases for rail roughnesses less than 0.020 inches. Slipper two overpredicts by about 10 percent on the average for this same rail classification. Roughnesses above this defined break point overpredict more severely. The modal simulation results (Figure 5.28b) mirror those of the rigid body, only the overpredictions are about 50 percent larger than for the rigid body.

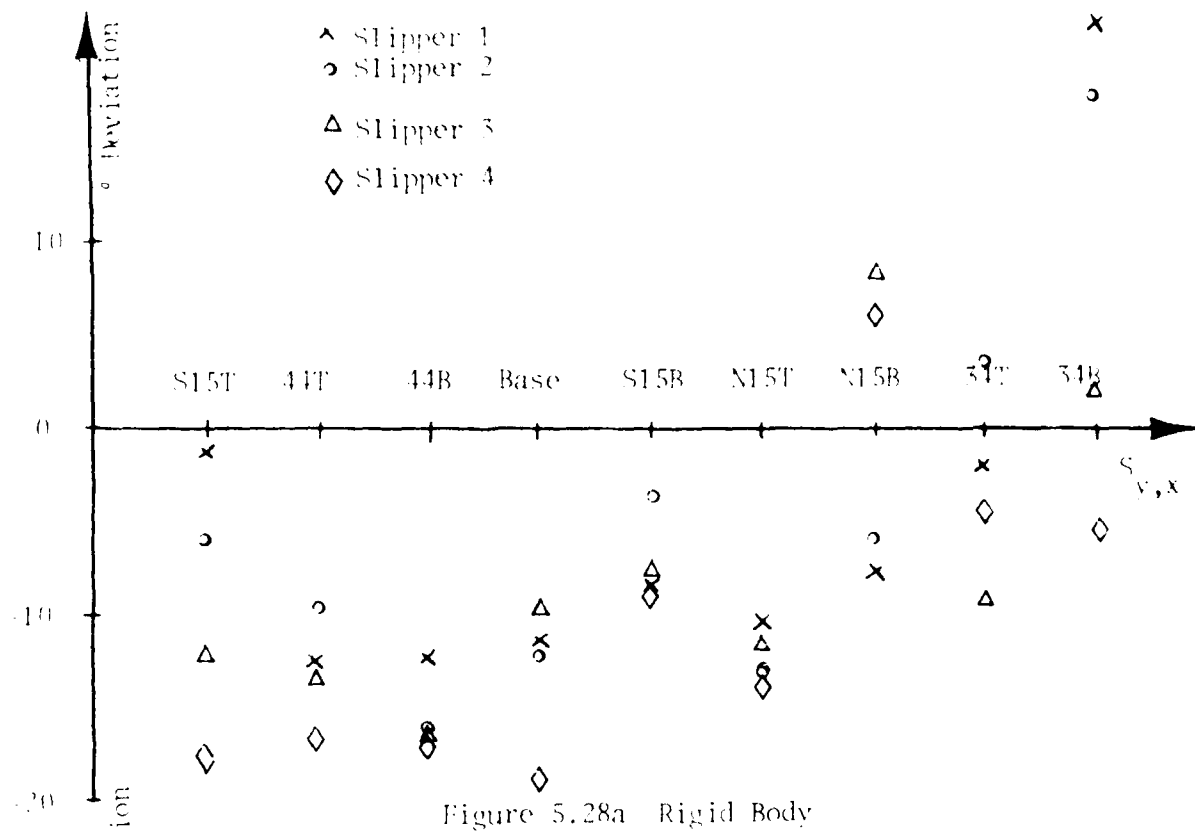


Figure 5.28a Rigid Body

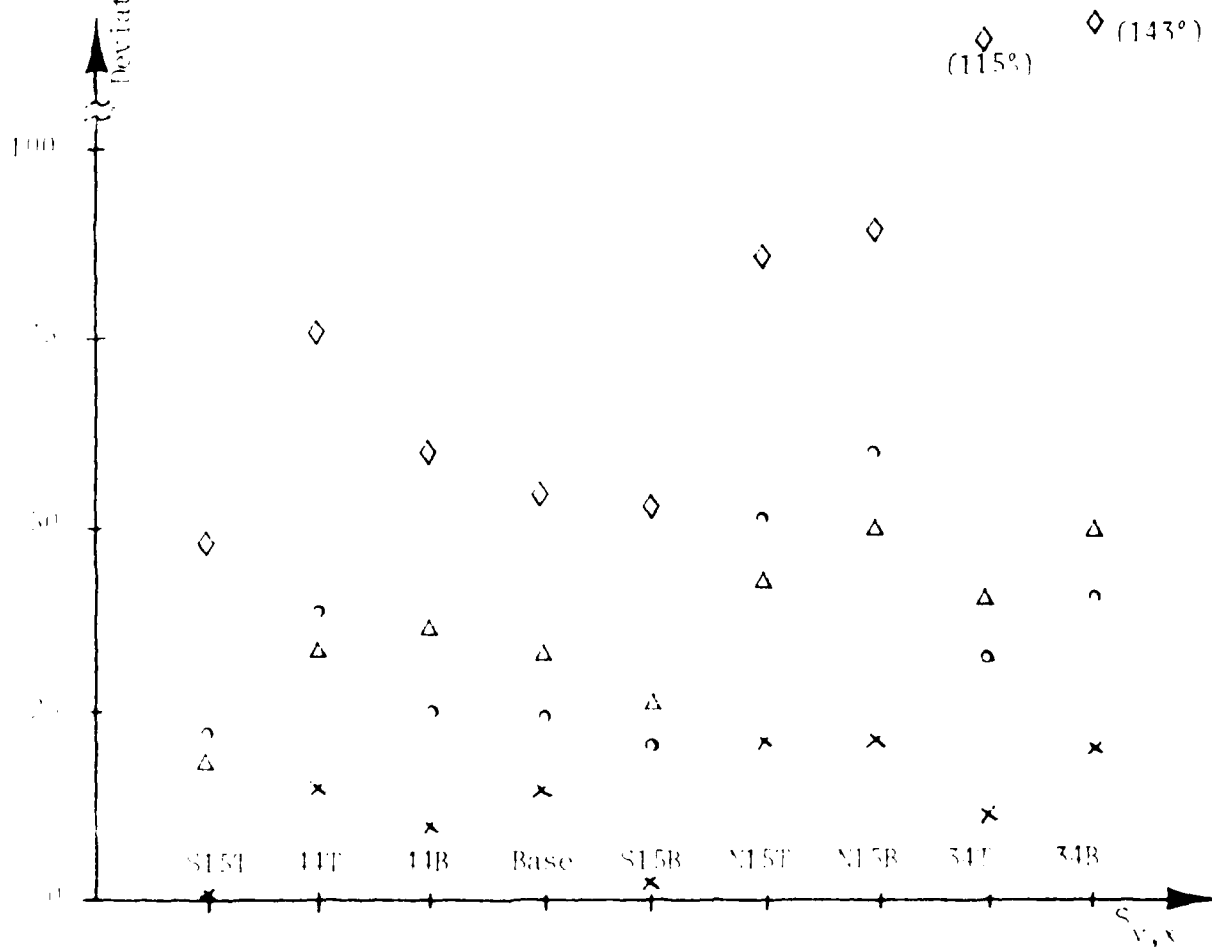


Figure 5.28b Modal Participation
Figure 5.28 Variable Velocity Deviations

Examination of the data output for the modal simulations shows all slippers peaking at times that correspond with the same Mach number as they did for the rigid body simulation. Since the rigid body contribution has to be constant between simulation cases, the differences must be due to the modal properties being excited. The particular modes being used in the modal simulations have frequency content primarily in the 25 to 30 hertz range. A forcing function distance of 45 to 55 feet must be present to excite these frequencies at this velocity. This encompasses the 50-foot survey looping distance common to all rail profiles. It is evident that this survey facsimile is exciting the predominant secondary modes and is adding approximately 30 percent to the slipper forces. The reason this did not occur in the constant velocity simulation is that this exact velocity was never encountered.

5.4.2 CONCLUSIONS

It is apparent that DASTARR accurately predicted the peak slipper forces for a dual rail sled from all data examined thus far. Depending on the rail function used, velocity option, or modal configuration the results are extremely good.

It is apparent that the constant velocity function

for a single sled will suffice for a given analysis situation. However, to use this option, the engineer will have to define the actual aerodynamic loads and the transmitted thrust acting on that sled. This option does not allow for the transmitted thrust transients to be considered. The multiple sled option with variable velocity should be used to counter this.

In this chapter, it was proven that the peak forces for a dual rail sled, either as a rigid body or coupled with the modal participation, are indeed a Rayleigh distribution as Mixon suggested. However, this distribution is strongly affected by the mean, or quasi-steady-state forces, and the standard deviation. That is, the Gaussian contribution is greatly enhanced by the lower the quasi-steady-state force component. Similarly the skewness of the distribution is dependent on the standard deviation. The smaller this deviation, the more skewed toward the mean is the distribution.

The rail function defined by the baseline rail of the bottom of north end of the track yields the best slipper estimates from a statistical standpoint. These functions apply to both rigid body and modal analyses for either constant or variable velocities.

Rail grinding is indeed effective but not as originally thought. It was supposed to smooth the rail for periods of length less than 52 inches. Instead it

smooths the long period, i.e., 30 to 50 feet in length. These long period effects are the ones that typically affect the secondary structural modes of the dual rail systems. This smoothing has the net effect of reducing the dynamic oscillation of the forces about the quasi-steady-state mean force. This statement has to be flagged because rail grinding does not affect the dynamic envelope if a mode shape is superimposed on a rigid body mode, i.e., first structural roll mode coupled with a rigid body vertical translation.

In general, a one percent reduction in peak forces is possible for each 0.001 inch reduction in rank rail roughness. In order to significantly affect slipper forces, the rank roughness needs to be held at or below 0.020 inches. Going below this demarcation does not reduce slipper forces as drastically as just attaining this level.

Verification of localized rough spots on the track has been achieved. The effect of reducing the localized high spot can now be studied to obtain the optimum level to which grinding should be performed.

One drawback to this analysis is in the definition of the forcing function. Present survey techniques introduce "spikes" into the data that in some instances adversely affect the results. These survey techniques must be improved to better future analyses. However, the

present definitions are more realistic than trying to assume a forcing function, as has been done previously.

Verification of the lateral results has not been attempted since no lateral force data exist for dual rail sleds. The lateral forces, which are purely dynamic in nature under this simulation, are averaging about 60 percent of the vertical dynamic component. This ratio is the same ratio of lateral to vertical dynamic forces noted for monorail sleds. Accelerometer measurements on dual rail sleds exhibit the same ratio but these have not been correlated to the lateral forces.

Examination of frequency content found in the simulation shows excellent correlation with the real world. Table 5-5 summarizes the modal content of the sled for various conditions. As can be seen, the math model has been verified through environmental vibration testing. The frequencies found in the actual run data match those of the math model, and these are also identified in the LASTAKK simulations.

Comparison of the rigid body simulation to the modal analysis indicates that the rigid body case should be used as a first pass at sled design to rough size the structure for dynamic loads. The modal participation will refine the design as an approximate 10 percent reduction in peak loads is possible.

TABLE 5-6 SUMMARY of RAMJET
NATURAL FREQUENCIES

Mode Number	Mode	Rigid Body Hand Calc's.	NASTRAN Model	Vibration Lab Shake Tests	Run Data	Rigid Body PASTARR	PASTARR With Modal
1	Isolator Roll-Payload	NC	5.94	NM	NM	NA	NA
2	Isolator Pitch-Payload	4.14	4.98	NM	5.50	NA	NA
3	Isolator Heave-Payload	11.60	10.37	8.5-14.0	9.5-14.0	NA	NA
4	1 st Sled Pitch-Rigid	18.86	19.94	NM	18.00	17.50	17.50
5	Apportioned Front Heave	20.00	25.11	17.05	20.00	20.00	20.00
6	Apportioned Aft Heave	21.03	25.11	17.05	21.00	21.00	21.00
7	1 st Sled Heave-Rigid	21.75	25.11	17.05	24.00	24.00	24.0-26.0*
8	1 st Sled Roll-Rigid	25.40	25.92	NM	NM	25.50	24.0-26.0*
9	Payload Heave	NC	26.50	28.0-30.0	28.0-30.0	NA	28.50*
10	Payload Pitch	28.50	26.80	28.0-30.0	27.60	NA	28.50*
11	INFNW	NC	34.00	NM	55.00	52.00	32.50
12	Sled Heave-Pitch Coupl.	40.64	NC	NM	58.00	41.00	41.50
13	INFNW	NC	47.72	NM	44.00	46.00	45.00
14	INFNW	NC	49.27	NM	NM	52.00	49.00

NA-Not Applicable
NC-Not Calculated
NM-Not Measured

* Large frequency spread at this frequency range, distinct peaks are not distinguishable

CHAPTER SIX

MONORAIL SLED SIMULATION--INSTRUMENTED MONORAIL

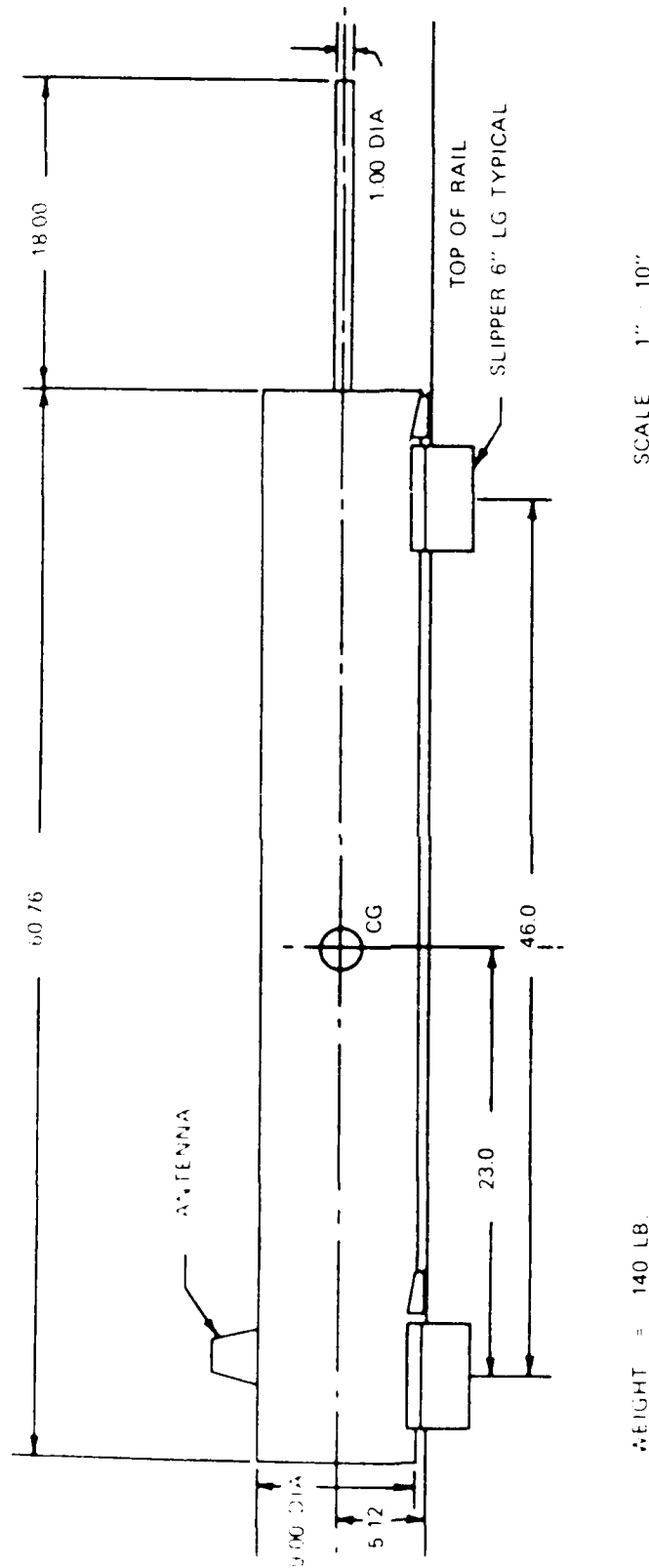
6.1 GENERAL

6.1.1 INSTRUMENTED MONORAIL SLED DESCRIPTION

The Instrumented Monorail sled was a special monorail sled developed in support of the hypersonic monorail environmental studies performed in the late 1950's. (See Figure 6.1.) This sled had special force transducers designed to interface between the slippers and the sled structure. Load force transducers are shown depicted in Figure 6.4 and described in detail by Wick. These transducers were calibrated to be accurate within $\pm 1.4\%$ and $\pm 1.5\%$, depending on direction of applied loading.

Between October of 1958 and May of 1959, a series of track runs were performed using the instrumented monorail sled. The specific objectives of this test series are summarized below.

1. Measure the vertical, oscillatory, and quasi-steady-state slipper loads on a spike monorail sled for velocities up to 4000 feet per second.
2. Determine the effect of an isolated slipper on



INSTRUMENTED MONORAIL SCHEMATIC

the vibration response of the vehicle.

- 3) Determine the effect of a cone configuration on the steady state and oscillatory slipper forces.
- 4) Determine the effect of a download configuration on the oscillatory slipper forces.
- 5) Measure the response of the aluminum shell structure to the transmitted slipper forces.
- 6) Obtain the base pressure measurements.
- 7) Test a nine-inch-diameter aerodynamic brake module at 2500 feet per second.

Results of the force measurements indicated that for speeds in excess of Mach 2.0, there was an insignificant difference in slipper loads between the spike or cone configurations. Based on this similarity of results, Nixon combined results from both configurations. These results are shown in a series of figures based on quarter Mach number increments, with no distinction made between thrusting or coasting conditions.

Nixon then generated a math model of the sled to determine model and structural parameters. Based on these parameters, he made the first attempt at predicting dynamic slipper forces. The results of this effort were discussed in Chapter One.

6.1.2 SLED FORCES

Based on figures presented by Nixon, enough information was available to duplicate his efforts and see if better correlation would be available by using DASTARR. The critical factor at this stage is, as mentioned earlier, to accurately define the lift force and the location of its center of pressure.

The first step taken to calculate the quasi-steady-state lift force is to duplicate the trajectory of the mission. From this, it will be possible to determine the thrust, drag, and inertial loadings acting on the sled as quasi-steady-state. Using these values, along with Nixon's given quasi-steady slipper reactions, the lift force can be found.

Shown in Figure 6.2a is the actual run trajectory used by Nixon. Figure 6.2b shows the generated profile that attempts to mirror the profile of Nixon. The shape and velocity maximum between the two are consistent; however, the time of peak velocity occurred is different. This is due to a faster burning propellant now used in that rocket motor. The motor impulse is still the same so the net velocity effect is the same; the time of peak velocity just occurs sooner in the run.

Shown in Figure 6.3 are the slipper quasi-steady-state forces used by Nixon in his simulation attempt.

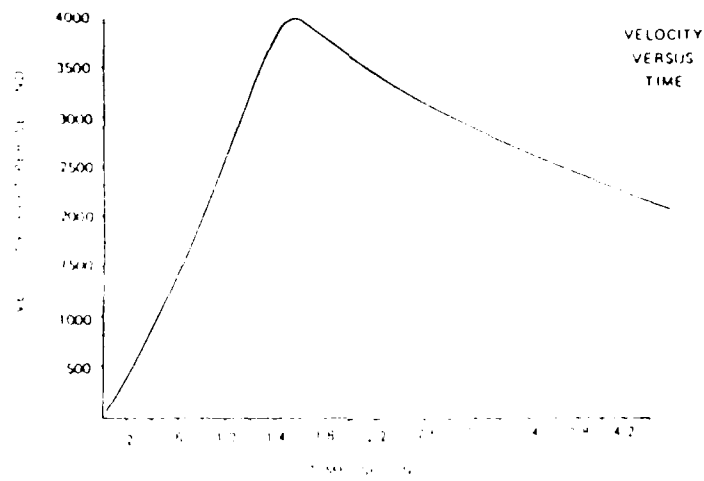
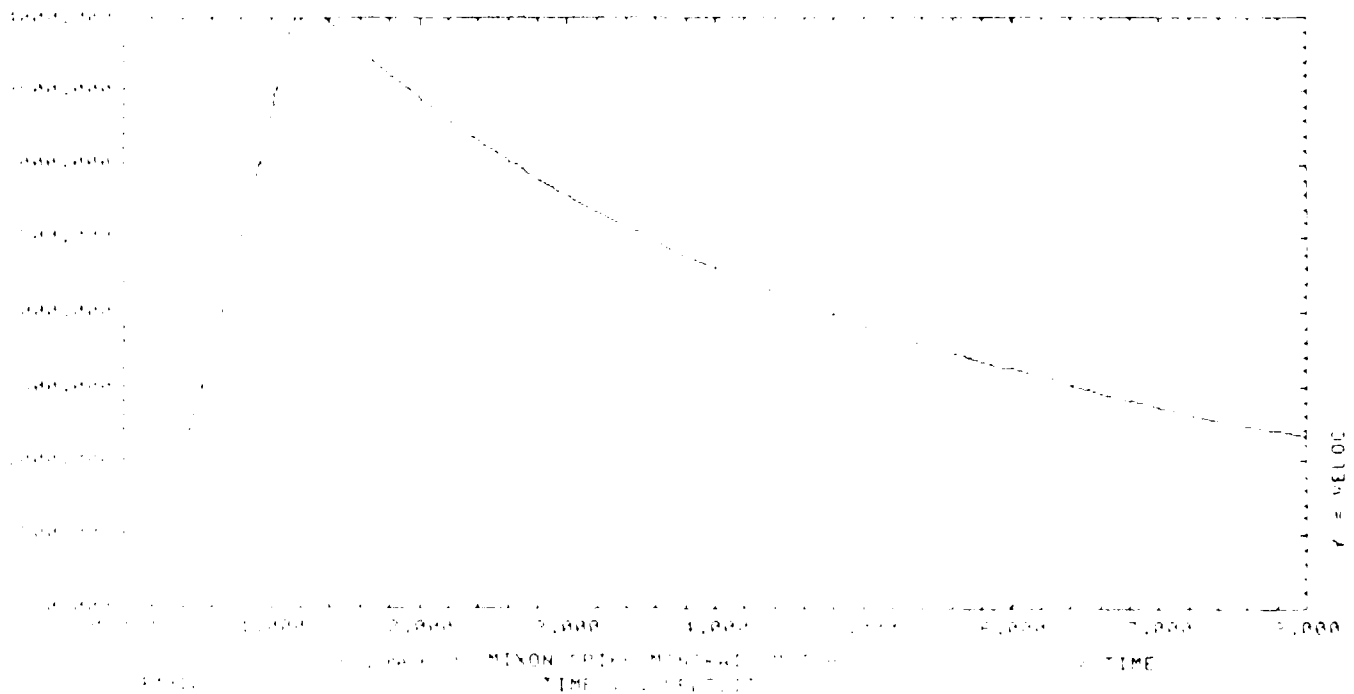


Figure 10-4 Drag Velocity Time Curve



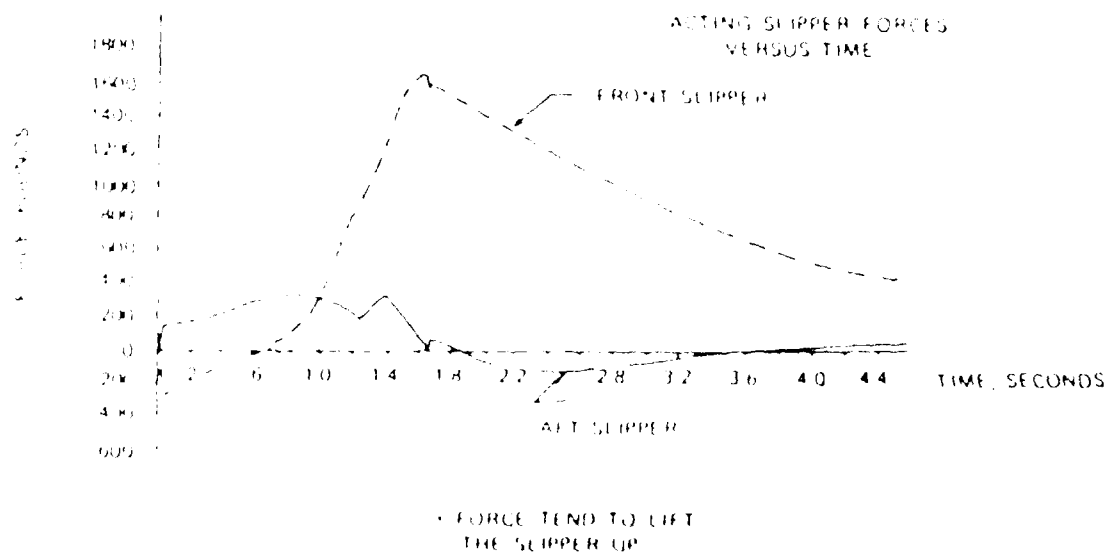


Figure 6.3a Mixon QSS Slipper Forces

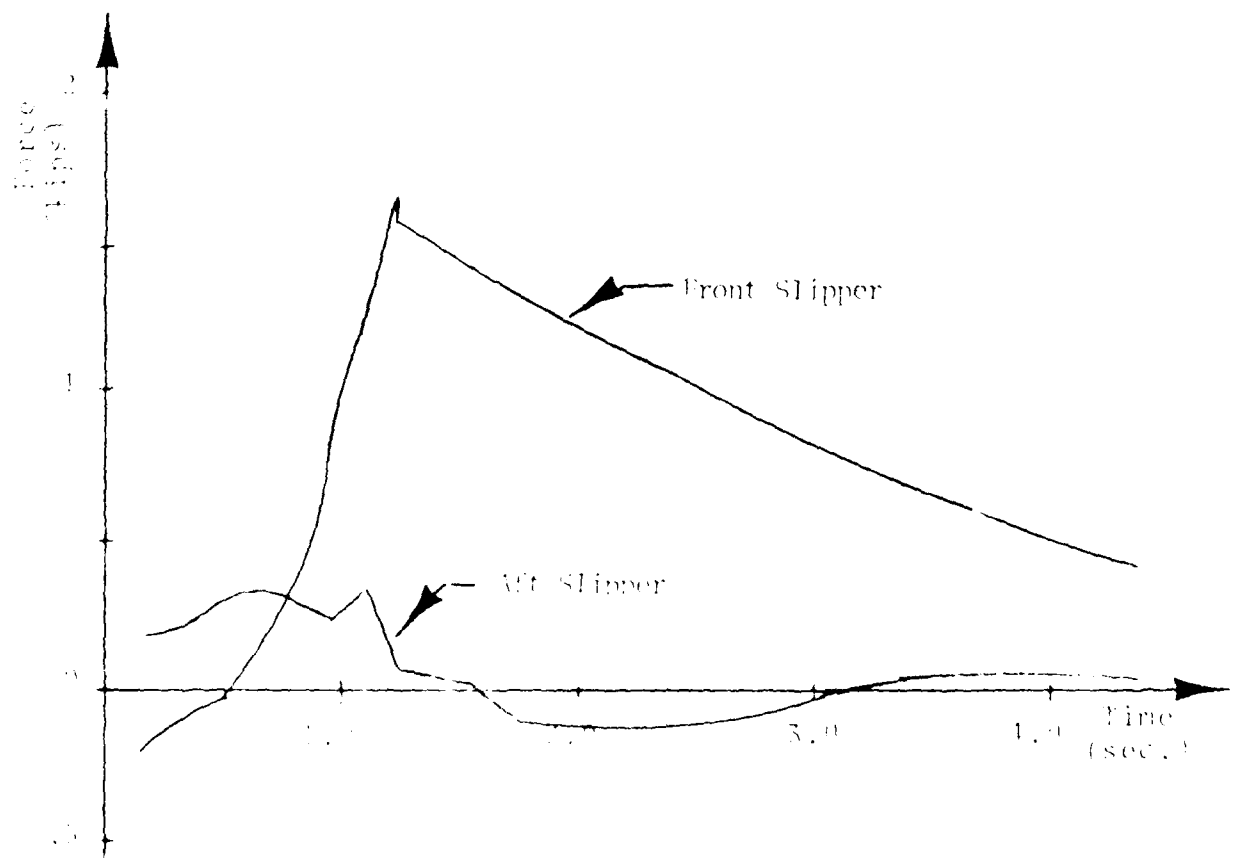


Figure 6.3b QSS Slipper Force Calculated

Figure 6.3 QSS Slipper Force Match

Solving the static freebody equations of motion about the sled, the lift and its center can be calculated using the scaled quasi-steady-state values of Figure 6.3a. Figure 6.4 shows the resultant lift force that was computed by following the above procedures at each quarter Mach number between 1.0 and the maximum velocity. Superimposed in circles on this figure are the estimated lift forces derived from wind tunnel testing on a 40% scale model.²¹ As a check the quasi-steady slipper loads were recomputed using the calculated lift force and these are shown in Figure 6.5b. The shape and magnitudes of the forces match those of Mixon's. Table 6-1 contains the instantaneous quasi-steady-state values used in these calculations for the lift forces.

6.2 RIGID BODY SIMULATION

The simulation consisted of running each instantaneous condition shown in Table 6-1, or twelve thrusting conditions from Mach 1.0 to Mach 3.62, the maximum velocity. There were also seven conditions under coast from maximum velocity back to Mach 2.0. It should be noted that the lift forces between Mach 1.0 and 2.0, under thrust, are suspect since they were found by extrapolation from the wind tunnel results.

The simulation amounted to running all 19 conditions

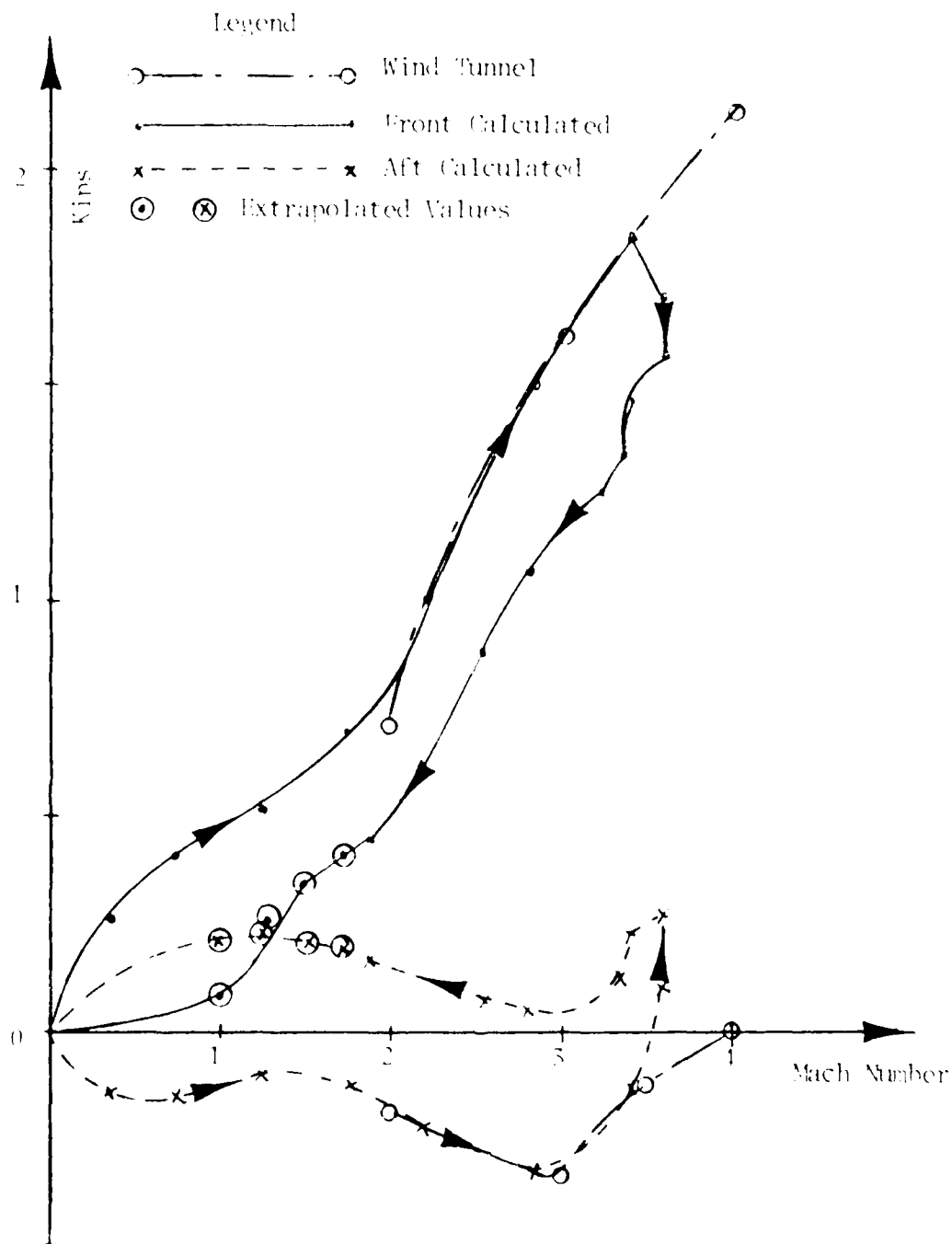


Figure 6.1 OSS Lift Vs. Mach Number

TABLE 6-1 DASTARR Parameters-

Instrumented Monorail QSS Loads

Comments	Velocity (ft/sec)	Time ⁽¹⁾ (sec.)	Accel. (\ddot{x} -g's)	Drag (lb _f)	Thrust (lb _f)	Lift (lb _f)	\bar{L} ⁽²⁾ (in.)
M=1.00 Thrusting+	1132.5	3.62	98.99	610.6	14175.3	333.22	5.490
M=1.26 Thrusting+	1426.6	2.88	104.74	1040.4	15383.8	406.80	10.506
M=1.51 Thrusting+	1703.5	2.41	110.85	1284.9	16462.2	498.47	11.754
M=1.74 Thrusting+	1959.0	2.10	116.40	1588.0	17526.5	584.15	12.281
M=2.01 Thrusting	2266.6	1.81	123.09	2021.4	18875.2	695.33	10.939
M=2.26 Thrusting	2550.4	1.61	128.99	2457.9	20118.7	807.93	10.202
M=2.50 Thrusting	2823.4	1.46	132.56	2847.2	20996.9	964.70	10.409
M=2.75 Thrusting	3104.0	1.32	136.22	3438.2	22088.1	1128.01	10.564
M=2.99 Thrusting	3369.9	1.22	139.65	3972.5	23091.6	1326.46	13.736
M=3.25 Thrusting	3663.9	1.12	137.43	4596.4	23411.8	1549.91	17.566
M=3.50 Thrusting	3949.5	1.04	89.64	5252.2	17530.0	1760.92	22.278
M=3.62 Burnout	4089.1	1.01	-3.43	5568.6	5114.0	1816.80	25.958
M=3.51 Coasting	3956.7	1.04	-29.88	4072.0	0.0	1790.00	29.811
M=3.25 Coasting	3663.0	1.12	-26.49	3607.5	0.0	1350.00	26.180
M=3.00 Coasting	3382.9	1.22	-23.42	3188.5	0.0	1200.00	25.025
M=2.76 Coasting	3117.9	1.32	-20.63	2808.0	0.0	1070.00	25.259
M=2.49 Coasting	2809.2	1.46	-17.95	2440.0	0.0	950.00	27.477
M=2.25 Coasting	2543.0	1.62	-15.29	2076.0	0.0	805.00	30.561
M=2.00 Coasting	2251.0	1.82	-12.83	1740.0	0.0	670.00	34.133

Notes:

- ① Time is simulation time to travel approximately 4000 feet of track
 ② \bar{L} is the distance from center of lift to downtrack CG, + is to front beam
 + Lift values extrapolated from M=0. to M=2. from curves

for each rail function at a track length of 4000 feet for a given constant velocity, or a total of 171 iterations for the rigid body case. The subsequent analysis compared the predicted slipper peak values to those scaled from the figures generated by Mixon. Table 6-2 contains the scaled average force values as well as the extremes encountered for that Mach number. Notice that no sign is given so only the absolute values may be compared. Also, since no distinction between thrusting or coasting conditions have been defined, it is assumed that the value given applies to either condition at that Mach number.

Comparison of the lateral to vertical slipper peak forces from Table 6-2 indicate that lateral forces range between 40 and 60 percent of the peak vertical force. If the quasi-steady portion of the peak vertical force is removed from the peak, the lateral force ranges between 50 and 70 percent of the dynamic vertical force. Present track design guidelines call for the lateral dynamic forces to be 60 percent of the vertical dynamic force and are a direct result of this comparison.

As was done for dual rail sleds, the analysis will statistically average all conditions for a given rail function for each slipper. The results of this sampling are to be presented as a percentage deviation between actual and predicted forces and the standard deviation

TABLE 6-2 SCALED PEAK OSCILLOGRAPH
FORCES FROM INSTRUMENTED MONORAIL
TEST RUNS, OPLAN 44X

Mach No.	Vertical-Front			Vertical-Aft		
	Ave.	Max.	Min.	Ave.	Max.	Min.
1.00	6.00	6.50	5.50	7.40	8.00	6.80
1.25	9.15	10.50	7.80	10.00	11.60	8.40
1.50	9.25	9.50	9.00	10.40	11.60	9.20
1.75	9.50	9.50	9.50	12.40	12.40	12.40
2.00	9.38	10.00	8.75	12.60	13.60	11.60
2.25	10.00	10.75	9.25	11.60	11.60	11.60
2.50	12.25	14.00	10.50	11.60	12.20	11.00
2.75	11.75	12.00	11.50	10.60	12.80	8.40
3.00	13.50	14.50	12.50	12.00	14.00	10.00
3.25	14.25	15.50	13.00	15.20	17.60	12.80
3.50	16.00	16.25	15.75	19.20	19.40	19.00

Mach No.	Lateral-Front			Lateral-Aft		
	Ave.	Max.	Min.	Ave.	Max.	Min.
1.00	3.25	----	----	3.45	4.30	2.60
1.25	2.83	6.88	1.75	4.50	4.80	4.20
1.50	4.08	6.13	2.00	6.40	6.40	6.40
1.75	4.02	5.50	2.00	5.10	6.00	4.20
2.00	4.55	7.00	2.88	3.55	3.80	3.30
2.25	5.14	8.13	3.38	6.45	6.60	6.30
2.50	5.19	7.38	3.75	4.50	4.80	4.20
2.75	6.14	8.75	4.25	3.35	3.70	3.00
3.00	5.60	9.00	3.63	4.90	6.00	3.80
3.25	6.38	7.38	5.38	3.50	3.50	3.50
3.50	6.41	7.25	5.38	4.75	4.90	4.60

Notes:

Forces are in units of kips

about this mean.

6.2.1 DATA ANALYSIS--AMPLITUDE DOMAIN

6.2.1.1 PEAK FORCES

The simulation consisted of 171 computer runs of the 19 conditions for each of the nine rail profiles. Results of the peak force simulations are shown plotted in Figures 6.5 through 6.8 for the four slipper conditions. The front vertical and lateral slipper forces are shown in Figure 6.5 and 6.6. Figures 6.7 and 6.8 represent the aft slipper vertical and lateral forces. The solid line is the average force shown in Table 6-2, and the dotted lines correspond to the extremal values for that given Mach number. It is interesting to note that the lateral force predictions are equal to or exceed the measured forces, whereas the best Mixon could do was to predict approximately 40 percent of the value. It appears that for monorail sleds, track roughnesses in excess of 0.014 inches tend to grossly overpredict values; and roughnesses less than or equal to this value tend to estimate very closely the results of Mixon.

The statistical deviation analysis is represented in Figure 6.9 and summarized in Table 6-4 for all slipper

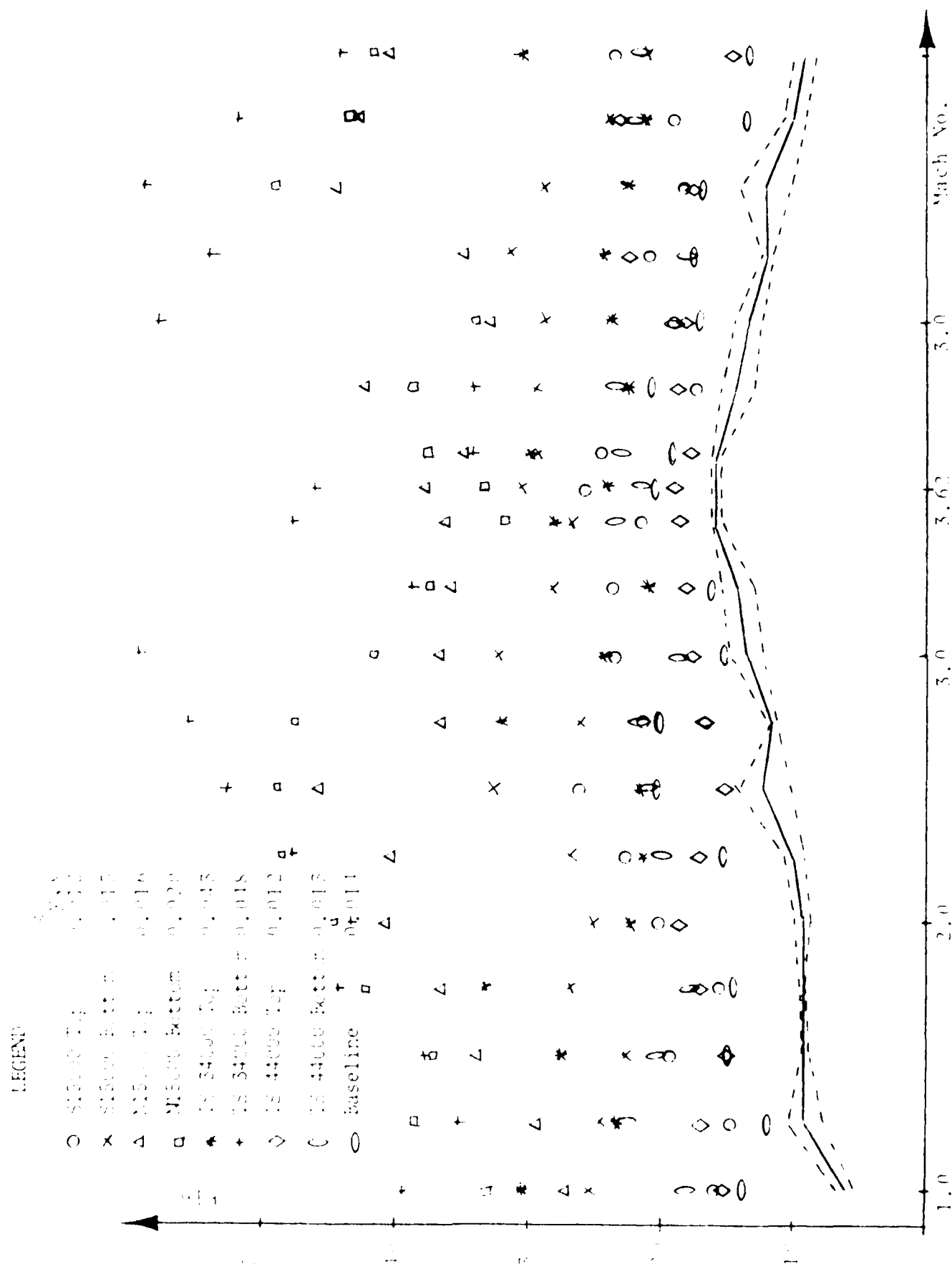
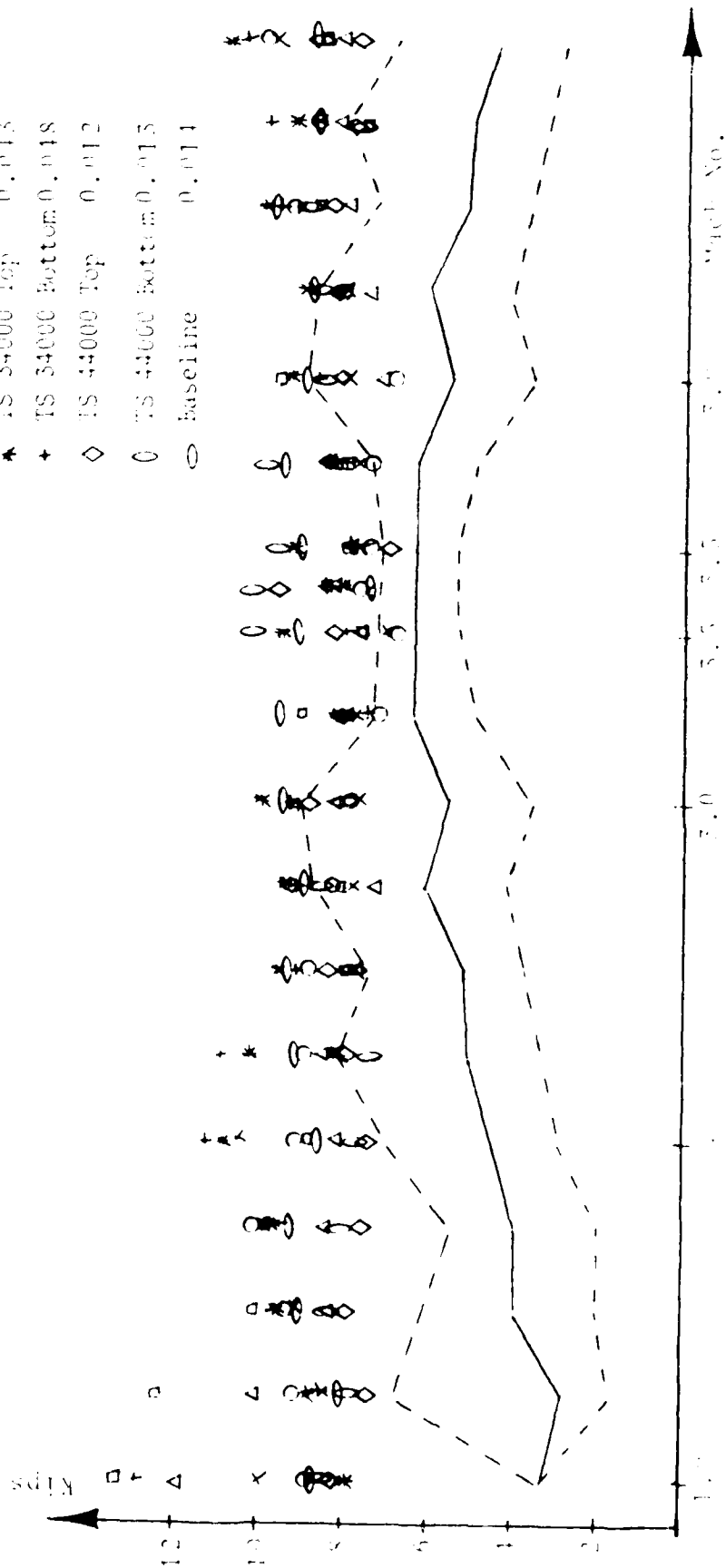


Figure 6.5 Front Vertical Peak Force Vs. Predicted

LEGEND

	$S_{y,x}$
○ S15000 Top	0.012
× S15000 Bottom	0.015
△ N15000 Top	0.016
□ N15000 Bottom	0.020
★ TS 34000 Top	0.013
+ TS 34000 Bottom	0.018
◇ TS 44000 Top	0.012
○ TS 44000 Bottom	0.015
○ Baseline	0.011



Legend

- 11-11
- × 11-12
- △ 11-13
- 11-14
- ★ 11-15
- + 11-16
- 11-17
- 11-18
- 11-19
- 11-20
- 11-21
- 11-22
- 11-23
- 11-24
- 11-25
- 11-26
- 11-27
- 11-28
- 11-29
- 11-30
- 11-31
- 11-32
- 11-33
- 11-34
- 11-35
- 11-36
- 11-37
- 11-38
- 11-39
- 11-40
- 11-41
- 11-42
- 11-43
- 11-44
- 11-45
- 11-46
- 11-47
- 11-48
- 11-49
- 11-50
- 11-51
- 11-52
- 11-53
- 11-54
- 11-55
- 11-56
- 11-57
- 11-58
- 11-59
- 11-60
- 11-61
- 11-62
- 11-63
- 11-64
- 11-65
- 11-66
- 11-67
- 11-68
- 11-69
- 11-70
- 11-71
- 11-72
- 11-73
- 11-74
- 11-75
- 11-76
- 11-77
- 11-78
- 11-79
- 11-80
- 11-81
- 11-82
- 11-83
- 11-84
- 11-85
- 11-86
- 11-87
- 11-88
- 11-89
- 11-90
- 11-91
- 11-92
- 11-93
- 11-94
- 11-95
- 11-96
- 11-97
- 11-98
- 11-99
- 11-100

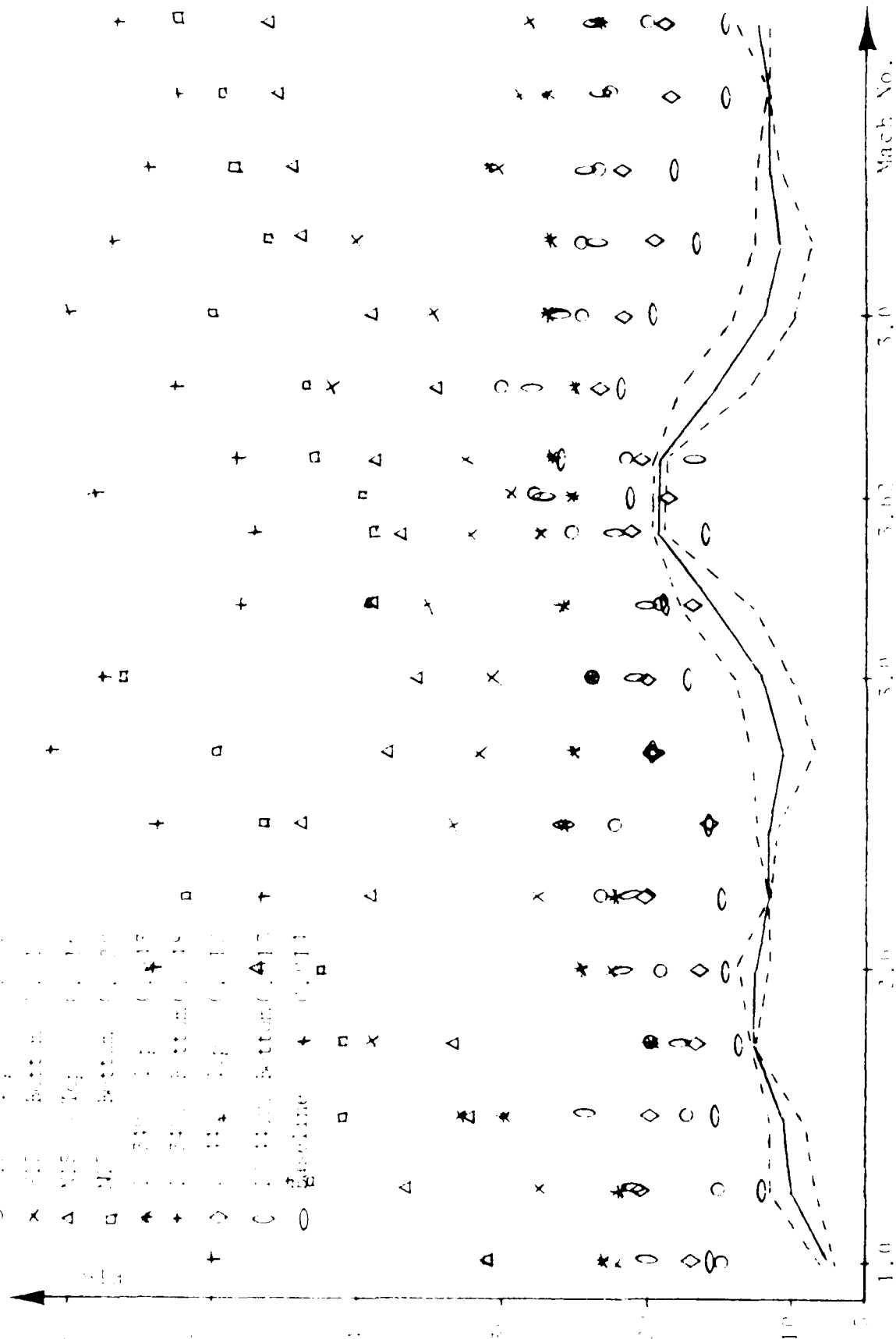


Figure 6.7 Aft Vertical Peak Force Vs. Predicted

116-ENT

\circ 0.015 γ 0.012
 \times 0.015 Bottom 0.015
 Δ 0.015 γ 0.016
 \square 0.015 Bottom 0.020
 $+$ 0.015 γ 0.017
 $+$ 0.015 Bottom 0.018
 \diamond 0.015 γ 0.012
 \circ 0.015 Bottom 0.013
 \circ Baseline 0.011

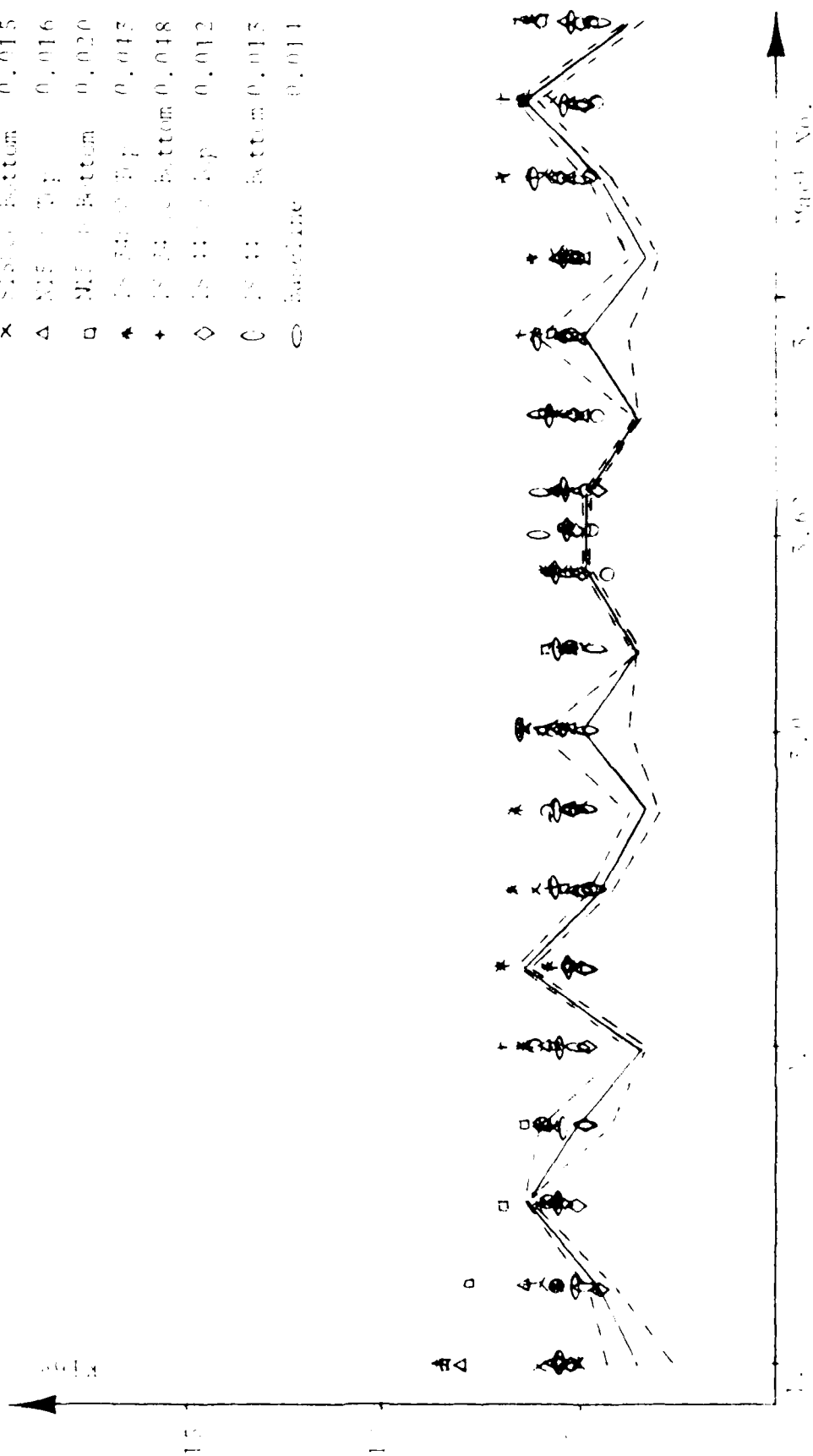


Figure 6.5 Art Lateral Peak Curve No. Predicted

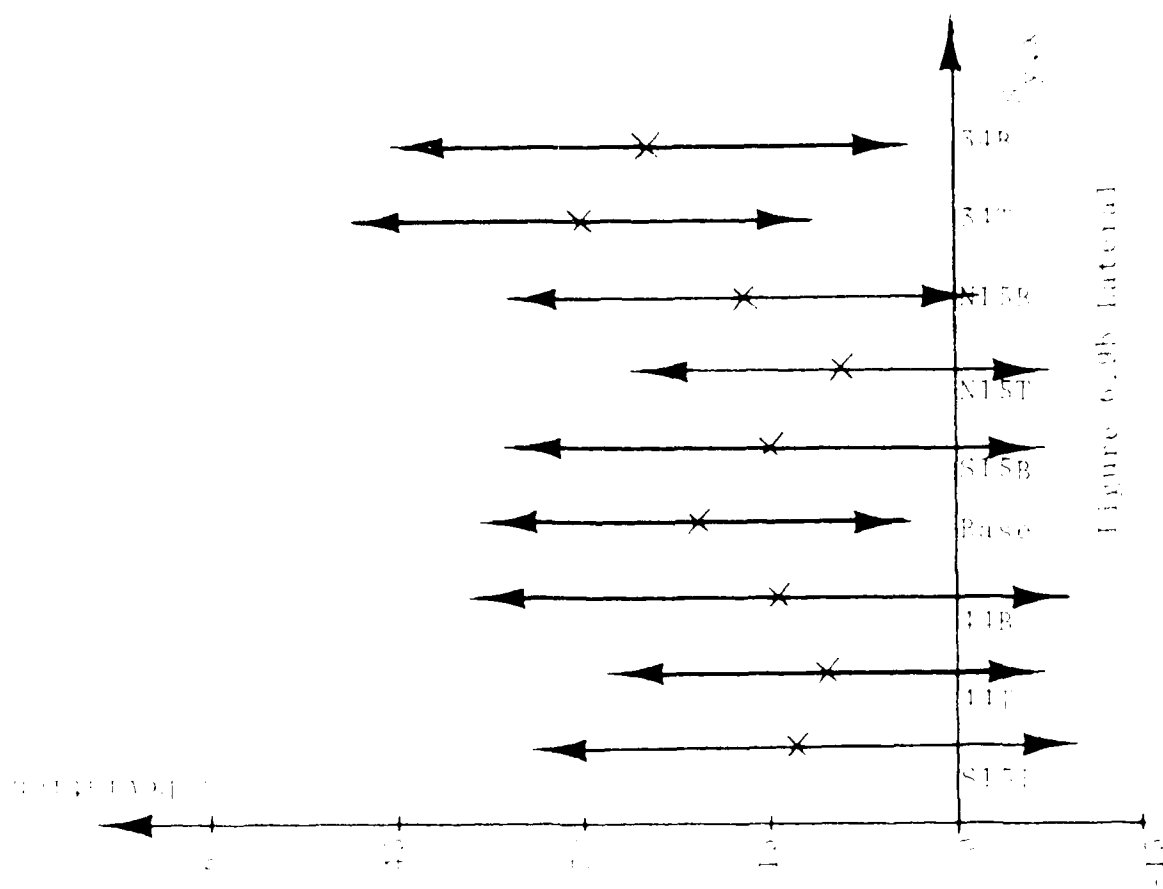


Figure 6.9b Lateral

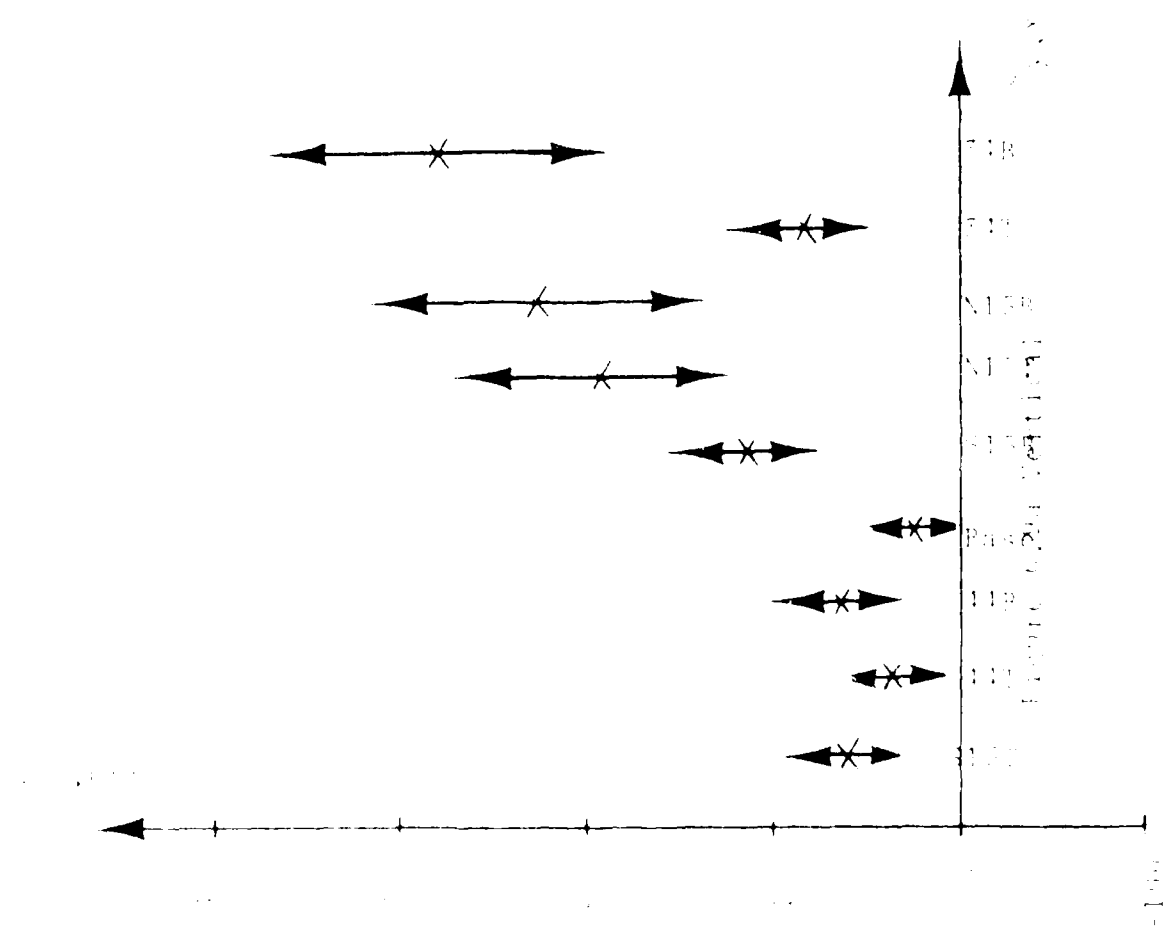


Figure 6.9a Front

Figure 6.9 Front Slipper Statistical Representation

TABLE 6-3 STATISTICAL SUMMARY
of MONORAIL RIGID BODY PREDICTIONS
VERSUS RANK ROUGHNESS
FROM MACH 2 THRUSTING TO MACH 2 COASTING

Rail	S _{y,x} (in.)	Vertical+++		Lateral+++	
		Average	1 Sigma	Average	1 Sigma
34,000 Bottom++	0.048	+279.11	82.3	+24.71	20.0
34,000 Top++	0.043	+85.11	32.7	+29.81	18.7
N15,000 Bottom	0.020	+225.61	83.2	+16.71	18.7
N15,000 Top	0.016	+193.41	68.5	+9.31	16.5
S15,000 Bottom	0.015	+117.71	33.1	+15.11	20.7
Baseline	0.014	+25.71	16.4	+20.81	16.6
44,000 Bottom++	0.013	+63.61	26.6	+14.41	23.6
44,000 Top++	0.012	+37.41	22.8	+10.51	16.7
S15,000 Top	0.012	+62.31	22.2	+12.91	21.5

Notes:

++ Denotes periodic rail content

+++ Resultant sum of both slippers acting in that direction

1. All values listed are percentages

2. Positive sign denotes overprediction

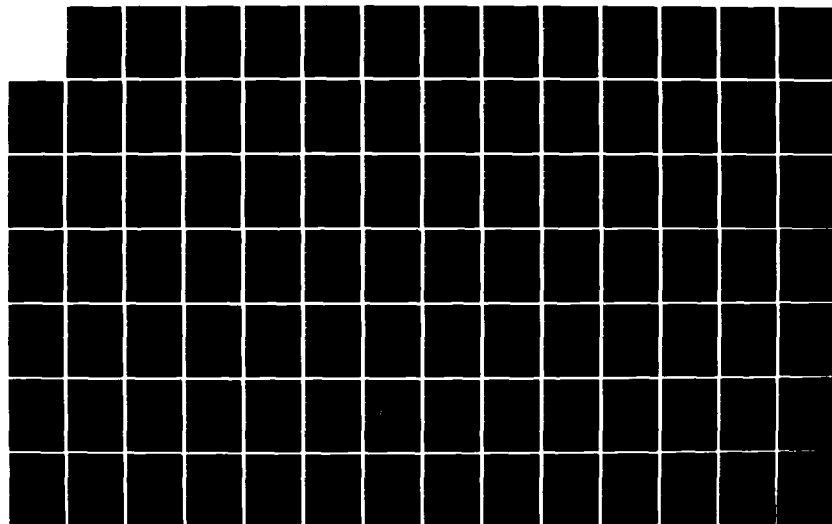
3. Negative sign denotes underprediction

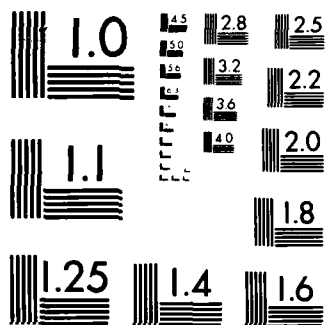
AD-A156 589 DYNAMIC ANALYSIS OF A SLED TRAVELING ALONG A ROUGH RAIL 374
(U) ARMAMENT DIV (AFSC) EGLIN AFB FL G L FERGUSON
15 MAY 85 AD-TR-85-39

UNCLASSIFIED

F/G 12/1

NL





MICROCOPY RESOLUTION TEST CHART
NATIONAL BUREAU OF STANDARDS-1963-A

conditions. The "x" denotes where the average deviation for the 19 simulations occurs. The heavy-arrowed vertical line indicates the ± 1 sigma value about the mean.

6.2.1.2 PEAK FORCES VERSUS TIME

The only plot of force versus time presented by Mixon was a short data clip on the front slipper at an average velocity of approximately 3400 feet per second. This corresponds to a Mach number of 3.00. The plotted forces are the total vertical and lateral forces acting on the front slipper for a 0.095 second time period. This condition coincides with a data case being simulated so a direct comparison is available. Figures 6.10a and 6.11a are reproduced copies of Mixon's data clips for the front vertical and lateral slipper forces, respectively (page 68 of reference 6). Shown in Figures 6.10b and 6.11b are the simulated force-time plots for the baseline rail function of these slipper forces. The remaining eight function plots are shown in Appendix C, Figures C.33 through C.48. The sign convention for the simulated output of DASTARR is opposite that for the actual data.

Examination of the actual run data for the front slipper vertical indicates the forces stayed in an envelope between +8 kips to a -12 kips, and centered

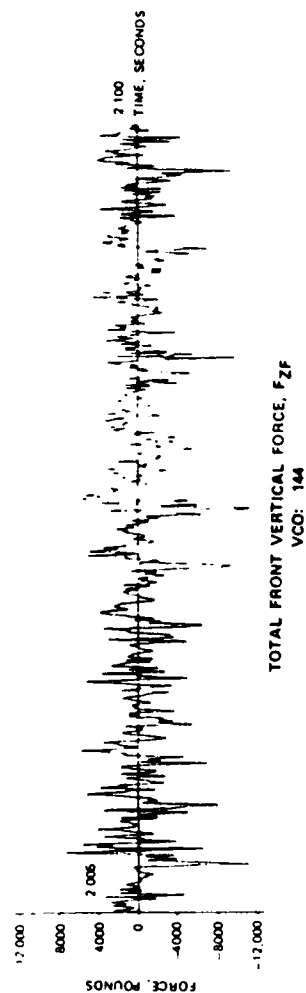
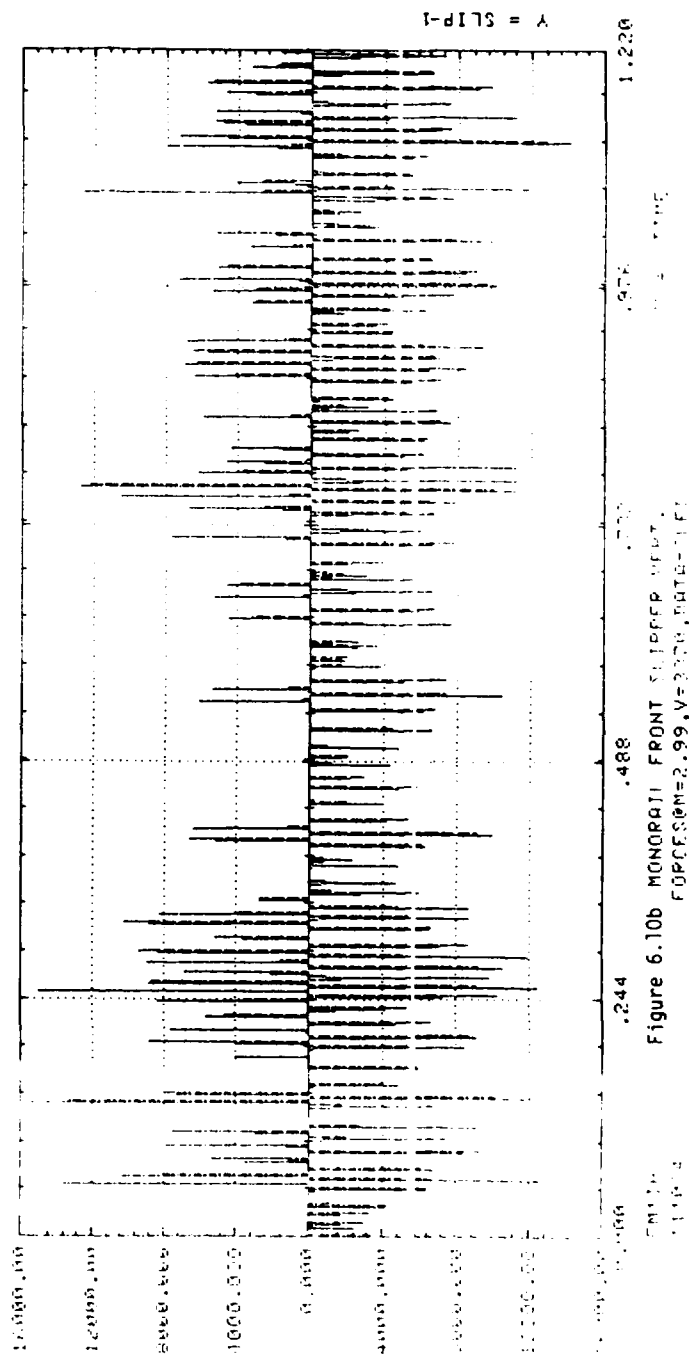


Figure 6.10a Front Vertical Peak Forces Vs. Time



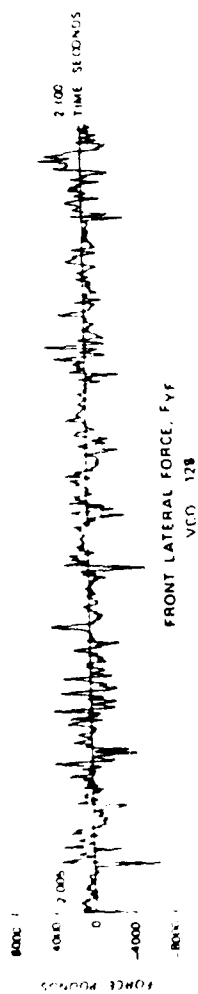


Figure 6.11a Front Lateral Peak Forces Vs. Time

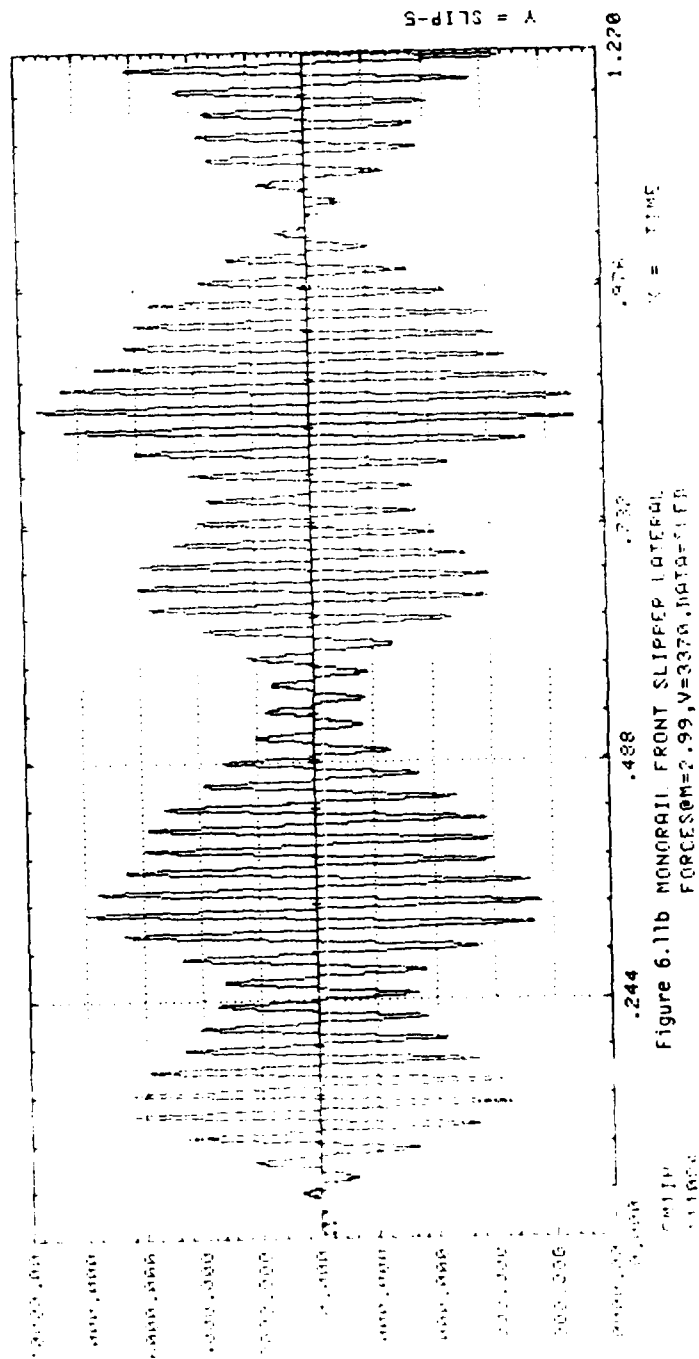


Figure 6.11b MONORAIL FRONT SLIPPER LATERAL
FORCES=2.99,V=3370,DATA=11P

about a negative one or two kips. This centering is to be expected as the quasi-steady forces on this slipper are approximately one kip negative. Looking at the plots for the various rail surfaces for this slipper indicates the same phenomenon, a centering about a negative one or two kips and envelopes of varying size. The envelope sizes were all larger than the measured forces and appear to be a function of rail roughness. Of interest on monorail sleds is the amount of flight time. The amount of flight time appears to be related to rail roughness. The smoother the rail the more flight time involved.

The front slipper lateral forces for the actual run data centered about zero kips and ranged predominantly between plus or minus four (4) kips. This centering is expected since there is no lateral quasi-steady forcing function involved. These results should be strictly dynamic forces induced by rail roughness. Examination of all simulations for the lateral forces indicated the same thing, centering about zero kips and modulating an equal magnitude on either side of it. The interesting thing about the lateral simulation is the ringing seen in the output. The forces increase, peak, and decrease just as mechanical systems do when approaching and passing through a natural frequency; however, this ringing is not seen in the actual rail data.

6.2.1.3 FORCE HISTOGRAM

Discussed in Chapter Five is the histogram feature of DASTARR as it applied to dual rail sleds. It was concluded that Mixon's hypothesis for dual rail sled peak forces is true; peak forces do follow a Rayleigh distribution. It was noted in the discussion for dual rail sleds that the magnitude of the quasi-steady-state forces strongly influences the distribution. The larger this value, the more biased toward a Rayleigh distribution is the data sample. In contrast, the smaller the quasi-steady component the more closely the distribution approximates a normal or Gaussian function. For the case of this monorail, the data indicates a small quasi-steady value and plots like a slightly skewed normal distribution as shown in Figure 6.12. The distribution in reality appears to be a cross between a normal and Rayleigh distribution. Mixon in his monorail work did an extensive amount of research in determining how much of a distribution is Rayleigh content and how much is due to a normal distribution. He did this through an error function analysis approach. He noted in his work that the Rayleigh component was dependent on the bias introduced by the quasi-steady loading. These results indicate the same thing.

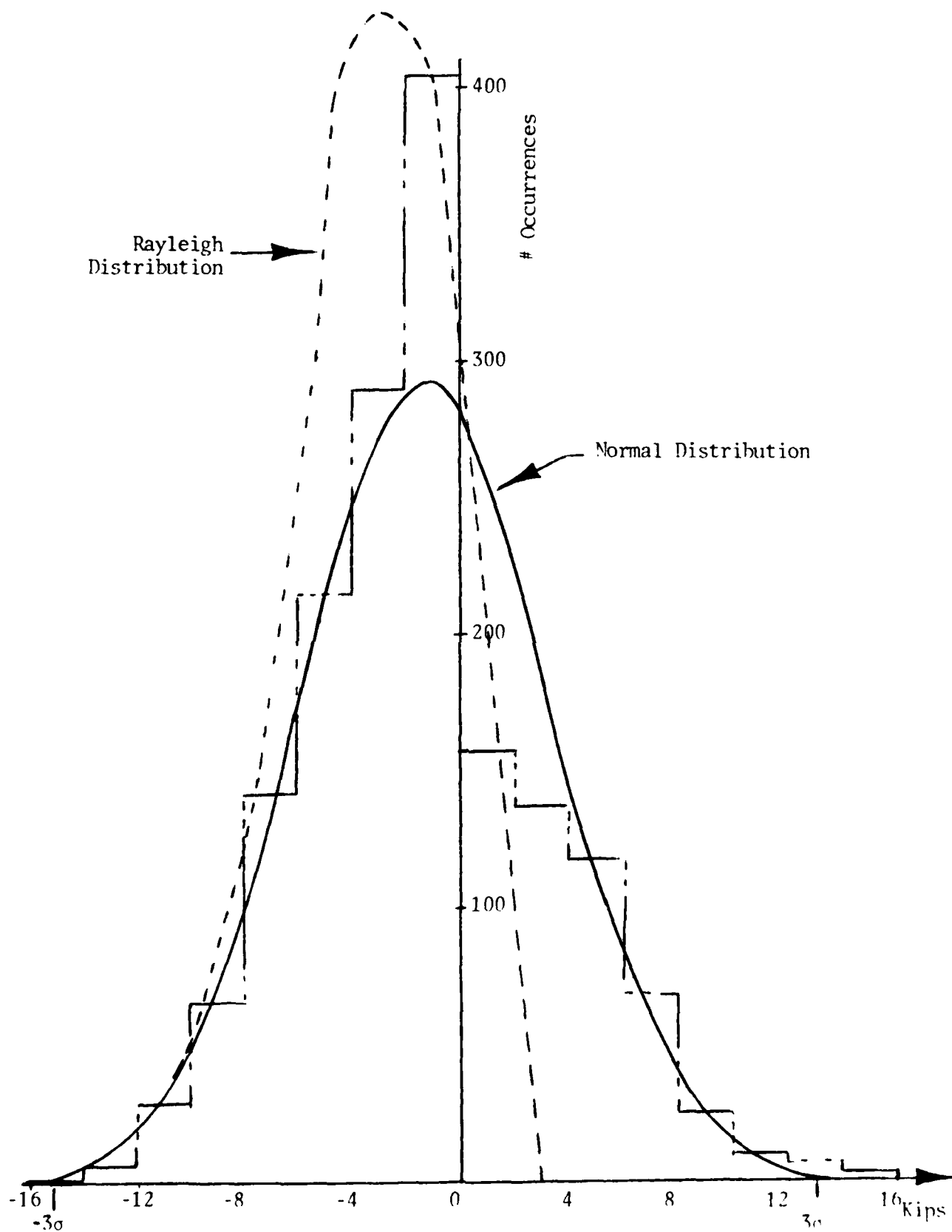


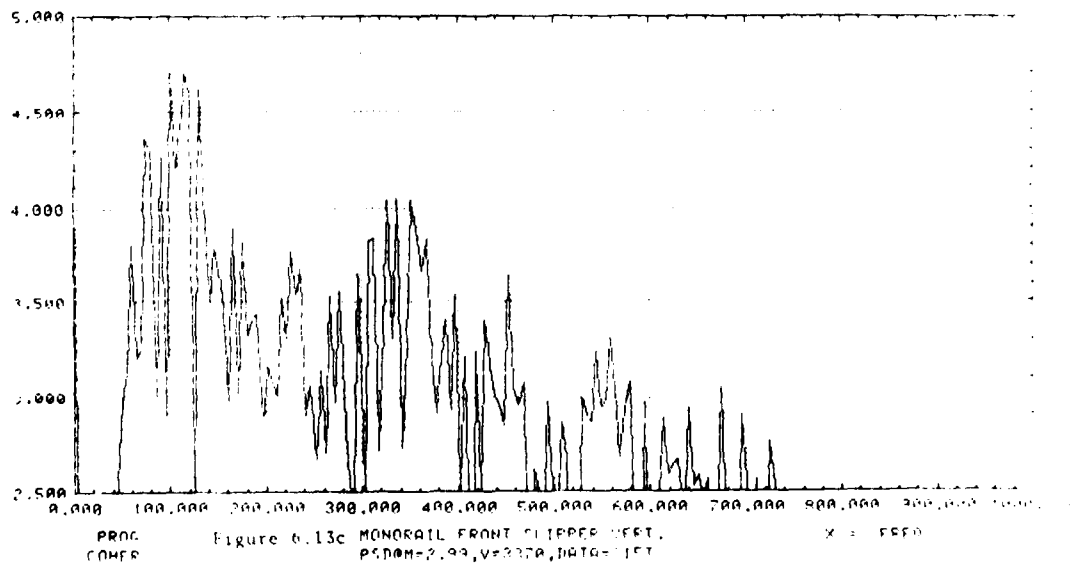
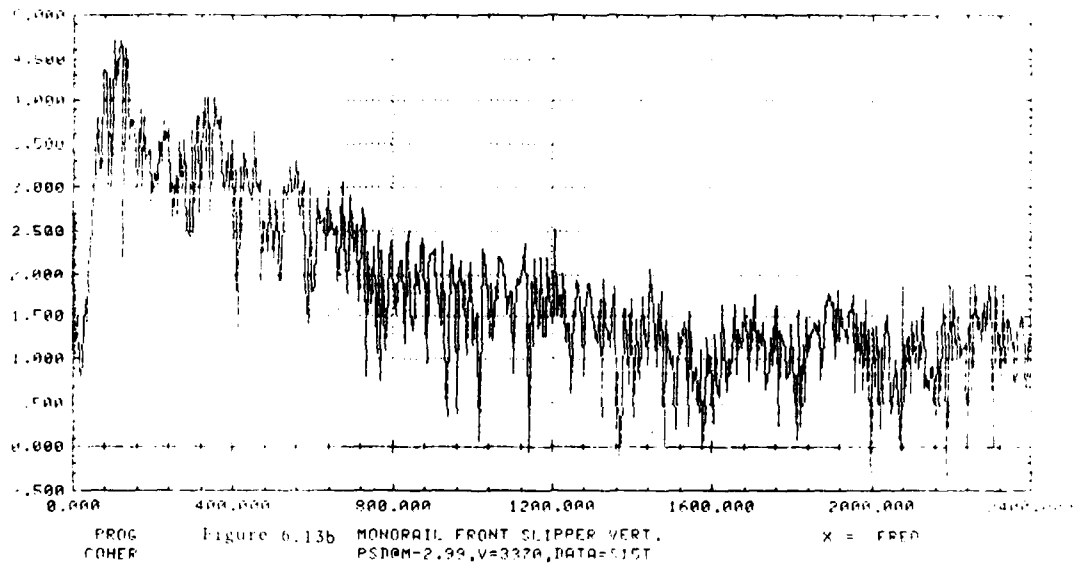
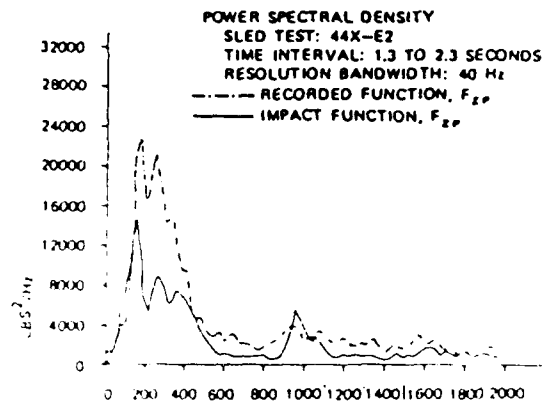
Figure 6.12 Histogram Distribution

6.2.2 DATA ANALYSIS--FREQUENCY DOMAIN

Due to the nature of monorail sleds, fundamental natural frequencies generally occur in excess of 100 hertz in the vertical direction. It is not uncommon for frequencies up to 500 hertz to cause structural excitement and possible damage to the sled. There are a sufficient number of occurrences for the monorail simulation that it is possible to analyze the system response spectrum through 2500 hertz.

An examination of PSD plots for the given data of Mixon, shown in Figures 6.13a and 6.14a for the vertical and lateral directions of the front slipper, shows maximum energy content in a frequency range of 100 to 150 hertz. Sharp rolloff occurs above this value, and noise appears above 600 hertz. As explained above, this is a typical response spectrum for monorail sleds.

Figures 6.13b and 6.14b show typical wide spectrum response for the rigid body monorail sled simulation sequence for the same given velocity condition discussed in Figures 6.13a and 6.14a. Again, sharp rolloff is noticeable above 120 hertz, and noise is encountered above 800 hertz. Figure 6.13c and 6.14c are blowups of Figures 6.13b and 6.14b, respectively, in the 0 to 1000 hertz region, only clipping the power axis at $10^{2.5}$ and $10^{5.0}$. With these figures, it is possible to isolate



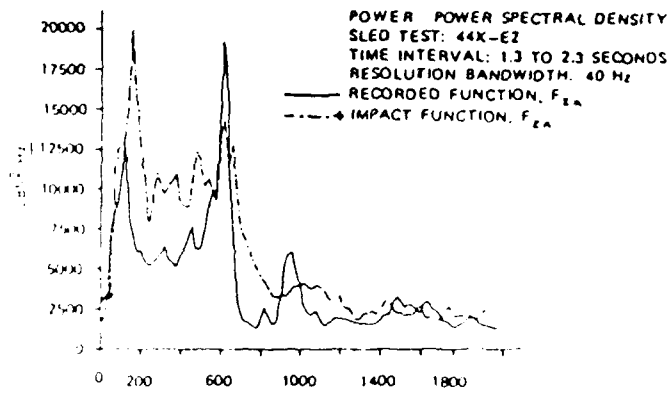
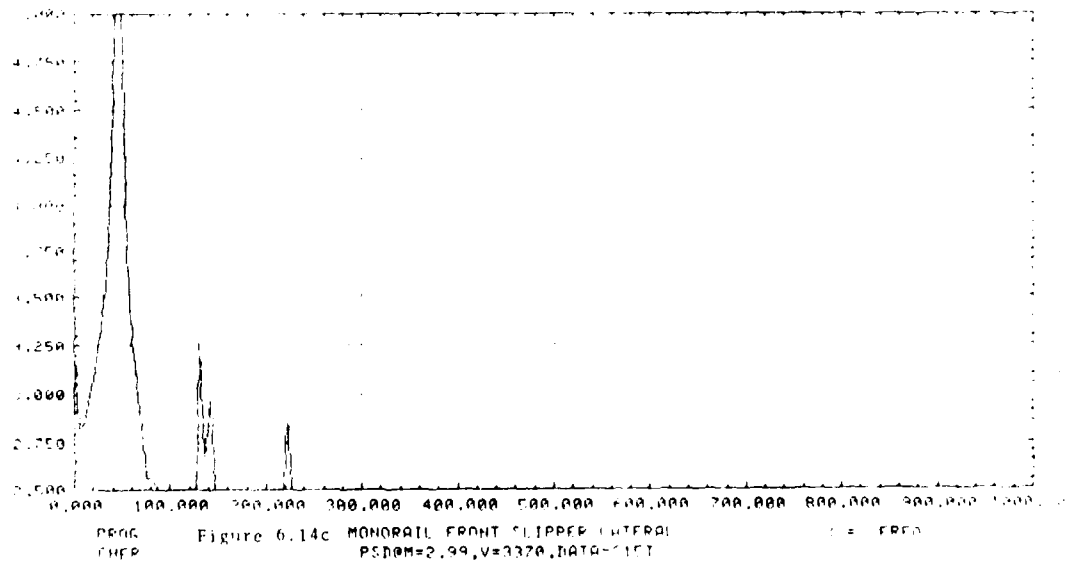
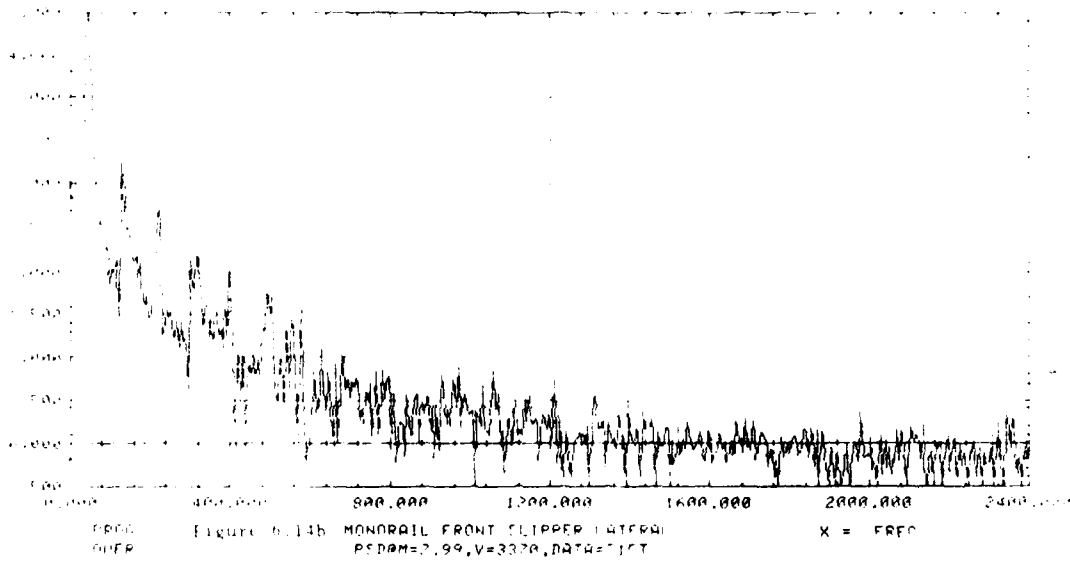


Figure 6.14a FREQUENCY, Hz



individual frequencies that were excited, and look at the level of energy contained in that frequency band.

Close examination of the plots for the actual versus predicted PSDs indicates frequency contents that are almost identical, considering that the actual data have been smoothed by a 40-hertz filter. Due to this filtering, only predominate power levels will show and will peak within 40 hertz of the true frequency. Because of this, many modes and rigid body frequencies may be impossible to isolate. The measureable frequency content is summarized in Table 6-6, in the concluding section for monorail sleds.

Power levels for the frequencies are all in excess of that from the actual run data; however, they are well within an order of magnitude difference. Examination of the PSD's again show that rail roughnesses in excess of 0.014 inches have power levels that greatly exceed those from the run, while roughness levels less than this value have energy content that is relatively close to the actual content.

Reviewing the PSD's indicated the following phenomena associated with the frequency content. The frequency occurring at 86 hertz is the physical rail length of 39 feet. The tie down spacing of 52 inches occurs at a frequency of 780 hertz but this spike is hard to observe since so little energy resides at this

frequency. The ringing phenomenon seen in the lateral direction occurs at about 55 hertz, which is the fundamental lateral frequency. The frequency due to the 50-foot data survey iteration at this velocity is 65 hertz. It appears that the ringing is being caused by the fundamental lateral frequency being excited by the forcing function frequency. Each ringing envelope repeats at a frequency of about 7 hertz, which is the track data set looping end to end.

6.2.3 RIGID BODY CONCLUSIONS AND SUMMARY

This section concludes the rigid body simulation and analysis phase of the monorail sled verification study. It will address all areas posed in the rail roughness study directive as it pertains to monorail sleds in a rigid body mode of operation.

6.2.3.1 PERIODICITY VERSUS NONPERIODICITY

As with dual rail sleds, the effect of periodicity may be examined by looking at the statistical results of TS44000 top and the south 15000 bottom. The rails generate the same standard deviation for both the vertical and lateral responses. The periodic rail, TS44000 top, underpredicts the mean by 60 percent of the

nonperiodic rail in the vertical direction and by 19 percent in the lateral.

Comparing the roughness contribution of periodic rails can be done by looking at TS 34000 versus TS 44000, both top and bottom. Here it is evident that rough periodicity affects both the mean, by as much as 200 percent overprediction compared to the smooth rail, and the standard deviation, by as much as a 25 percent larger prediction.

The extent of the effect of periodicity is unknown since a proper combination of rail period and sled velocity is not available that will generate the 250 hertz heave frequency of the sled. Excitation of the 250 hertz frequency, based on the 208-foot rail period, would require a sled to travel at an unreasonable velocity of 50000 feet per second. On the other hand, if a periodic rail length of 39 feet existed, the sled could be excited at its fundamental frequency by a velocity of 10000 feet per second. This velocity is not entirely unreasonable since the Track has successfully tested sleds at velocities to 9000 feet per second.

6.2.3.2 RAIL GRINDING

Comparison of means and standard deviations for the north and south 15000 feet of track can be done to

determine rail grinding effectiveness for monorails. Looking at the rail roughness functions, it is readily seen that the rougher the rail the larger the overprediction and the larger the standard deviation spread in the vertical direction.

It was hypothesized that the long period frequency content (rail lengths of 30 to 50 feet) controlled the standard deviation. If these rail lengths corresponded to the sled frequencies existing above the fundamental frequencies, i.e., the secondary frequencies, a lowering of the standard deviation could be expected. For a monorail traveling at these velocities, these rail lengths correspond to forcing function frequencies in the range of 67 to 112 hertz, well below the fundamental vertical sled frequencies. This indicates that the secondary frequency effects cannot absorb any of the rail energy and thus lower the standard deviation.

Looking at the lateral direction it is seen that the means are relatively close to each other and do not appear to be related significantly to rail roughness. However, the standard deviation for the north 15000 feet of rail is less for both rail surfaces than is the south end of the track. This should be expected if the hypothesis is true about secondary effects. The forcing frequencies for the long period rail content do coincide with frequencies above the fundamental resonances in this

case.

It is evident that rail grinding is effective in reducing the long period rail content. The long period rails are what control the amplitude swings in the dynamic contributions. This fact for monorail sleds may not necessarily be beneficial unless the forcing function frequencies associated with these long period rails coincide with the sled's secondary structural frequencies. This frequency overlap is typically not the case in the vertical direction, but can be so in the lateral direction.

6.2.3.3 FINAL RAIL PROFILE SUMMARY

Examining Table 6-3, it is seen that all rail functions overpredict actual forces by quite an extreme range. Noting results previously cited for monorail work, the modal participation should absorb between 20 and 30 percent of the forces. Therefore, an ideal rail for the rigid body simulation should be one that overpredicts the actual by less than 30 percent. This condition is met by only one rail function in the vertical direction, the baseline function. However, a second rail function is close to meeting this criterion and should be considered. It is the top of the rail at TS 44000. All functions meet this criterion in the

lateral direction, but it is unknown whether the modal participation will absorb this much energy in the lateral direction since lateral prediction has never before been successful.

Based on the data presented, it appears that rail roughnesses in excess of 0.014 inches tend to grossly overpredict monorail vertical forces. This roughness value corresponds to another roughness break point classed by Mixon⁹. It is the class existing between the second and third defined roughness groupings.

Based on the rigid body work, the best vertical simulation is made by rail roughnesses of less than 0.014 inches. Lateral simulation appears to be relatively independent of roughness although, in general, rougher rails tend to overpredict more than smoother rails. Rail smoothing on monorails does not appear to be particularly effective in the vertical direction. It does seem to be of benefit in the lateral direction; reductions of up to 25 percent are evident. As for the dual rail sleds, rail grinding affects only the long period rail content.

6.3 MODAL SIMULATION

The response of the sled system in the rigid body monorail analysis was limited to the direct structural modes of the slipper assemblies. The structural modes

identifiable with the sled body must be superimposed onto the rigid body system to accurately reflect the true sled behavior. The spike monorail sled has eight secondary modes identified, two of which are second lateral bending modes of the suspension system. These frequencies are summarized in Table 6-5 in the concluding section of this chapter.

Now that the secondary structural response has been identified, the procedure is to identically repeat the simulations done with the rigid body analysis. The modal analysis amounts to running 19 different trajectory conditions for each of the nine rail functions, or a total of 171 modal simulations. However, it was concluded from the rigid body analysis that the conditions existing for Mach 1 to Mach 2 under thrust were invalid. Therefore, the modal simulation consisted of running the 15 valid trajectory conditions for each of the nine rail functions, or 135 total computer runs.

Each rail roughness simulation, consisting of the 15 valid conditions, was statistically averaged to determine the effect of the modal participation. The results of this analysis are presented as an average deviation between the actual forces (see Table 6-2 for the actual forces) and the estimated values from the simulation sequence. Also, the standard deviation about the mean deviation has been calculated.

The effect of modal participation was discussed in Chapter 5 as it pertained to earlier work done on this monorail sled. It was concluded that six modes shapes and five percent damping would reduce the percentage deviation by about 30 percent. This section will attempt to verify this conclusion.

6.3.1 DATA ANALYSIS--AMPLITUDE DOMAIN

6.3.1.1 PEAK FORCES

The modal analysis consisted of performing 135 simulations combining the monorail rigid body system with eight structural modes at three percent damping. Results of the peak force predictions for this analysis are shown plotted in Figures 6.15 through 6.18 for the four slipper conditions examined. The front slipper resultants are shown in Figure 6.15 for the vertical direction and Figure 6.16 for the lateral direction. Figures 6.17 and 6.18 contain the aft slipper vertical and lateral directions, respectively. The solid line is the average force described in Table 6-2, and the dotted lines correspond to the maximum and minimum values for that Mach number.

Examination of the figures indicate the vertical and lateral directions for the monorail sled appear to be

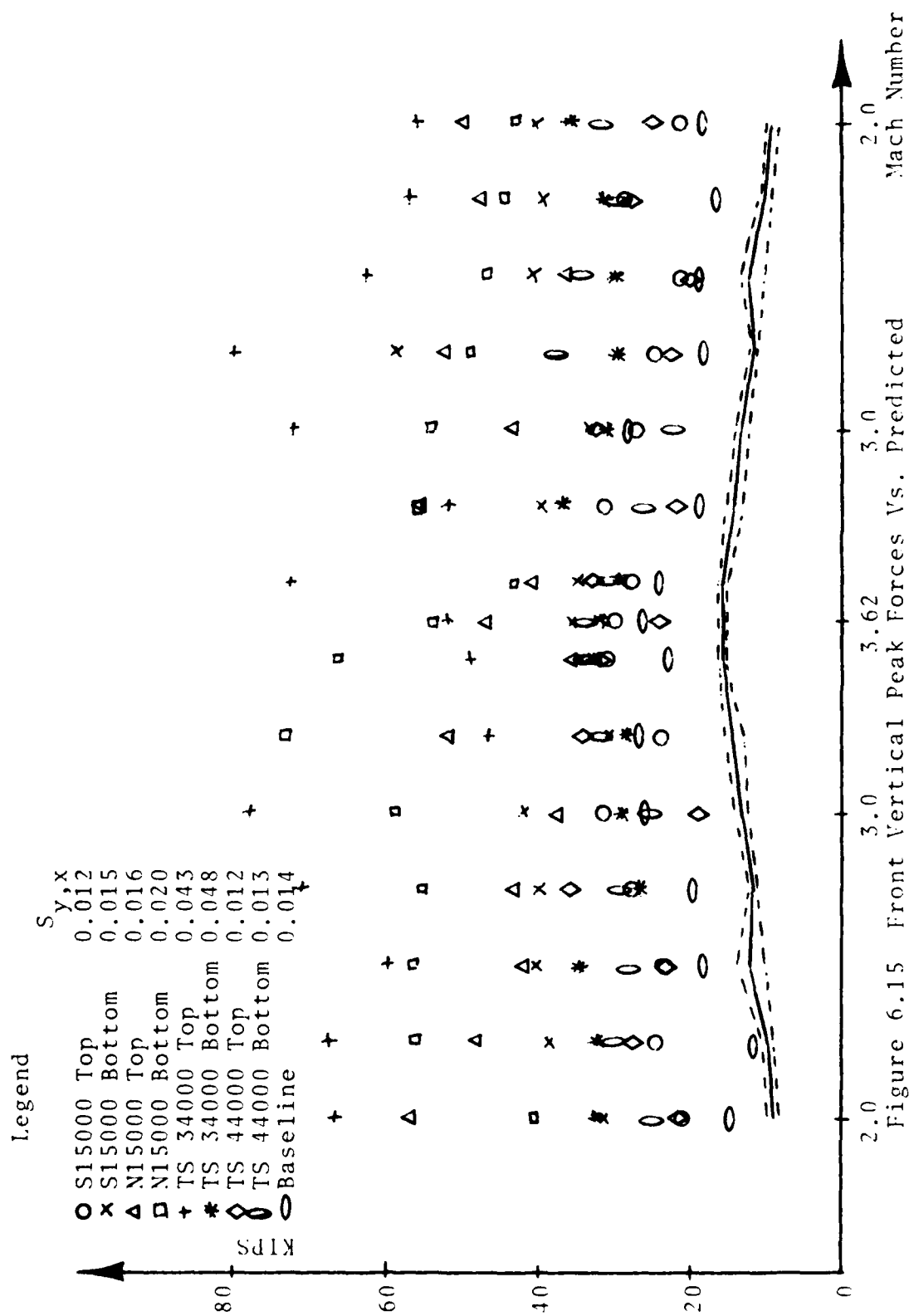
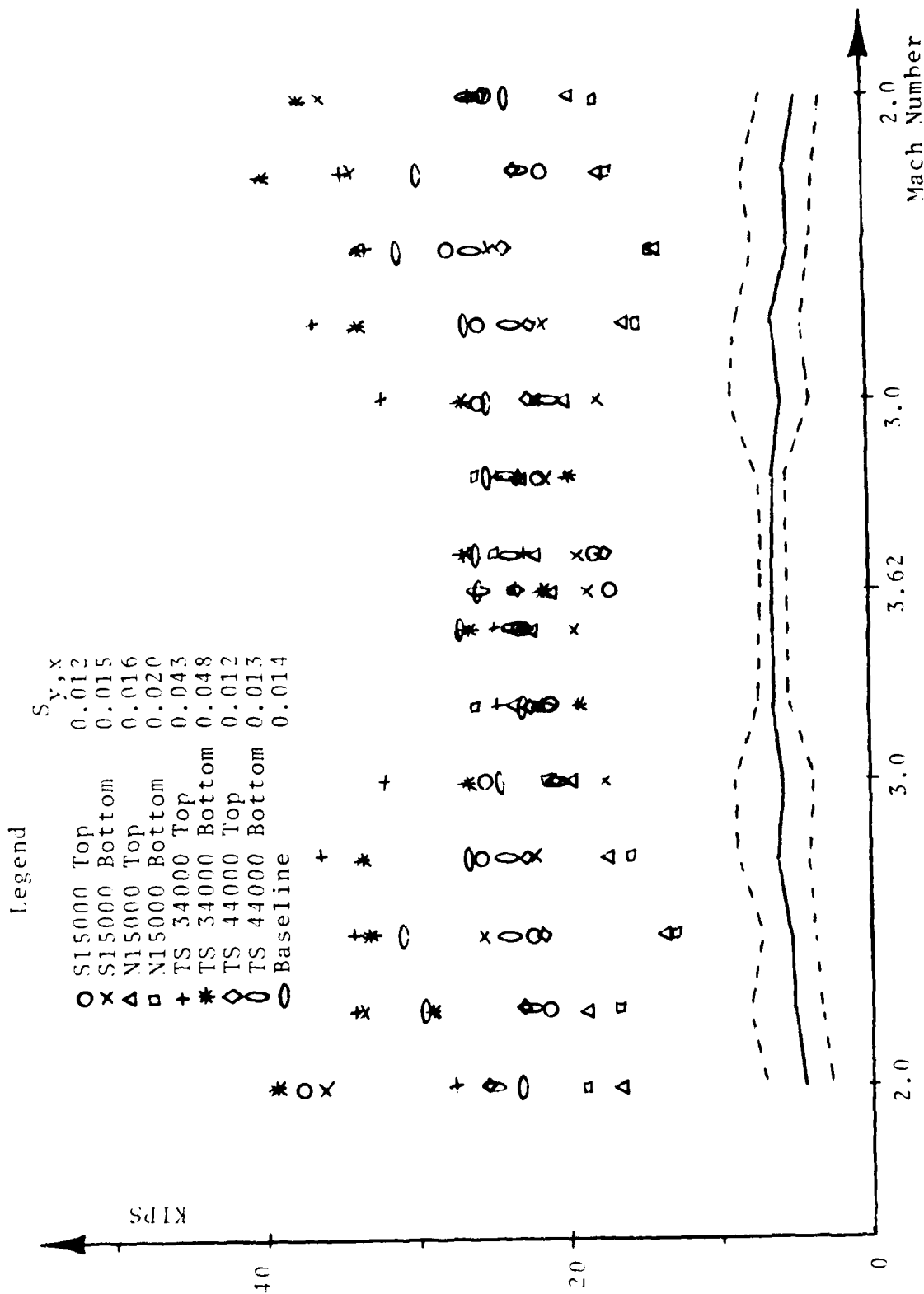


Figure 6.15 Front Vertical Peak Forces Vs. Predicted



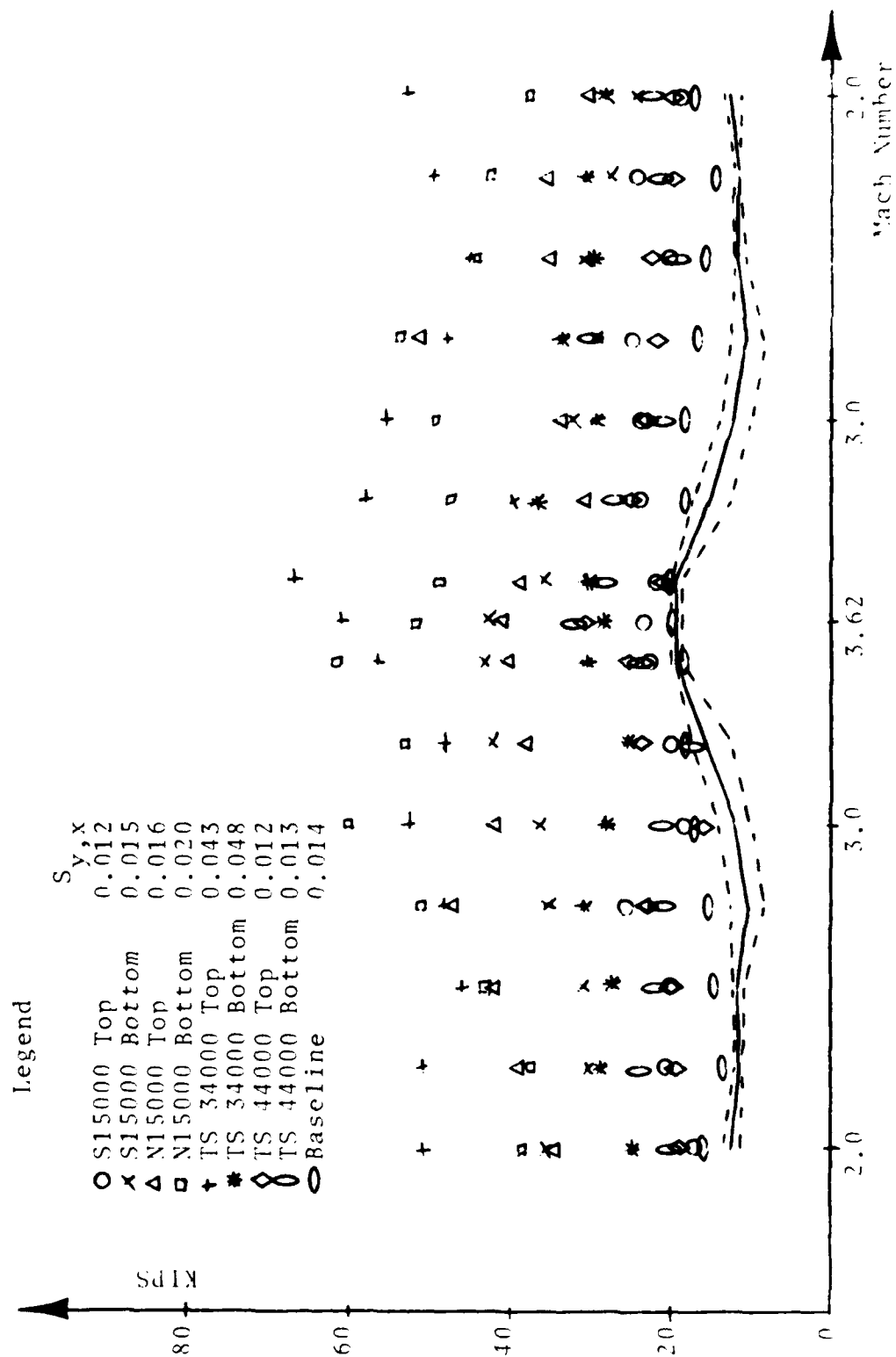


Figure 6.17 Aft Vertical Peak Forces Vs. Predicted

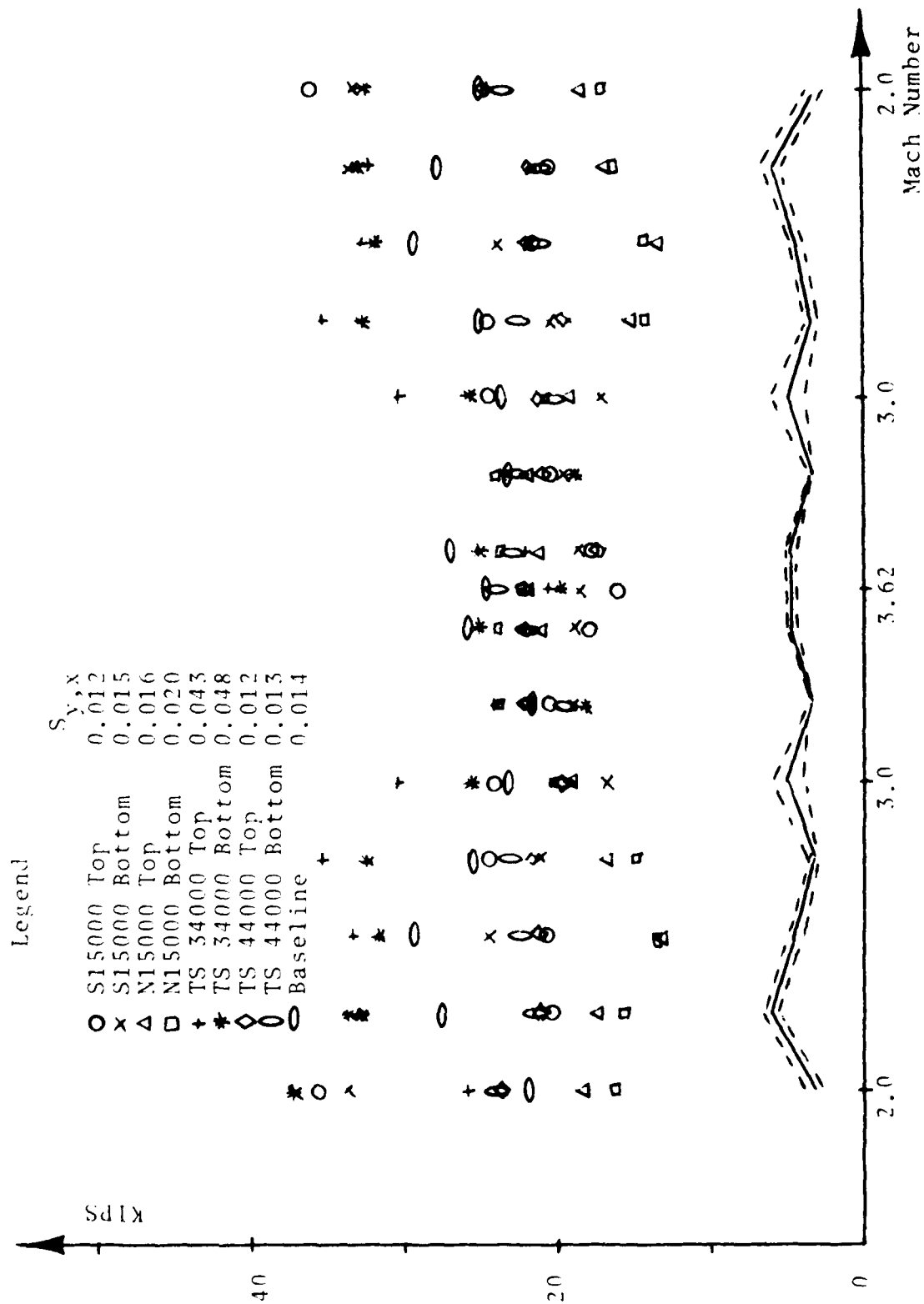


Figure 6.18 Aft Lateral Peak Forces Vs. Predicted

overpredicting more than in the rigid body case. The lateral direction overprediction appears to be at least an order of magnitude larger than it was in the rigid body case.

The statistical deviation analysis is presented in Figure 6.19 and summarized in Table 6-4 for all slipper conditions. The "x" denotes where the average deviation between actual and predicted peak forces occurs. The heavy-arrowed line represents the ± 1 sigma value about the mean deviation.

Looking at the table, it is seen that a distinct break point in overprediction in the vertical direction occurs at a rank roughness of 0.014 inches. This distinct break point applies to the average deviation as well as the standard deviation in the vertical direction. A defined break point is not readily apparent in the lateral direction.

Comparison of Tables 6-3 and 6-4 will show the effect of modal participation. It was earlier hypothesized that the modal participation would absorb up to 30 percent of the forces; however, it is seen that the average peak forces increase anywhere from 15 to 50 percent in the vertical direction. The standard deviation increase in the vertical direction remains approximately the same. Examining the lateral direction indicates a gross increase in force overprediction. The range of

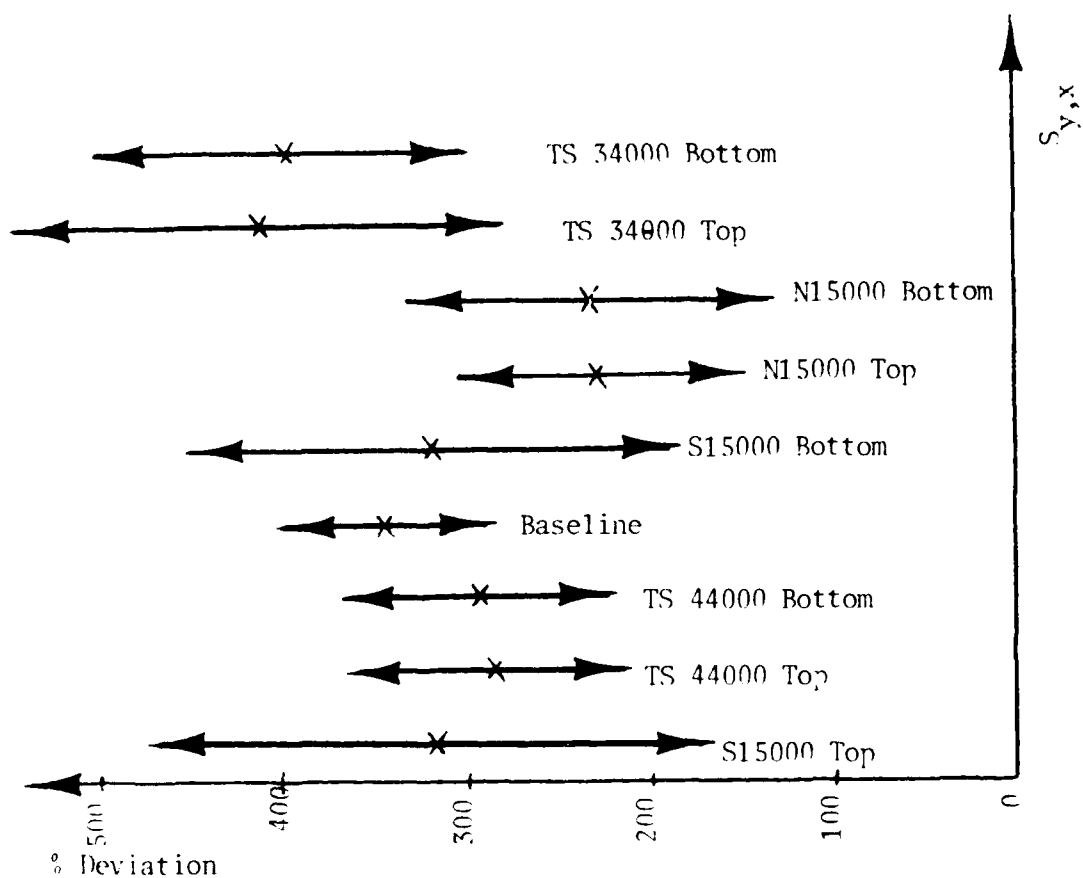


Figure 6.19a Vertical

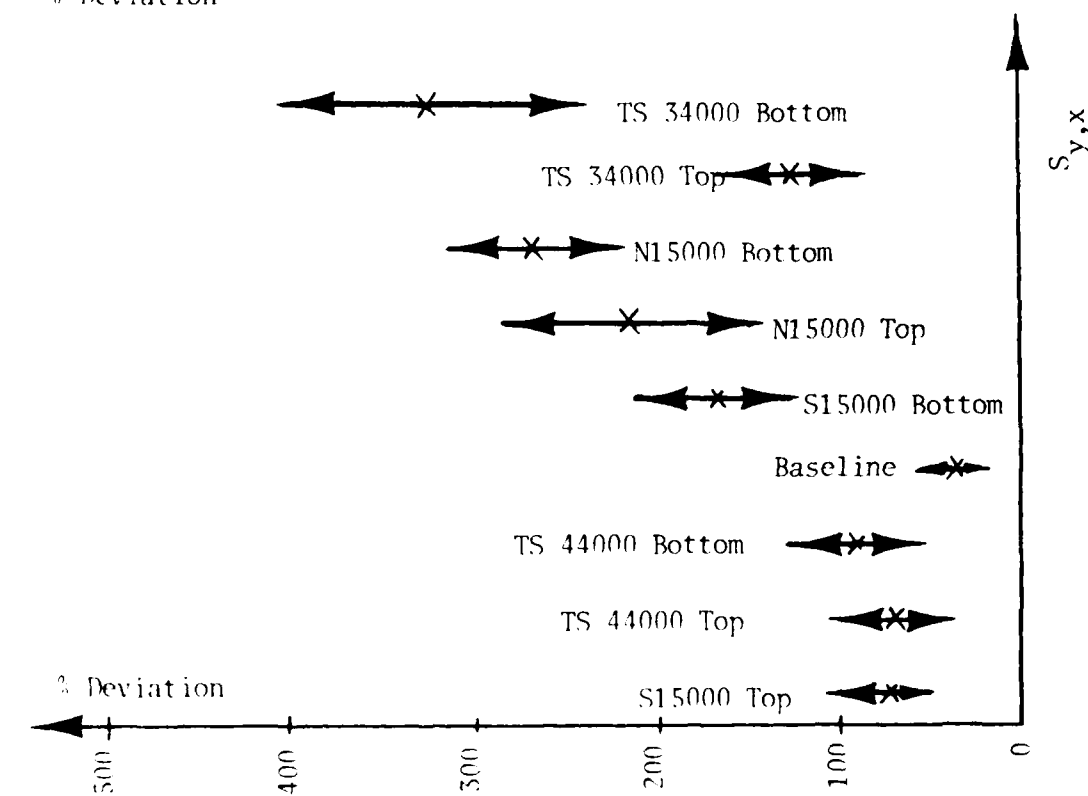


Figure 6.19b Lateral

Figure 6.19 Front Slipper Statistical Representation

TABLE 6-4 STATISTICAL SUMMARY
of MONORAIL MODAL PREDICTIONS

VERSUS RANK ROUGHNESS

FROM MACH 2 THRUSTING TO MACH 2 COASTING

Rail	$S_{y,x}$ (in.)	Vertical+++		Lateral+++	
		Average	1 Sigma	Average	1 Sigma
34,000 Bottom++	0.048	+323.01	83.0	+398.81	101.3
34,000 Top++	0.043	+126.61	40.4	+413.81	135.5
N15,000 Bottom	0.020	+264.71	48.2	+234.91	98.2
N15,000 Top	0.016	+213.51	68.2	+227.31	78.7
S15,000 Bottom	0.015	+167.31	45.1	+319.21	134.7
Baseline	0.014	+38.11	13.8	+345.21	59.8
44,000 Bottom++	0.013	+92.11	38.6	+296.31	75.4
44,000 Top++	0.012	+71.61	33.9	+287.11	74.3
S15,000 Top	0.012	+75.51	28.1	+316.21	149.8

Notes:

++ Denotes periodic rail content

+++ Resultant sum of both slippers acting in that direction

1. All values listed are percentages

2. Positive sign denotes overprediction

3. Negative sign denotes underprediction

overprediction increase is between 100 and 400 percent. The standard deviation in the lateral direction increased also, by as much as 7 times that of the rigid body case.

These findings are in direct conflict with the monorail modal findings expressed by MRI, so an attempt was made to find out why this discrepancy occurred. The MRI work was reviewed to determine exactly what procedure was used in arriving at the stated results. The following excerpt, found on page 36 of Reference 7, was found and explains how MRI manipulated the data.

..A method was adopted based on Mixon's scheme for reducing data from the Instrumented Monorail tests. He extracted the peak slipper force from each quarter Mach number velocity range. During the acceleration phase, that corresponded to about .1 second intervals. This was done for several runs giving a number of peak amplitudes for each value of Mach number. These were averaged and plotted as average peak versus Mach number. The analogous method used with the computer simulation is to make a run of constant velocity and look at the peak amplitude in each .1 second interval. A run of 1.0 second, for example, yields ten values which are then averaged.

After this analysis method was determined to have been used, a routine was added to the program that would average the peak values for each tenth second interval of the simulation run. A simulation was performed which matched the one simulation case quoted by MRI. These results are shown in Table 6-5.

TABLE 6-5

COMPARISON OF RESULTS
SLEDYNE VERSUS DASTARR

	FRONT			AFT		
	Meas.	Peak	Average	Meas	Peak	Average
MRI-vertical	16.00	20.68	16.61	19.00	23.28	16.52
DASTARR-vert		22.76	17.00		17.89	15.57
DASTARR-lat	7.25	27.00	13.63	4.90	25.85	13.26

Notes:

1. Forces are in kips
2. Condition is at 4000 fps under thrust

As can be seen from the table, MRI's results increased when modal participation was added and the peak averaging was not done. Results in the vertical direction compare exceptionally well between DASTARR and SLEDYNE for both peak values and average values.

However, the peak averaging method discussed is extremely questionable and should be avoided.

6.3.1.2 PEAK FORCE VERSUS TIME

Contained in Figures 6.20a and 6.21a are the data clips from the actual monorail sled runs discussed earlier. Figures 6.20b and 6.21b are the simulated force-time plots for the front vertical and lateral slippers, respectively. The figures represent the same velocity condition (3370 feet per second under thrust) for the south 15000 top rail function. The remaining eight rail function histories are contained in Appendix C, Figures C.49 through C.64.

Actual run data for the front slipper vertical indicates the forces stayed in an envelope between +8 kips and -12 kips, and centered about a negative one or two kips. The simulation plots for the various rail profiles indicate the same centering about a negative one or two kips. However, the envelope size varies, and in all cases is larger than the measured case. Additionally, the envelope size increases with increasing rail roughness.

The front slipper lateral forces for the actual run data centered about zero kips and ranged between plus and minus 4 kips. Examination of the plots for the front

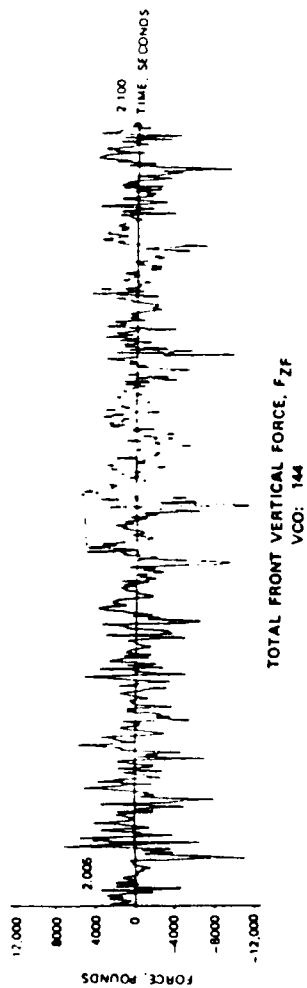


Figure 6.20a Front Vertical Peak Force Vs. Time

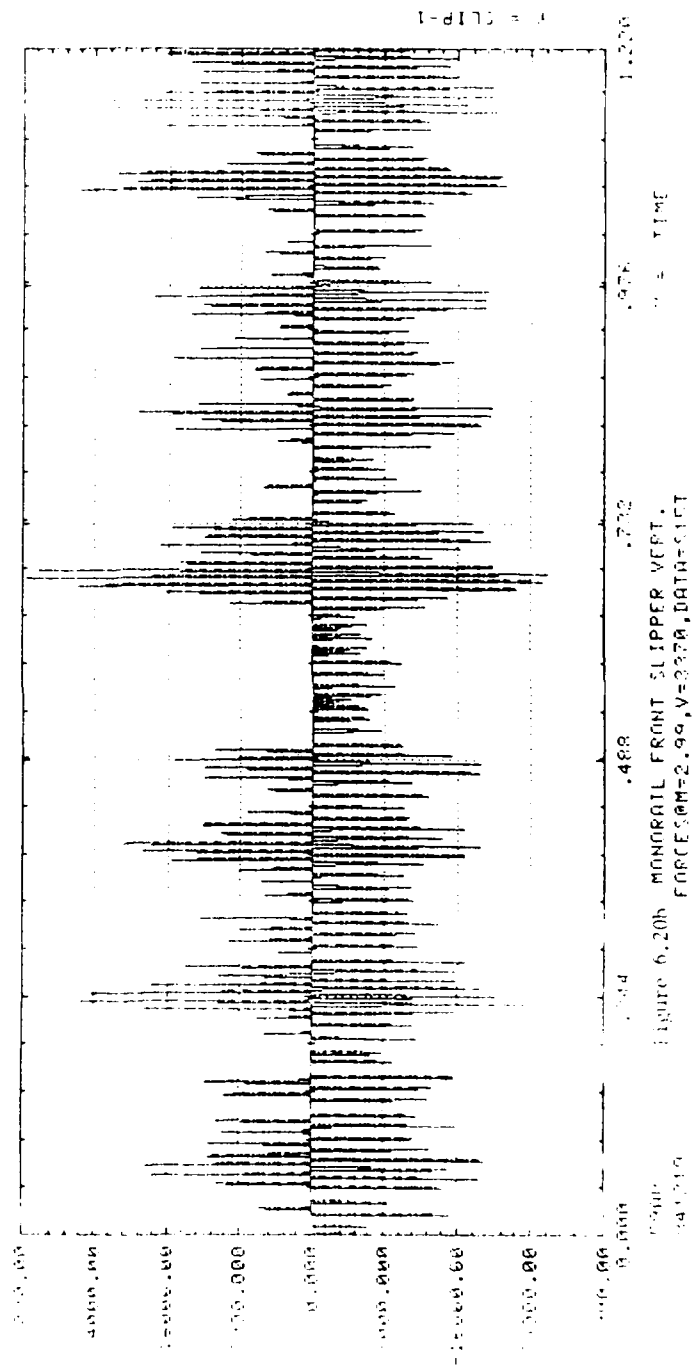


Figure 6.20b MONORAIL FRONT SLIPPER VERT.

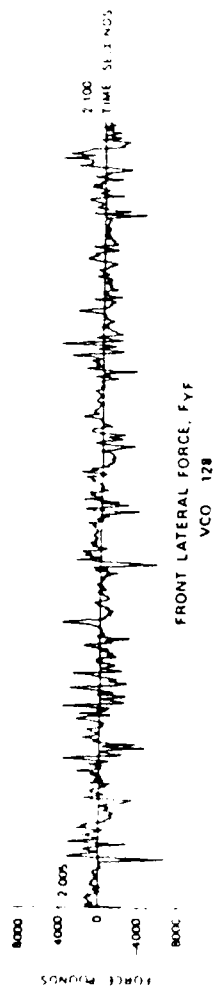


Figure 6.21a Front Lateral Peak Force Vs. Time

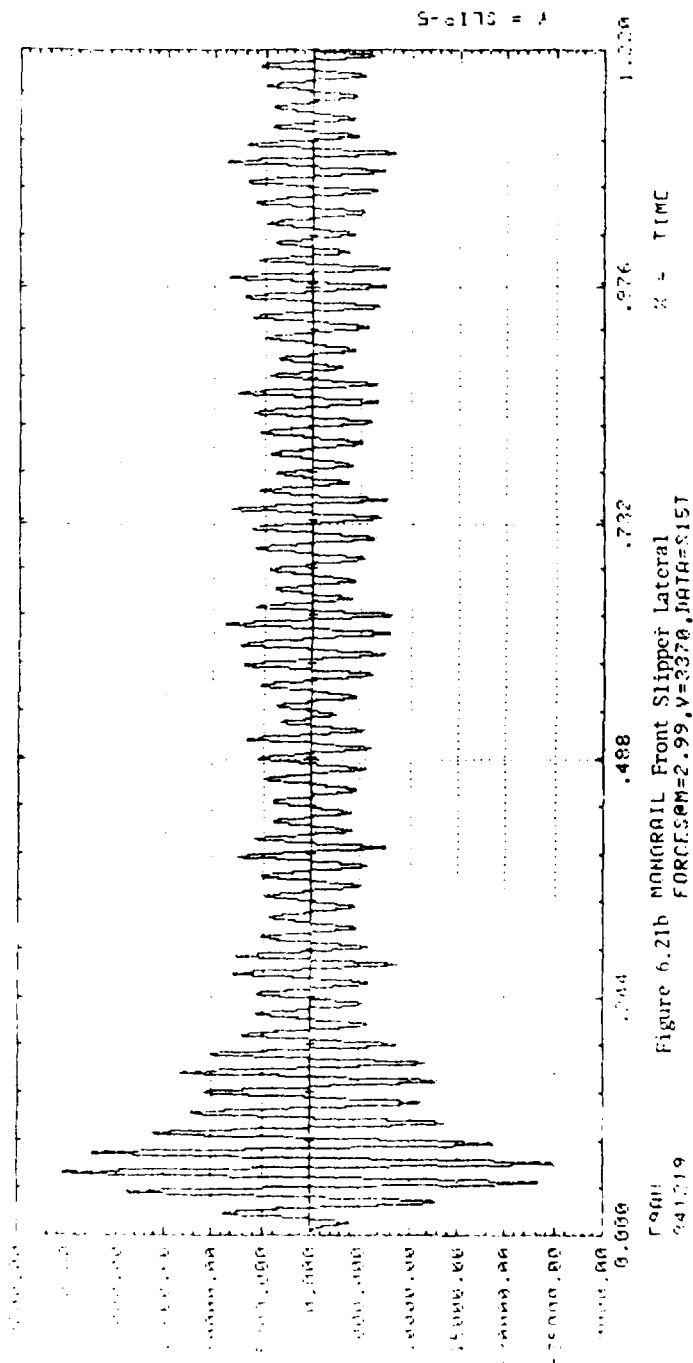


Figure 6.21b Manicrail Front Slipper Lateral Force Vs. Time

lateral slipper exhibits the same centering about zero kips, and modulates an equal magnitude on either side of zero. The range of modulation is up to six times as large as the run data, and appears to be related to rail roughness.

The ringing phenomenon seen in the lateral direction for the rigid body case is again present for the modal simulations. The only difference is that after the first ringing cycle, the amplitude damps to the level of the actual lateral measured forces. This phenomenon is referred to in nonlinear vibrations as superharmonic response.²² Superharmonic response occurs when the forcing function frequency is in resonance with a natural frequency, and is also an integer multiple of a higher natural frequency. The amplitude of the higher harmonic is then superimposed on the resonant frequency amplitude. When the damping is relatively small the superposition of the amplitudes dies out within one or two cycles. The rigid body simulation did not contain higher frequencies that could be superimposed onto the fundamental frequency. The first elastic lateral mode occurred at four (4) times the forcing frequency and thus became superimposed upon the rigid body frequency for one cycle.

Examination of the simulated force-time history for the south 15000 top indicates that the peak forces occur where the localized rough spots exist for this rail

function, and repeat as the profile loops end to end. This phenomenon is that same one that was discussed in the rigid body dual rail work simulation for this rail function.

6.3.1.3 FORCE HISTOGRAM

The discussion on force histograms for rigid body monorails indicated that the force distribution was strongly dependent on the mean, which in reality is the quasi-steady-state portion of the forces. The smaller the mean, the closer the approximation is to a normal distribution. The larger the quasi-steady-state contribution, the more like a Rayleigh distribution the estimated forces become. The quasi-steady-state content for the modal monorail is small so the expected distribution should be a slightly skewed Gaussian one. Shown in Figure 6.22 is a typical modal monorail distribution, and it is readily seen that it closely approximates a normal distribution due to the small mean value.

6.3.2 DATA ANALYSIS--FREQUENCY DOMAIN

The highest frequency content for the rigid body monorail sled simulation was about 2500 hertz. Repeating

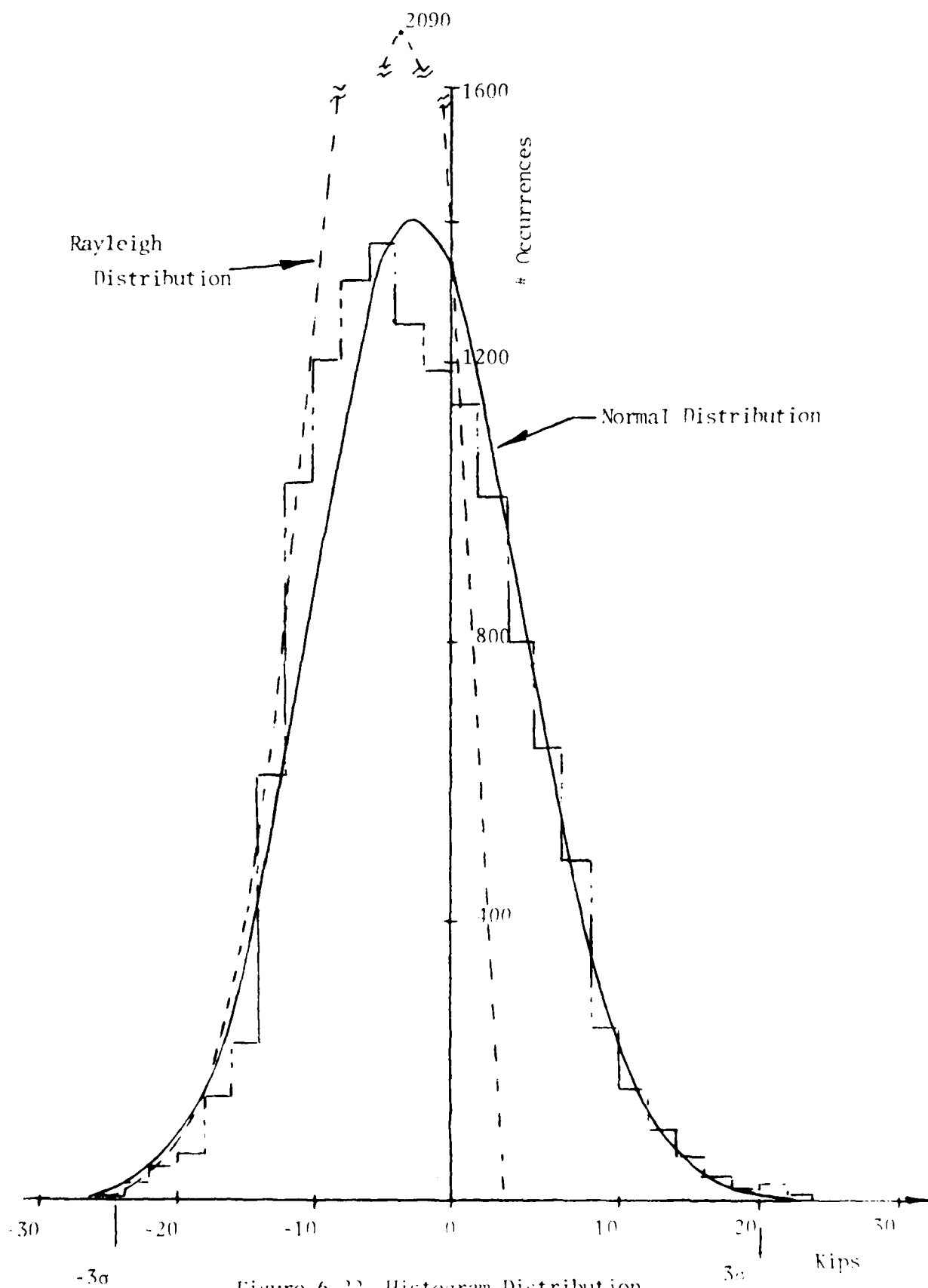


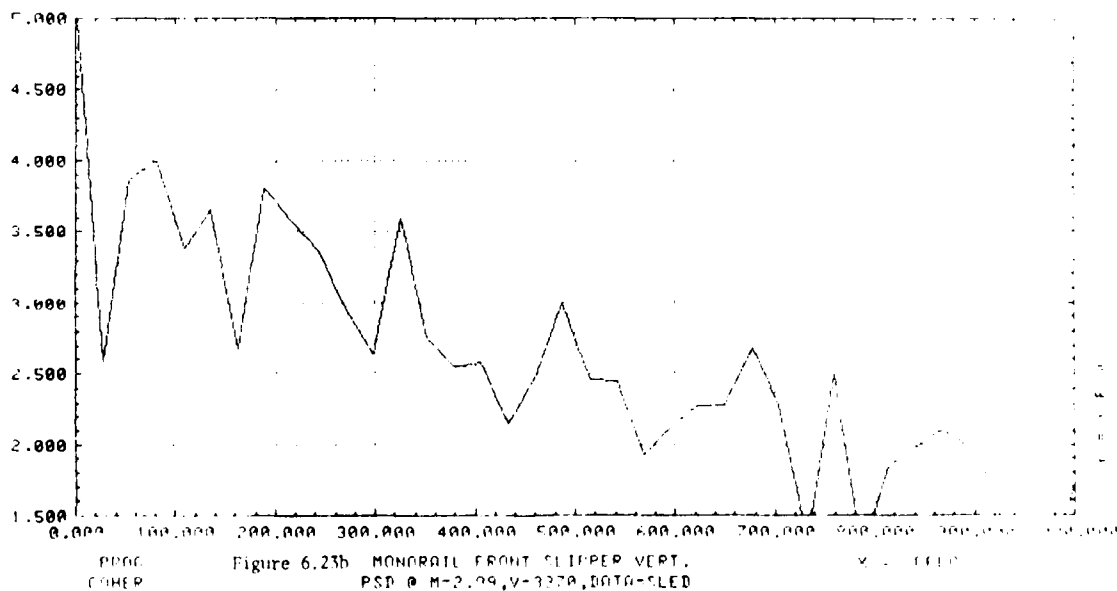
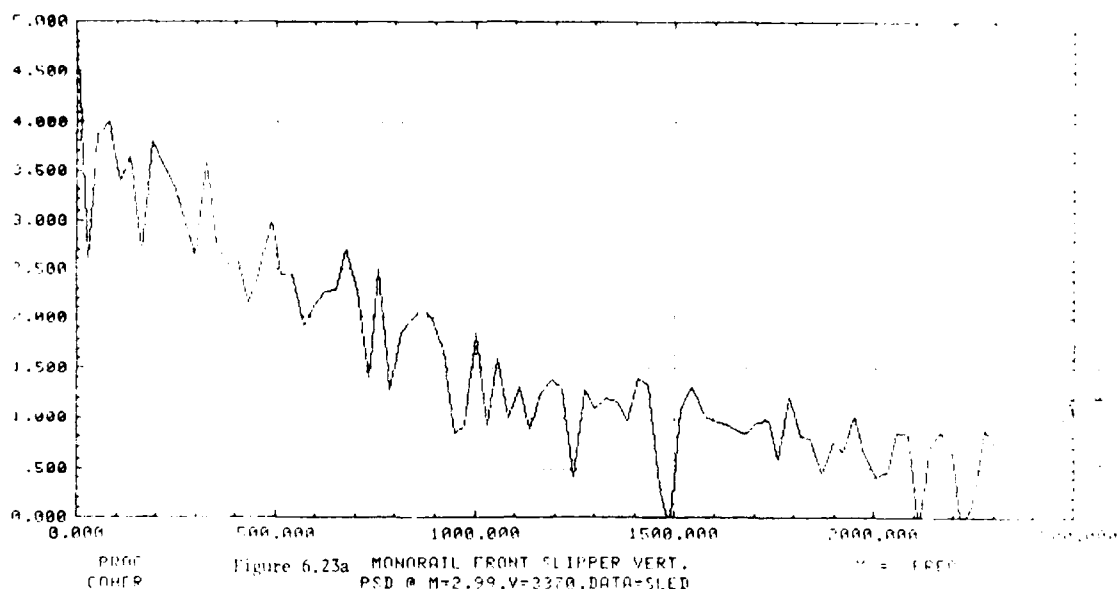
Figure 6.22 Histogram Distribution

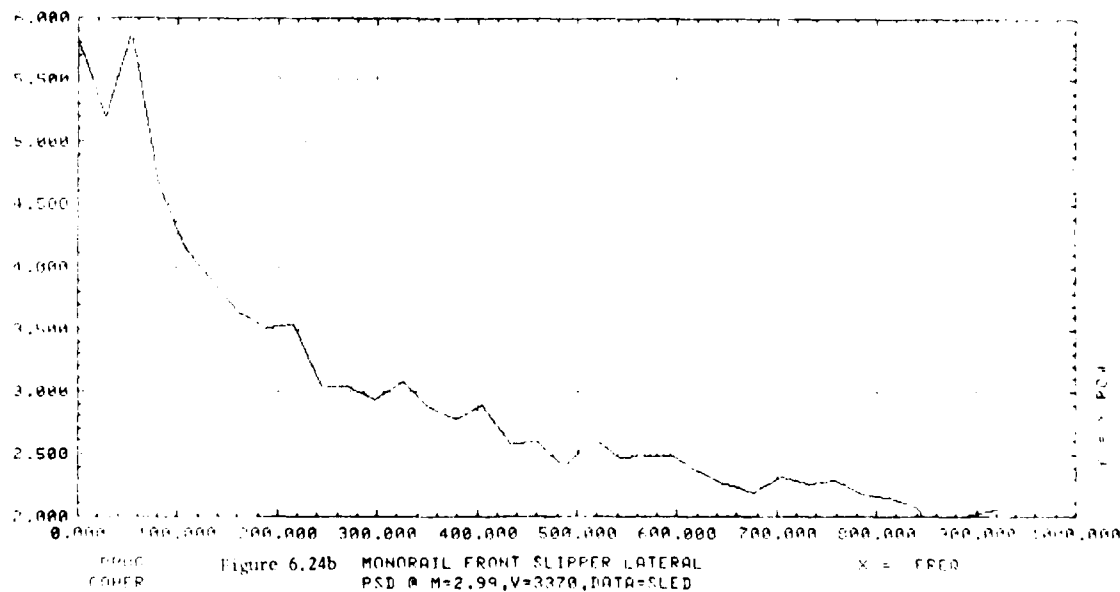
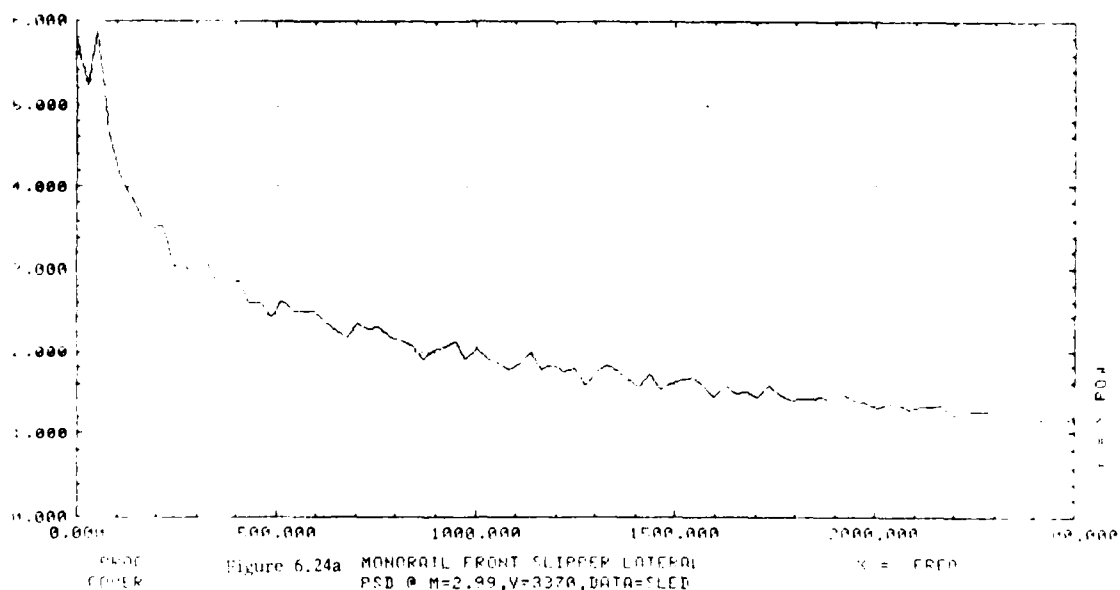
the simulation sequence for the modal participation adds a sufficient number of data points to increase the upper frequency limit to approximately 13,000 hertz. This frequency is well beyond the normal structural excitation range, so the analysis will only examine the response spectrum through 2500 hertz.

Shown in Figures 6.23a and 6.24a are the typical wide spectrum response for the modal monorail simulations for the front slipper in the vertical and lateral directions, respectively. These figures are directly comparable to those shown in Figures 6.13a and 6.14a for the actual run data. Figures 6.23b and 6.24b are blowups of Figures 6.23a and 6.24a, respectively, in the 0 to 1000 hertz range and clipping the power axes. Using the later figures, it will be possible to isolate the individual frequency content of the system.

The response of these slippers indicate typical monorail frequency content. Maximum energy is contained in an energy band between 100 and 200 hertz with sharp rolloff above this value. Noise predominates the energy above 600 hertz.

Comparison of the actual versus predicted PSDs indicates frequency contents that are almost identical. The frequency content from the actual run, the rigid body simulation, and the modal simulation are summarized in the concluding section in Table 6-6.





Power levels for the frequencies match up quite well with the values seen in the rigid body case, yet these levels are still in excess of the actual run case. Examination of the plots again show the distinct break point seen at a rail roughness of 0.014 inches in the amount of excess energy contained. Roughnesses less than this break point have energy content only marginally in excess of the actual run data.

The frequency content associated with the track survey iteration distance (65 hertz) and the 39-foot rail lengths (86 hertz) are masked by the data filtering of the PSD program. The program, for this upper frequency limit, filters the data in 25-hertz increments; therefore, these particular frequencies are combined with actual sled frequencies. The ringing seen in the lateral direction occurs at a frequency of about 55 hertz, which corresponds to the fundamental lateral frequency and appears to be excited by the 50 foot survey iterations. Again the ringing envelopes repeat at the corresponding frequency for the data looping end to end.

6.3.3 MODAL CONCLUSIONS AND SUMMARY

This section concludes the modal simulation analysis for monorail sleds. It will address all questions posed in the rail roughness study directive from a modal

participation point of view.

6.3.3.1 PERIODICITY VERSUS NONPERIODICITY

As with the rigid body monorail work, the smooth periodic rail's prediction is closer to the actual measured forces than is the nonperiodic rail. Both rails experienced an increase in the average deviation from the rigid body to the modal participation case. The periodic rail deviation increased by 35 percent in the vertical direction, whereas the nonperiodic rail increased by only 13 percent. The standard deviation for both rails increased by approximately 10 percent.

Comparing the roughness contribution of periodic rails can be done by looking at TS34000 versus TS44000. The rough periodic rail content average overprediction increased by about 50 percent from the rigid body to the modal case. The rough rails still grossly overpredict compared to the smooth rails by as much as a factor of two on the average deviation for the vertical direction. The standard deviations for the rough periodic rail remained relatively unchanged between simulation cases, yet is also up to twice as large as the smooth periodic rail.

It appears that the increase in force prediction in the vertical direction is due to the sled bending modes

being excited. The tie downs can excite the first vertical bending mode at a velocity of 1350 feet per second. Similarly, the second bending mode in this direction corresponds to the frequency generated by the tie downs at Mach 3.0. Examining data output showed both of these sled modes exhibiting significant acceleration levels in the vertical direction. Laterally, the tie downs can also excite the first and second bending modes with sled velocities at Mach 1.0 and 3.5, respectively. The first lateral bending occurs at a frequency low enough where significant structural excitement is possible and explains the nearly doubling of the lateral force predictions.

6.3.3.2 RAIL GRINDING

It was concluded in the rigid body section for monorails that rail grinding was virtually ineffective in the vertical direction. The results of the modal analysis arrive at the same conclusion.

Laterally, the rigid body analysis concluded rail grinding is effective in reducing the dynamic operating envelope seen by the sleds. Based on the modal results, the same conclusion is drawn. The dynamic envelope is smaller for the ground rail than the unground rail; however, the envelope size is still 5 times larger than

in the rigid body case. The increase in envelope size is a direct result of the tie down spacing exciting the sled laterally.

6.3.3.3 FINAL RAIL PROFILE SUMMARY

The rigid body work concluded that the baseline rail function would be the ideal rail to use in the vertical direction since it only overpredicted by 25 percent. Consideration of modal energy absorption hypothesized this overprediction would be reduced to zero. After performing the modal analysis, it was found that the tie down spacing excites the sled bending modes enough that force reduction does not occur. However, the modal results indicate the baseline is still the best rail profile since the overprediction only increased slightly, i.e., 12 percent, and the standard deviation actually decreased.

6.3.3.4 MODAL SUMMARY

Utilizing all data examined thus far, it is inherent that rail roughnesses in excess of 0.014 inches significantly increase the forces subjected to the sled when modal participation is added if the model is accurate. This break point holds for both front and aft

slippers for both the average deviation and the standard deviation.

The modal content for monorails affects the forces in varying degrees but in all cases the average deviation increases from the rigid body case, particularly in the lateral direction. Vertically, the increase ranges from 15 to 50 percent and is strongly dependent on rail roughness and long period undulations.

Based on the modal simulations, the peak slipper forces can be reduced significantly, even more than seen for dual rail sleds, by reducing rank roughness. The reduction for monorails is not as straight forward as the dual rails but a two to three percent reduction in the vertical overprediction is possible for each 0.001 inch reduction in rank rail roughness.

Rail smoothing appears to be effective in the lateral direction, but rail alignment at the tie downs seems to be more critical.

6.4 MONORAIL SUMMARY AND CONCLUSIONS

An extreme number of computer runs were performed in an effort to verify DASTARR for monorail sleds. The simulations were all performed using the constant velocity option for a single sled, and it was found that the monorail sled was particularly sensitive to rail

roughness data transients such as the tie down spacing and survey iteration distances.

6.4.1 MONORAIL VARIABLE VELOCITY SIMULATION

Making note of the monorail sensitivities to the rail function data irregularities and the uncorrelated lift functions through Mach 2.0, an attempt was made to perform the variable velocity simulations knowing the results might be suspect. The results of this attempt were very discouraging. The rigid body modes, as the sled traveled through the velocity regime, became more and more excited yielding a diverging solution that resulted in totally unrealistic slipper forces. Final force predictions for the rigid body analysis approached 5×10^7 pounds, which indicated the calculated slipper deflections were allowed to reach impossible proportions, i.e., 135 inches.

Results for the modal variable velocity simulation reached the same conclusion, only the peak forces maximized at one million pounds. The times of peak occurrence were identical in both cases and equated to a Mach number of three. At this time no viable explanation for the divergence of the solution is possible. Further investigation into this anomaly is recommended.

6.4.2 CONCLUSIONS

It is apparent that DASTARR can predict peak slipper forces for monorail sleds in a manner that is totally acceptable to engineering judgment. The results for the monorail are strongly dependent on the rail function, velocity option, and modal considerations used.

It is concluded that the constant velocity function for a single rigid body monorail yields the best results. The results become even more attractive when the data averaging technique suggested by MRI is applied. However, it is strongly recommended that this option not be used.

It was shown in this chapter that peak forces for monorail sleds fall between a Rayleigh and a normal distribution. The amount of contribution of each function is strongly affected by the quasi-steady-state forces, and the dynamic envelope. The smaller the quasi-steady-state force contribution, the closer the data approximates a Gaussian distribution. The skewness of the distribution is then controlled by the standard deviation.

Rail grinding appears to be marginally effective in the lateral direction. The simulation results indicate the tie down spacing alignment is more critical in reducing forces for monorails than is rail grinding. In

general, a two to three percent reduction in forces is obtainable for each 0.001 inch reduction in rank rail roughness. Rail smoothing is particularly effective until a rank roughness of 0.014 inches for monorails has been achieved. Results do not improve significantly by smoothing to less than this value.

Verification of localized rough spots on the Track have been accomplished for monorails. The effect of localized polishing can now be studied to determine optimal grinding values.

When considering rail functions, the baseline function generates the best slipper estimates for both the rigid body and modal cases. Peak forces, in the lateral direction, have been correlated for absolute magnitude values for the first time, though actual simulation force-time plots do not mirror real run results. The simulation plots exhibit a ringing sensation that resembles narrow band response. Narrow band response is when a single degree of freedom oscillator, or a sharply resonant system, is subjected to a forcing function whose energy is relatively constant over a substantial frequency range when compared to the oscillator frequency.²² The resultant is defined as a narrow band response spectrum. Laterally, the math model is idealized as a single degree of freedom system for the rigid body case, or as a sharply resonant system for the

modal analysis. The forcing function is relatively flat over a frequency range well in excess of the system resonant frequency. Much of this energy is at frequencies caused by the data anomalies generated by survey techniques and data set looping. These frequencies do not occur in reality and account for the lateral direction simulation discrepancies encountered.

Frequency contents found in the simulation are summarized in Table 6-6. Excellent correlation was obtained in the vertical direction. The lateral direction exhibited inconsistencies that have just been discussed.

Comparing the modal analysis to the rigid body case indicates that for monorail sleds a rigid body analysis will adequately define the slipper loads. Modal participation does not refine the structural loads as hypothesized, in fact the loads increase due to structural modes' excitement caused by the rail tie downs.

TABLE 1 VIBRATION TESTS

MODE NO.	MODE DESCRIPTION	PREDICTOR BODY HANE CALC.	NASTRAN MODEL	VIBRATION TESTS	DATA	RESIDUAL PCT. POSTAGE	POSTAGE WITH M.C.A.
1	Rigid body yaw translation	45.85	69.38	47	80	55	55
2	Rigid body yaw rotation	54.96	89.59	121	160	130	130
3	Rigid body pitch translation down	198.66	204.44	247	200	180.20*	180.20*
4	Rigid body pitch translation up	230.32	204.44	247	200	180.20*	180.20*
5	1st bending - yaw plane	NC	292.72	247	3	NA	270
6	Rigid body pitch rotation	257.81	351.01	304	270	1.24*	340
7	1st bending - pitch plane	NC	429.78	421	360	NA	460
8	2nd bending - pitch plane	NC	788.72	660	300	NA	595
9	2nd bending - yaw plane	NC	886.83	600	550	NA	620
10	1st lateral suspension bend-front	NC	959.39	NM	NA	NA	850
11	1st lateral suspension bend-aft	NC	982.87	NM	NA	NA	940
12	3rd bending - pitch plane	NC	1386.37	NM	NA	NA	1400
13	1st longitudinal buckling	NC	1593.62	NM	NA	NA	1600
14	3rd bending - yaw plane	NC	1735.56	NM	NA	NA	1740
15	2nd longitudinal buckling	NC	1860.25	NM	NA	NA	1870

* All approximate due to 40 Hz filtering

+ Due to predictor corrector method for time step (either 1/2, full or double) valve can be either 1/2, actual or double.

NA-Not Applicable

NM-Not Measured

NC-Not Calculated

CHAPTER 7

CONCLUSIONS AND RECOMMENDATIONS

7.1 GENERAL

Detailed in Chapter One were the proposed areas of study to be accomplished during this research. These were expanded under the rail roughness study directive described in Chapter Four. These objectives are summarized again.

- 1) Define the equations of motion for up to three coupled sleds for six degrees of freedom. These equations were to be defined such that they would collapse to predict one sled as well as three. Finally, the equations were to collapse such that pitch plane simulation could be achieved so the results would mirror the existing SLEDYNE program.
- 2) Allowance for a variable velocity input instead of being limited to a constant velocity simulation.
- 3) Allowance for variable slipper gap definitions.
- 4) Allowance for an easier slipper stiffness definition that will eliminate the need for modifying the NASTRAN math model. Presently a secondary modal analysis that is compatible with

SLEDYNE requirements is necessary.

- 5) Establish a final and fixed rail forcing function to use for all simulations.
- 6) Establish a fixed length of rail for optimizing force predictions for the constant velocity simulation cases.
- 7) Determine the effect of long period rail undulations on slipper impact forces.
- 8) Establish if rail grinding is effective in reducing the slipper impact forces.

7.2 CONCLUSIONS

Each of the proposed areas will be discussed and general conclusions drawn about them. The next section, Chapter 7.3, will discuss the limitations found and make recommendations for future research to expand on the work that has been accomplished here.

7.2.1 DEFINITION OF THE EQUATIONS OF MOTION

The equations of motion were derived for coupled sled systems in Chapter Two. The equations were developed in matrix form to ease the required computational effort. Since the equations were derived in matrix form, the matrices were allowed to collapse to

handle either one, two, or three sleds coupled together. These equations were defined to allow the system of matrices to further collapse into only a pitch plane analysis.

The validity of this collapsing capability was verified in Chapter Four. A sled that had been extensively analyzed in the pitch plane using the SLEDYNE program was subjected to an analysis on DASTARR in the one sled, pitch plane only configuration. Adequate correlation of this configuration was obtained.

The equations of motion for a single sled, either dual rail or monorail, at a constant velocity were correlated in Chapters Five and Six. This correlation examined the difference between performing a rigid body simulation and the superposition of modal properties onto that rigid body system.

Not discussed previously is the effect of sled coupling, due to an insufficient number of appropriate sleds having adequate math models to allow for the proper sled train configurations. However, this option of the program has been tested through a series of fictitious rigid body sled trains. These fictitious rigid body sleds had properties defined that were on the order of magnitude of real sled properties used under various track coupling configurations. Results of these simulations gave values that appear to be valid, or at

least fall into an expected range of forces based on track experience for similar systems. It should be caveated that transmitted thrust transient predictions cannot be correlated until these math models have been developed and verified.

7.2.2 VARIABLE VELOCITY OPTION

The program was written to allow the user to specify a variable velocity function for use in the simulation. This velocity function is defined to be an output file from the Test Track trajectory program, TSLED. Using specific parameters from the velocity profile, the program can integrate the equations of motion to obtain the required force output. The validity of the results using the variable velocity were confirmed in Chapter Five for dual rail sleds. Due to rail function idiosyncracies modulated by velocity, the monorail solutions tended to diverge under this option and have not yet been correlated.

7.2.3 VARIABLE SLIPPER GAPS

The program was designed to allow the user to define a slipper gap. This gap was then assumed to be constant throughout the computer simulation. This gap assumption

does not meet the requirement levied for a variable slipper gap; however, one may vary a constant gap between simulations to determine the effect of the gap. No attempt has been made to determine the "ideal" gap or to study the effects of varying the gap thickness.

The need for a variable slipper gap stems from the variations in the cap thickness for the railhead and to slipper wear occurring during the sled run. This parameter of the program can eventually be modified to account for these effects. An extensive amount of survey data, which is unavailable to date, is required to account for the cap deviations. Once this data is obtained, the program can be modified in the way it handles the rail roughness parameter to yield a variable slipper gap. The slipper wear problem cannot be addressed until sufficient data is available to define the slipper wear as a function of velocity. When this happens, an additional table may be incorporated into the program to handle gap increases due to the slipper wear.

7.2.4 SLIPPER STIFFNESS DEFINITION

Under the existing SLEDYNE program, the modal participation was limited to the secondary structural modes. Definition of these modes was accomplished by redefining the structural constraints of the model to

eliminate the "rigid body" contributions. This model redefinition resulted in defining two math models to examine the sled, and still did not address simplification of the slipper stiffness definition.

Based on DASTARR programming, the user is allowed to define the modes to be used in the simulation. This modal selection lets the user develop one math model with realistic support constraints and then delete the defined rigid body modes in the modal definitions. This procedure eliminates the need to define two math models, but again the slipper stiffness definition is not simplified.

One can take the approach suggested by Mixon⁶ for slipper stiffness; that is, develop an extensive math model of the structural suspension system, statically load it, and calculate the stiffness based on the deflection. This approach is the best method for monorail sleds since the slipper itself is the primary suspension element. For dual rail sleds, one may determine the slipper beam stiffness based on the unit dummy load method to calculate a deflection under a given load. This method is relatively simple to apply for dual rail sleds since the beam spanning the rails is the primary suspension element. The approach used for monorails is best for special case dual rail sleds, those without standard slipper beams.

An alternative method to the above procedures would be to include all suspension elements in the modal analysis. Using the calculated frequency for the rigid body motions, one can derive the required stiffnesses based on the proper apportionment of the sled mass. This procedure was alluded to in Table 5-6 for dual rail sleds, under the rigid body modes heading that apportioned the mass to calculate the rigid body heave frequencies.

7.2.5 FINAL AND FIXED RAIL FUNCTION

Based on the discussions of Chapters Five and Six, it was concluded that the Baseline function yielded the best results under all conditions, with the function for TS 44000 top being a secondary choice. While these profiles yielded acceptable results, they introduced facsimilies into the data that may or may not exist. These data irregularities have been previously discussed and are a result of survey techniques used to obtain the preliminary rail roughness measurements and the looping of the data set to generate a rail of sufficient length.

7.2.6 FIXED RAIL LENGTH

Based on all rail functions studied, a fixed length

of 4000 feet appears to optimize rail force predictions. Rail lengths shorter than 4000 feet have not reached the peak force predictions, and lengths in excess of this value do not increase the force prediction estimates.

7.2.7 LONG PERIOD UNDULATION

Large amplitude, long period rail undulations do increase the predicted impact forces provided the proper period length, sled velocity, and fundamental frequency are consistent. That is, a typical dual rail sled having a fundamental heave frequency of 15 hertz and traveling at a velocity of 3000 feet per second can have this mode excited by a rough rail period of approximately 200 feet. Similarly, secondary structural modes can be excited by the proper combination of sled frequency, sled velocity, and physical rail period lengths. These periodic lengths are not limited to actual rail undulations, but can be any physical rail parameters, such as rail length (39 feet) or tie down spacing (52 inches).

7.2.9 RAIL GRINDING EFFECTIVENESS

Rail grinding has been determined to be effective but not as originally envisioned. It was thought that rail grinding would smooth the rail between tie downs,

but it has the effect of smoothing the longer rail durations, i.e., 30 to 50 foot periods. Spectral analysis of the rail roughness functions support this theory. There is more energy in the long period in the unground rail, i.e., the south end of the track, than in the ground rail at the north end of the track. Conversely, there is more energy in the ground rail at the shorter rail lengths than the unground south end.

Simulation results also confirm this fact. The longer rail periods, when considering sled velocity for dual rail sleds, generally fall into the secondary structural mode range. The dynamic force contribution to the total slipper force tends to be minimized when the long rail periods fall into the secondary structural mode range. The quasi-steady-state portion of the total is controlled by the rank rail roughness. This conclusion has been found to hold for monorail sleds, primarily in the lateral direction. Typically monorail sleds have secondary pitch plane structural frequencies sufficiently large enough that to affect the dynamic envelope, by rail grinding, would require sled velocities considerably in excess of 20,000 feet per second.

7.2.10 FINAL CONCLUSIONS

Simulation results have been successfully correlated

to existing measured sled slipper data for both dual rail and monorail sled systems, in both the vertical and lateral directions. The Test Track now has a viable design tool in DASTARR for predicting sled track interaction forces. Additionally, the program was developed to allow sleds to be coupled so that transmitted thrust transients could be examined for the first time. With this new design tool, sleds can now be designed more efficiently to reflect an optimum strength to weight ratio. This optimum strength to weight ratio will allow for using existing propulsion to accomplish attaining the higher velocity requirements safely.

7.3 RECOMMENDATIONS

The research involved in developing the DASTARR simulation program resulted in a viable design tool for the Test Track. The program has been verified as to the quality of the results; however, there are still areas that need to be investigated. These areas are discussed below and are not given in any priority.

7.3.1 TRANSMITTED THRUST TRANSIENTS

It was discussed in the previous section that transmitted thrust transients were not correlated, as a

direct result of not having appropriate math models available. Verification of the transmitted thrust feature of DASTARR must wait until these models have been developed. Additionally, sufficient track run data on these transients must be taken to obtain an adequate data base for comparison with the predicted forces.

7.3.2 RAIL ROUGHNESS PROFILE

It was concluded that the Baseline rail profile yielded the best force prediction results. Even though the results were correlated, the survey techniques used to obtain the data introduced errors into the functions. A forcing function should exist that spans at least 4000 feet of track in order to accurately estimate rail forces in the future. A rail of this length will eliminate the cycling effect of looping the data end to end. Also, a new survey procedure must be established that will eliminate the 50-foot sections of data taking. Something along the line of a laser survey that can measure the roughness for at least 5000 feet of continuous track is desirable. The entire 50,000 plus feet of track should be measured, for all surfaces on each of the rails to completely delineate the rail profile. When the complete rail has been defined, the study should be repeated with the larger data base to determine whether a given section

of rail will satisfactorily predict slipper forces, or whether the entire rail definition is required.

7.3.3 MASS VARIATIONS

Under the present version of DASTARR, mass variations of the sled cannot be studied except in the constant velocity case. The time-varying mass problems associated with pusher sleds as the propulsion is expended is precluded. Preliminary studies have indicated that varying the mass, and its associated center of gravity, have a pronounced effect on the results. The program can be modified to allow a time or velocity dependent mass and center of gravity to be defined. This modification will take care of the rigid body contribution to the total slipper forces due to the mass changing. However, the extent of the modal contributions cannot be determined until an extensive parametric study has been performed investigating how the mode shapes change as a function of the mass change. The mass variation is an important area of interest as certain rocket motors, particularly at burnout, become longitudinally excited and this excitement in turn can excite sled downtrack modes and then induce transient spikes into the transmitted thrust vector.

7.3.4 LATERAL FORCING FUNCTIONS

The program, as written, does not account for possible secondary forcing functions, such as those in the lateral direction. The lack of this definition can be remedied by allowing additional forcing function table definitions, such as was done for the lift and center of lift tables. The addition of this feature will be appropriate to study the design requirements on sleds subject to explosion testing. Explosion testing is when explosives are detonated beside the track to study blast-created pressure waves and how these waves affect various test platforms as the vehicle travels through the pressure wave. Another potential use for this feature will be to define cross track aerodynamic forces when the sled, particularly monorails, yaws with respect to the rail centerline.

7.3.5 RAIL GOUGING

A problem encountered on high speed monorail sleds is a phenomenon known as rail gouging. Rail gouging is the physical removal of a piece of track when the sled travels over a section of rail. There are several theories to explain gouging, and the two most likely are concerned with the physical interaction of the slipper

with the rail.

One theory holds that matter particulate, probably debris from slipper wear, is caught between the slipper and the rail. Under this condition of infinitely high pressure, the particulate flashes into a plasma and literally blows a piece of rail out. The second theory states that at these high velocities, the slipper impacting the rail creates an extremely high localized pressure that causes an instantaneous weld to occur between the rail and slipper. Then, as the sled continues down the track, the slipper pulls a section of rail out.

The second of these theories has the potentiality to be investigated with DASTARR. The program can be modified to examine the physical interaction of the slipper and the rail when impact does occur. From this interaction it will be possible to ascertain whether the required pressure to cause this instantaneous welding can occur.

7.3.6 RAIL GRINDING

Although rail grinding is effective in reducing the dynamic force envelope, proper alignment of the rail at the tie downs will result in a greater force reduction. It is recommended that rail grinding be suspended in lieu

of rail alignment. Localized rail polishing should be used to smooth the rail once the alignment process has been accomplished.

REFERENCES

1. Rasmussen, H. S., Survey of Braking Techniques For High Speed Track Vehicles, ADTC, HAFB, N. M., September 1976.
2. The Holloman Track: Facilities and Capabilities, AFSWC, HAFB, N. M., 1974.
3. ISTRACON Handbook, ISTRACON Report No. 60-1, December 1961.
4. Krupovage, D. J., Mixon, L. C., Pokorny, O. T., Wind Tunnel and Full-Scale Forces on Rocket Sleds, AFMDC, HAFB, N. M., MDC-TR-67-12, January 1967.
5. Mixon, L. C., Status of Monorail Sled Design, AFMDC, HAFB, N. M., In-House Report, 1968.
6. Mixon, L. C., Final Report-Sled Design Techniques, AFSWC, HAFB, N. M., AFSWC-TR-71-3, February 1971.
7. Greenbaum, G. A., Garner, T. N., Platus, D. L., Development of Sled Structural Design Procedures, AFSWC, HAFB, N. M., AFSWC-TR-73-22, March 1974.
8. Tischler, V. A., Venkayya, V. B., Palazotte, A. M., Dynamic Analysis of High Speed Rocket Sleds, AFWAL,

W-PAFB, OH., AFWAL-TR-81- , January 1981.

9. Nixon, L. C., Evans, C. B., Gilliam, W. C., Rail Roughness Study of the Holloman High Speed Rocket Sled Test Track, AFSC, EAFB, FL., AD-TR-81-62, September 1981.

10. Thomson, William T., Theory of Vibrations With Applications, Prentice-Hall, Englewood Cliffs, New Jersey, 1972.

11. Meirovitch, Leonard, Analytical Methods in Vibrations, Collier-MacMillan, London, England, 1967.

12. Mixon, L. C., Transmitted Thrust on a Large Dual Rail Rocket Sled, AFSC, EAFB, FL., November, 1983.

13. DASTARR Program Documentation Guide, Holloman Working Paper, 6585th Test Group, HAFB, NM, September, 1984.

14. Henrici, P., Discrete Variable Methods in Ordinary Differential Equations, John Wiley and Sons, New York, NY, 1962.

15. Hildebrand, F. B., Introduction to Numerical Analysis, McGraw-Hill, New York, NY, 1956.

16. SLEDING Users Manual and Documentation Guide, Holloman Working Paper, 6585th Test Group, HAFB, NM, September, 1984.
17. Test Event Report-Ramjet Test Sled, 6585th Test Group, HAFB, NM, February, 1983.
18. Ramjet Qualification Checkout Report, Holloman Working Paper, HAFB, NM, August, 1984.
19. Bendat, J. S., Piersol, A. G., Measurement and Analysis of Random Data, John Wiley and Sons, New York, NY, 1967.
20. Benjamin, J. R., Cornell, C. A., Probability, Statistics, and Decision Making for Civil Engineers, McGraw-Hill, New York, NY, 1970.
21. Strike, W. T. Jr., Lucas, E. T., Evaluation of Wind Tunnel Tests On AFMDC Monorail Cone- and Spike-Nose Sled Configurations at Mach Numbers From 2.0 To 5.0, Von Karman Gas Dynamics Facility, AEDC, Arnold Air Force Station, Tenn., AEDC-TR-68-193, December 1968.
22. Harris, C. M., Crede, C. E., Shock and Vibration Handbook: Volume 1, McGraw-Hill, New York, NY, 1961.

APPENDIX A DERIVATION OF DAMPING COEFFICIENTS

To compute the damping coefficients associated with the flexing of the slipper beams, consider the following figure for bounce conditions.

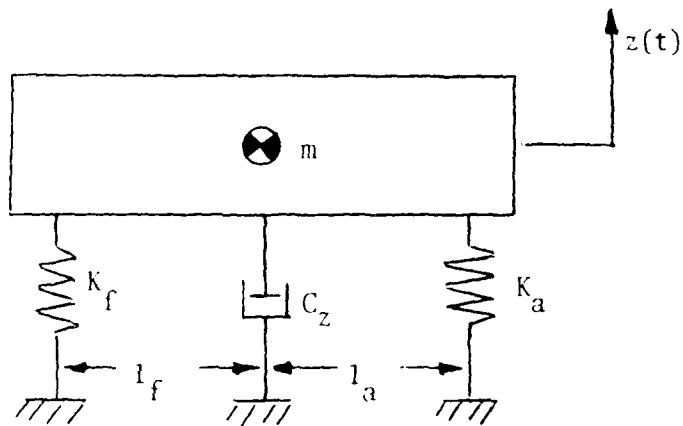


FIGURE A.1 VERTICAL BOUNCE DAMPING COEFFICIENT

By summing forces in the vertical direction, the equation of motion can be derived as

$$m\ddot{z} + K_f z + K_a z + C_z \dot{z} = 0 \quad (A1)$$

where K_f and K_a are the sum of the stiffnesses for the fore and aft slipper assemblies, respectively. Equation

A1 can be rewritten as

$$\ddot{z} + \frac{C_z}{m} \dot{z} + \frac{(K_f + K_a)}{m} z = 0 \quad (A2)$$

From equation A2, the natural frequency is given by

$$\omega_n = \sqrt{\frac{K_f + K_a}{m}} \quad (A3)$$

Since this is the natural frequency for bounce, define

$\omega_b = \omega_n$. Also, from vibration theory, for a damped system

$$\frac{C_z}{m} = 2 \zeta_z \omega_b \quad (A4)$$

where ζ_z is the viscous damping factors in the z direction. Substituting A3 into A4 and rearranging gives

$$C_z = 2 \zeta_z m \sqrt{\frac{(K_f + K_z)}{m}} \quad (A5)$$

or

$$C_z = 2 \zeta_z \sqrt{m(K_f + K_z)} \quad (A6)$$

Thus the damping coefficient at each slipper for bounce is expressed as

$$C_b = \frac{C_z}{4} = \frac{\zeta_z}{2} \sqrt{m(K_f + K_a)}$$

For pitch damping consider the following spring-mass-damper system where C_p represents the rotary damper for pitch. By inspection of the figure it is seen that under rotary effects one spring extends and the other spring contracts.

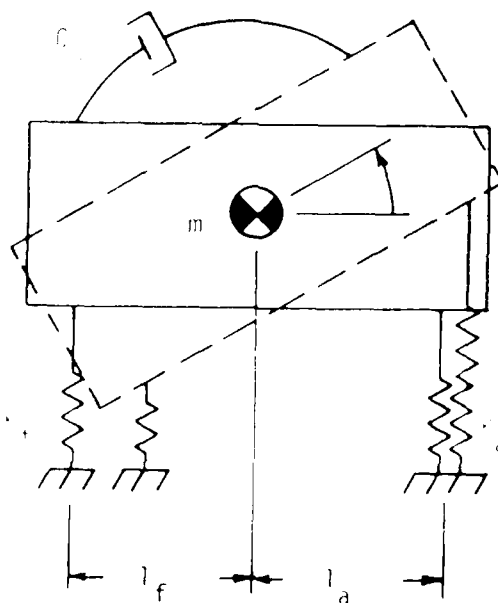


FIGURE A.2 PITCH DAMPING COEFFICIENT

For small values of the spring forces may be written as

$$F_f = l_f \cdot K_f \quad (A3)$$

$$F_d = l_d \cdot K_d$$

The equation of motion can be derived by summing moments about the CG, or

$$I_p \ddot{\theta} + C \dot{\theta} + I_f F_f + I_a F_a = 0 \quad (A9)$$

Substituting equation A8 into A9 and dividing by I_p gives

$$\ddot{\theta} + \frac{C}{I_p} \dot{\theta} + \frac{(I_f^2 K_f + I_a^2 K_a)}{I_p} \theta = 0 \quad (A10)$$

So the natural frequency for pitch, ω_n , is given by

$$\omega_n = \sqrt{\frac{(I_f^2 K_f + I_a^2 K_a)}{I_p}} \quad (A11)$$

Also from equation A10

$$\frac{C}{I_p} = 2\zeta\omega_n \quad (A12)$$

where ζ is the rotary viscous damping factor.

Substitution of equation A11 into A12 gives

$$C_p = 2\zeta\omega_n \sqrt{I_p(I_f^2 K_f + I_a^2 K_a)} \quad (A13)$$

So the pitch damping per slipper, C_p , is

$$C_p = \frac{C_p}{2(I_f^2 + I_a^2)} = \frac{\zeta\omega_n}{I_f^2 + I_a^2} \sqrt{I_p(I_f^2 K_f + I_a^2 K_a)} \quad (A14)$$

For roll damping, consider Figure A.2 only acting in the roll plane. So instead of I_f there will be I_l and I_r .

replaces l_a and θ becomes ϕ . For small angular rotations the associated spring forces are given by

$$\begin{aligned} F_l &= l_l K_l \\ F_r &= l_r K_r \end{aligned} \quad (A15)$$

where $K_l = k_1 + k_3$ and $K_r = k_2 + k_4$. By repeating the process shown for pitch damping, the roll damping factor can be derived as

$$C_r = 2\zeta_r \sqrt{l_r(l_l^2 K_l + l_r^2 K_r)} \quad (A16)$$

So the roll damping coefficient for each slipper can be given as

$$C_r = \frac{\zeta_r}{l_l^2 + l_r^2} \sqrt{l_r(l_l^2 K_l + l_r^2 K_r)} \quad (A17)$$

These three damping terms represent the total equivalent damping at a slipper provided the sled is symmetric. In other words,

$$C(i) = C_b + C_r + C_p \quad i = 1, 4 \quad (A18)$$

However, since a sled is not totally symmetric, the damping at a slipper will be assumed to be proportional to the stiffness associated with that slipper compared to the sled. So for any given slipper its damping

coefficient in the vertical direction will be given by

$$C(i) = \frac{4K(i)}{\sum_{i=1}^n K(i)} (C_b + C_p + C_r) \quad (19)$$

To compute the damping coefficients acting in the lateral bounce direction, consider Figure A.3.

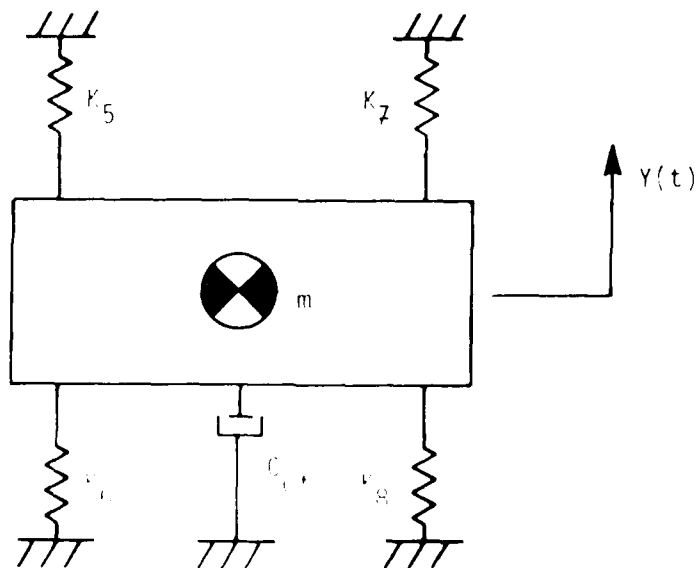


FIGURE A.3 LATERAL BOUNCE DAMPING COEFFICIENT

By summing forces in the horizontal direction, the equation of motion can be found to be

$$m\ddot{y} + C_{ct}\dot{y} + (K_5 + K_6 + K_7 + K_8)y = 0 \quad (A20)$$

Following the procedure for bounce, the equation reduces to

$$C_{ct} = 2F_v \sqrt{m(K_5 + K_6 + K_7 + K_8)} \quad (A21)$$

or the lateral damping per slipper is

$$C_l = \frac{C_{ct}}{4} = \frac{F_v}{2} \sqrt{m(K_5 + K_6 + K_7 + K_8)} \quad (A22)$$

For yaw damping consider Figure A.4. The equation of motion for this system is

$$I_y \ddot{\theta} + C \dot{\theta} + [I_f^2(K_5 + K_6) + I_a^2(K_7 + K_8)]\theta = 0 \quad (A23)$$

which eventually results in an equation for damping of the form

$$C = 2F_v \sqrt{I_y [I_f^2(K_5 + K_6) + I_a^2(K_7 + K_8)]} \quad (A24)$$

This can now be expressed as a damping per slipper component as

$$C_y = \frac{F_v}{I_f^2 + I_a^2} \sqrt{I_y [I_f^2(K_5 + K_6) + I_a^2(K_7 + K_8)]} \quad (A25)$$

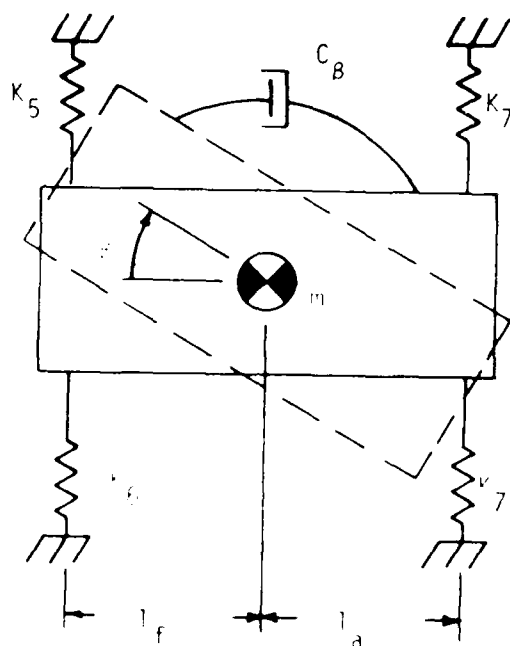


FIGURE A.4 YAW DAMPING COEFFICIENTS

Then the total lateral damping coefficient as a function of slipper stiffness is expressed as

$$C(i) = \frac{4K(i)}{8} (C_l + C_y) \quad (A26)$$

$$i=5$$

The derivation of damping terms up to this point has been based on the spring stiffness being the same in both tension and compression. However, under general sled conditions, spring stiffenesses are dependent on direction of travel. The derivation will still hold as

long as the directional distinction in spring stiffness is considered. Positive directional damping will be assumed to act in the direction of the positive coordinate system and negative directional damping in the opposite sense.

From track experience, it has been found that the recommended value for critical damping, ξ_1 , should be 0.03 or 3%.

APPENDIX B

DERIVATION OF STEADY STATE SLIPPER FORCES--COUPLED SLEDS

B.1 COUPLED SLEDS DEFINITION

Since sleds are coupled in the downtrack condition only (Figure B.1), velocity and acceleration of the sled train are considered to be constant. However, due to the spring between sleds (which represents the downtrack coupling stiffness) the sleds may have relative velocity and accelerations with respect to each other. Therefore, sled one (1) will be defined as the origin of the coordinate system, and to simplify matters it will be given the same downtrack velocity and acceleration as the sled train. Hence, for dynamic rigid body analysis, sled one has no downtrack accelerations, but the other sleds can accelerate relative to sled one. So,

$$\begin{aligned}\dot{V}(1) &= \dot{V}_T = \dot{V} \\ \dot{V}(2) &= \dot{V}(1) + \Delta\dot{V}_{(1-2)} \\ \dot{V}(3) &= \dot{V}(2) + \Delta\dot{V}_{(2-3)} = \dot{V}(1) + \Delta\dot{V}_{(1-2)} + \Delta\dot{V}_{(2-3)}\end{aligned}\tag{B1}$$

Downtrack equilibrium for the train ($\sum F_x = 0$) gives

$$m\dot{V} + D + BR - T = 0\tag{B2}$$


$$\dot{V}_T = \dot{V}(1) = \dot{V}(2) = \dot{V}(3) = \dot{V}$$
$$\dot{V}(2) = \dot{V}(1) + \Delta \dot{V}_{1-2} = \dot{V} + \Delta \dot{V}_1$$

$$\dot{V}(3) = \dot{V}(2) + \Delta \dot{V}_{2-3} = \dot{V} + \Delta \dot{V}_1 + \Delta \dot{V}_2$$

$$\sum_{\uparrow} F_{\uparrow}^x = 0$$

$$D_T + M_T \dot{V}_T + BR_T - T_T = 0$$

$$\text{or } \dot{V}_T = (T_T - D_T - BR_T)/M_T$$

but $D_T = D(1) + D(2) + D(3)$

Figure B.1 COUPLED SLED SCHEMATIC

or

$$\dot{V} = (T - D - BR)/m \quad (B3)$$

where D is the total train drag, or the sum of each individual sled's drag (D(i)). So D(i) may be expressed as a percentage of D based on the ratios of the $C_d A$ values for each sled to the total train $C_d A$. Let

$$PD(i) = (C_d A)_i / (C_d A)_T \quad i=1,2,\dots,n \quad (B4)$$

so

$$D(i) = PD(i) \times D \quad i=1,2,\dots,n \quad (B5)$$

Before an analysis of each sled as a freebody can be done, the transmitted thrust vector must be derived. This is the residual of the thrust that makes it to sled one. Summing downtrack forces about a sled gives (See Figure B.2)

$$D(i) + TT(i,2) + BR(i) - T(i) + m(i)\dot{V}(i) - T1(i,1) = 0 \quad (B6)$$

so

$$TT(i,2) = T(i) - m(i)\dot{V}(i) + TT(i,1) - D(i) - BR(i) \quad (B7)$$

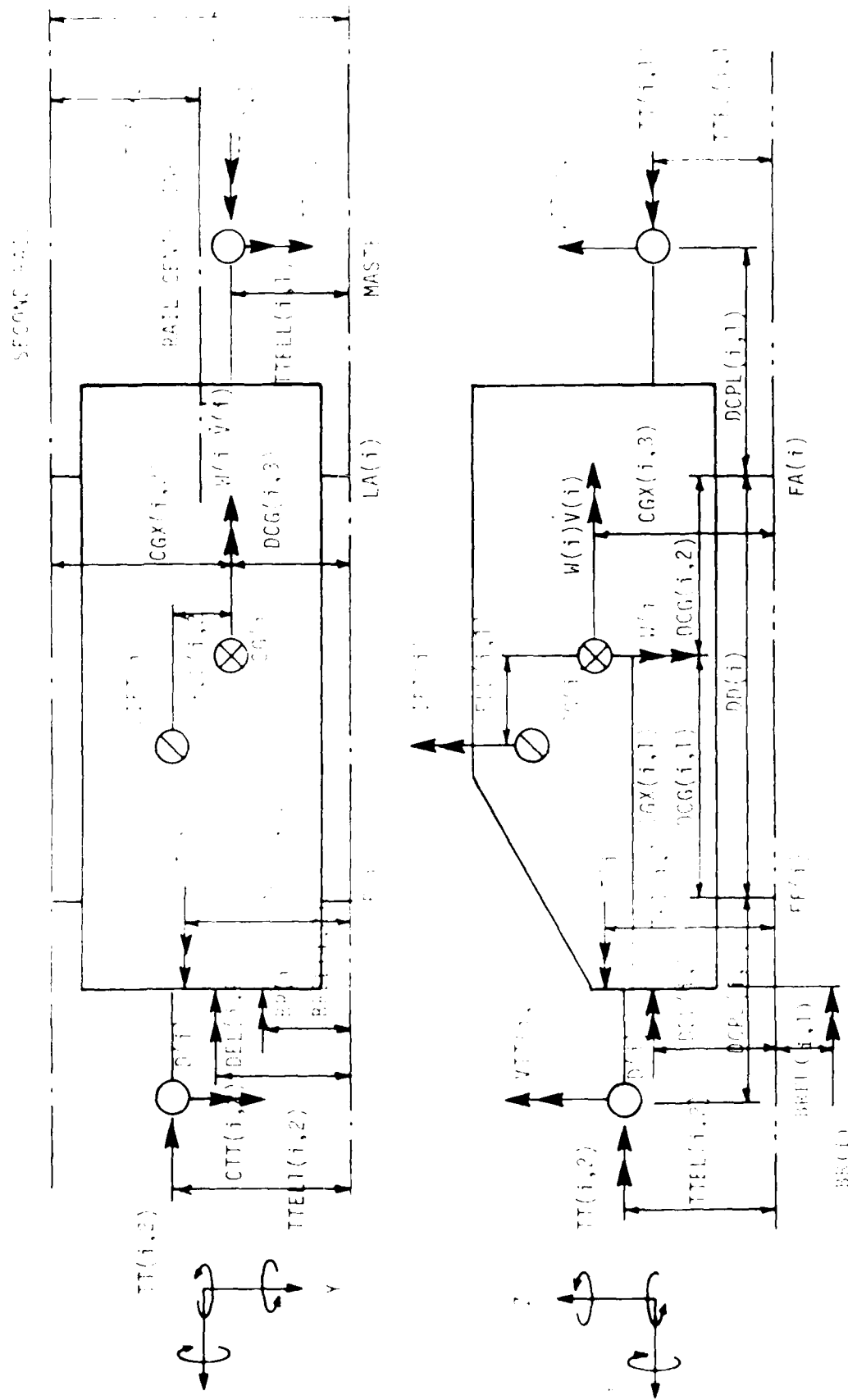


Figure B.2 FREEBODY OF SLID

However, if the coupling is assumed to be massless, the inertial force terms associated with the coupling may be ignored. Therefore the transmitted thrust on the front of one sled is equal in magnitude to the transmitted thrust on the aft of the sled in front of it, or

$$|TT(i,1)| = |TT(i-1,2)| \quad (B8)$$

so

$$TT(i,2) = T(i) + m(i)\dot{V}(i) - TT(i-1,2) - D(i) - BR(i) \quad (B9)$$

For the first sled in the train, the transmitted thrust term on the aft beam will be zero, or

$$|TT(1,1)| = |TT(0,2)| = 0 \quad (B10)$$

B.2 STEADY-STATE SLIPPER FORCES

Now that all forces acting on a sled are known, the slipper reactions can be solved for. Again examining Figure B.2 for sled i and summing moments about the front slipper beam gives

$$\begin{aligned}
\sum M_{SV(i,1)} &= 0 = BR(i)BREL(i) - D(i)DEL(i,1) \\
&- TT(i,2)TTEL(i,2) + T(i)TEL(i,1) + LIFT(i)(DCG(i,1) \\
&- ELL(i,1)) \\
&W(i)DCG(i,1) - W(i)\dot{V}(i)CGX(i,3) \\
&+ TT(i,1)TTEL(i,1) + DD(i)SV(i,2) - VTT(i,2)DCPL(i,2) \\
&+ VTT(i,1)(DCPL(i,1) + DD(i)) \quad (B11)
\end{aligned}$$

so upon rearranging terms to solve for $SV_{(i,2)}$

$$\begin{aligned}
SV(i,2) &= \frac{1}{DD(i)} \left\{ TT(i,2)TTEL(i,2) + D(i)DEL(i,1) \right. \\
&- BR(i)BREL(i) - T(i)TEL(i,1) - TT(i,1)TTEL(i,1) \\
&- LIFT(i)(DCG(i,1) - ELL(i,1)) \\
&+ W(i)(DCG(i,1) + \dot{V}(i)CGX(i,3)) + VTT(i,2)DCPL(i,2) \\
&\left. - VTT(i,1)(DCPL(i,1) + DD(i)) \right\} \quad (B12)
\end{aligned}$$

by summing forces vertically, $\uparrow F_v = 0$.

$$SV(i,1) = W(i) - LIFT(i) - SV(i,2) - VTT(i,1) - VTT(i,2) \quad (B13)$$

These are the resultant slipper beam reactions. They must be correlated to a slipper force. This is done as follows (reference Figure B.5):

$$\begin{aligned}
\sum M_{FRV(i,1)} &= 0 \\
DCX(i,2)SV(i,1) + DC(i)FRV(i,1) &= 0 \quad (B14)
\end{aligned}$$

or

$$\text{FRV}(i, j) = \frac{\text{CGX}(i, 2)}{\text{DCT}(i)} \quad \text{SV}(i, j) \quad (\text{B15})$$

and similarly

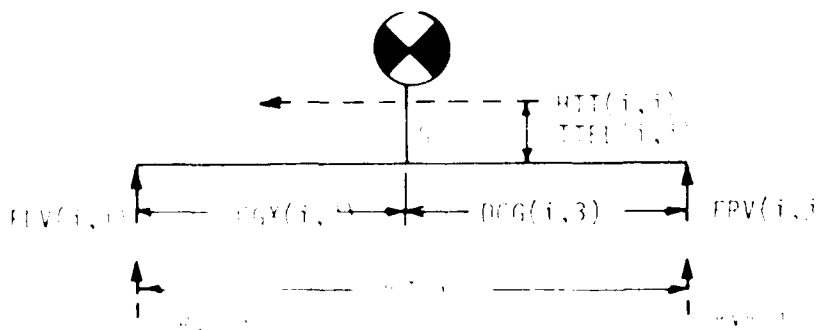
$$\text{FLV}(i, j) = \frac{\text{DCG}(i, 3)}{\text{DCT}(i)} \quad \text{SV}(i, j) \quad (\text{B16})$$

It should be noted that the horizontal cross-track components of the transmitted thrust vector will induce vertical slipper loads due to being above rail top. Examining Figure B.3 for the dotted lines, or the HTT force, the vertical reactions can be found by summing moments about the left slipper, or

$$DCT(i)SRVL(i)+HTT(i,1)TTEL(i,1)+HTT(i,2)TTEL(i,2)=0 \quad (B17)$$

or upon rearranging and solving for $SRVL(i)$

$$\text{SRVL}(i) = \frac{-1}{\text{DCL}(i)} \left\{ \text{HTT}(i,1)\text{TTEL}(i,1) + \text{HTT}(i,2)\text{TTEL}(i,2) \right\} \quad (\text{B18})$$



1. *Phragmites australis* (Cav.) Trin. ex Steud. (Common reed)

Summing forces vertically for the HTT force gives

$$SFVR(1) = -SFVL(1) \quad (B19)$$

However, each reaction just given is the sum of the front and aft slippers on that side of the sled. These forces must be weighted so as to distribute them between the front and rear slippers. Examining Figure B.2 we can define

$$DCP(1) = DCPL(1,1) + DCPL(1,2) + DD(1) \quad (B20)$$

Summing moments about the front slipper for the HTT forces will allow for a front-rear weighting ratio given as

$$FR(1) = \frac{1}{DCP(1)} \left\{ DCPL(1,1)HTT(1,2) + (DCP(1) - DCPL(1,2)) \cdot HTT(1,1) \right\} \quad (B21)$$

and

$$FA(1) = FR(1) - HTT(1,1) \quad (B22)$$

Thus we have

$$\begin{aligned} VL(1,1) &= SFVL(1) \times FR(1) \\ VL(1,2) &= SFVL(1) \times FA(1) \\ SVL(1,3) &= SFVL(1) \times FA(1) \\ SVL(1,4) &= SFVR(1) \times FA(1) \end{aligned} \quad (B23)$$

Since the thrust, drag, and downtrack acceleration line of actions may not lie on the centerline of the rail spacing, there is the possibility of lateral forces acting on the sled. Looking at a top view of the sled, Figure B.2, and summing moments about point A, $(\sum M_A = 0)$, gives

$$\begin{aligned}
 0 = & TT(1,2)(TTEL(1,2) - \frac{DCT(1)}{2}) + DD(1)SL(1,2) \\
 & + D(1)(DEL(1,2) - \frac{DCT(1)}{2}) + T(1)(TEL(1,2) - \frac{DCT(1)}{2}) \\
 & + W(1)\dot{V}(1)(CGX(1,2) - \frac{DCT(1)}{2}) + HTT(1,2)DCPL(1,2) \\
 & + TT(1,1)(TEL(1,1) - \frac{DCT(1)}{2}) + HTT(1,1)(DD(1) + DCPL(1,1)) \\
 & + BR(1)(BREL(1,2) - \frac{DCT(1)}{2}) \quad (B24)
 \end{aligned}$$

or rearranging terms and solving for $SL(1,2)$ gives

$$\begin{aligned}
 SL(1,2) = & \frac{1}{DD(1)} \left\{ TT(1,2)(TTEL(1,2) - \frac{DCT(1)}{2}) \right. \\
 & + D(1)(DEL(1,2) - \frac{DCT(1)}{2}) + T(1)(TEL(1,2) - \frac{DCT(1)}{2}) \\
 & + W(1)\dot{V}(1)(CGX(1,2) - \frac{DCT(1)}{2}) \\
 & + HTT(1,2)DCPL(1,2) + HTT(1,1)(DD(1) + DCPL(1,1)) \\
 & \left. + BR(1)(BREL(1,2) - \frac{DCT(1)}{2}) \right\} \quad (B25)
 \end{aligned}$$

Summing forces laterally, $\sum F_1 = 0$, gives

$$SL(i,1) = -SL(i,2) - HTT(i,1) - HTT(i,2) \quad (B26)$$

Again, $SL(i,1)$ and $SL(i,2)$ represent two slippers. There is no easy way to separate these into the two individual components. So it will be assumed that each component will receive one half of the lateral load.

Therefore for sled one, using program nomenclature for steady-state forces, SSF becomes:

$$\begin{aligned} SSF(1,1) &= SV(i,1) \times DCG(i,3)/DCT(i) + SVL(i,1) \\ SSF(2,1) &= SV(i,1) \times CGX(i,2)/DCT(i) + SVL(i,2) \\ SSF(3,1) &= SV(i,2) \times DCG(i,3)/DCT(i) + SVL(i,3) \\ SSF(4,1) &= SV(i,2) \times CGX(i,2)/DCT(i) + SVL(i,4) \\ SSF(5,1) &= SL(i,1)/2 \\ SSF(6,1) &= SL(i,1)/2 \\ SSF(7,1) &= SL(i,2)/2 \\ SSF(8,1) &= SL(i,2)/2 \end{aligned} \quad (B27)$$

B.1 COUPLING FORCE DERIVATION

All that now remains is to define the components of the coupling force that are acting on the sleds. By examining Figure B.1, it is seen that a term ELCPL is included. This represents an extra link needed to define the monoball type coupling. If the coupling type is a column (a universal joint) or a push pad, ELCPL becomes zero.

B.3.1 MONOBALL COUPLING

B.3.1.1 SLIPPER GAP GEOMETRY

By examining Figure B.4 it can be seen that the potential motion is a combination of slider translation and rotation, as a rigid body, through the gap until slipper-rail contact is made. As can be seen, the maximum vertical displacement obtainable by a slider is $ZF(i) + ZA(i)$, where i represents a counter for sliders (i =pusher sled, 2 =forebody sled). When divided by the length between slippers the maximum angle is described, or

$$\theta(i,v) = \sin^{-1} \left(\frac{ZF(i) + ZA(i)}{DD(i)} \right) \quad (B28)$$

By similar reasoning the maximum lateral rotation of the sled may be given as

$$\theta(i,l) = \sin^{-1} \left(\frac{LF(i) + LA(i)}{DD(i)} \right) \quad (B29)$$

Assuming no rigid body translation, the displacement of the coupling connection will be take length times the sine of the enclosed angle. However, the length now becomes the sum of the length between slipper beams plus

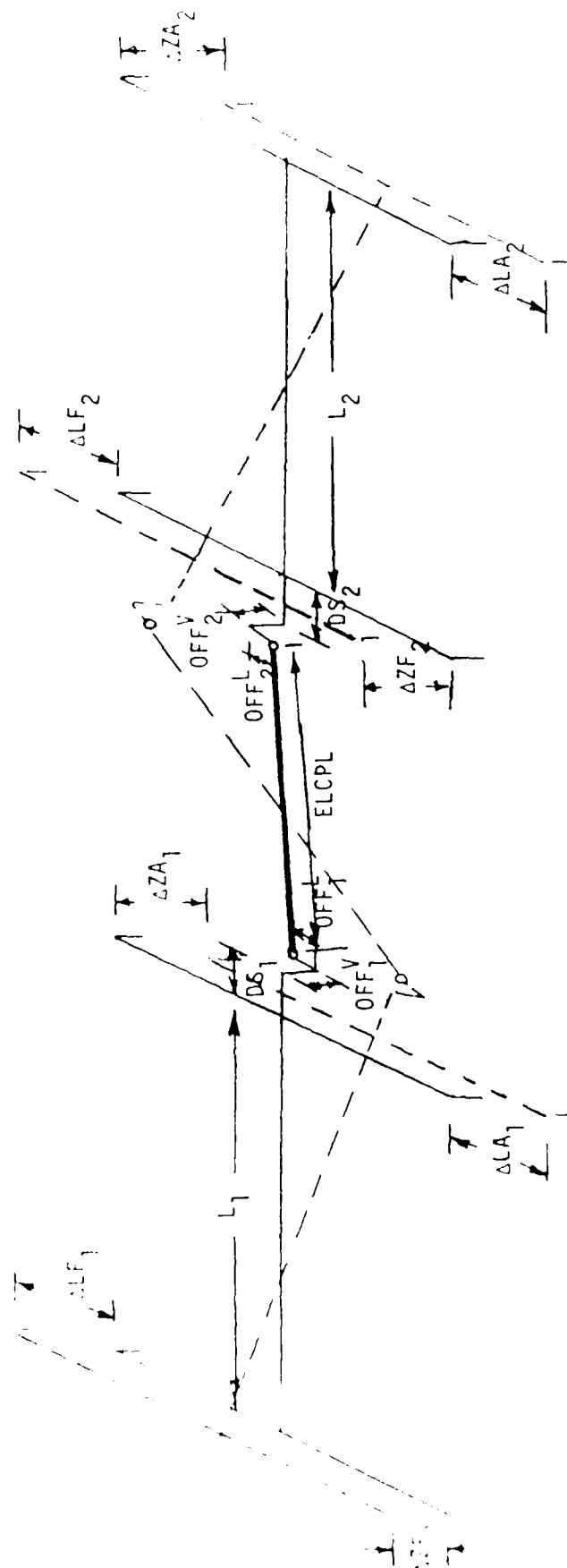


Figure B.4 TYPICAL COUPLED SLED GEOMETRY

the length from the nearest slipper beam to the coupling,
or

$$\Delta(i,j) = \frac{(DD(i) + DCPL(i,k))}{2} \sin(\theta(i,j)) \quad (B30)$$

where i =sled, j =lateral or vertical direction, and
 k =front of aft slipper beam distance.

Now that the relative displacements of each end of
the coupling column have been established, it is possible
to find the angle described by these displacements. The
relative end displacements may be given as

$$\Delta(c,j) = \Delta(i,j) - \Delta(i+1,j) \quad (B31)$$

Division of the relative displacements by the
coupling length then describes the enclosed coupling
angle, or

$$\theta(c,j) = \sin^{-1} \left(\frac{\Delta(c,j)}{ELCPL(i)} \right) \quad (B32)$$

B.3.1.2 MONOBALL FORCE ANALYSIS

Now that all geometric angles of the sled in free
flight have been defined, it still remains to be shown
how they affect the thrust that is transmittable to the

coupling. Examining Figure B.5 it can be seen that the thrust vector from the rear of the sled may be resolved into a vector that is solely in the downtrack direction (X-axis only), and a vector tangent to the X-axis. So we have

$$T1_x = T1/(\cos(\angle(1,L))\cos(\angle(1,V))) \quad (B33)$$

Similarly,

$$\begin{aligned} T1_t &= \sqrt{(T1_y)^2 + (T1_z)^2} \\ &= \sqrt{T1^2 \tan^2(\angle(1,v)) + \frac{T1^2 \sin^2(\angle(1,L))}{\cos^2(\angle(1,v))}} \\ &= \frac{T1}{\cos(\angle(1,v))} \sqrt{\sin^2(\angle(1,v)) + \sin^2(\angle(1,L))} \end{aligned} \quad (B34)$$

In order to put the dynamic system into equilibrium, we will have to resolve the actual transmitted thrust available to input into sled one. This is accomplished by reducing the total system thrust by the inertial and drag forces experienced by the coupling and the rear pusher sled. Typically these components on the sled train are insignificant compared to the thrust magnitude, therefore these parameters will be ignored (as mentioned in Section B.1). In other words, all thrust available at any given time from the pusher sled is directly

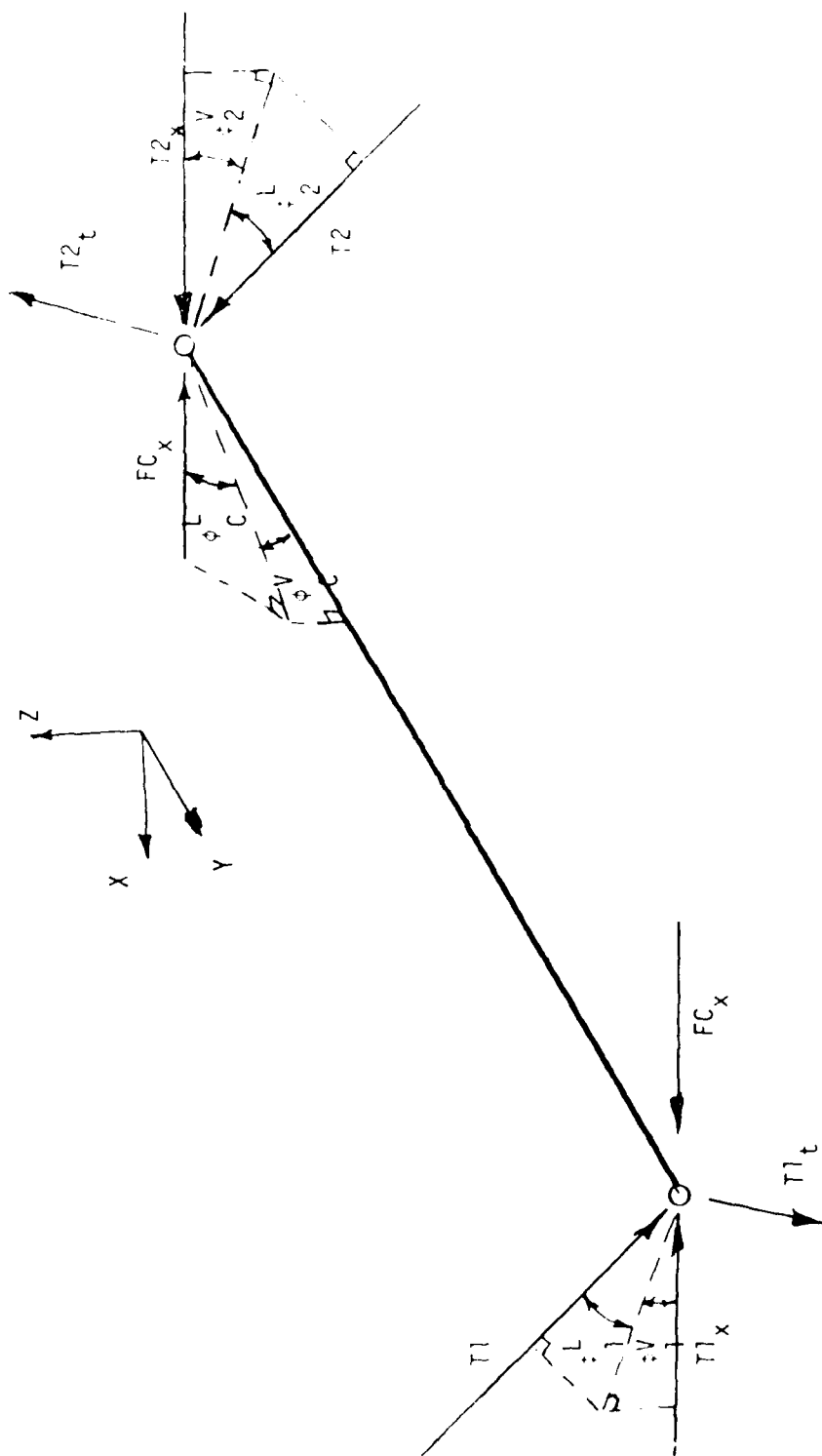


Figure B.5 TYPICAL COUPLED SLED FORCE GEOMETRY

transmitted through the coupling into the forebody sled. This means that the coupling must transmit $T1_t$ and $T1_x$ into the next sled through the angles described by the slipper gap analysis. These forces can then be resolved into an axial coupling force and a tangential force. So

$$FC_x = FC / (\cos(\angle(c,V)) \cos(\angle(c,L))) \quad (B35)$$

$$FC_y = FC \times \sin(\angle(c,L)) / \cos(\angle(c,V)) \quad (B36)$$

$$FC_z = FC \times \tan(\angle(c,V)) \quad (B37)$$

For equilibrium to hold FC_x must react $T1_x$, or

$$FC = T1_x \times \cos(\angle(c,V)) \cos(\angle(c,L)) \quad (B38)$$

or

$$FC = FC_A = T1 (\cos(\angle(c,V)) \cos(\angle(c,L))) / (\cos(\angle(1,V)) \cos(\angle(1,L))) \quad (B39)$$

Similarly

$$FC_t = \sqrt{(FC_y)^2 + (FC_z)^2} \quad (B40)$$

$$= \frac{FC}{\cos(\angle(c,v))} \sqrt{\sin^2(\angle(c,l)) + \sin^2(\angle(c,v))}$$

And this must react $T1_t$ for equilibrium.

Following this logic for the forebody sled, the thrust vector applied to it can be found to be

$$\begin{aligned} T2_x &= FC_x \\ &= T1/(\cos(\angle(1,V))\cos(\angle(1,L))) \end{aligned} \quad (B41)$$

Hence

$$\begin{aligned} T2 &= T2_x \times \cos(\angle(2,L))\cos(\angle(2,V)) \\ &= T1(\cos(\angle(2,L))\cos(\angle(2,V)))/(\cos(\angle(1,L))\cos(\angle(1,V))) \end{aligned} \quad (B42)$$

B.3.1 COLEMAN COUPLING AND PUSH PAD ANALYSIS

By examining Figure B.4, a Coleman Coupling or Push Pad, can be envisioned by letting the coupling length (ELCPL) be zero. By following the same derivation as for the Monoball Coupling, the Coleman Coupling or the Push Pad can be found. Since the coupling length is zero, it cannot be divided into the relative coupling displacement (equation B32), and this forces the defined coupling angles to be zero.

B.4 COUPLING DISPLACEMENT TERMS

In Section B.3.1.1, coupling displacement terms were used to derive the sled geometry for defining coupling forces. These coupling displacements are found by solving Newton's Second Law ($F = ma$) on the sled for the rigid body acceleration terms. The acceleration is then integrated into a velocity term and once again into displacements. This displacement term is then what is used for the coupling geometry analysis. It remains to define the interrelation of the sled's position on solving for this coupling displacement.

B.4.1 MONOBALL COUPLING

For the monoball coupling, the jawbone link of the coupling allows for independent motion of either sled about the link. Therefore, each sled can be solved independently of each other.

B.4.2 COLEMAN COUPLING

Due to the nature of Coleman Couplings, each joint is required to displace an amount equal to its mating point on the adjacent sled. Since the lateral and vertical coupling forces were included in the analysis to

solve for the acceleration terms, the displacements of the joints will be identical. Therefore, each sled of this type of coupling can be solved independently of each other.

B.4.3 PUSH PAD

Since this coupling type allows for relative motion with respect to each other (through slippage across the push pad surfaces), the integration of the acceleration terms can be done independently of sled interaction. However, the tangential direction coupling forces may have to be modified on the forebody sleds, if slippage occurs. Slippage will occur when the tangential coupling force exceeds the static frictional resistance force. This static frictional force is given by

$$FS(i,j) = TT(i,j) \times \mu(i) \quad (B43)$$

where μ is the coefficient of static friction for the mated materials of the push pads. Typically for steel-on-steel contact this is 0.3.

When slippage does occur, the tangential forces transmitted forward will be equal to the static frictional force, and the equations of motion should be solved around this.

APPENDIX C
FORCE-TIME SIMULATION PLOTS

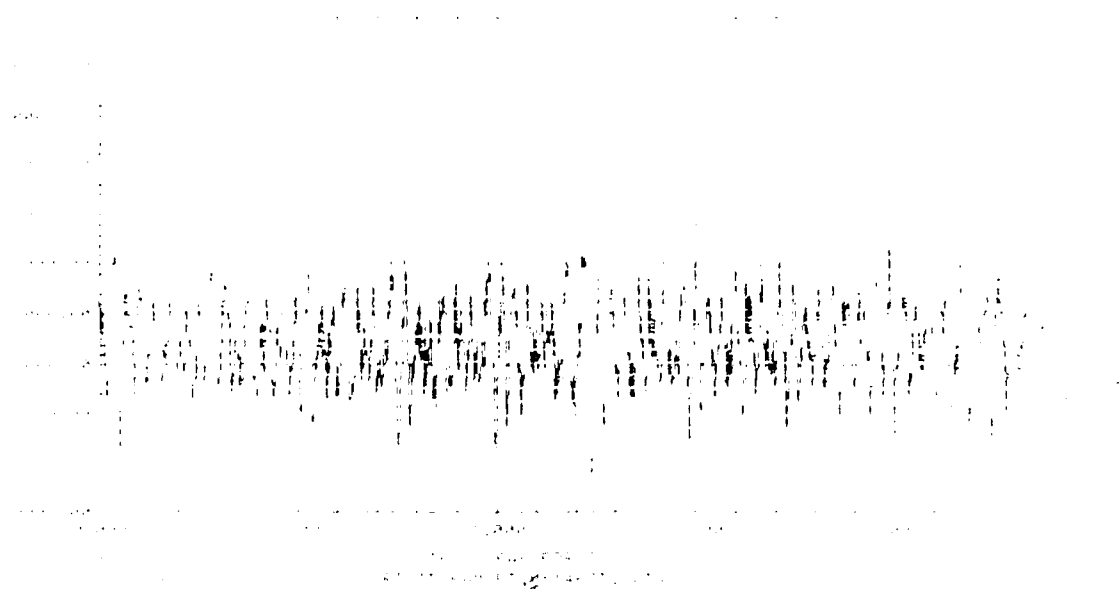


Figure C.1 Rigid Body Dual Plot, S15000 Top

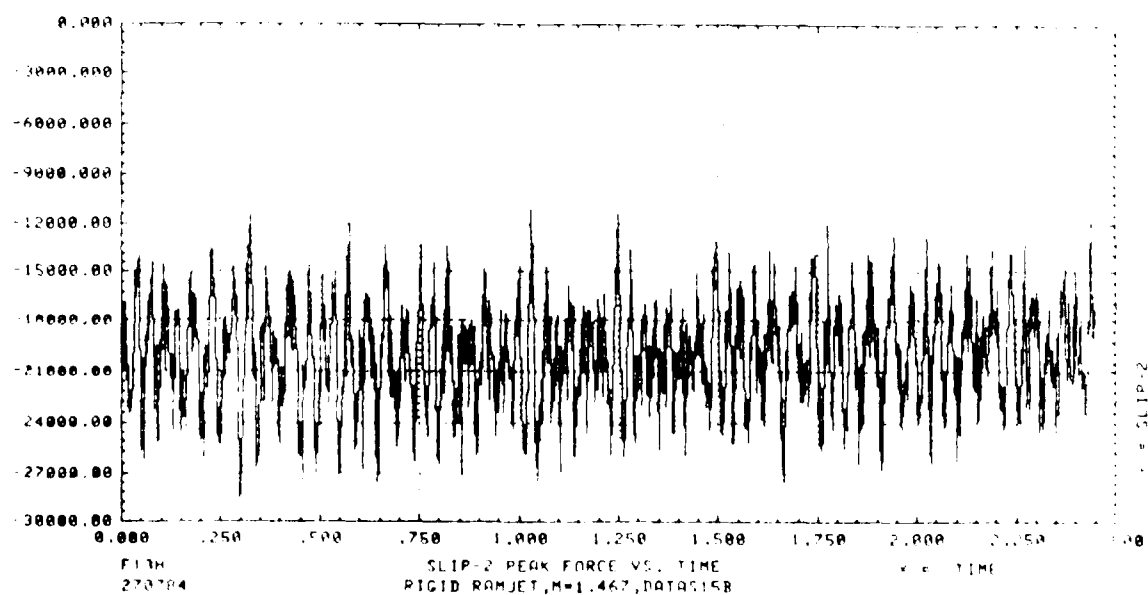


Figure C.2 Rigid Body Dual Plot, S15000 Bottom

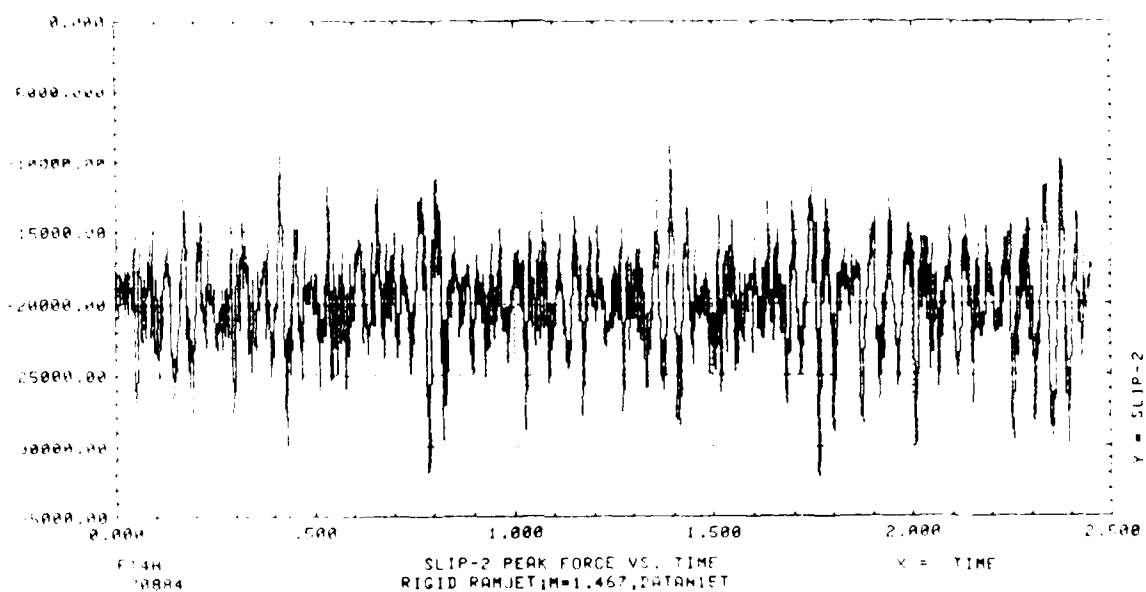


Figure C.3 Rigid Body Dual Rail, N15000 Top

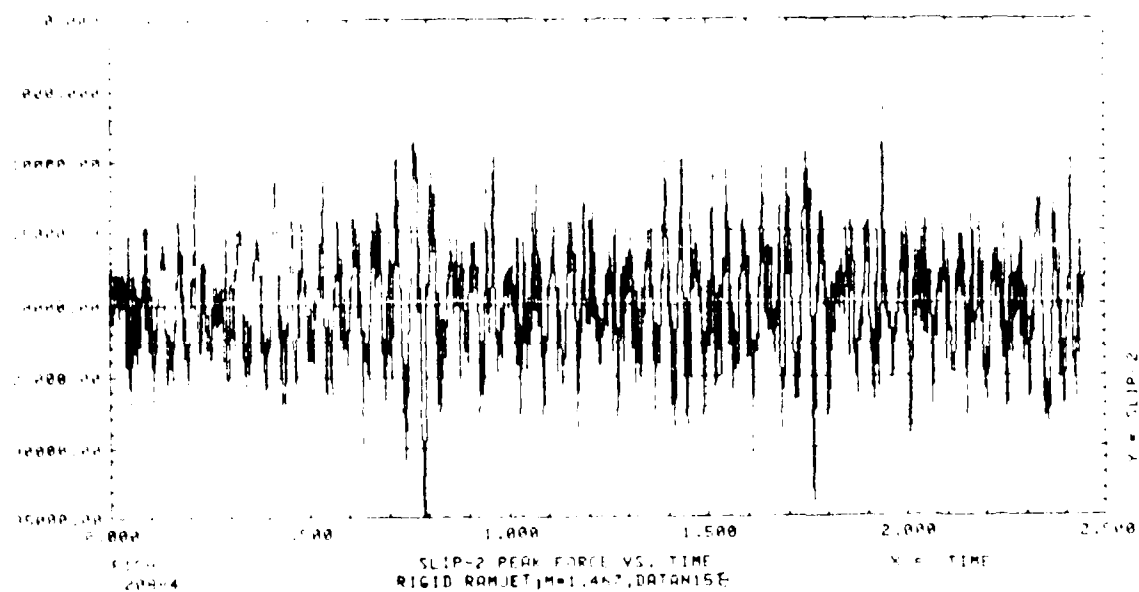


Figure C.4 Rigid Body Dual Rail, N15000 Bottom

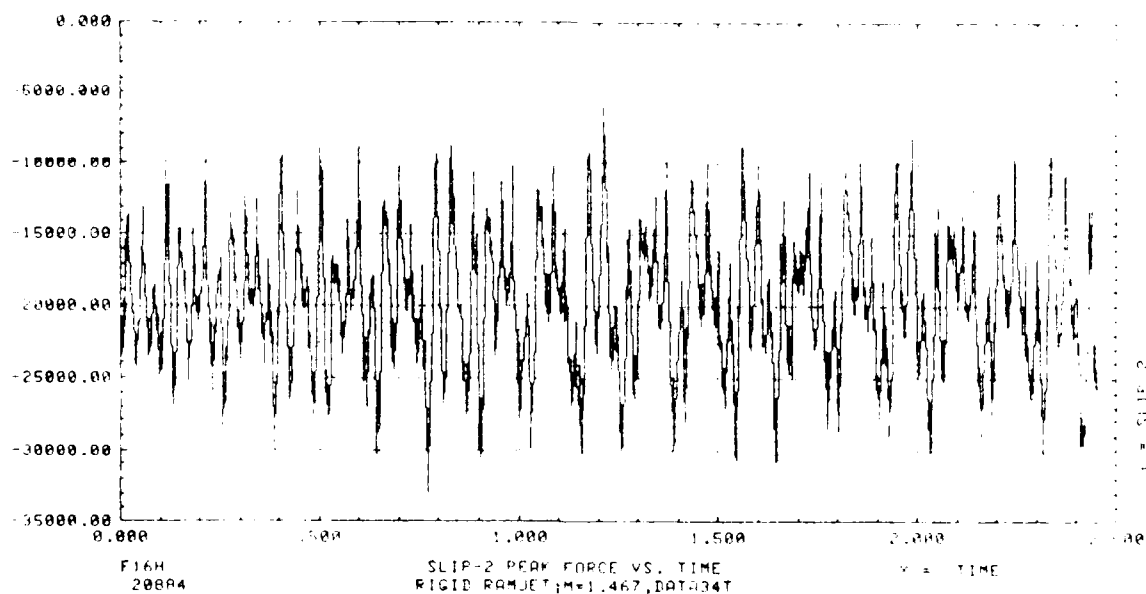


Figure C.5 Rigid Body Dual Path, 34000 Top

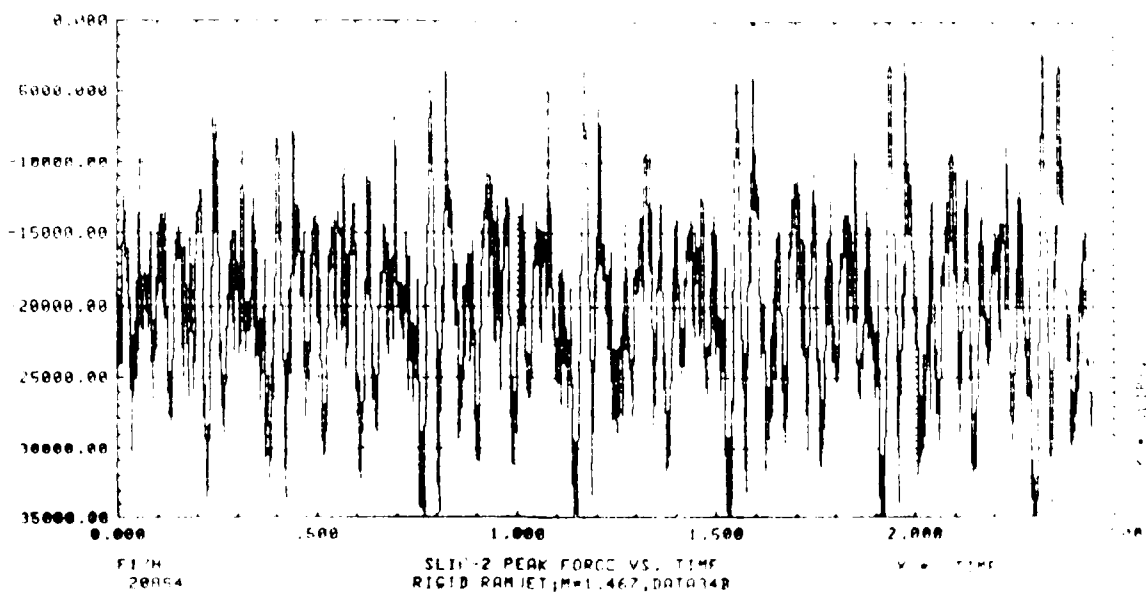
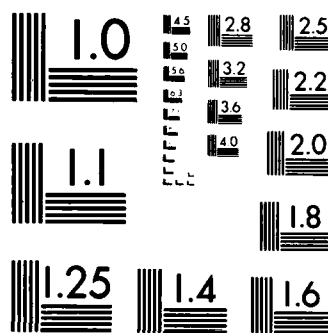


Figure C.6 Rigid Body Dual Path, 34000 Bottom

DYNAMIC ANALYSIS OF A SLED TRAVELING ALONG A ROUGH RAIL 4/4
(U) ARMAMENT DIV (AFSC) EGLIN AFB FL G L FERGUSON
15 MAY 85 AD-TR-85-39

F/G 12/1 NL

[illegible]



MICROCOPY RESOLUTION TEST CHART
NATIONAL BUREAU OF STANDARDS 1963-A

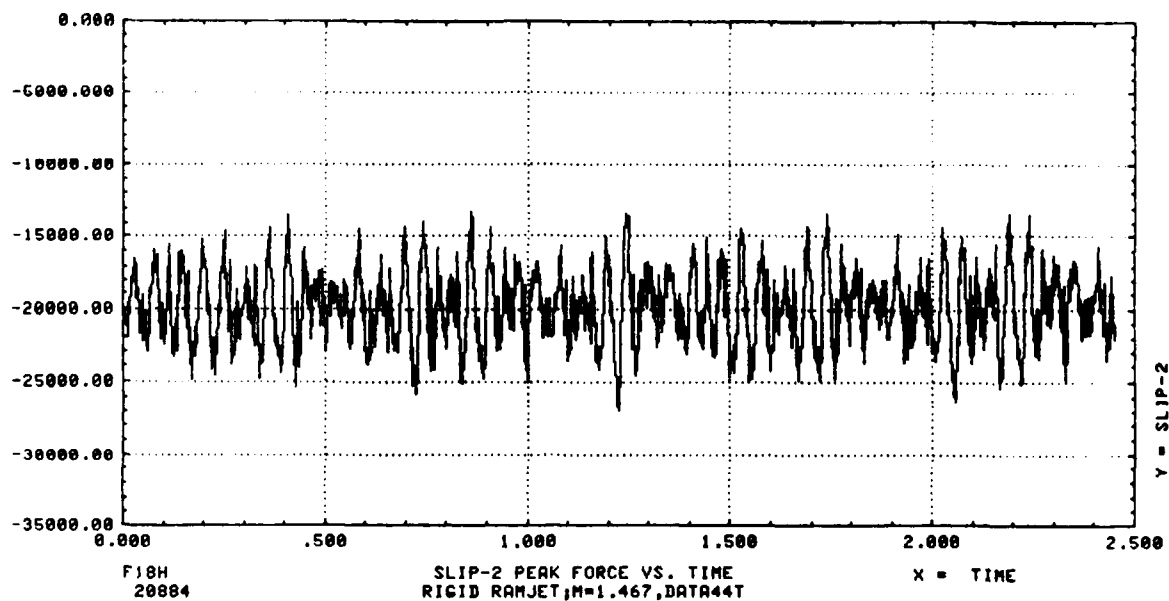


Figure C.7 Rigid Body Dual Rail, 44000 Top

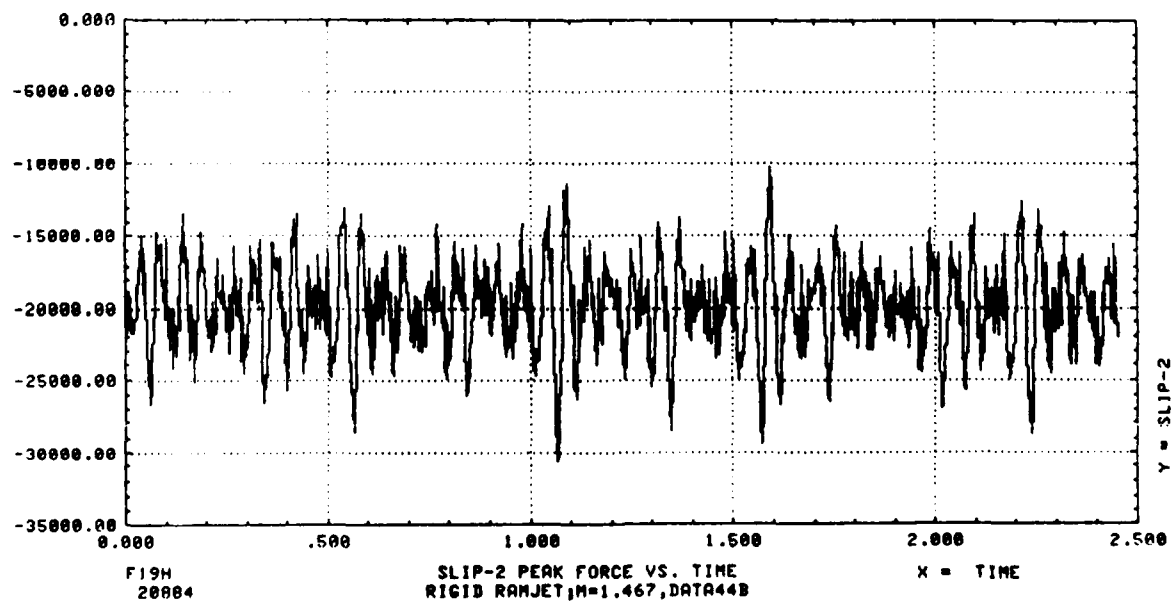


Figure C.8 Rigid Body Dual Rail, 44000 Bottom

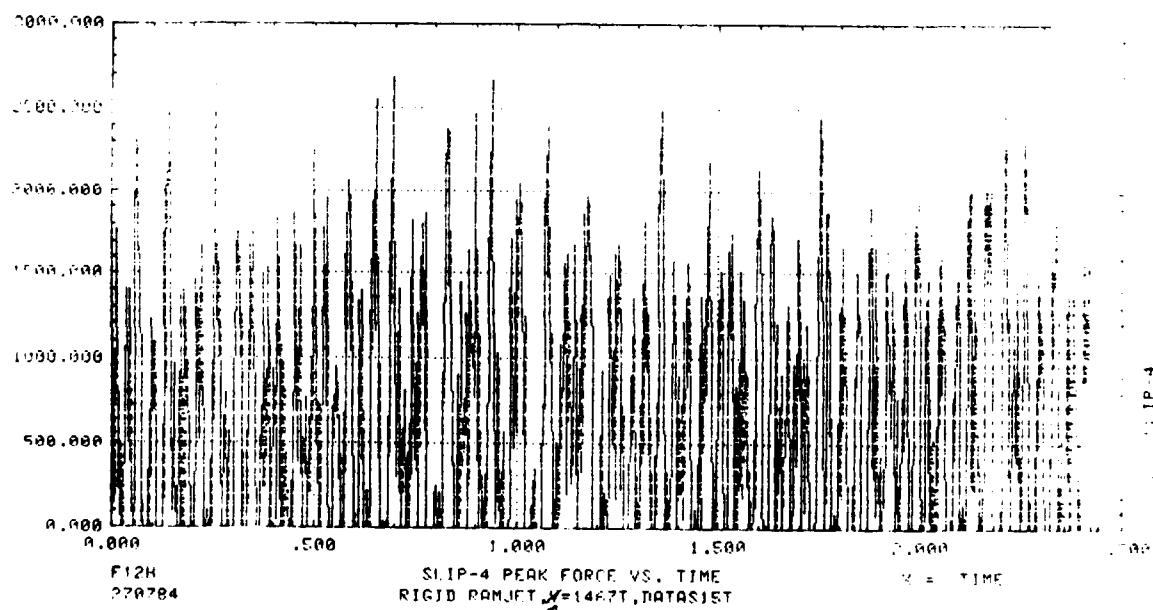


Figure C.9 Rigid Body Dual Rail, S15000 Top

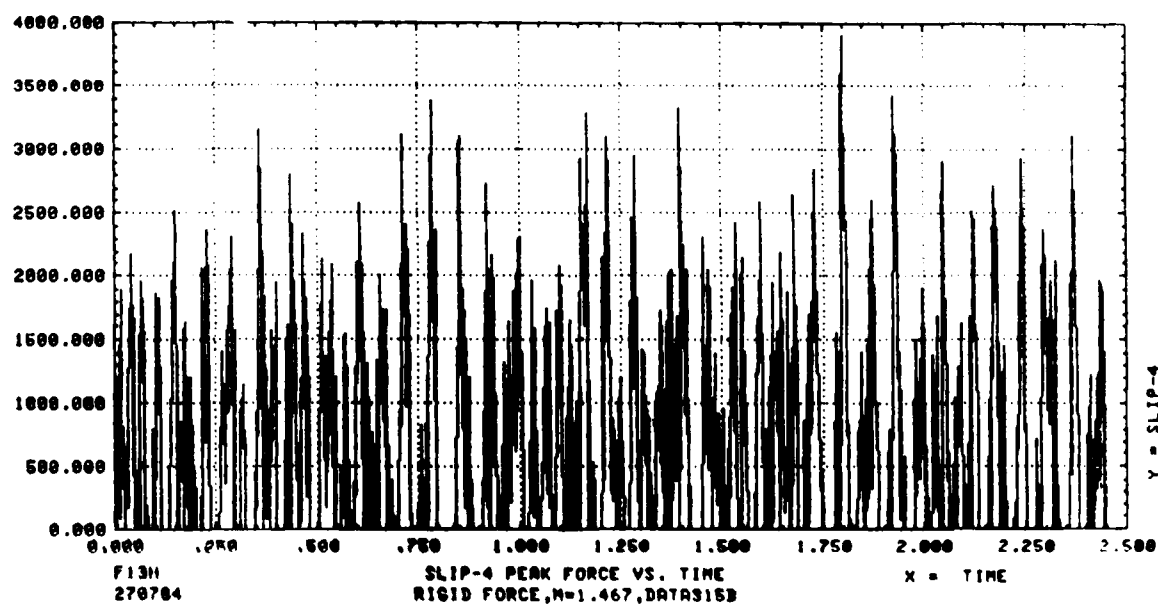


Figure C.10 Rigid Body Dual Rail, S15000 Bottom

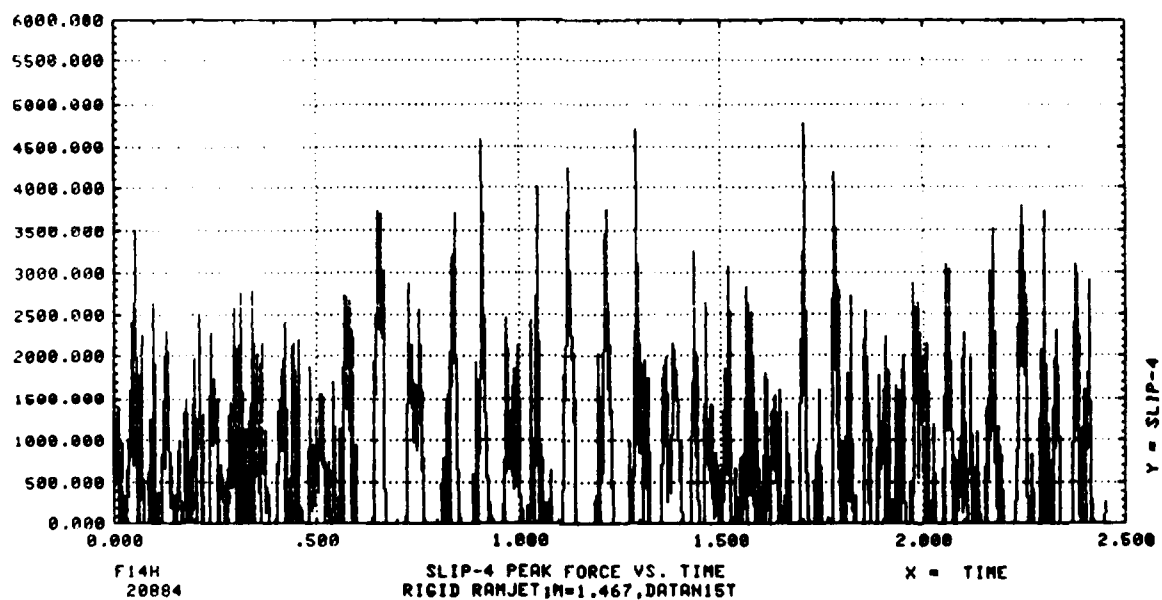


Figure C.11 Rigid Body Dual Rail, N15000 Top

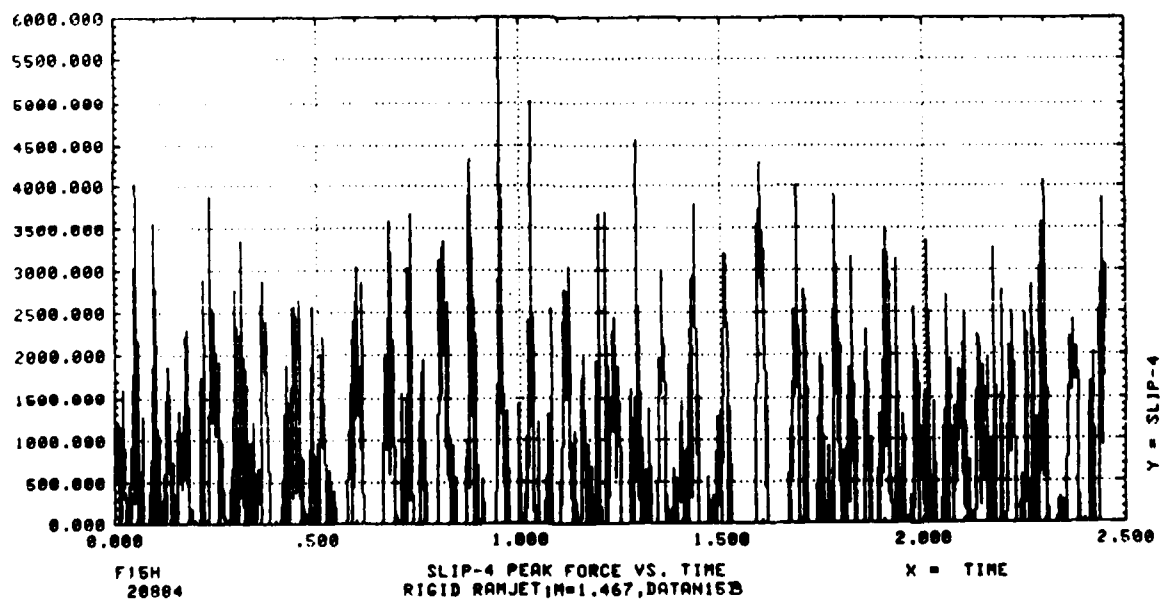


Figure C.12 Rigid Body Dual Rail, N15000 Bottom

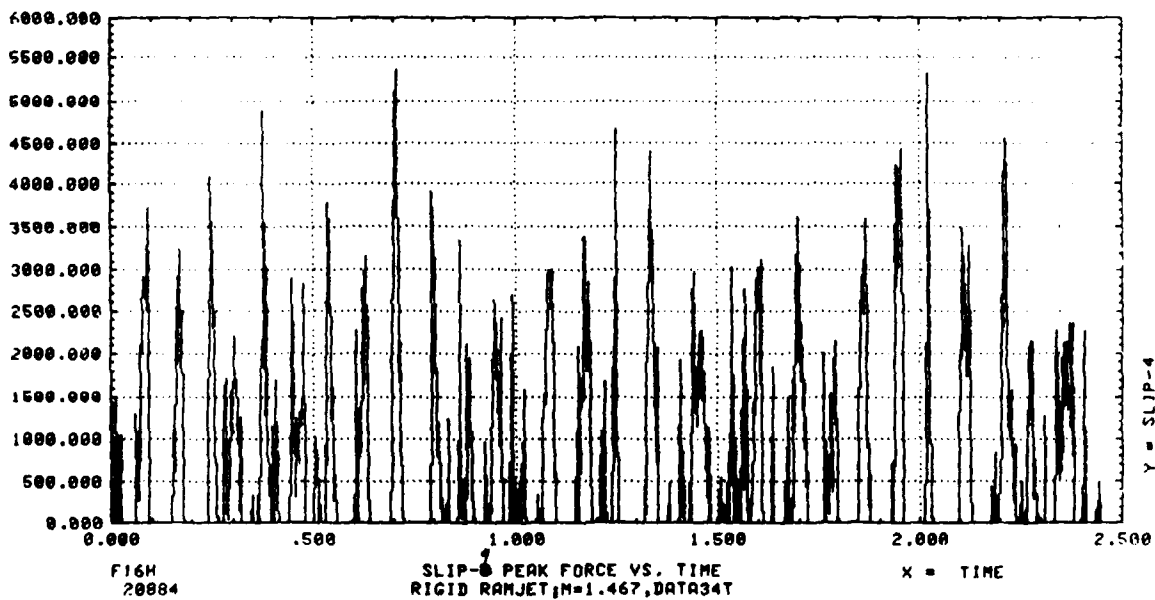


Figure C.13 Rigid Body Dual Rail, 34000 Top

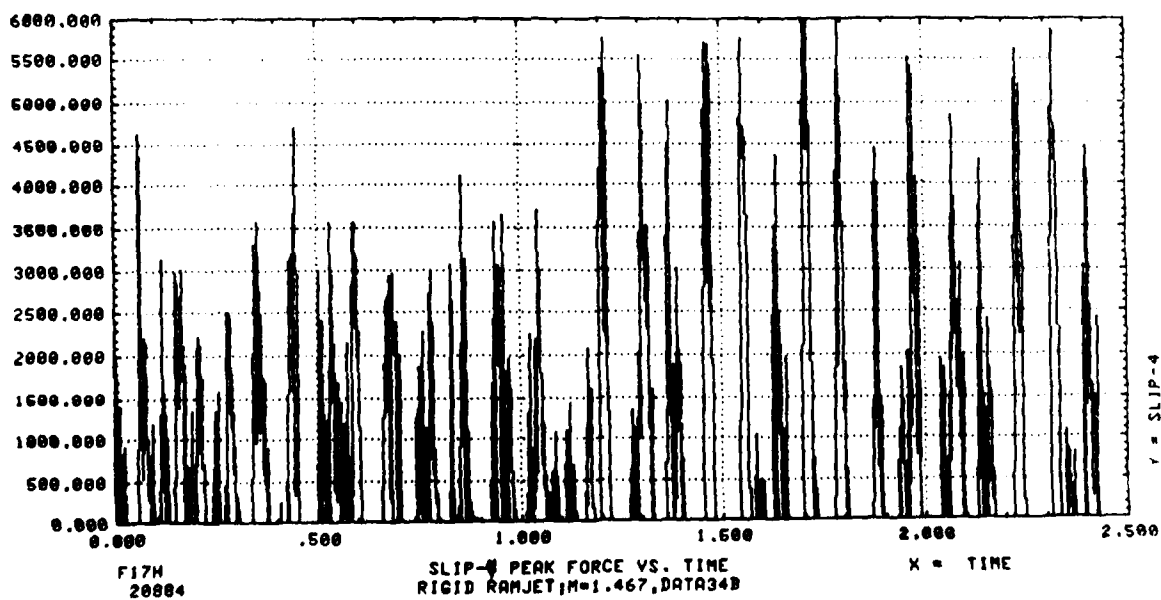


Figure C.14 Rigid Body Dual Rail, 34000 Bottom

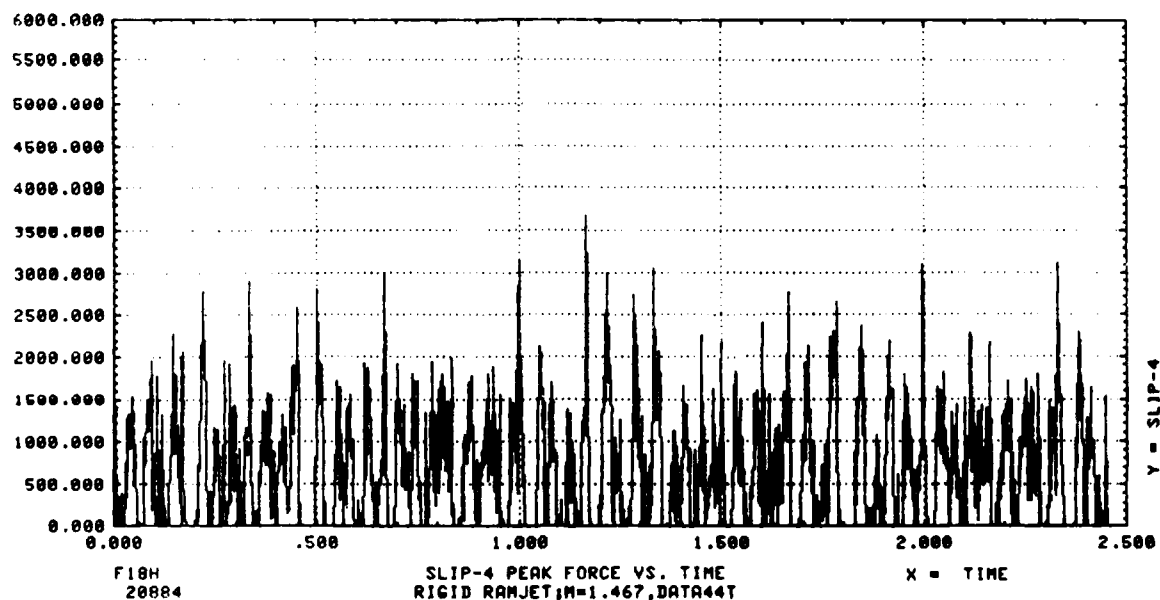


Figure C.15 Rigid Body Dual Rail, 44000 Top

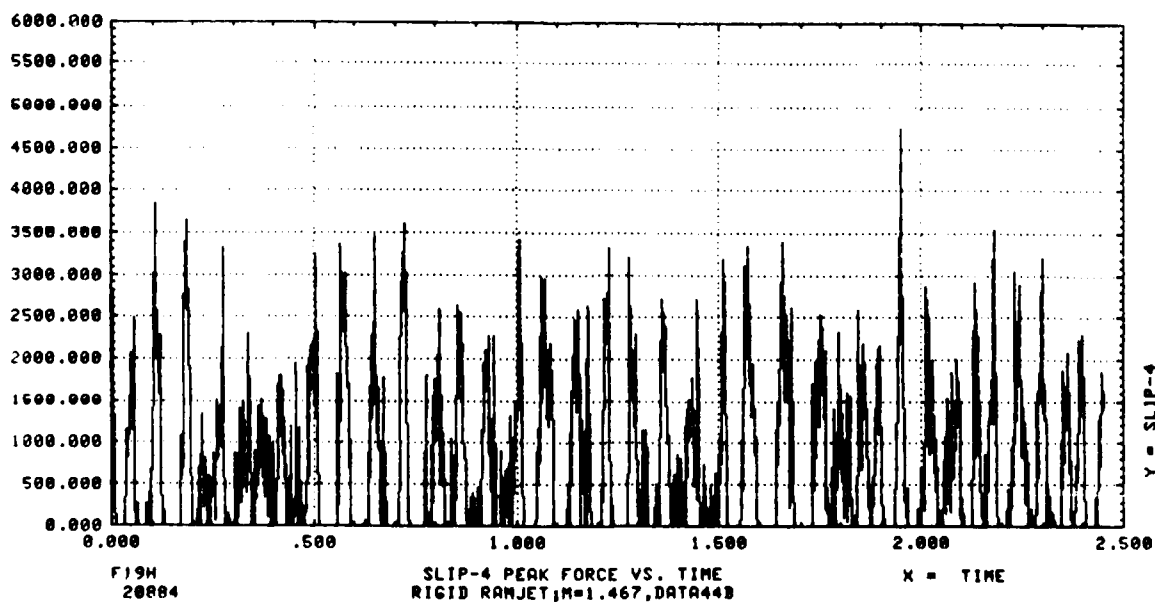


Figure C.16 Rigid Body Dual Rail, 44000 Bottom

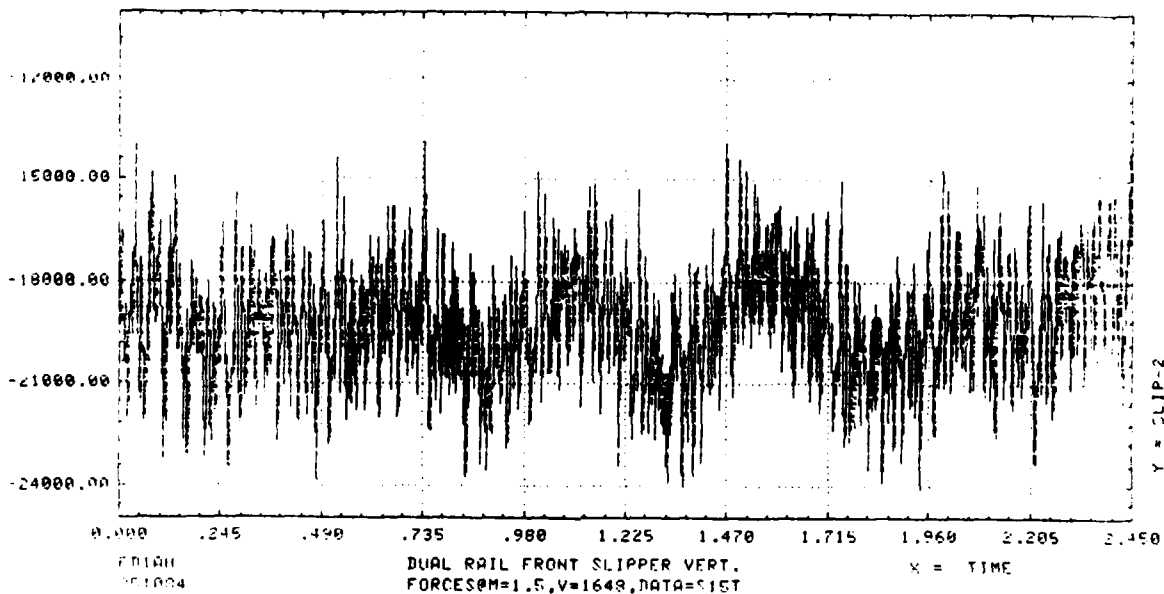


Figure C.17 Modal Dual Rail, S15000 Top

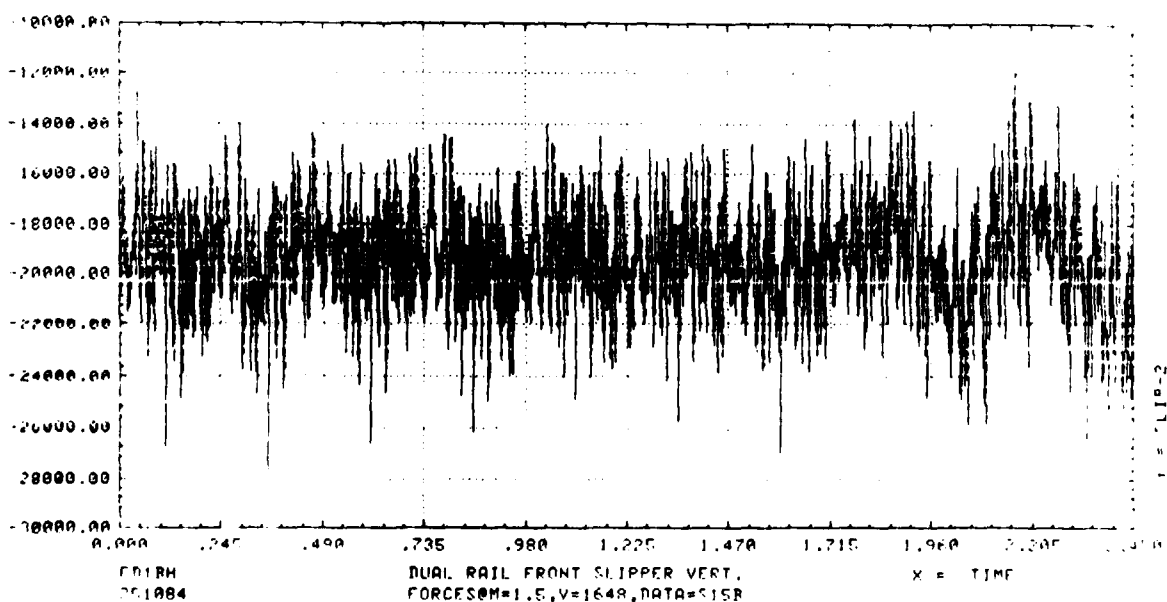


Figure C.18 Modal Dual Rail, S15000 Bottom

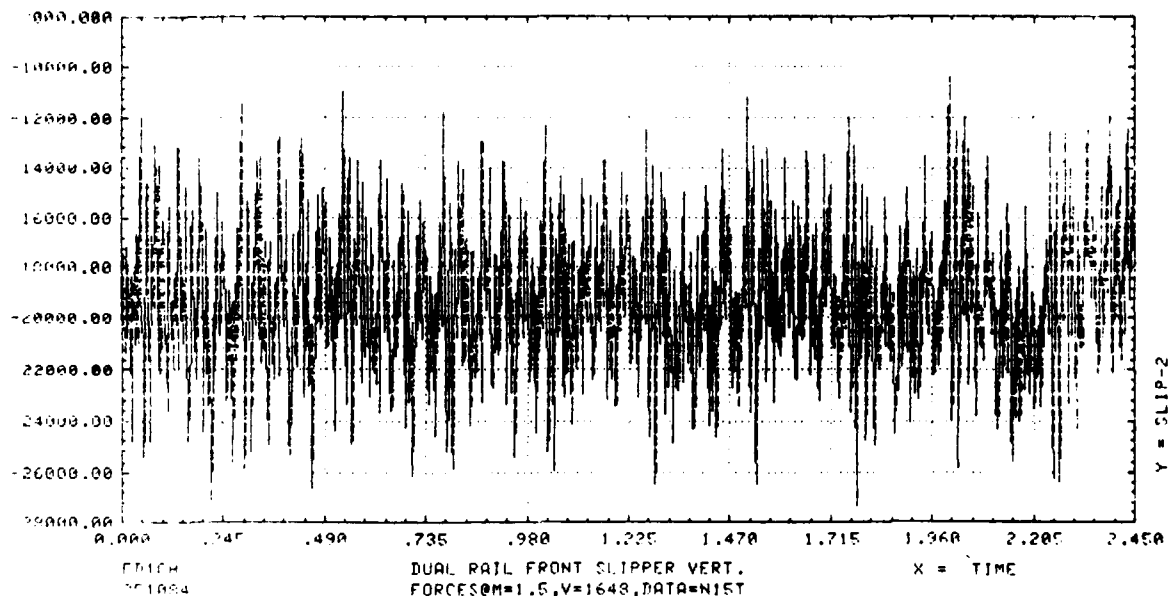


Figure C.19 Modal Dual Rail, N15000 Top

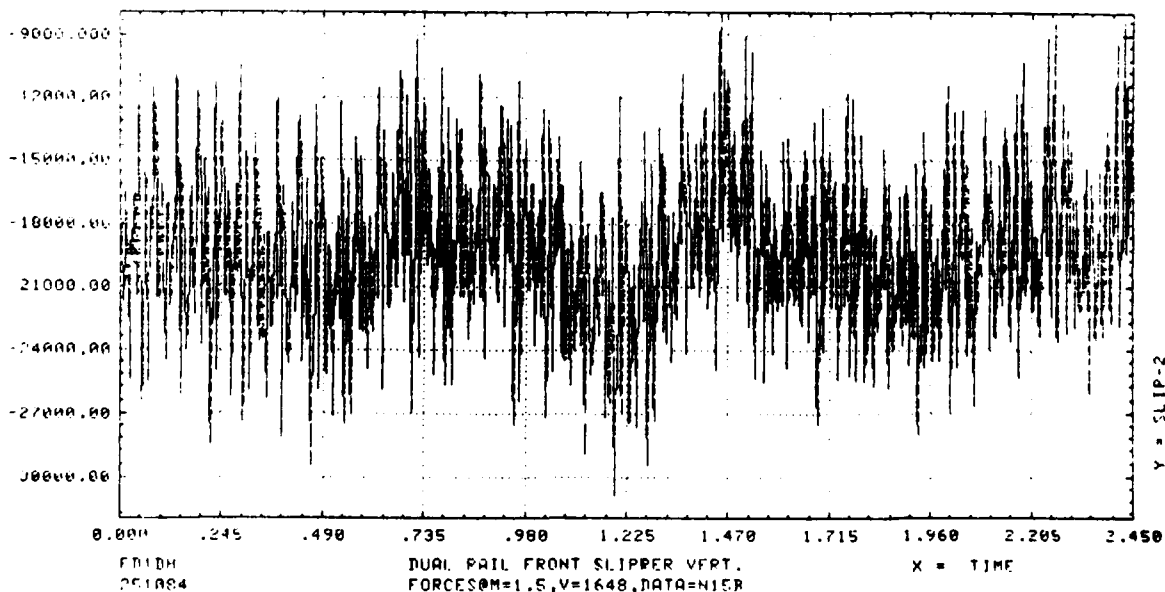


Figure C.20 Modal Dual Rail, N15000 Bottom

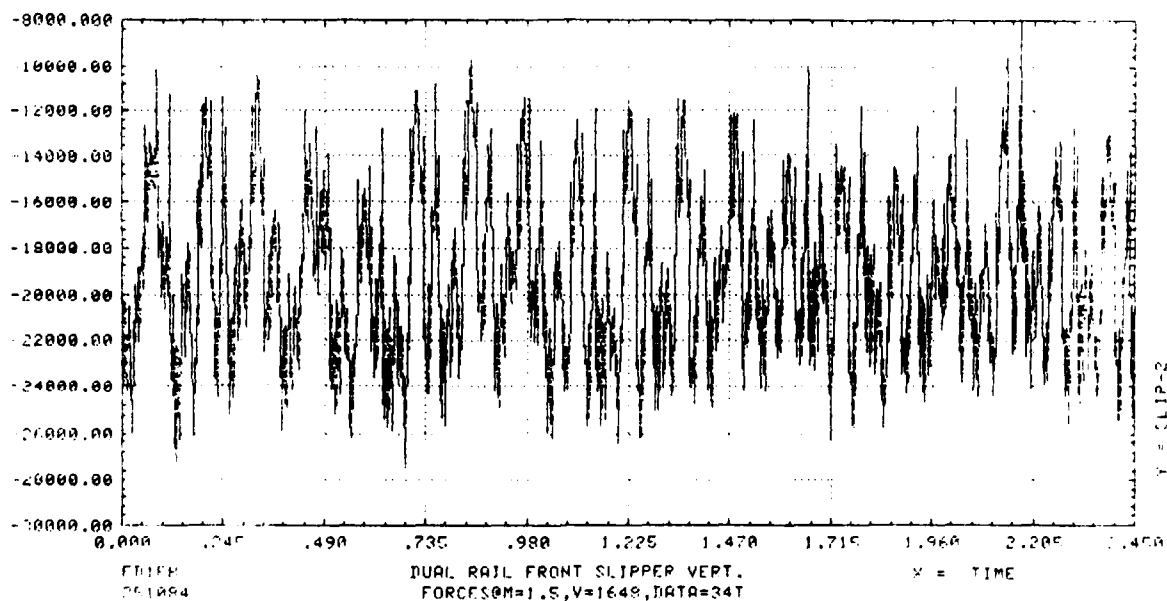


Figure C.21 Modal Dual Rail, 34000 Top

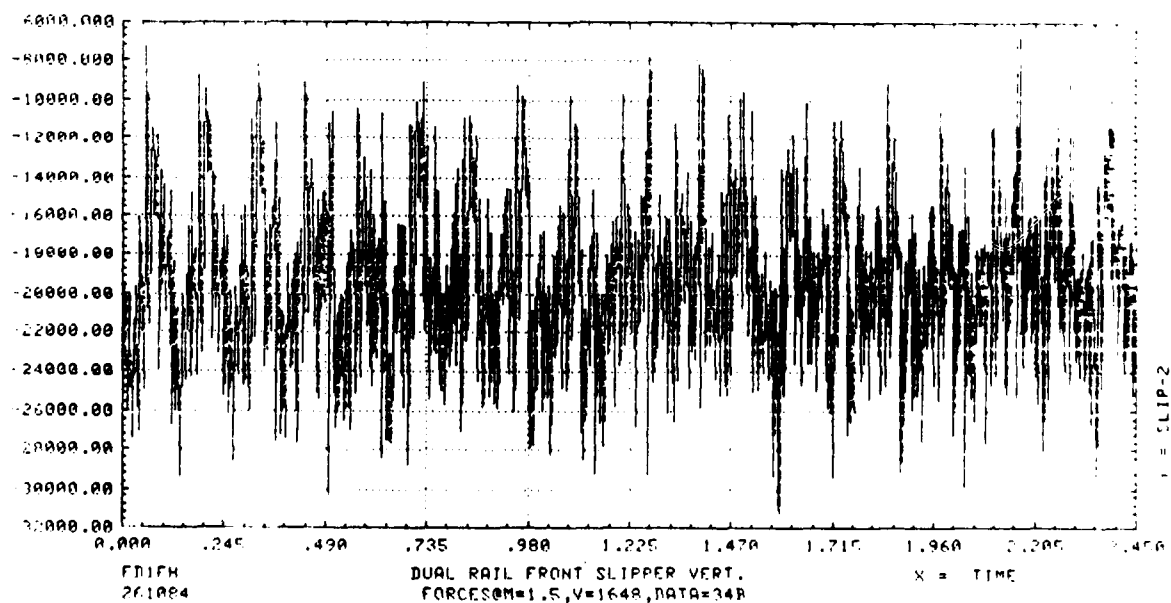


Figure C.22 Modal Dual Rail, 34000 Bottom

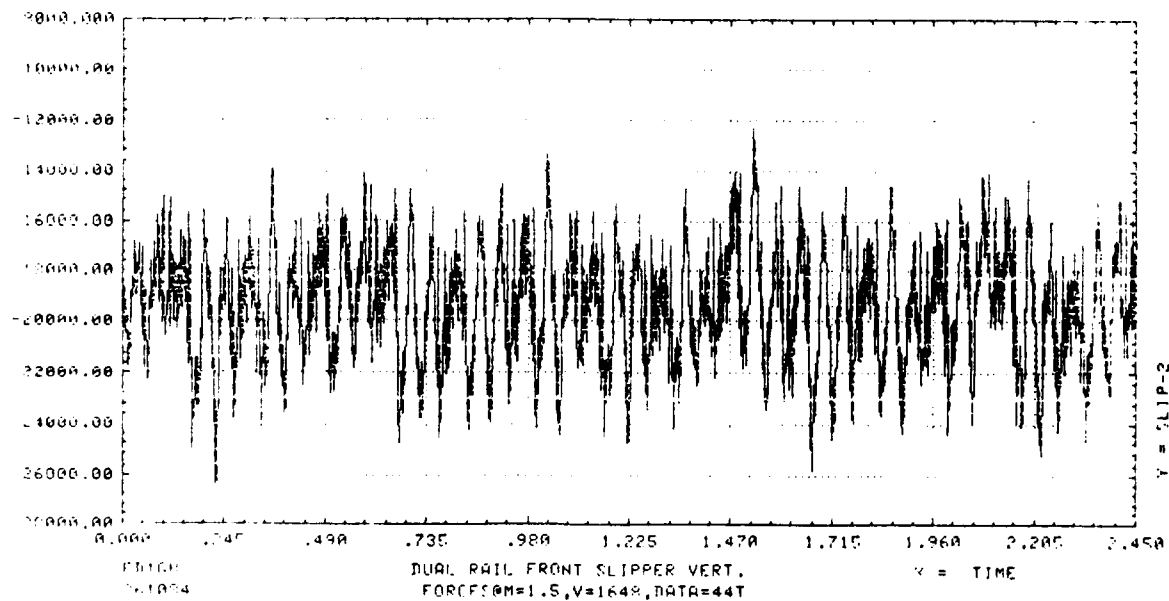


Figure C.23 Modal Dual Rail, 44000 Top

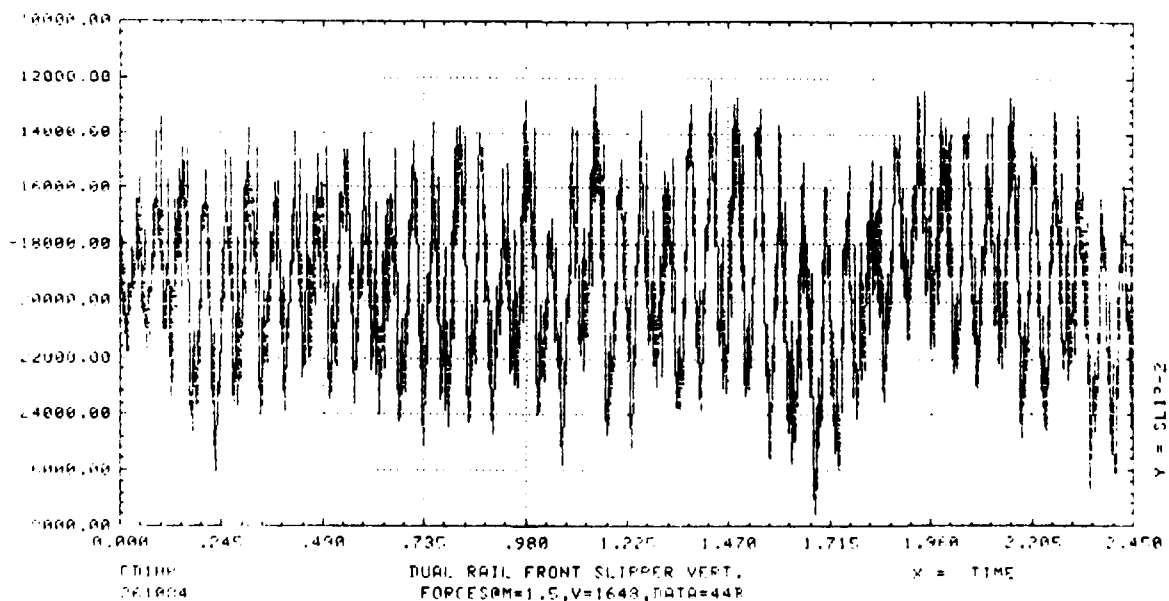


Figure C.24 Modal Dual Rail, 44000 Bottom

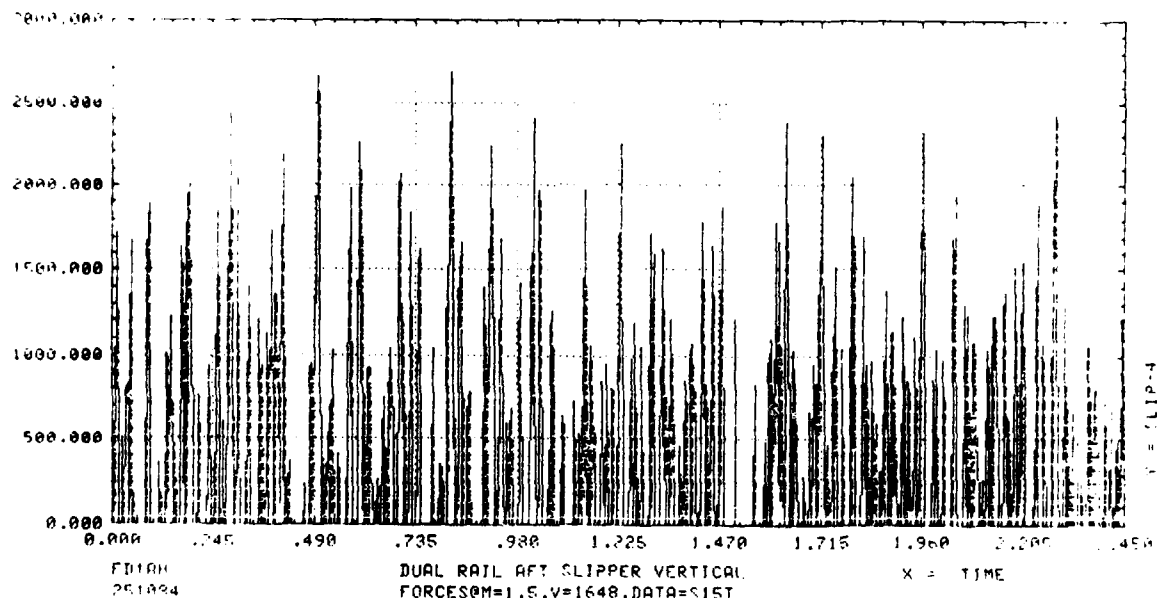


Figure C.25 Modal Dual Rail, S15000 Top

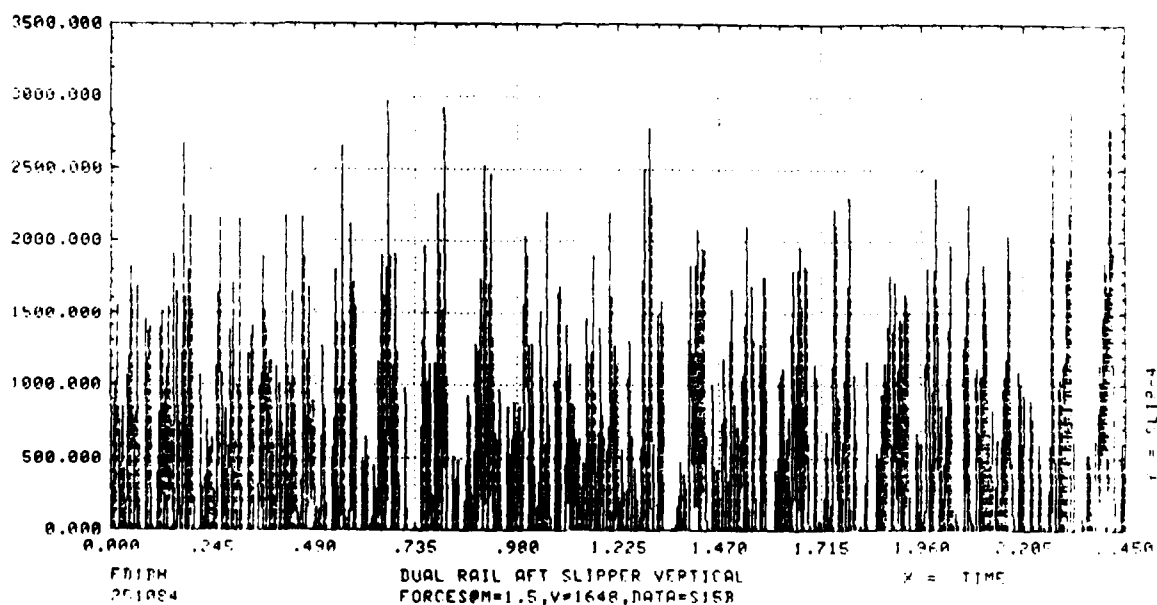


Figure C.26 Modal Dual Rail, S15000 Bottom

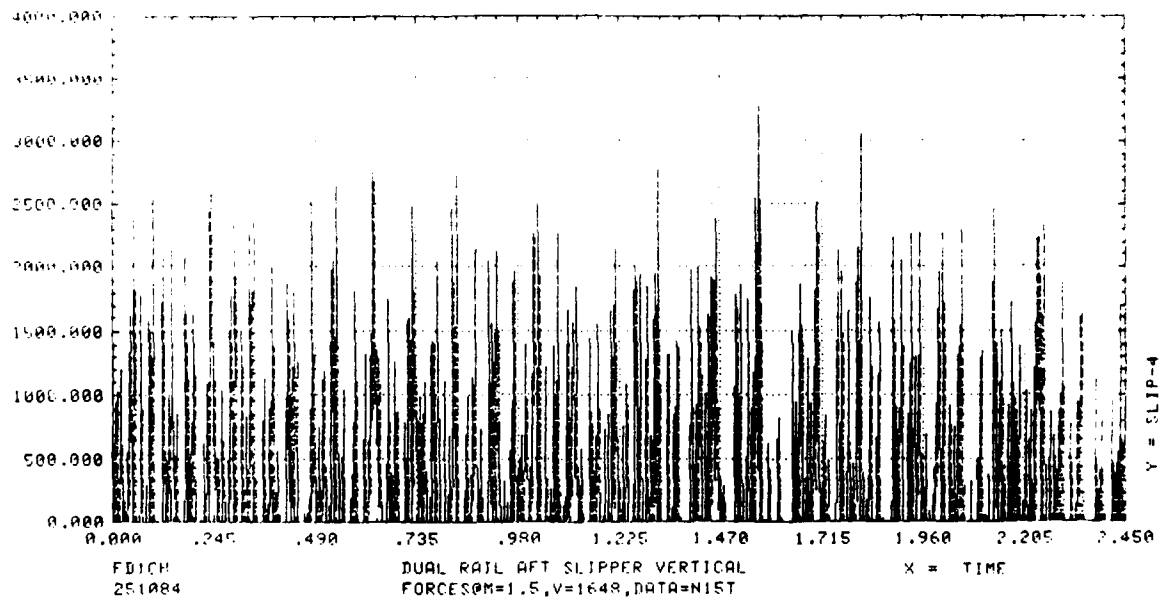


Figure C.27 Modal Dual Rail, N15000 Top

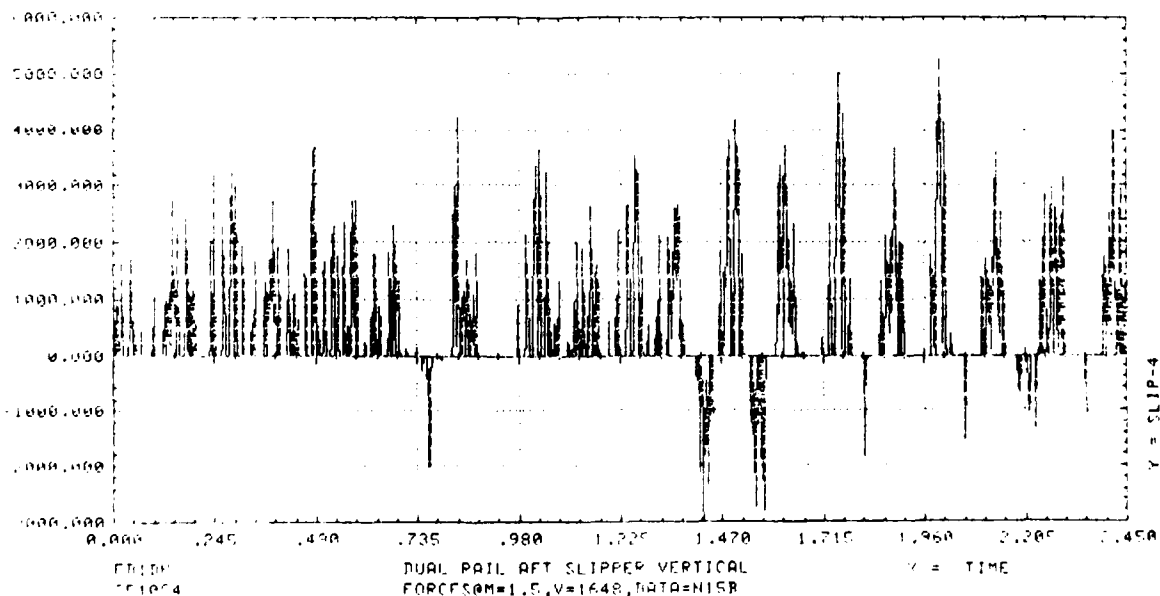


Figure C.28 Modal Dual Rail, N15000 Bottom

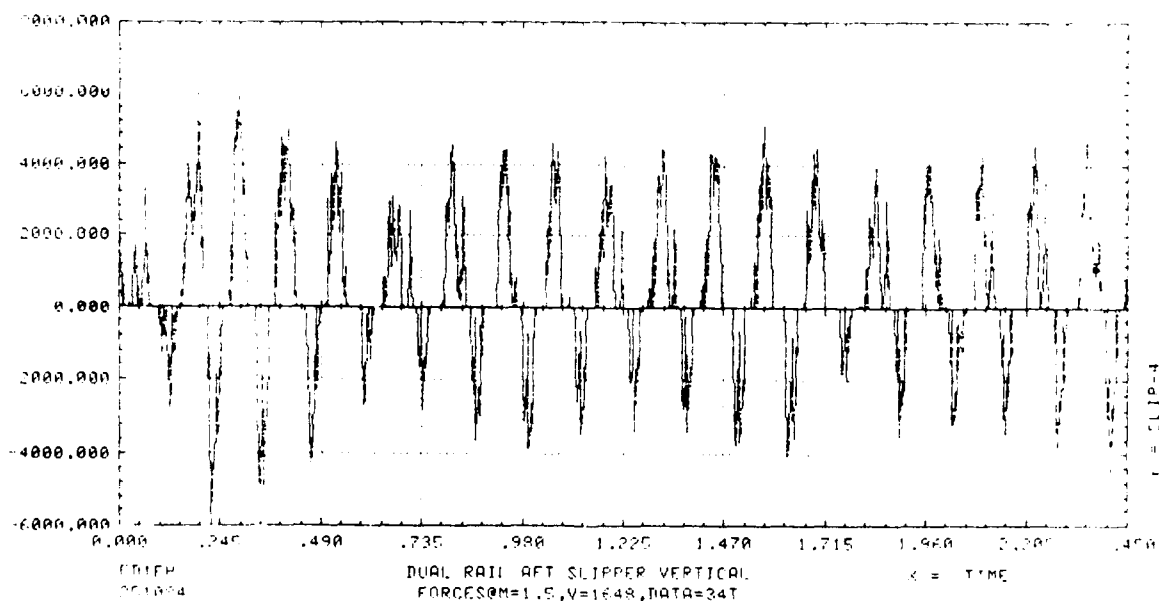


Figure C.29 Modal Dual Rail, 34000 Top

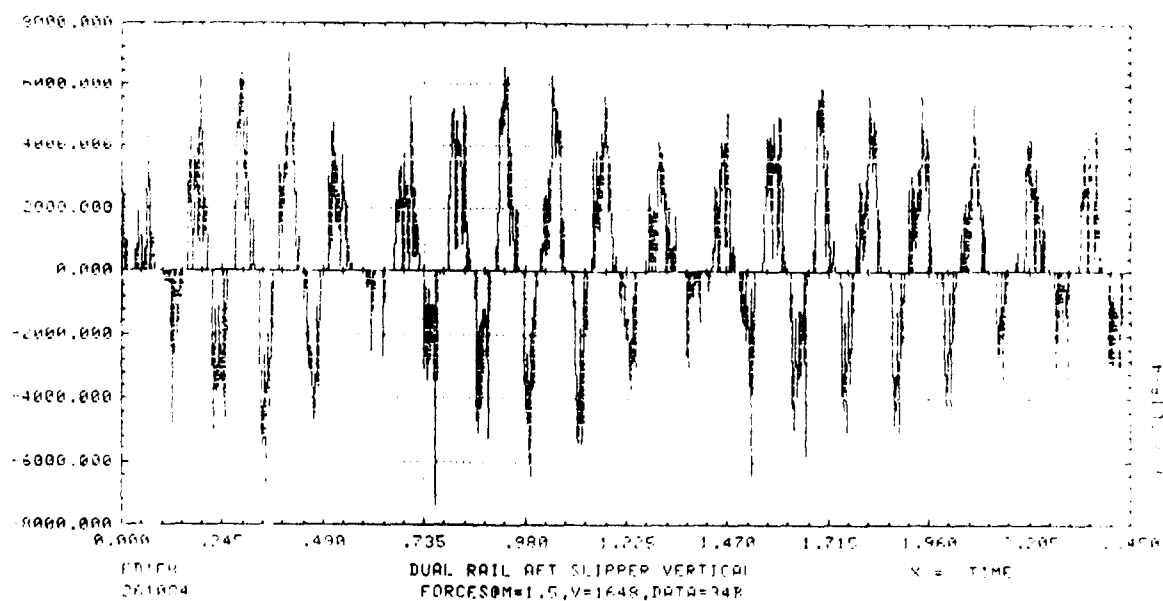


Figure C.30 Modal Dual Rail, 34000 Bottom

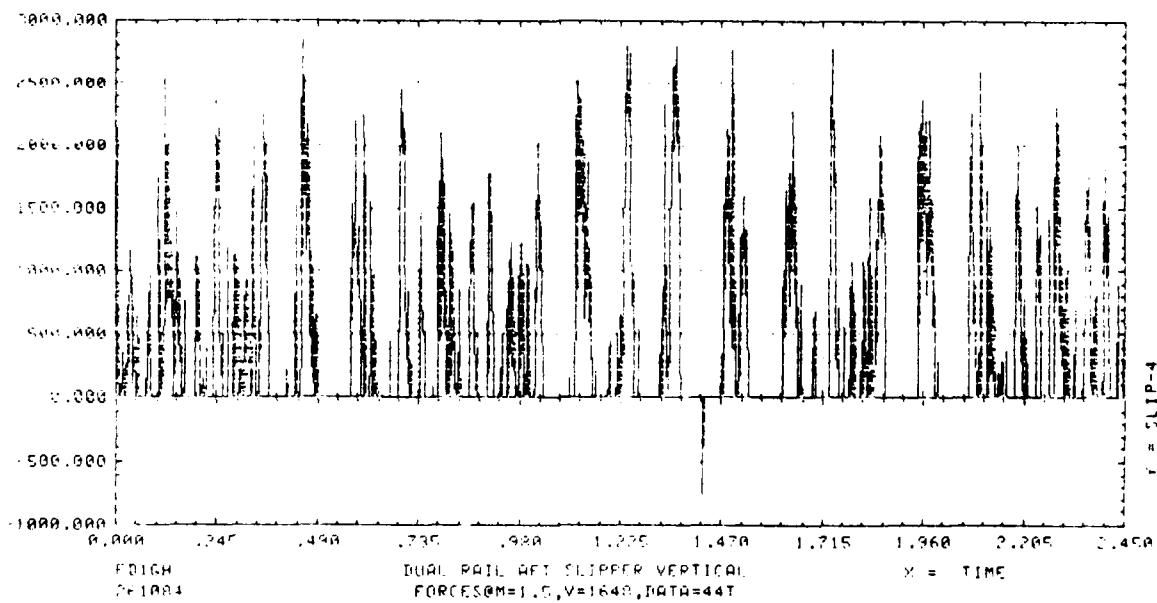


Figure C.31 Modal Dual Rail, 44000 Top

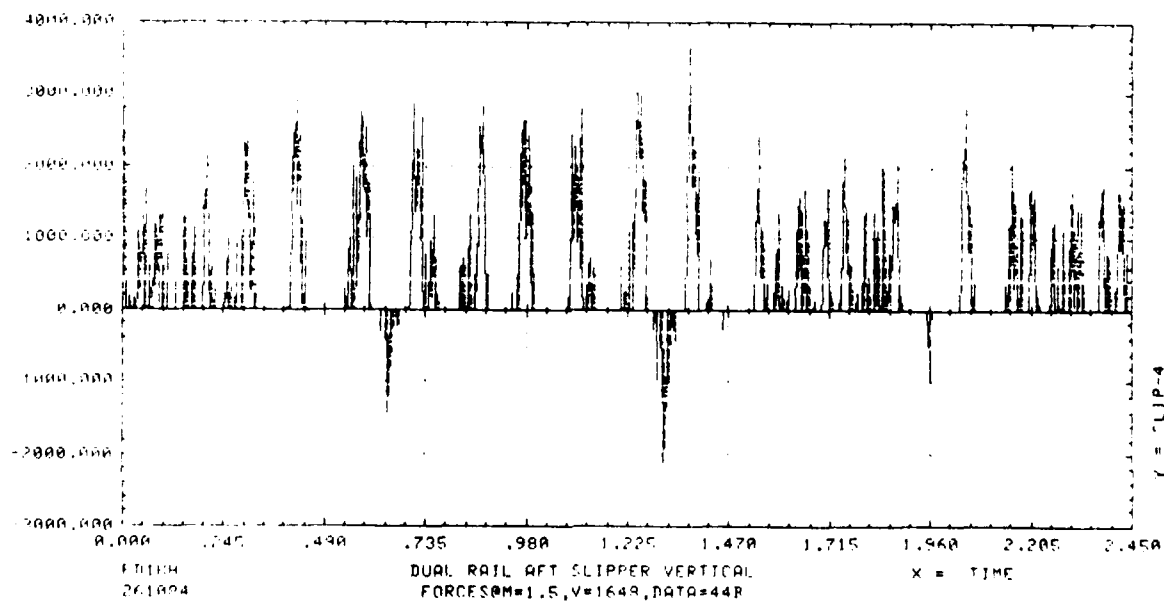


Figure C.32 Modal Dual Rail, 44000 Bottom

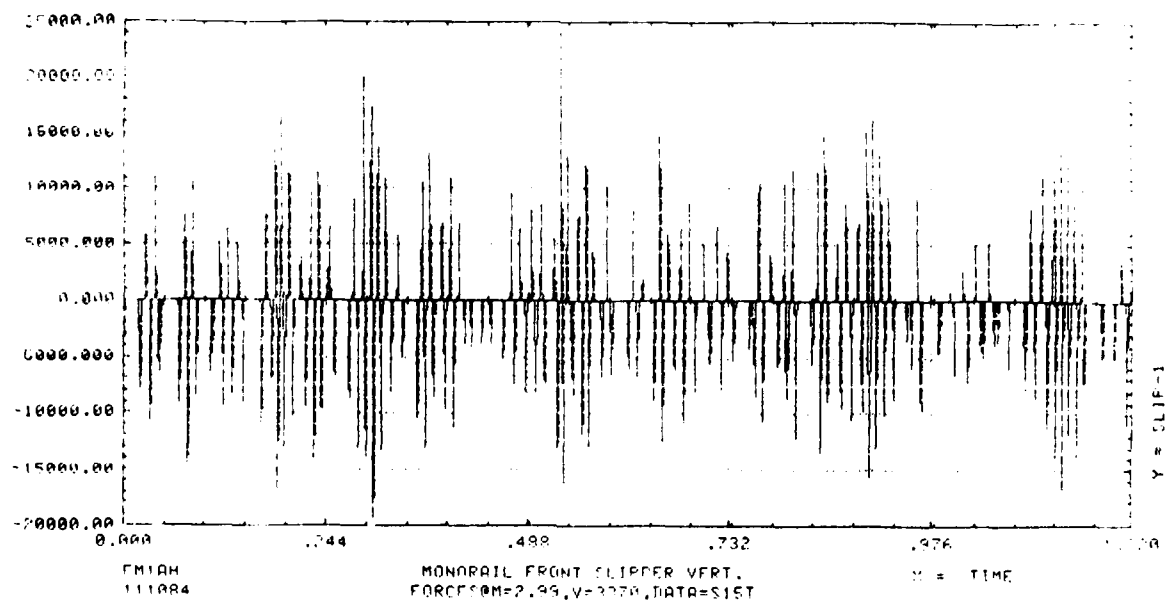


Figure C.33 Rigid Body Monorail, S15000 Top

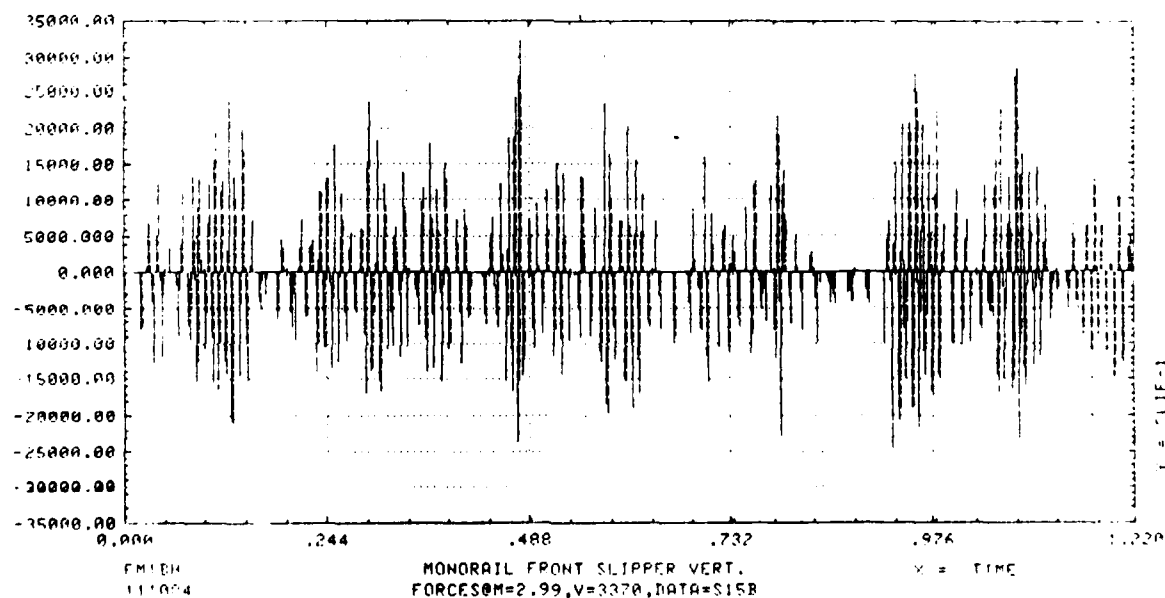


Figure C.34 Rigid Body Monorail, S15000 Bottom

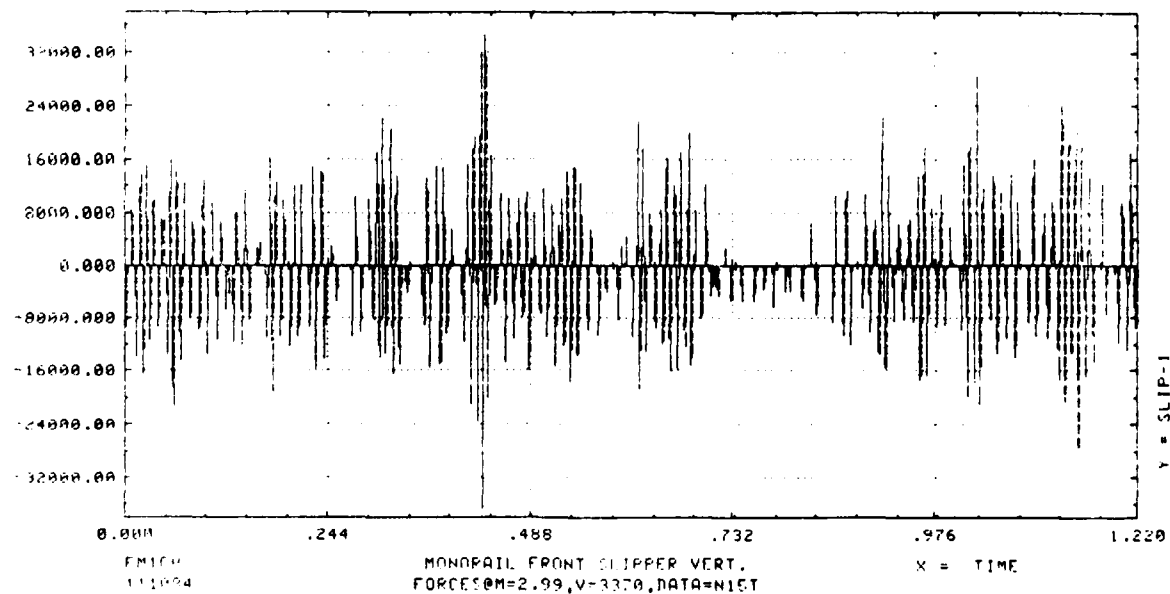


Figure C.35 Rigid Body Monorail, N15000 Top

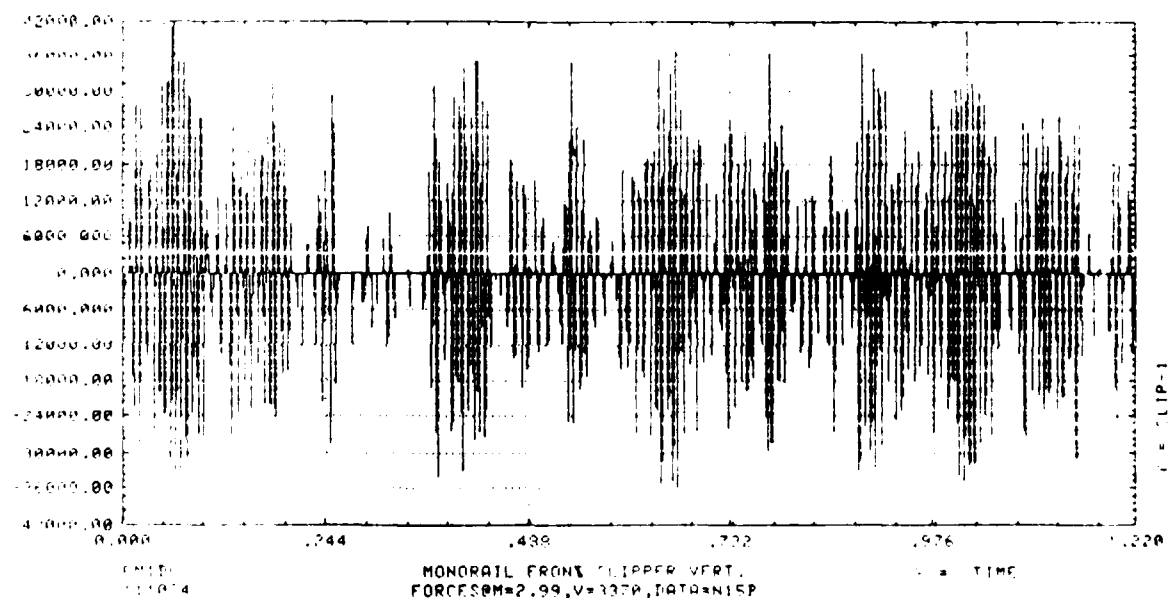


Figure C.36 Rigid Body Monorail, N15000 Bottom

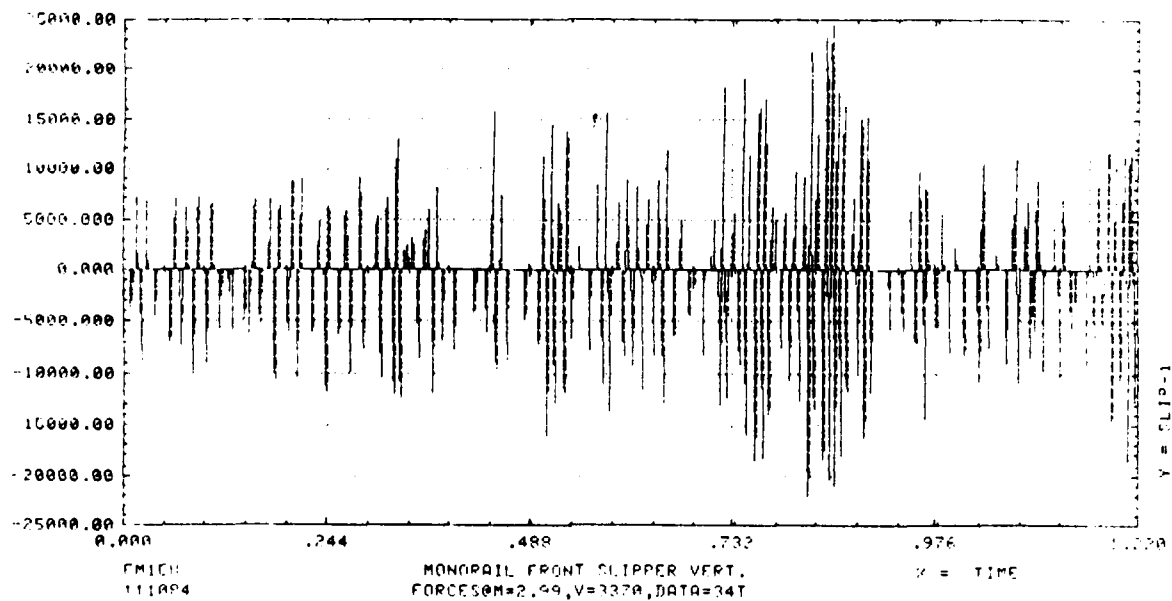


Figure C.37 Rigid Body Monorail, 34000 Top

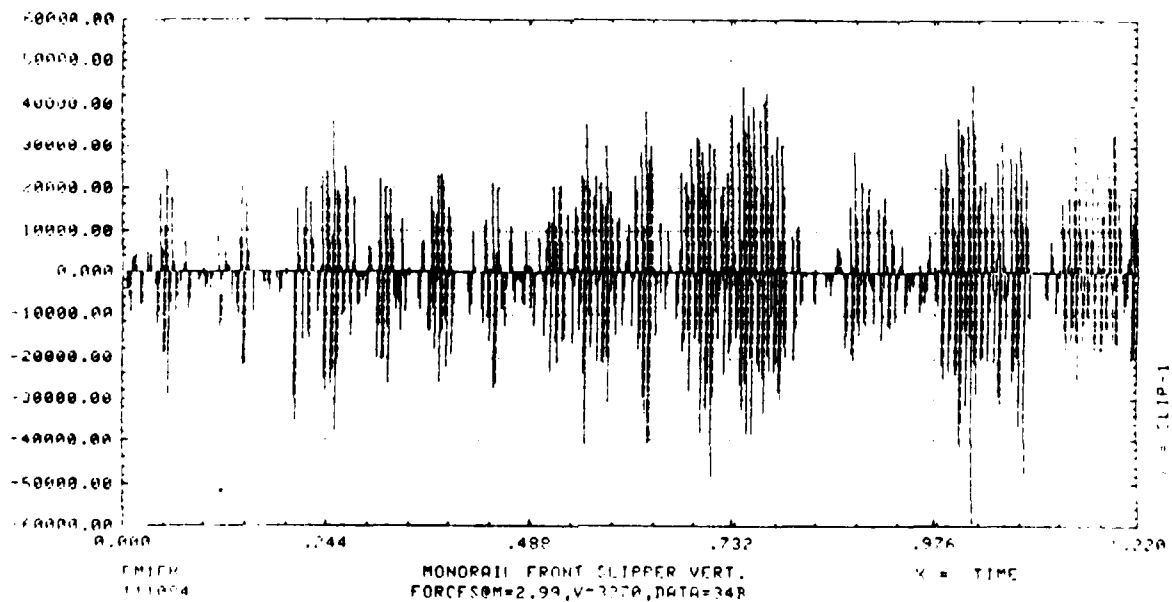


Figure C.38 Rigid Body Monorail, 34000 Bottom

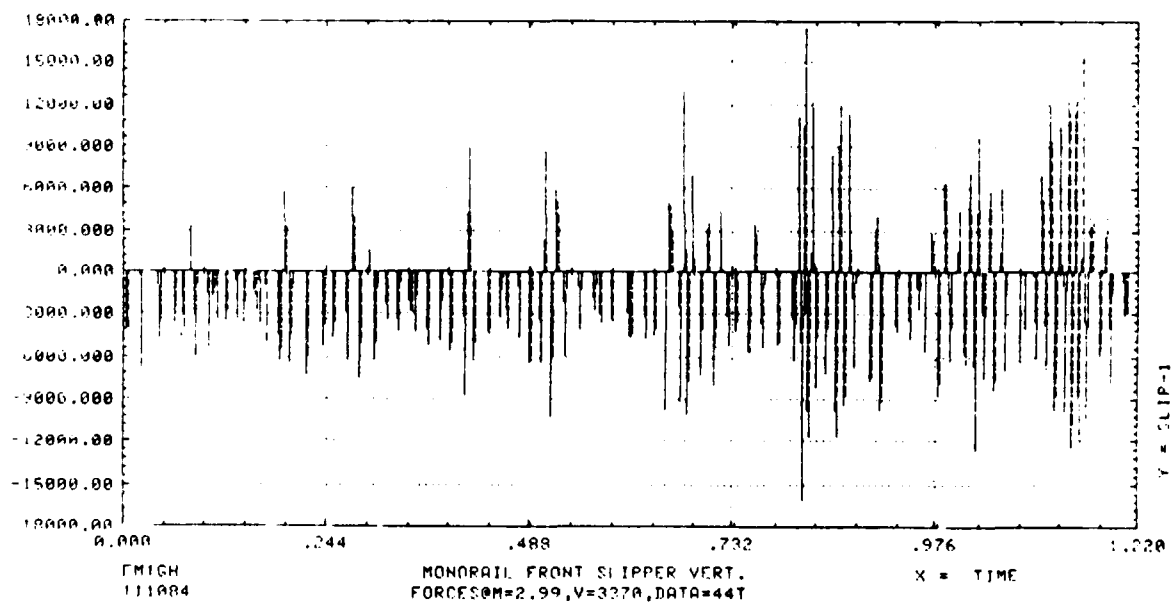


Figure C.39 Rigid Body Monorail, 44000 Top

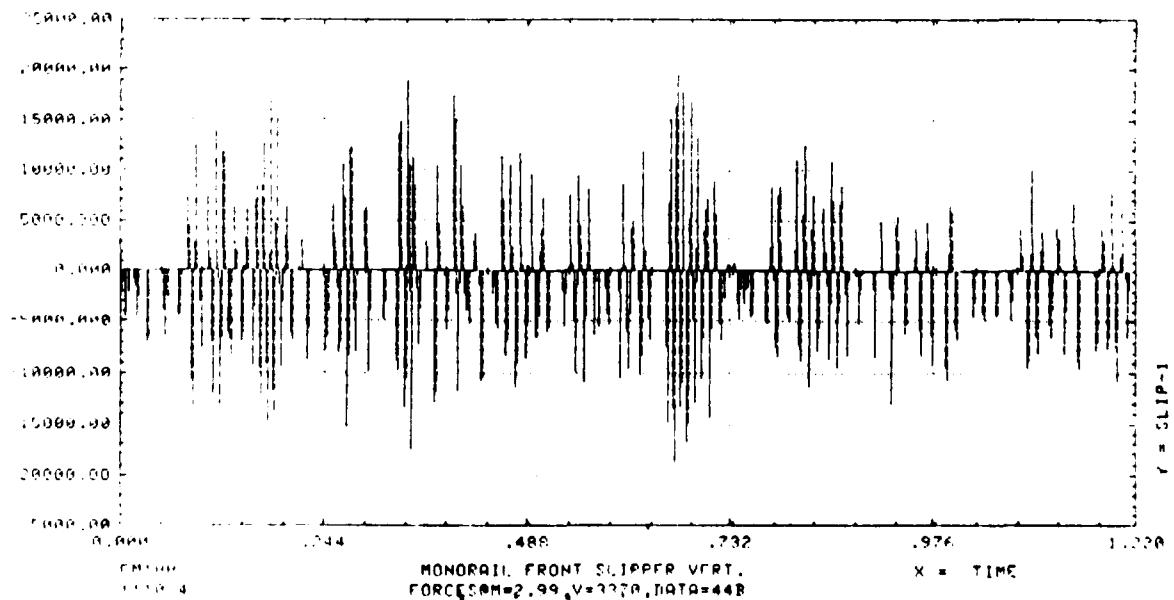


Figure C.40 Rigid Body Monorail, 44000 Bottom

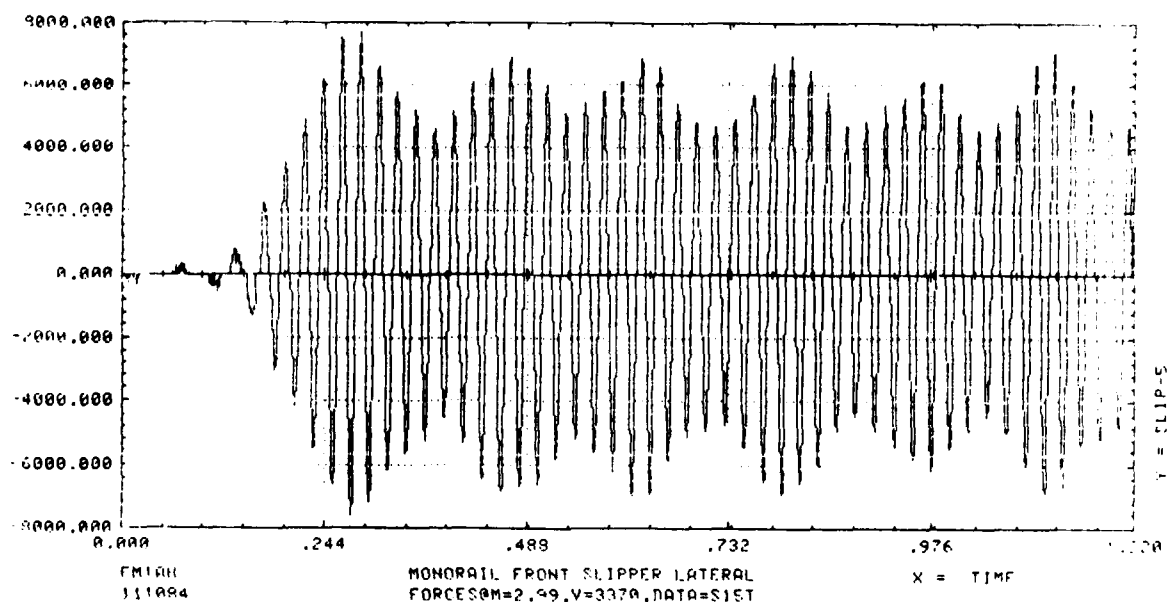


Figure C.41 Rigid Body Monorail, S15000 Top

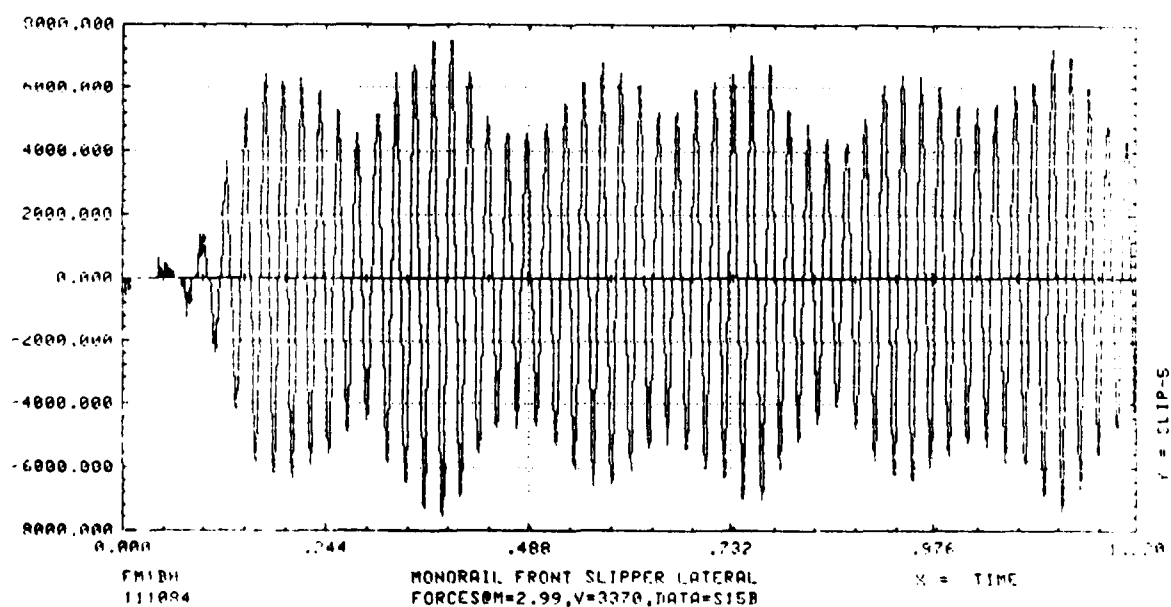


Figure C.42 Rigid Body Monorail, S15000 Bottom

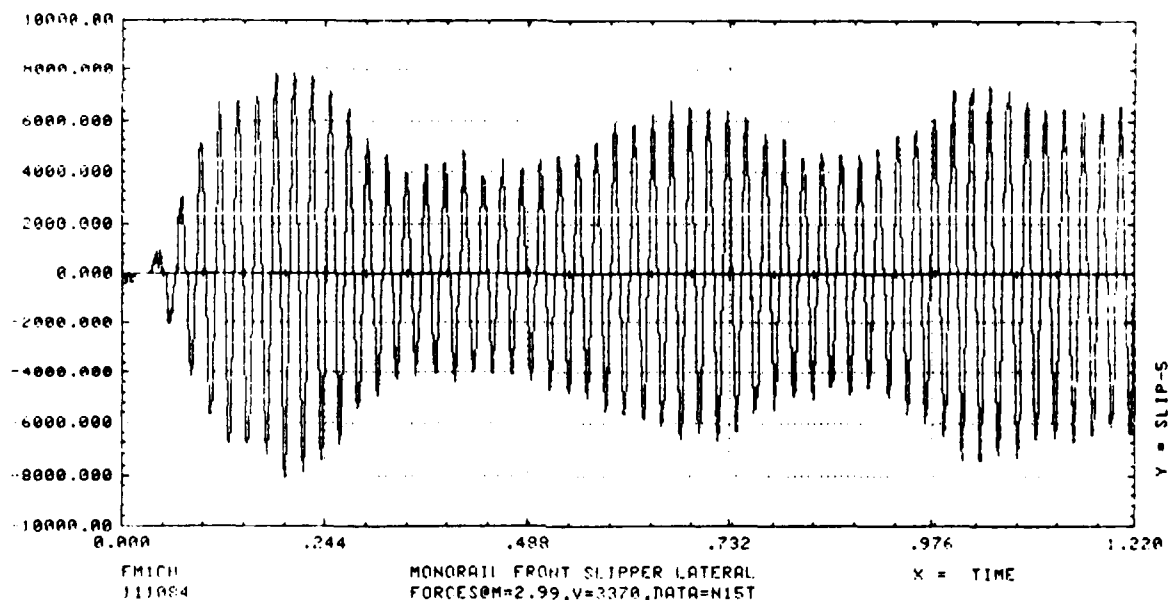


Figure C.43 Rigid Body Monorail, N15000 Top

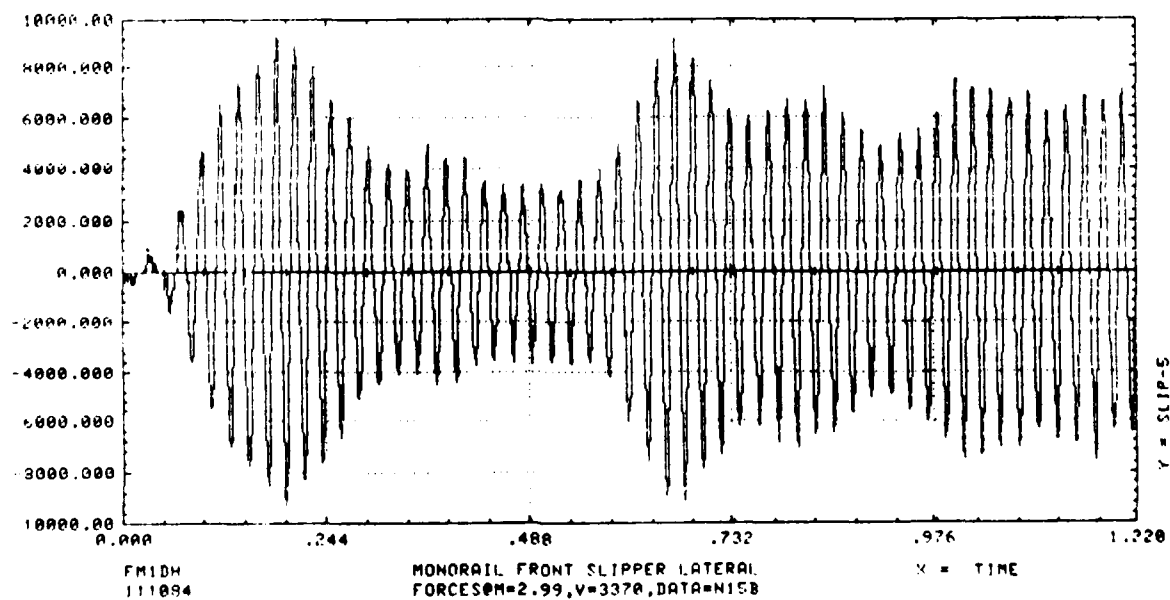


Figure C.44 Rigid Body Monorail, N15000 Bottom

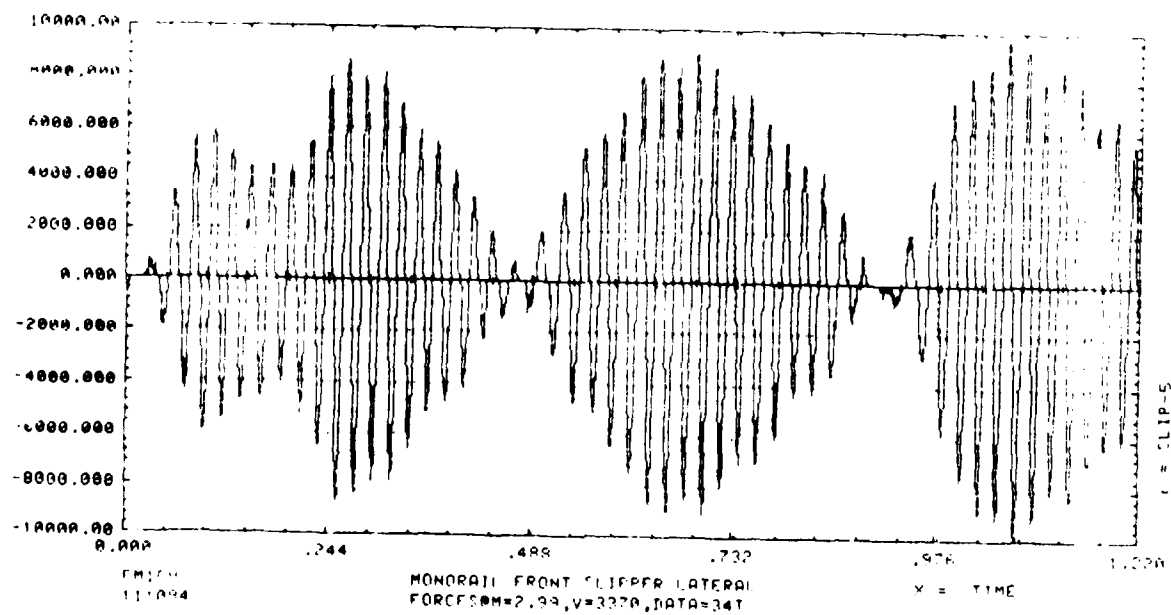


Figure C.45 Rigid Body Monorail, 34000 Top

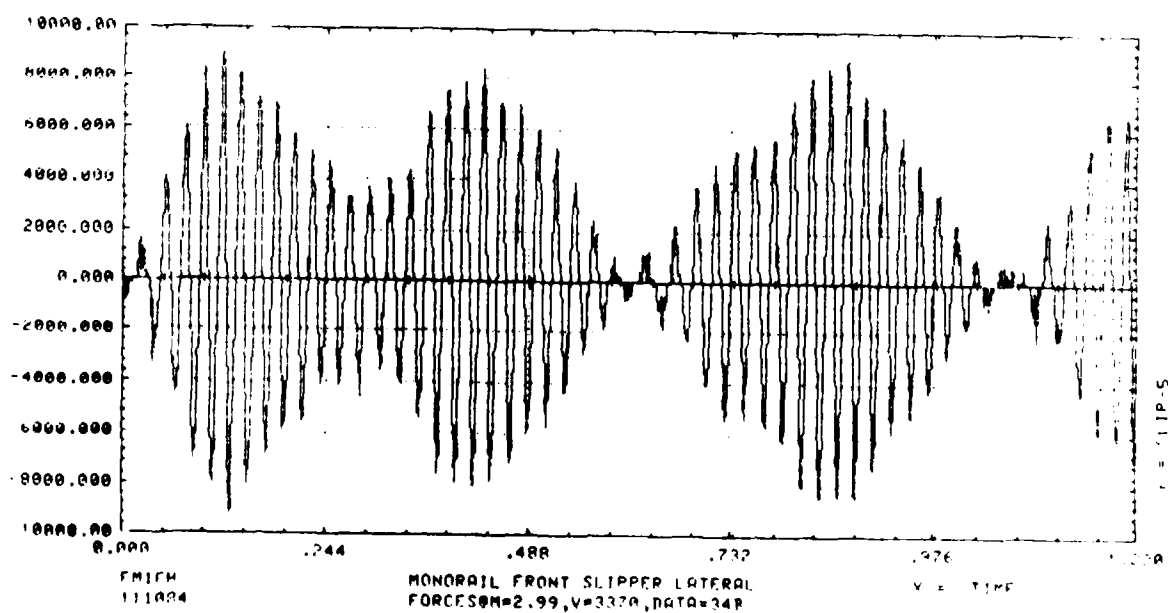


Figure C.46 Rigid Body Monorail, 34000 Bottom

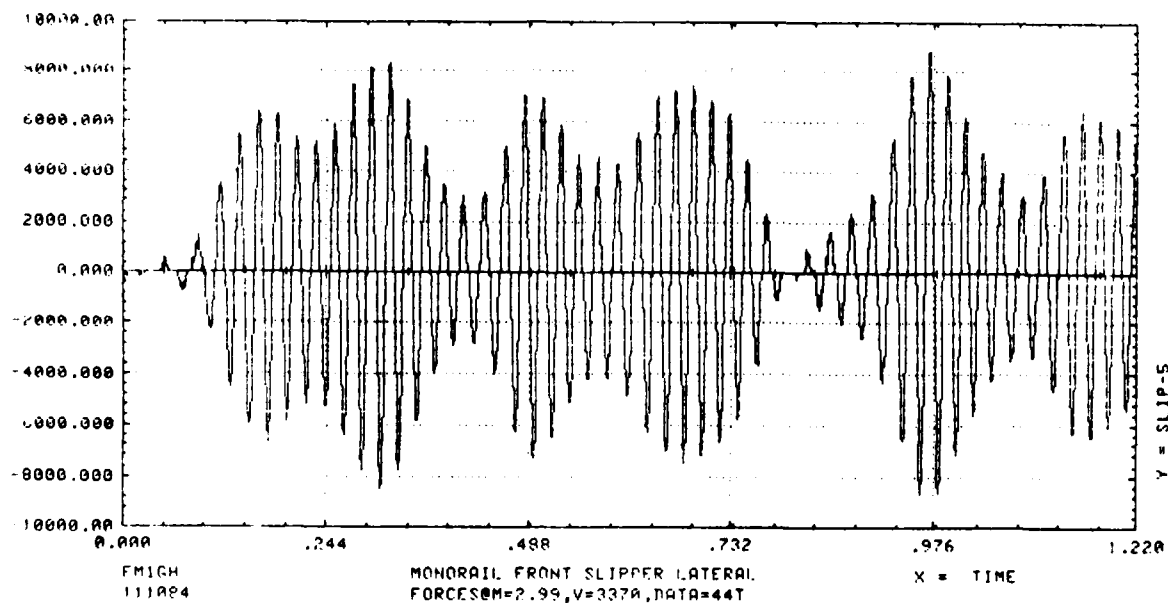


Figure C.47 Rigid Body Monorail, 44000 Top

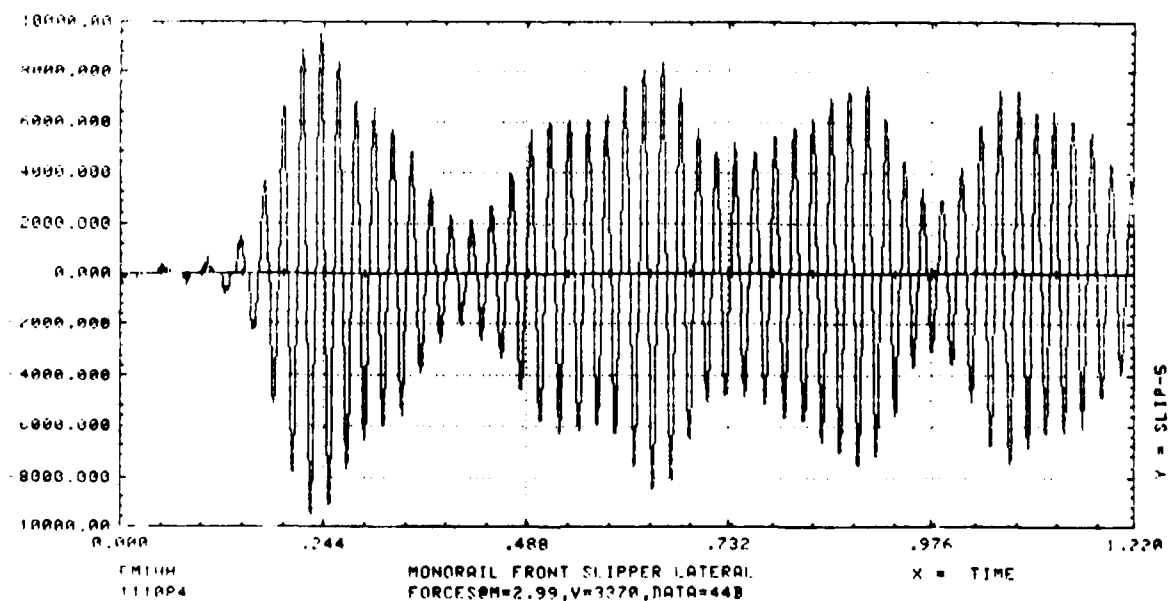


Figure C.48 Rigid Body Monorail, 44000 Bottom

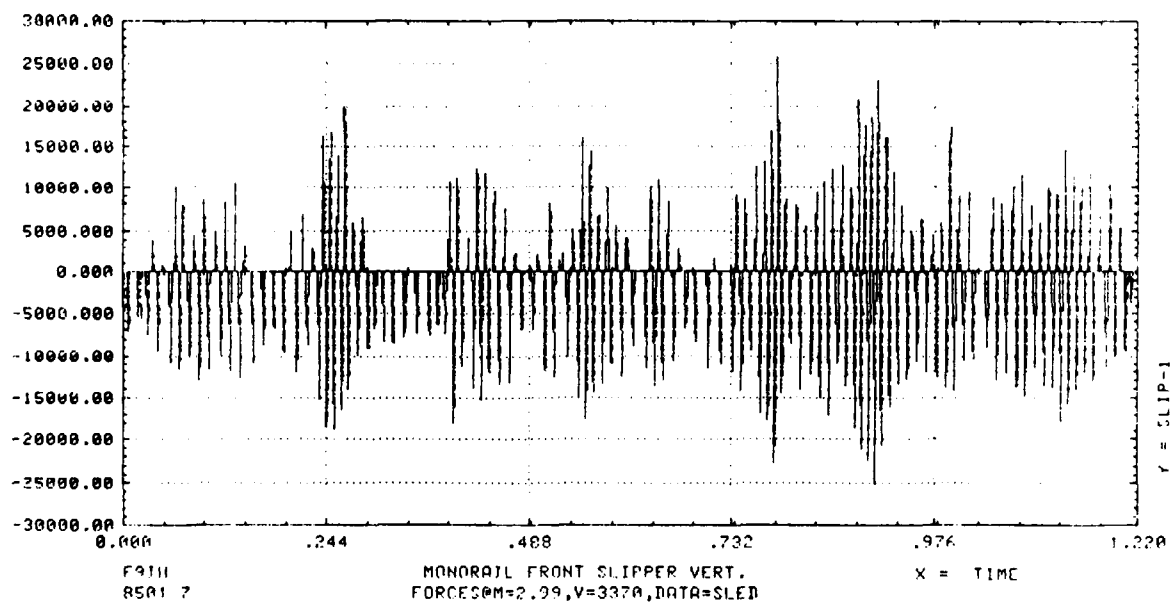


Figure C.49 Modal Monorail, Baseline

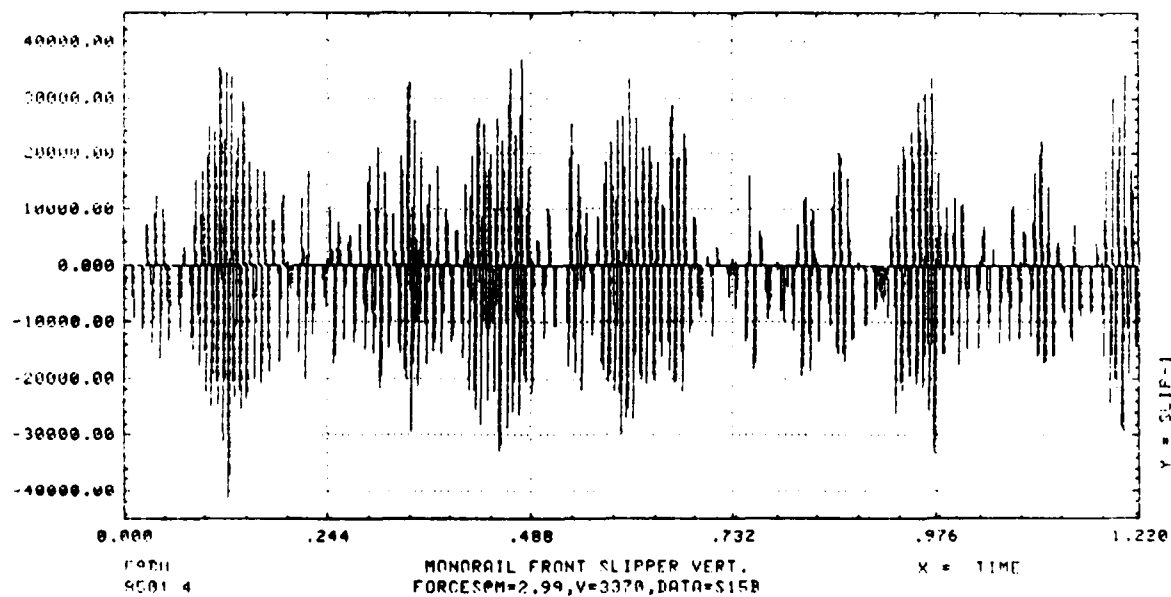


Figure C.50 Modal Monorail, S15000 Bottom

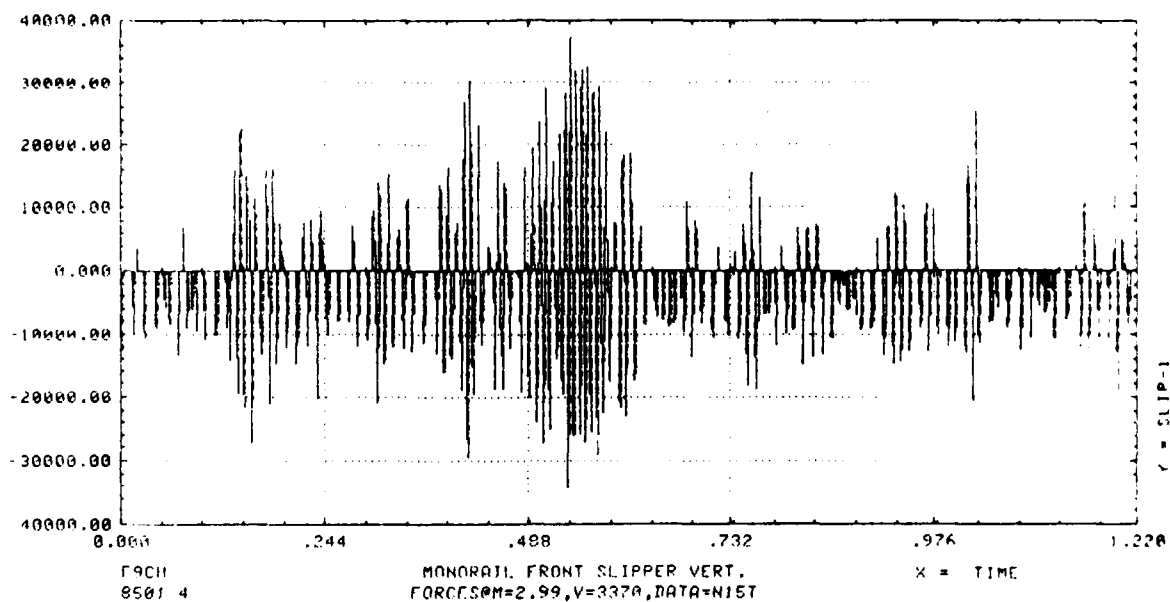


Figure C.51 Modal Monorail, N15000 Top

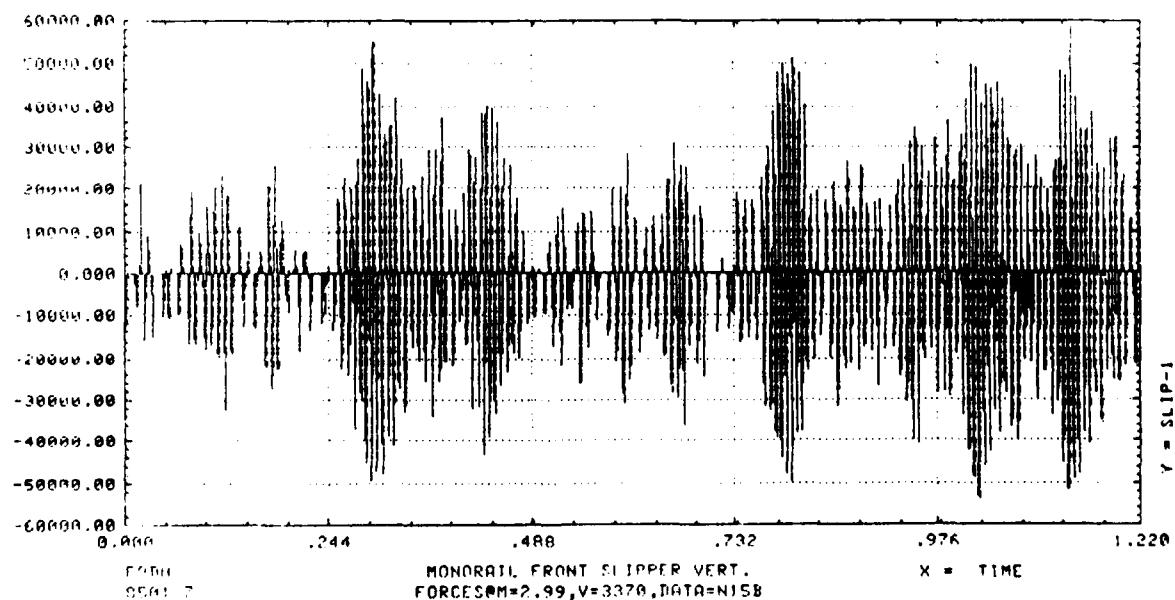


Figure C.52 Modal Monorail, N15000 Bottom

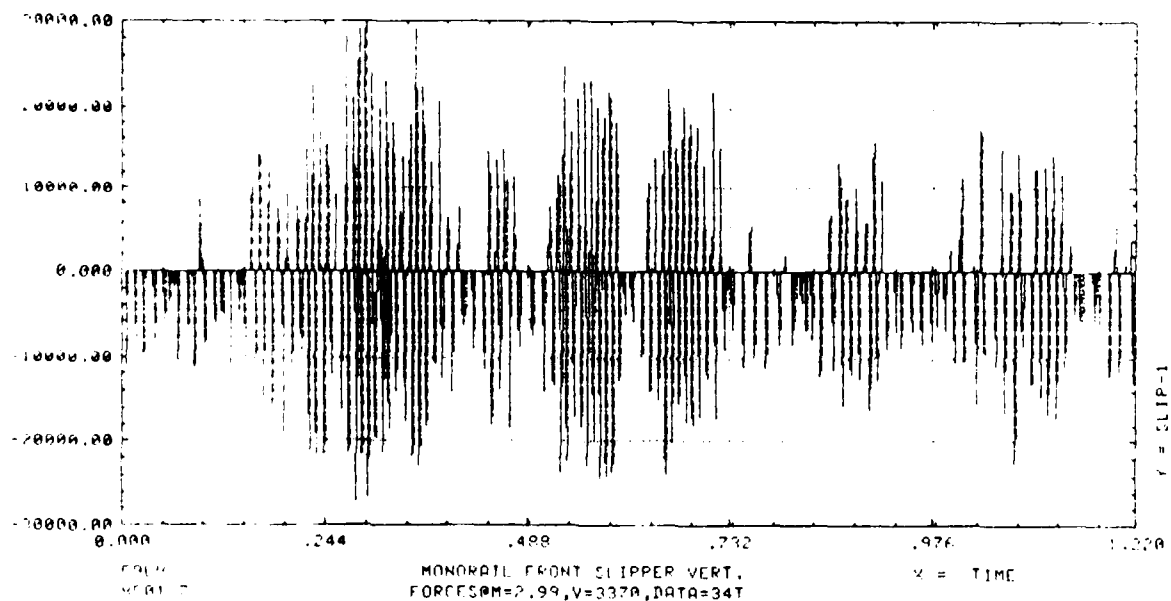


Figure C.53 Modal Monorail, TS 34000 Top

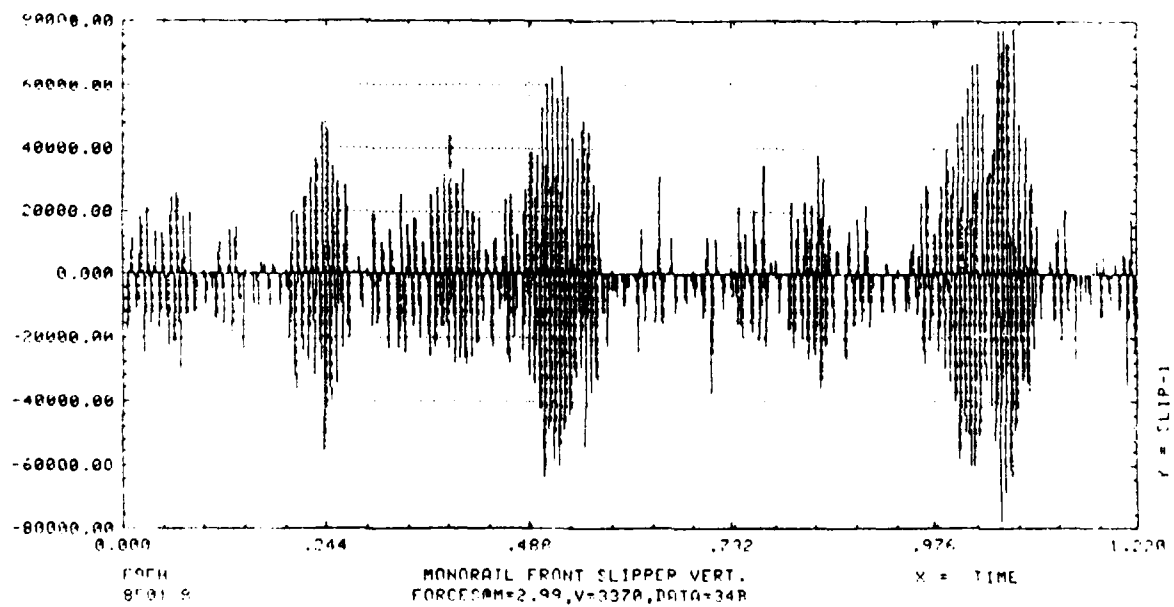


Figure C.54 Modal Monorail, TS 34000 Bottom

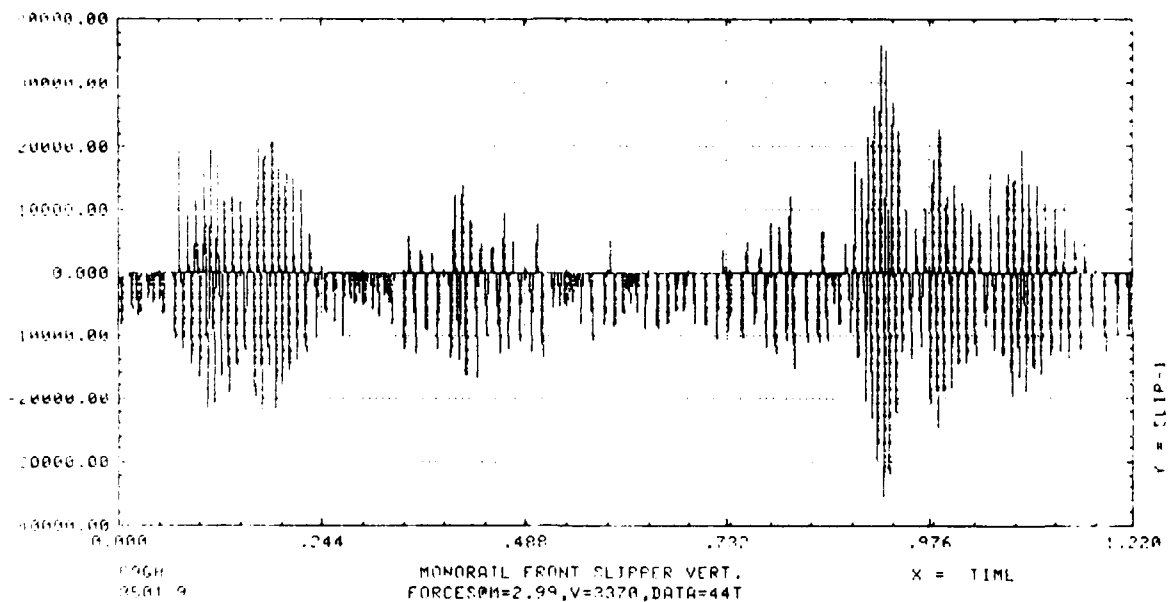


Figure C.55 Modal Monorail, TS 44000 Top

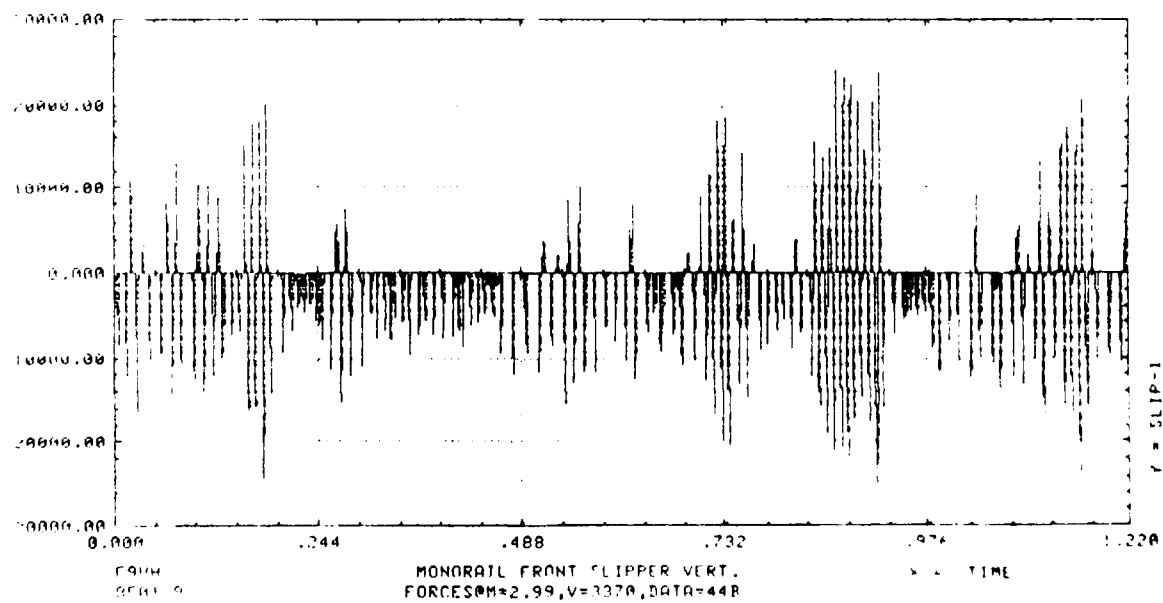


Figure C.56 Modal Monorail, TS 44000 Bottom

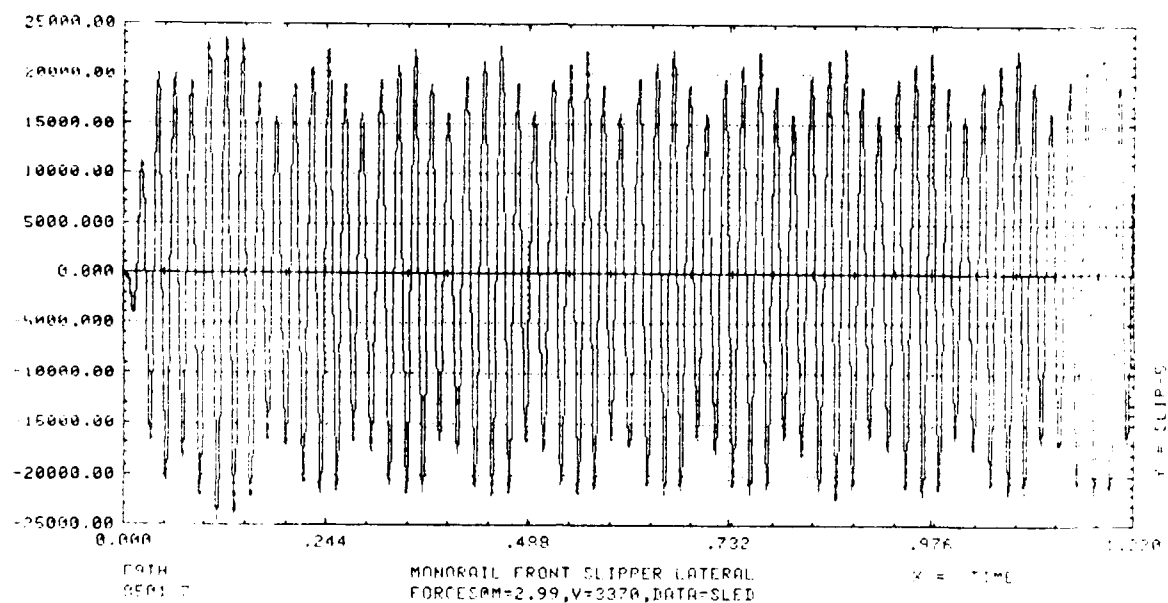


Figure C.57 Modal Monorail, Baseline

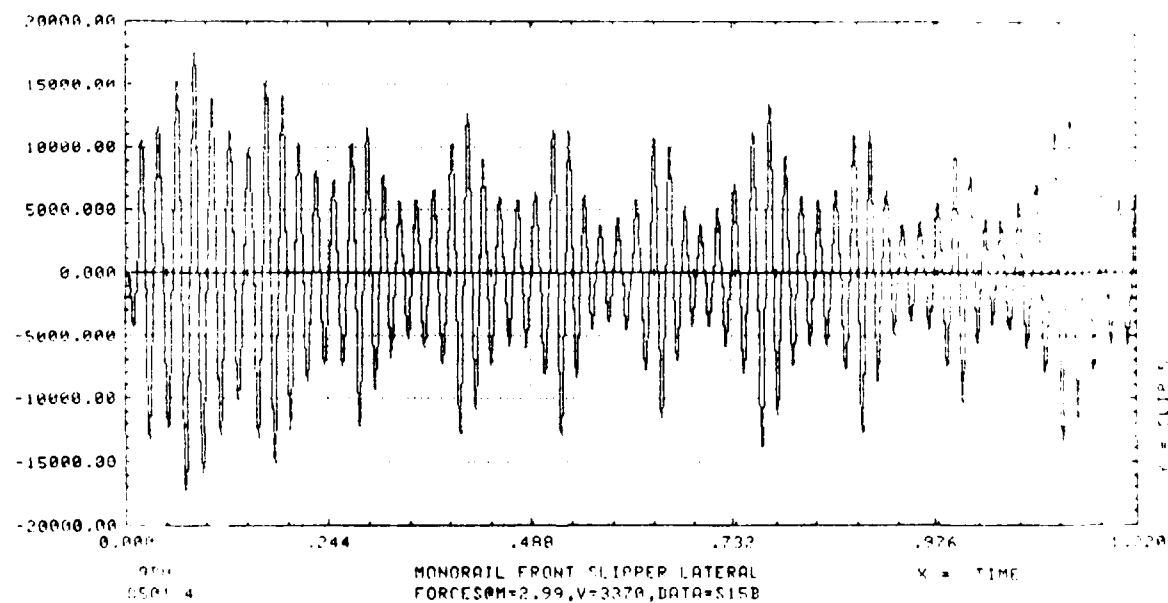


Figure C.58 Modal Monorail, S15000 Bottom

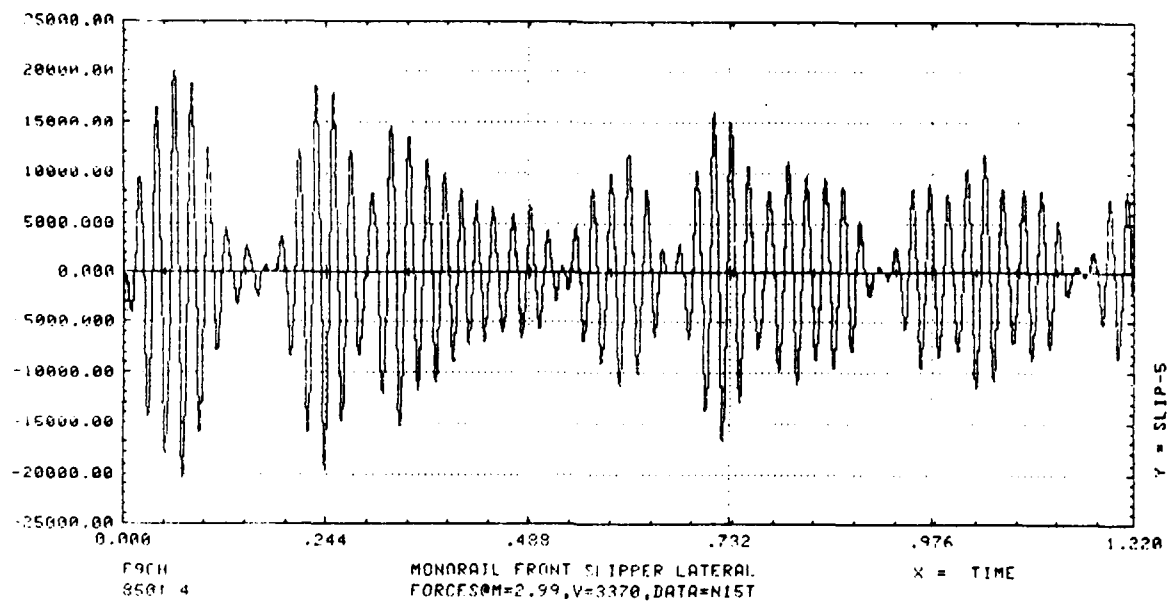


Figure C.59 Modal Monorail, N15000 Top

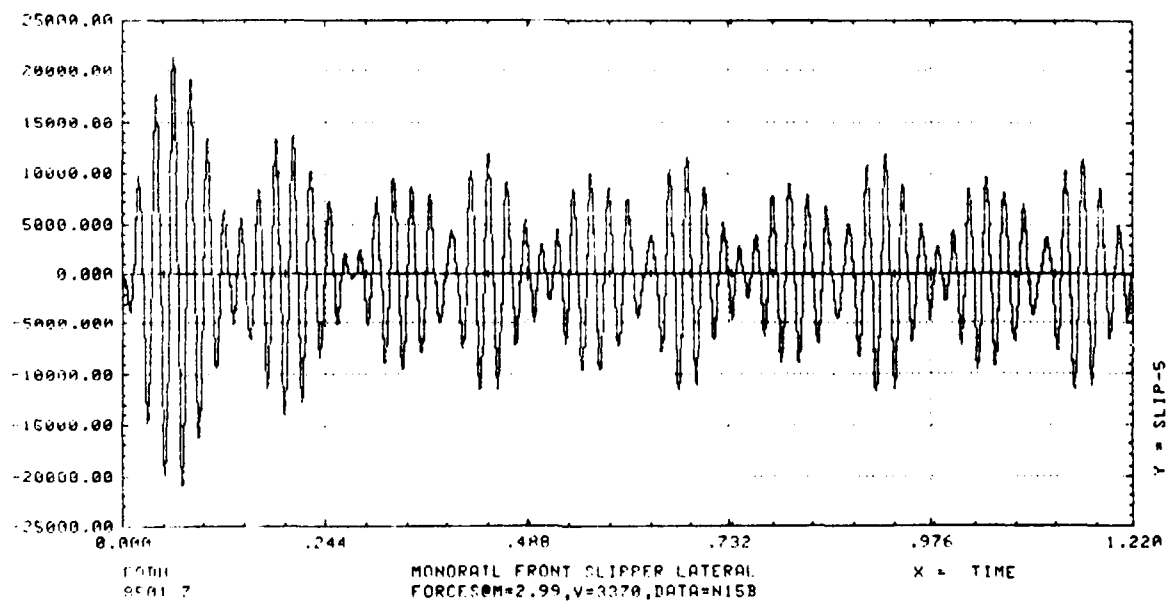


Figure C.60 Modal Monorail, N15000 Bottom

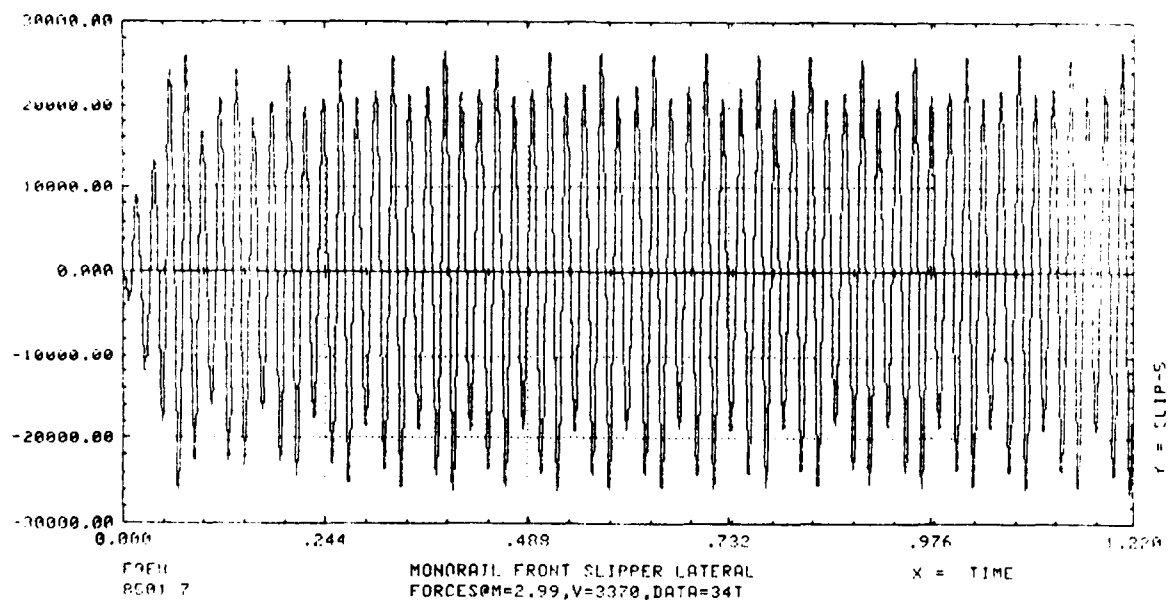


Figure C.61 Modal Monorail, TS 34000 Top

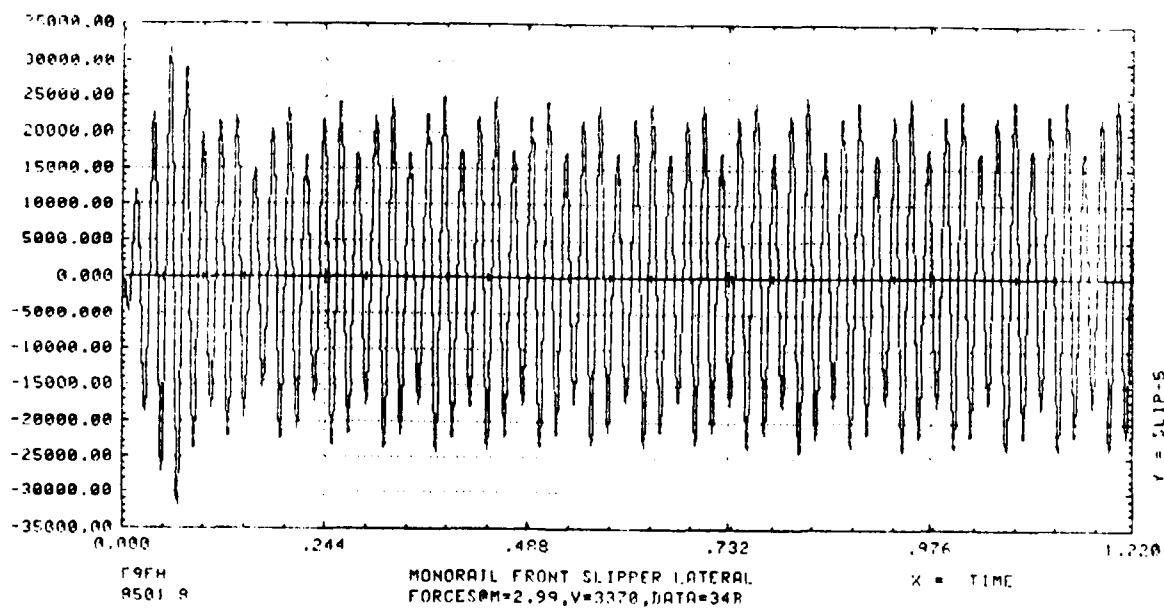


Figure C.62 Modal Monorail, TS 34000 Bottom

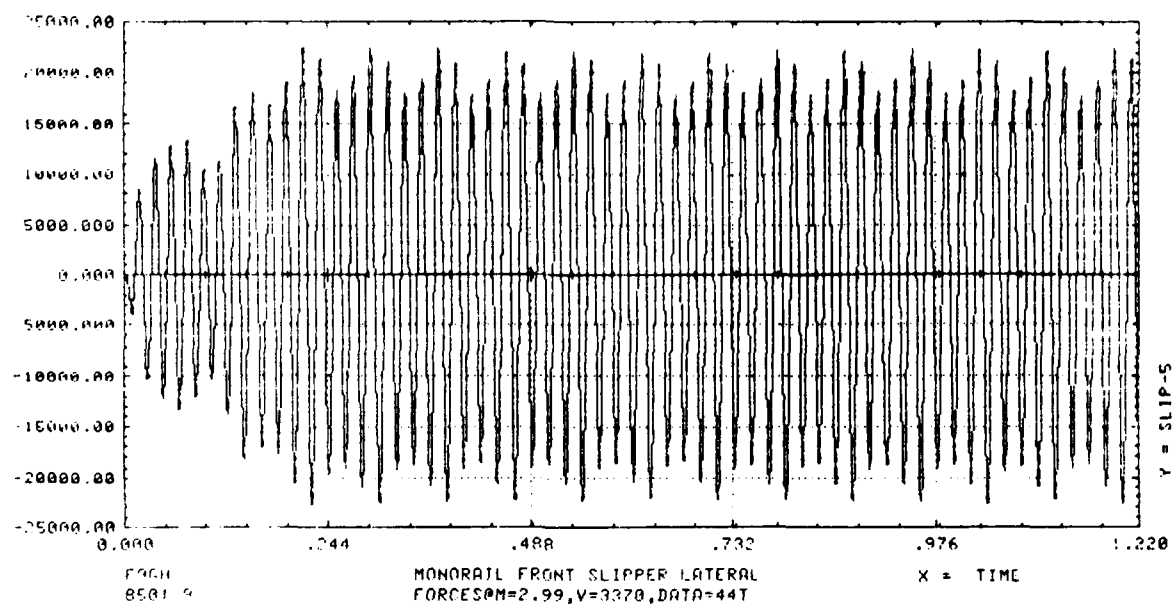


Figure C.63 Modal Monorail, TS 44000 Top

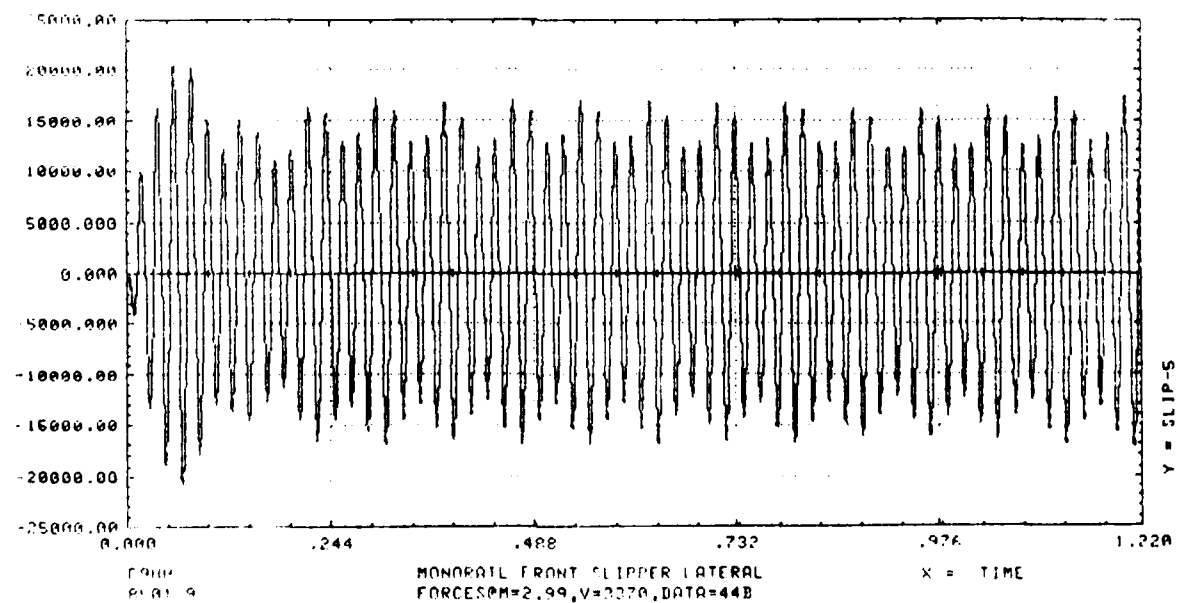


Figure C.64 Modal Monorail, TS 44000 Bottom

END

FILMED

8-85

DTIC